Carboxylate metallogels - an adventure in supramolecular chemistry.

Savannah Clare Zacharias

Thesis presented for the degree of
Doctor of Philosophy

Department of Chemistry
University of Cape Town
South Africa
January 29, 2018

Supervisors:
Professor Susan A. Bourne
Dr Gaëlle Ramon

The process of getting a PhD can be summed up beautifully by
“...it takes ages to get any real coherence out of them. Alas, this is the curse of academia.”
Unseen Academicals - Terry Pratchett
and Johnny Cash in *A Boy Named Sue*, “Kicking and a’ gouging in the mud and the blood and the beer.”

I am sure this can be appreciated by both academics and students.

Acknowledgements

I would to thank my supervisors Professor Susan A. Bourne and Dr Gaëlle Ramon for their guidance, kindness, deep wells of patients, and support.

There are many people whom I wish to thank for their contribution to this body of work:

Professor Delia Haynes, Stellenbosch University, for her kind assistance with the collection of electron spin resonance data.

Professor Timothy Egan for insightful conversations, about the inorganic chemistry of iron and as well as electron spin resonance.

Professor Peter Mallon, Stellenbosch University, for a very insightful discussion into applying differential scanning calorimetry to polymers.

Professors Mino Caira and Luigi Nassimbeni for always answering my questions about the finer points of chemistry and to Professor Nassimbeni for deeming me deserving of chocolate.

Ms Jacqueline Naidoo and Ms Jocelyn Browne at Anton Paar for making the Anton Paar MCR 72 Rheometer available to me and for their help with the collection of the viscosity data.

Dr Clive Oliver for his help with gas sorption experiments.

Dr David Kuter for his kind assistance with the magnetic susceptibility, this assistance was invaluable and greatly appreciated.

Dr Hong Su for the single crystal data collection and processing.

Mr Yaasien Ely and Mr Pieter de Kock for keeping equipment working and the building standing.

Mrs Deirdre Brooks and Mrs Karin Badenhorst for heroic efforts in keeping paperwork away.

My deepest thanks to Dr Vaughan Maurel for discussions, kindness and many, many cups of tea.

Ms Shakeela Sayed for thought provoking discussions in parking lots.

Ms Nikki Dare for always being available as a sounding board for ideas and early morning cups of tea.

Mr Jared Peacock for being wickedly awesome.

To my friends and family for their love and support.

I am grateful to the NRF for providing student funding in the form of the NRF Innovation Doctoral Scholarship. Any conclusions expressed in this presentation are those of the author and the NRF does not accept liability in this regard.

I would like to acknowledge the University of Cape Town for providing the equipment and facilities required to complete this work as well financial assistance.

Presentations

Parts of this thesis have been presented at various conferences and symposiums:

International Conference on Chemistry of the Organic Solid State XXIII Stellenbosch, South Africa.
2 - 7 April 2017
Oral presentation: The role of the ligand in formation of iron(III) supramolecular gels.
Savannah C. Zacharias, Susan A. Bourne, Gaëlle Ramon.

South African Chemical Institute, Western Cape Young Chemists Symposium, Stellenbosch, South Africa.
24 October 2016
Oral presentation: Characterisation and dye sorption studies of iron(III) supramolecular gels.
Third prize for oral presentation awarded.
Savannah C. Zacharias, Susan A. Bourne, Gaëlle Ramon.

Indaba 8, Serendipity vs Prediction, Skukuza, South Africa.
Poster presentation and flash oral presentation: Characterization and dye sorption studies of iron(III) supramolecular gels.
16 - 21 August 2015
Savannah C. Zacharias, Susan A. Bourne and Gaëlle Ramon.

South African Chemical Institute, Western Cape Young Chemists Symposium, Cape Town, South Africa.
Poster presentation: Characterisation and dye sorption studies of iron(III) supramolecular gels.
10 April 2015
Savannah C. Zacharias, Susan A. Bourne and Gaëlle Ramon.

Carboxylate metallogels - an adventure in supramolecular chemistry.

Savannah Clare Zacharias

Abstract

The field of supramolecular gels has attracted a great deal of attention as these versatile materials have been shown to be highly tunable and responsive to stimuli making them attractive for a multitude of potential applications such as drug delivery, energy and gas storage, and waste water treatment.

Serendipity still plays a role in gel discovery. However, with the ever growing library of gels, design is becoming a greater possibility. Interactions involved in the formation of gels are closely related to those in the field of crystal engineering.

There are two parts to this body of work. The first follows the exploration of factors that influence carboxylate gel formation. The second is to examine the response of the iron(III)-carboxylate metallogels to external stimuli.

For the gel formation, a range of small carboxylic acids (ligands), solvents, metal salts, and temperatures were used to investigate their respective roles. Systematic study showed that gels from ligands with carboxylate moieties in the *ortho* position passed the "inverted vial test" most consistently. Of the solvents used, only those with polarities between 4 and 7.2 resulted in gel formation. In general, the rate of gel formation increased with an increase in temperature.

It was found that the nature of the counter ion influences the outcome of gelation. Inorganic counter ions such as nitrate and halides resulted in gel formation, while organic counter ions such as acetylacetonate and oxalate did not.

Characterisation was performed using thermal analysis, Fourier transform-infrared spectroscopy, microwave plasma atomic emission spectroscopy, scanning electron microscopy, and powder X-ray diffraction. It was found that the gels were *ca.* 95-99% solvent. The creation of xerogels, by oven or freeze drying, allowed for better characterisation.

The response of the gel to stimuli was explored and they were shown to interact with their environment. Dyes bromocresol green and methyl orange were both sorbed, in different amounts, by the two carboxylate-iron(III) metallogels, Fe-5nite-DMF and Fe-tri-DMF. This was monitored using UV-visible spectrophotometry.

Gas sorption experiments were performed using carbon dioxide, hydrogen, nitrogen, and water vapour. This was done in order to determine the response of selected xerogels to gas as well as to examine the effect of the drying method on pore size and gas sorption capability. In all cases, water vapour was adsorbed in the greatest quantity. A range of 184.54 cm^3 (STP) g^{-1} to 577.36 cm^3 (STP) g^{-1} at a relative pressure of 0.760 was seen.

Separation of compounds with similar boiling points was attempted using Fe-phens-EtOH, Fe-tri-EtOH, and Fe-5nite-EtOH. The compounds, 2- and 3-methylpiperidine, disrupted the stabilising interactions within the gel and no separation took place.

During the investigation into the role of an organic counter ion in gel formation, three novel crystal structures were obtained from iron(III) acetylacetonate and 2,6-pyridinedicarboxylic acid. The structures elucidated were found to be dependent on the temperature and length of time allowed for the reaction.

Multiple factors influence gel formation and with a better understanding of these, tunable materials for specific applications may be created.

Abbreviations and compound codes

I	$[Fe(C_5H_7O_2)(C_7H_3NO_4)(H_2O)]\cdot CH_3CN$
II	$Fe(C_5H_7O_2)(C_7H_3NO_4)$
III	$[Fe(C_5H_7O_2)(C_7H_3NO_4)]_4$
IV	$Co(CHO_2)_2\cdot 2H_2O$
V	$3[Co(C_9H_3O_8)(C_3H_6NO)_2\cdot\frac{2}{3}(C_3H_6NO)]$
1245btc	1,2,4,5-Benzenetetracarboxylic acid
25pca	2,5-Pyridinedicarboxylic acid
26pca	2,6-Pyridinedicarboxylic acid
35pca	3,5-Pyridinedicarboxylic acid
2D	Two dimensional
3D	Three dimensional
5nite	5-Nitroisophthalic acid
Ace	Acetone
Al	Aluminium(III) nitrate nonahydrate
BET	Brunauer - Emmett Teller
Co-acac	Cobalt(III) acetylacetenoate
DCM	Dichloromethane
DMA	*N*,*N*-Dimethylacetamide
DMF	*N*,*N*-Dimethylformamide
DMSO	Dimethylsulfoxide
DSC	Differential scanning calorimetry
EDS	Energy dispersive spectroscopy
ESR	Electron spin resonance spectroscopy
EtOH	Ethanol

Abbreviations and compound codes continued.

Fe	Iron(III) nitrate nonahydrate
Fe-acac	Iron(III) acetyleacetenoate
$FeBr_3$	Iron(III) bromide
$FeCl_3$	Iron(III) chloride hexahydrate
Fe-ox	Iron(II) oxalate dihydrate
Fe-sul	Iron(III) sulphate hydrate
$(\text{Fe-tri-DMF})_{crystal}$	$Fe(C_9O_6H_6)_4 \cdot x$solvent
FT-IR	Fourier transform-infrared spectroscopy
H_2O	Water
HSM	Hot-stage microscopy
ICP-OES	Inductively coupled plasma optical emission spectrometry
iso	Isophthalic acid
MeCN	Acetonitrile
MePH	Toluene
MOF	Metal organic framework
MP-AES	Microwave plasma – atomic emission spectroscopy
phens	Phenylsuccinic acid
PhCN	Benzonitrile
PrOH	Propanol
PXRD	Powder X-ray diffraction
SEM	Scanning electron microscopy
terept	Terephthalic acid
TGA	Thermogravimetric analysis
tri	Trimesic acid
UV-vis	Ultraviolet visible spectrophotometry

Contents

Chapter 1

Introduction

1.1 Gel characteristics and characterisation

Gels are all around us, from wobbly dessert to face cream, we interact with gels on a daily basis. Humans have used gels for centuries, the ancient Egyptians used a fat based hair gel.[1] Although these ubiquitous materials are all around us, as Dorothy Jordan Lloyd noted in 1926, "The colloidal condition, the gel, is one which is easier to recognize than to define.".[2,3] Gel theory was first described in 1861 by Thomas Graham.[4] If one examines the chemical composition of the substances historically termed gels this group is a seemly disparate collection of materials.

Historically, it included lamellar mesophases, inorganic clays, vanadium pentoxide gels, phospholipids, certain disordered (or partially disordered) proteins, and of course, three-dimensional or network polymers.[5] It came about at a time when elucidation of the molecular composition of a sample was only possible for the simplest compounds and was an attempt to classify materials using their morphologies and physical characteristics.[4] In part, physical attributes are included in today's accepted definition which was advanced by Paul John Flory in 1974.

"A gel is solid-like in its rheological behaviour and exists in a continuous state on an analytical time-scale.".[5] Paul John Flory subdivided gels into four classes:

1. Well-ordered lamellar structures, including gel mesophases. Examples of these include soap gels, phospholipids and clay. The forces in phospholipids are predominantly van der Waals forces and dipole interactions. The lamellae are well defined and are arranged in parallel which leads to comparatively long range order chiefly governed by electrostatic forces.
2. Covalent polymeric networks; which are completely disordered; these include vulcanized rubbers, elastin, vinyl-divinyl copolymers, alkyde phenolic resins, paint films, and

polysilicic acids.

3. Polymer networks formed through physical aggregation such as gelatin.
4. Particulate, disordered structures, precipitates consisting of highly anisotropic particles (*i.e.* needles or matted fibres) or reticular networks of fibres.

It is gels of the fourth type which will be examined in this study.

The definition of a gel has evolved over time and currently includes materials formed by the self-assembly of low molecular weight compounds into supramolecular gels. This colloid state is formed from the interaction of two or more components immobilising a large volume of liquid. They are macroscopic, homogeneous materials which are solid-like in their rheological behaviour and they do not flow.[6] Terms commonly used include low molecular weight gelators (LMWGs), organogels, and hydrogels, depending on the nature of their fluid component. Organogels have an organic fluid component and hydrogels a water fluid component.[7] A xerogel is obtained when the liquid component has been removed by evaporation. This often results in extreme shrinkage of the material. Metallogels contain a metal ion, and can be classified further depending on the role of the metal ion (Figure 1.1). Discrete metal complex gelators are those which assemble through non-covalent interactions and are extended by the ligand or the metal ion. An example of this type is the zinc(II) metalloporhyrinate gel.[8] The metallogels in which the metal ions act as nodes between the organic linkers are known as coordination polymer gels.[9]

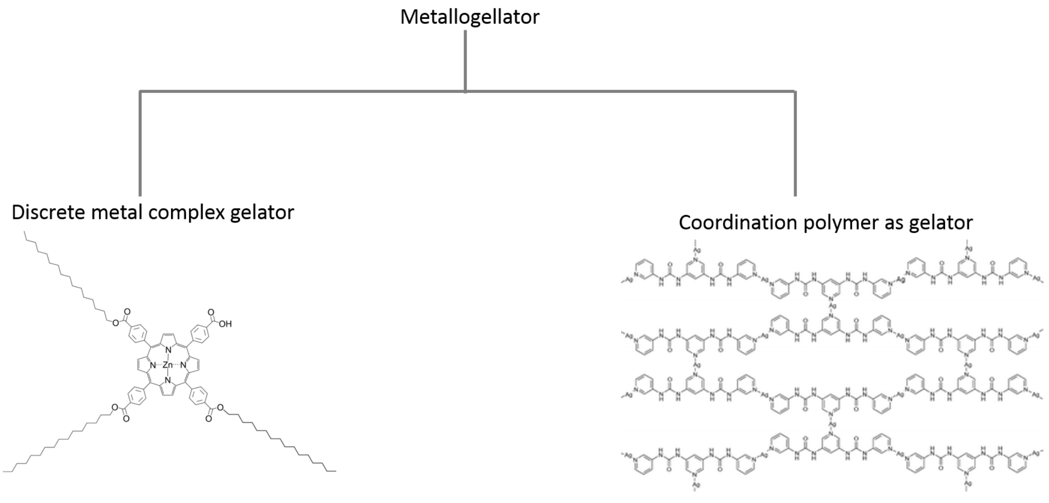

Figure 1.1: Classification of metallogels adapted from multiple sources.[8,10,11] The structure on the right is of the proposed binding in the two-dimensional fibre sheet of a bis(urea) silver metallogel.[11]

The self-assembly of these materials is driven by non-covalent interactions such as hydrogen bonding, van der Waals forces, $\pi - \pi$ interactions, metal coordination and host-guest inclusion.[12] These non-covalent interactions allow for reversible gel-to-sol phase transitions.[13] A network is formed by self-assembly and the non-covalent interactions result in the formation of higher order structures, that may be seen on the nano scale. Examples of this include fibers, ribbons, sheets, and spheres which entangle a large volume of solvent.[12] During gel formation there is competition with other amphiphile aggregations such as micelles, vesicles, lamellae and amorphous or microcrystalline precipitates.[14] Figure 1.2 shows simple schematic of this process.

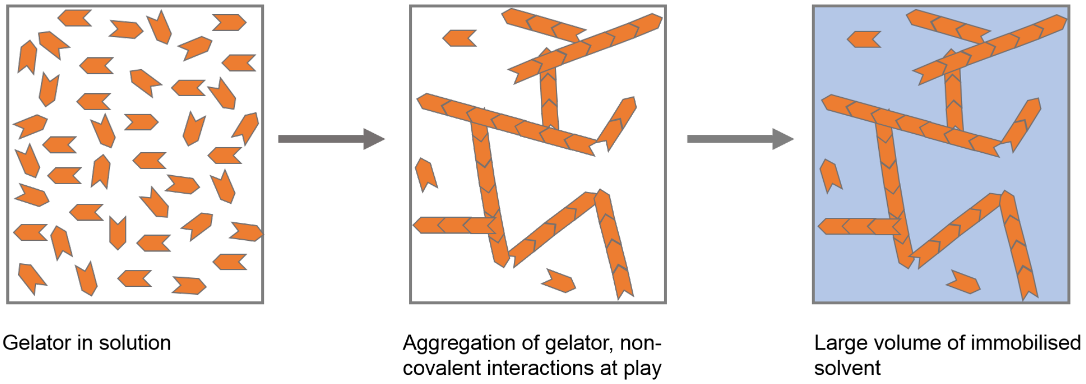

Figure 1.2: A simple cartoon illustrating gel formation which has been adapted from Buerkle and Rowan.[12]

Gels are complex soft materials, which are not quite solid nor quite liquid. This poses a challenge for their characterisation and handling. One of the first gels was described by Thomas Graham in 1864 as a "jelly of silicic acid". It is a hydrogel of 1% silicic acid[15] and the phenomenological characteristics of the substance were described in terms of properties and behaviour. The initial recognition of a gel is the inverted vial test as gels are resistant to gravitational forces when their vessel is inverted.[16]

The high concentration of solvent present can make determining the connectivity of the gel components difficult. Therefore the material is dried before analysis. In such cases an xerogel is prepared by removing the solvent component of the gel. Fourier transform-infrared and Raman spectroscopy can be used to understand their chemical connectivity.

The advancement of technology has allowed for the development of experimental equipment and techniques which can be used to characterise and understand gels. Nevertheless, accurate observation still plays a key role in describing the behaviour of gels.

Rheology is used to determine the viscosity of the material. Yield stress and the complex dynamic modulus, G, are obtained from rheological experiments and give information about the rigidity of the material. There are two components: elastic storage modulus, G', and elastic loss modulus, G'', which give the elastic and viscous behaviours of the material respectively. Information about the structure of the gel can be determined when the storage and loss moduli as well as yield stress are modelled mathematically as a function of applied stress or oscillatory frequency and concentration.

The morphologies of gels are examined using scanning electron microscopy (SEM) and transmission electron microscopy (TEM). A variety of structures are seen, as shown in Figure 1.3 ranging from long fibres[17] to blocks.[18] Gels are often freeze dried to try to maintain the original morphology. These results can be coupled with those obtained from neutron and small angle X-ray scattering, which are used to model the fibres or nanoparticles present.

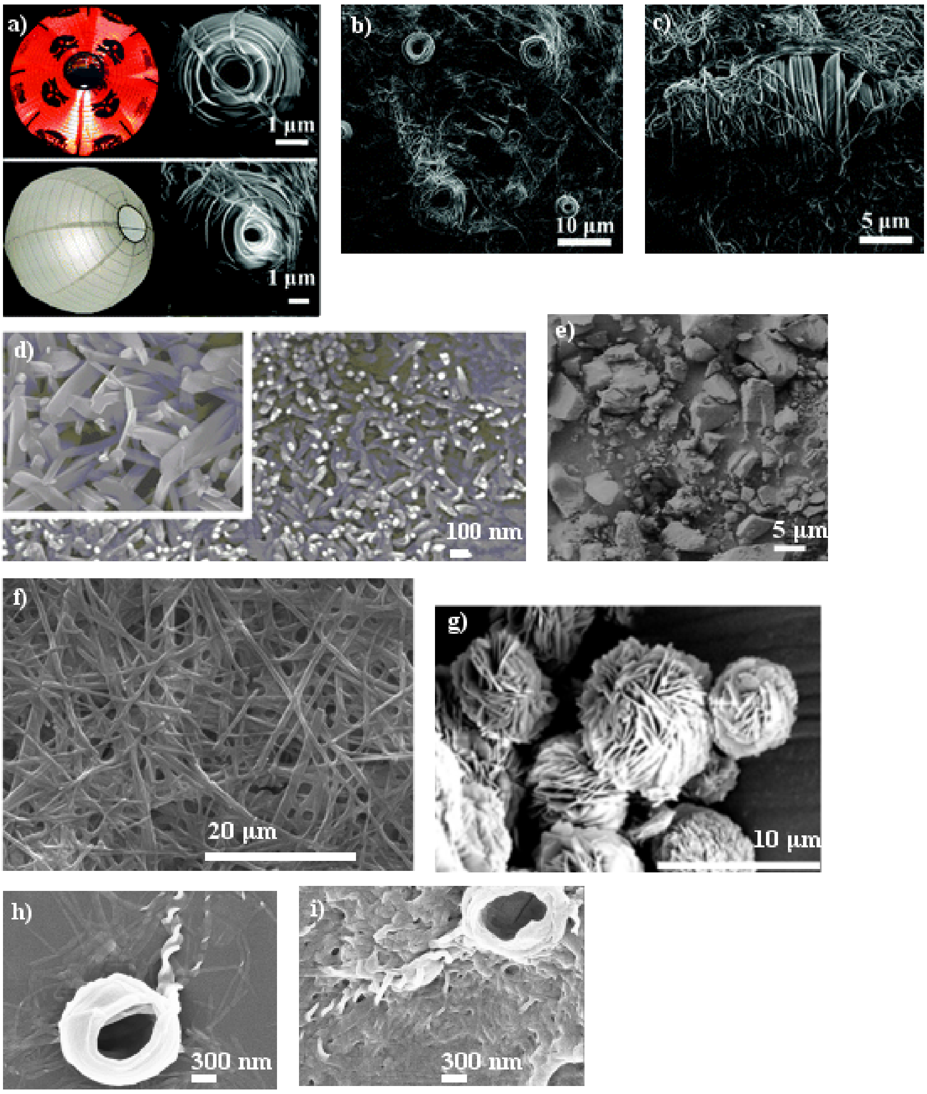

Figure 1.3: Morphologies of various gels viewed using SEM adapted from various sources.[18–23] A multitude of morphologies have been reported including; a-c) lantern shaped coiled gel (lanterns were added for reference),[19] d) short rods,[20] e) block-like shapes,[18] f) randomly arranged fibres,[21] g) petal like structure[22] and h-i) super-coiled helices.[23]

The thermal properties of gels are studied using thermal analysis including hot-stage microscopy (HSM) and differential scanning calorimetry (DSC), as well as thermal gravimetric analysis (TGA). TGA can be used to determine the thermal stability and the solvent content of the gel. Information about possible phase transitions such as glass transitions, and freezing point of solvent trapped in the gel pockets can be gained using DSC.

In isolation these techniques do not give in depth information about the interactions within the gel. A combination of rheology and DSC data can be used to determine the heats of activation for the setting of gels.

Recently, nuclear magnetic resonance (NMR) techniques have been combined to explore structures within the gel and the dynamics of the chemical species. Cross-polarisation solid-state NMR is used to detect the solid-like fibres of gels.[24] The interfaces of the fibres and the solution can be investigated using pulsed-field gradient high-resolution magic angle spinning NMR. These techniques give greater insight into gel formation and how the addition of various molecules impact the properties of a gel.

1.2 Factors influencing gel formation

Gels have often been discovered serendipitously. However, as the field grows the ability to design and synthesise a gel with the desired properties or for a specific purpose becomes more possible. This continues to improve as our understanding of influencing factors at the molecular level improves.[25,26] These materials have been shown to be highly tunable[27] and multiple factors including metal, counter ion[28] and solvent[21] play a role in gel formation. The ligands and metal ions chosen will impart properties to the material.

Variations in ligand can result in changes in gelation behaviour, morphology and conformations. Chan *et al* have developed one such system which varies the chain length of the 2,6-bis(*N*-dodecylbenzimidazol-2′-yl)pyridine pincer ligand.[29] These are dinuclear alkynylplatinum(II) metallogels (referred to as **1**, **2**, and **3**) stabilised by $\mathrm{Pt}\cdots\mathrm{Pt}$ and π-π interactions. Figure 1.4 illustrates the differences in morphology with increasing chain length. The morphology of **1** (which has the shortest chain) shows nanowires, which may be a result of aggregation of the extended chain structure of **1**. As the chain length is increased in **2** a continuous fibrous structure is seen, stabilised by the $\mathrm{Pt}\cdots\mathrm{Pt}$ and π-π stacking interactions which give rise to high-order hierarchical architecture. The extended chain length of **3** results in unstable helical turns which could result in the loosely formed nanofibres.[29]

Banerjee and co-workers report a system where the physical properties of a gel can be tailored

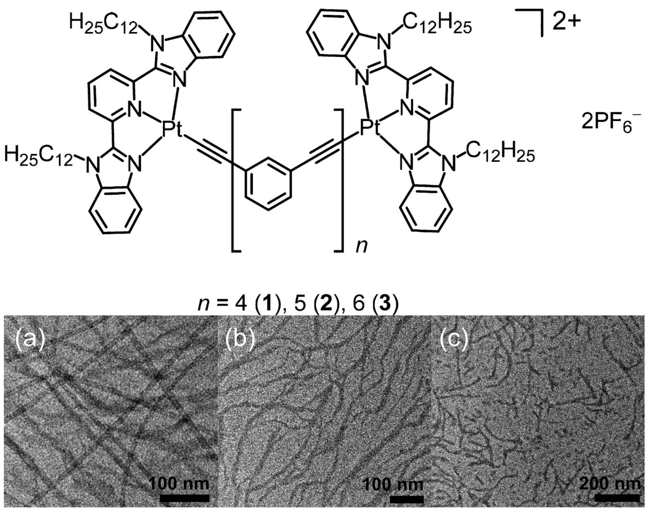

Figure 1.4: Change in morphologies of platinum 2,6-bis(*N*-dodecylbenzimidazol-2′-yl)pyridine gels viewed using transmission electron microscopy (TEM), adapted from Chan *et al* 2017.[29] Above) Ligand increasing in chain length. Below) Corresponding TEM images with increasing chain length. The samples were prepared in acetonitrile.

by modifying the ligands.[30] The chain length of the ligand influences the rigidity of the gel formed with Ni(II) ions. A series of tyrosine based amphiphiles was examined and it was found that the rigidity of the gel increased with increasing chain length.[30]

The efficiency of gelation can also be modified with the use of metal ions. Byrne *et al* report an increase of stability in a series of pyridyl urea gels when metals such as Cu(II) and Ag(I) are used (Figure 1.5).[31] This enhancement of stability is attributed to the change from urea$\cdots$pyridyl hydrogen bonding in the free ligands to a metal ion cross linked urea tape motif.

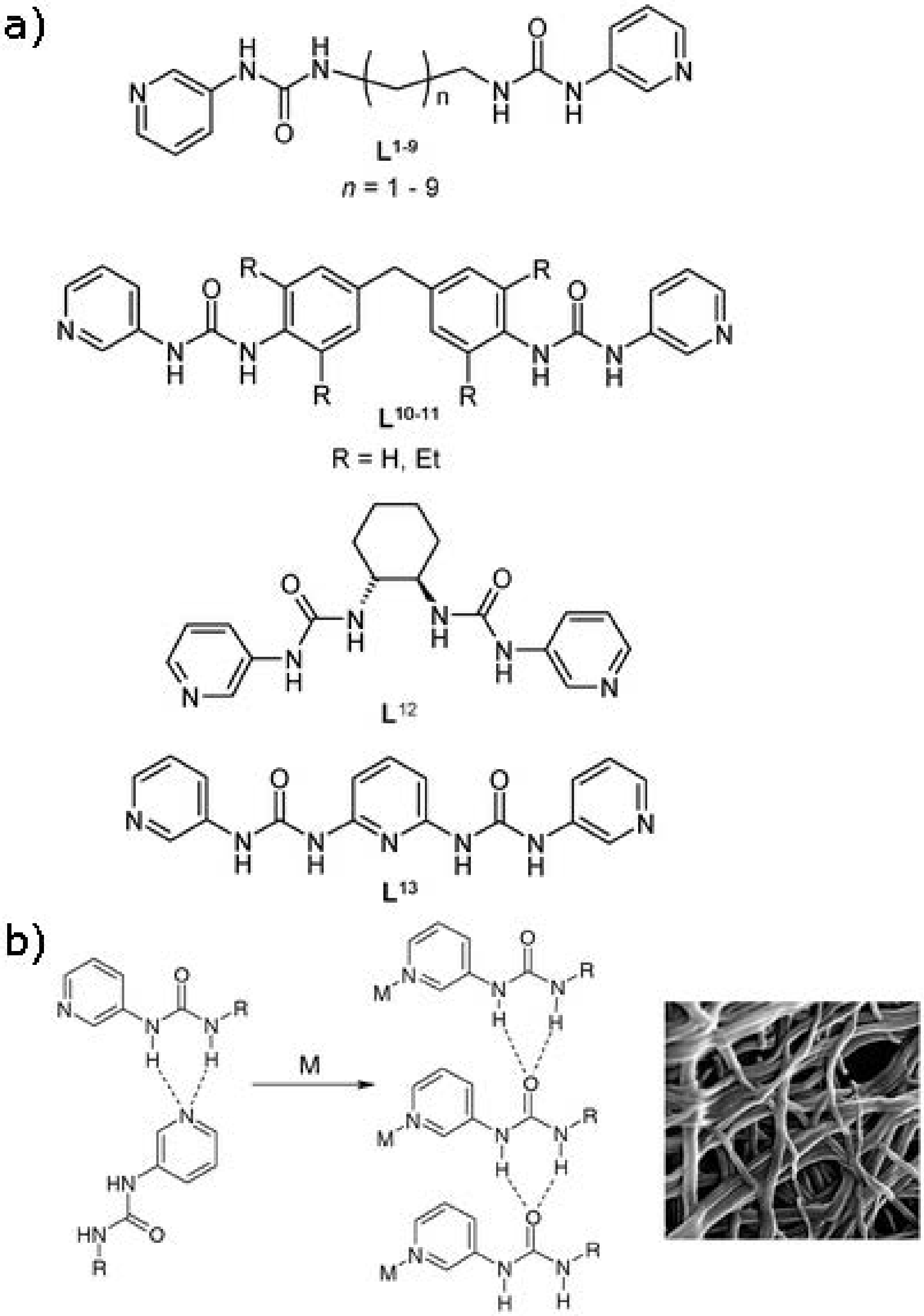

Figure 1.5: a) Pyridyl urea ligands used. b) Schematic illustration of metal ion binding to the ligands and a SEM image of the fibres formed. Adapted from Byrne *et al.*[31]

Cases have been reported where gelation only occurs for a selected metal ion. One such system is a Cu(II)-selective hydrogelation of a *p*-pyridyl ended oligophenylenevinylene system.[32] Gels will only form when $CuCl_2{\cdot}H_2O$ is added to an aqueous solution of the ligands. Other chloride salts of transition metals such as Co(II), Ni(II), Cu(II), Zn(II), Cd(II), and Hg(II) and Ag(I) as silver trifluoromethanesulfonate (AgOTf) were used. None of these resulted in gel formation. Characterisation of these gels showed the Cu(II) ion to have a distorted square planar geometry. The ligand has to fold into a specific conformation in order to achieve this distorted square planar geometry. It is proposed that this folding triggers π - π interactions and van der Waals forces through interdigitation of the oxyethylene chains (Figure 1.6). This results in gel formation.

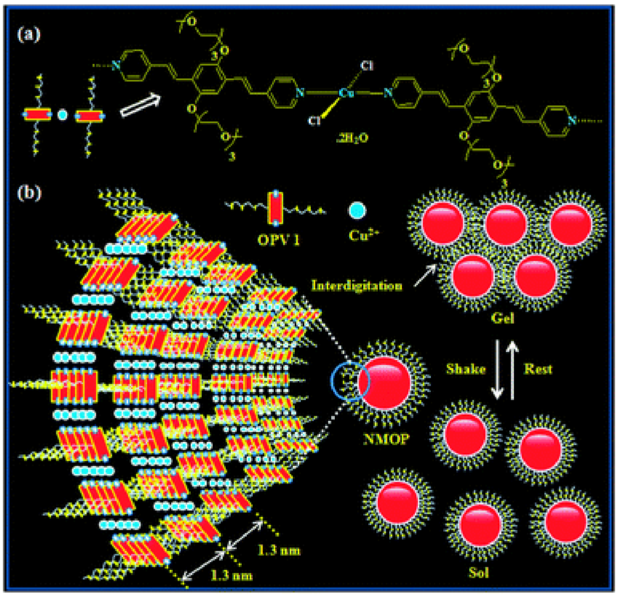

Figure 1.6: a) Coordination of Cu(II) to the *p*-pyridyl ended oligophenylenevinylene ligand. Cu(II) has a distorted square planar geometry. b) Schematic representation of supramolecular metallogel formation as a result of the folding of ligand. Reproduced from Bhattacharjee *et al.*[32]

The choice of counter ion of the metal salt is also an important consideration. An inorganogel (one which only has inorganic components) was formed from aqueous silver nitrate and ammonium vanadate.[33] Other Ag(I) salts such as $AgNO_3$, Ag(OAc), and Ag_2SO_4 were investigated. It was found that the counterion had no bearing on the formation of the inorganogel. However, in other cases the counterion plays a significant role and gel synthesis can be hindered by the use of a different counterion.

Figure 1.7 shows the results reported by Terech and co-workers.[34] Gels are only synthesised when the chloride salts of either cobalt(II) or nickel(II) are used in an acetonitrile solution of a cyclam-bis-terpyridine ligand. The key factors in this case were the electrostatic interactions and the solubility of the species. The metallopolymer-chloride system has a higher solubility in acetonitrile than its nitrate counterpart, resulting a gel formation.[34]

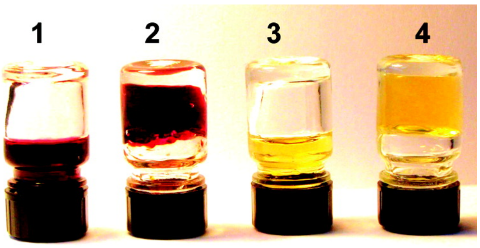

Figure 1.7: Gel or solution formation in an acetonitrile solution of cyclam-bis-terpyridine ligand when different counterions are used (1) $CoCl_2$, (2) $Co(NO_3)_2$, (3) $NiCl_2$, and (4) $Ni(NO_3)_2$. Adapted from Terech *et al.*[34]

The role of solvent is complex and system dependent. This was the subject of a review by Rogers *et al.*[35] The gelator-solvent interactions vary with class of gelator and there is enormous diversity in these interactions. It has been found that each class is able to gel a limited solvent set.[35] Which lead the authors to conclude that '...the quest for the universal gelator should be left in the hands of Don Quixote and as researchers we must focus on identifying gelators capable of gelling classes of solvents as there is likely no one gelator capable of gelling all solvents.'.[35] Nevertheless, trends can be established for specific gelators. This is illustrated by modifying the gelator R-12-hydroxystearic acid (HSA) and testing its efficiency to gel silicon oil in aromatic solvents.[36] When the carboxylic acid moiety of HSA is modified, the gelation efficiency has the following order - primary amide $>$ carboxylic acid $>$ secondary amides $\gg$ amines in silicon oil.

The use of different solvent may result in crystal growth instead of gel formation. Such a system is reported by Nandi and co-workers.[21] Here a gel is formed from 3,5-pyridinedicarboxylic acid and lanthanide metal salts, $La(NO_3)_2 \cdot 6H_2O$ or $Ce(NO_3)_2 \cdot 6H_2O$, when *N*,*N*-Dimethylacetamide (DMA) is used. In *N*,*N*-Dimethylformamide (DMF), crystals of these complexes are formed. The structures elucidated were three-dimensional polymeric networks with solvent accessible hexagonal channels (Figure 1.8). The authors attribute this to the difference in size of the solvents. DMA is the larger of the two and this increased size results the immobilisation of the solvent and gel is formed.[21] Perhaps the larger size is less favourable for the formation of long range order. The importance of investigating metal organic framework (MOF) architectures in gel formation is illustrated.[21]

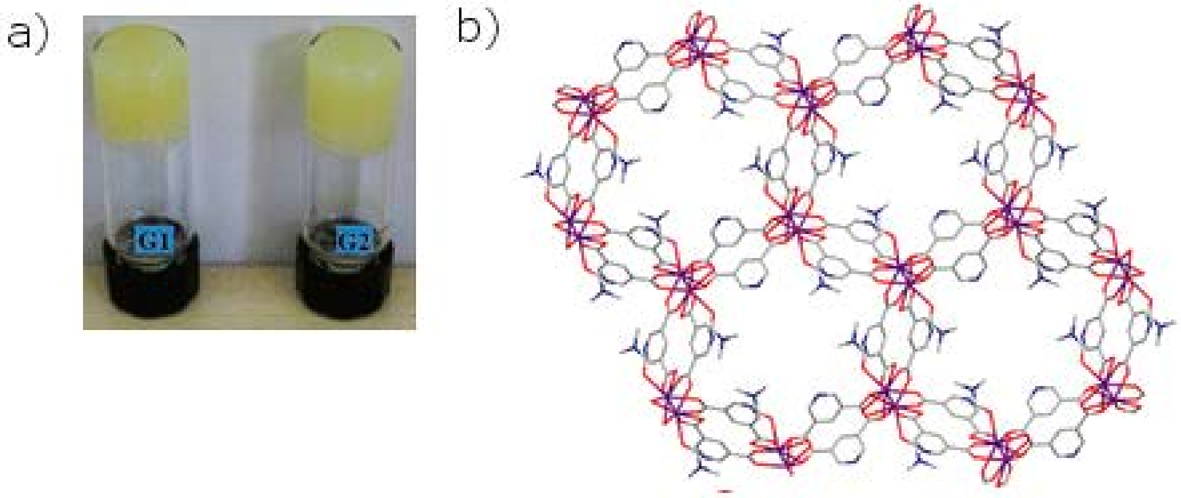

Figure 1.8: a) Metallogels formed from 3,5-pyridinedicarboxylic acid and either $La(NO_3)_2{\cdot}6H_2O$ (**G1**) or $Ce(NO_3)_2{\cdot}6H_2O$ (**G2**) when DMA is used as a solvent. b) Crystal structure of the MOF showing the hexagonal channels down the *a*-axis. Crystals are obtained when DMF is used as the solvent. Adapted from Nandi *et al.*[21]

Gelation can be turned on and off by disrupting the intermolecular interactions of the chosen gelator. As a result of this highly tunable nature, gels can be designed to respond to a specific stimulus. Physical stimuli such as heat, light, and mechanical forces can also be used to switch between solution and gel phases. Unlike chemical stimuli, physical stimuli can be applied remotely and non-invasively.[37]

Temperature is one of these stimuli. An example of a temperature dependent gel was reported by Danjo *et al.* This supramolecular gel is based on D_3-symmetric tris(spiroborate) cyclophanes and $[Ir(tpy)_2](PF_6)_3$. An orange gel is only formed at temperatures greater than 78.5 °C (Figure 1.9).[38] Molecular recognition is shown by the macrocycle which adopts a shape resembling a back-to-back twin bowl and interacts via π-π and electrostatic interactions with the guest. Once the solution is heated above 78.5 °C rapid polymerisation occurs and a gel is formed. The gel returns to solution after 15 min at room temperature, and thus this process is reversible.

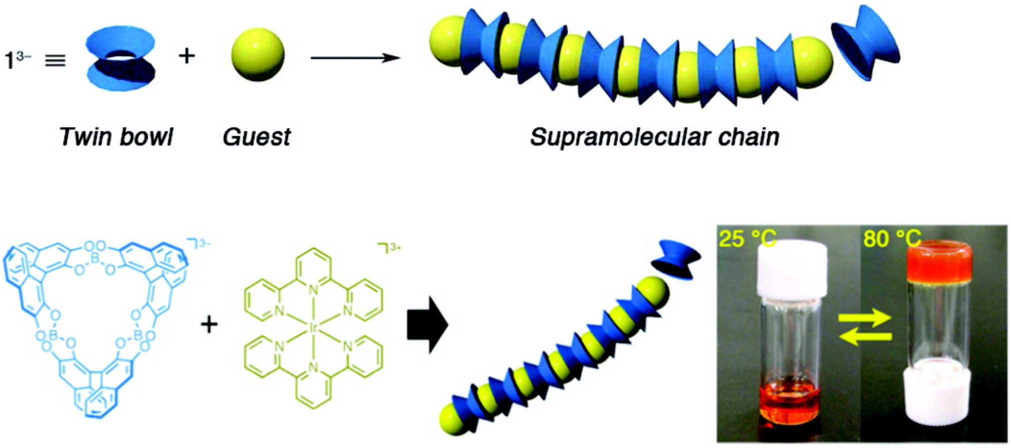

Figure 1.9: An example of a gel which only forms at elevated temperatures, from Danjo *et al.*[38] The D_3-symmetric tris(spiroborate) cyclophanes and $[Ir(tpy)_2](PF_6)_3$ gel only forms at temperatures greater than 78.5 °C, this is a reversible process and upon standing at room temperature it will return to solution form.

An example of pH-responsive sol-gel switching has been demonstrated by Rodríguez-Llansola *et al.*[39] This bisaromatic hydrogelator, compound **1**, contains a urea functional group and is derived from isophthalic acid. Figure 1.10 shows the structure of compound **1** and the change in colour of the solution upon acidification from red-orange to yellow as the carboxylate groups are protonated and gelation occurs. Other chemical stimuli that can be used to control sol-gel switching include acids, bases, ions, redox-active compounds, neutral species, reactive compounds, and enzymes.[40]

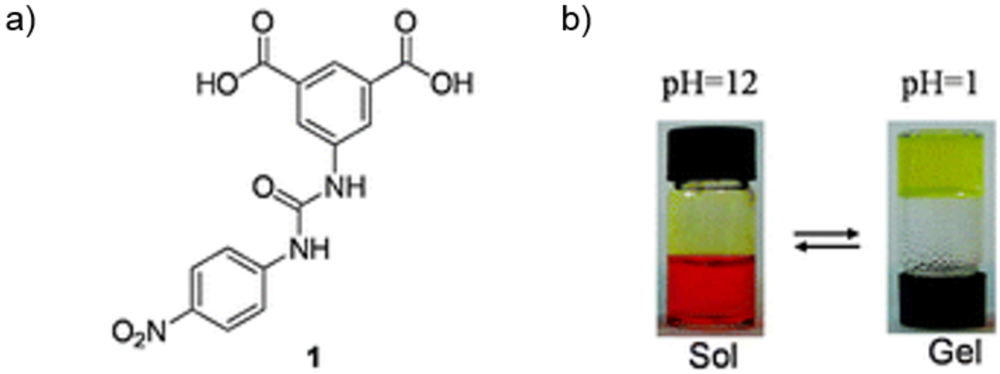

Figure 1.10: a) A pH-responsive bisaromatic hydrogelator (**1**). b) (left) 3 mM red-orange solution of **1** at pH 12 red-orange solution and (right) pH 1 yellow gel after acidification.[39] Image adapted from Rodríguez-Llansola *et al.*[39]

1.3 Smart materials

The self-assembly of metallogels is driven by non-covalent interactions such as hydrogen bonding, van der Waals forces, π-π interactions, metal coordination and host-guest inclusion. These weak interactions which hold the gel together result in the material being able to respond to stimuli.[12] Stimuli such as pH, temperature, the presence of other compounds can impart interesting mechanical properties to the system. This makes gels suitable for a wide variety of applications such as drug delivery,[41] pollutant removal[42] including oil spills,[43] heavy metals, petroleum by-products, pharmaceuticals,[42] dyes,[44–46] gas storage,[44] catalysis,[47] and chemosensors[48] (Figure 1.11).

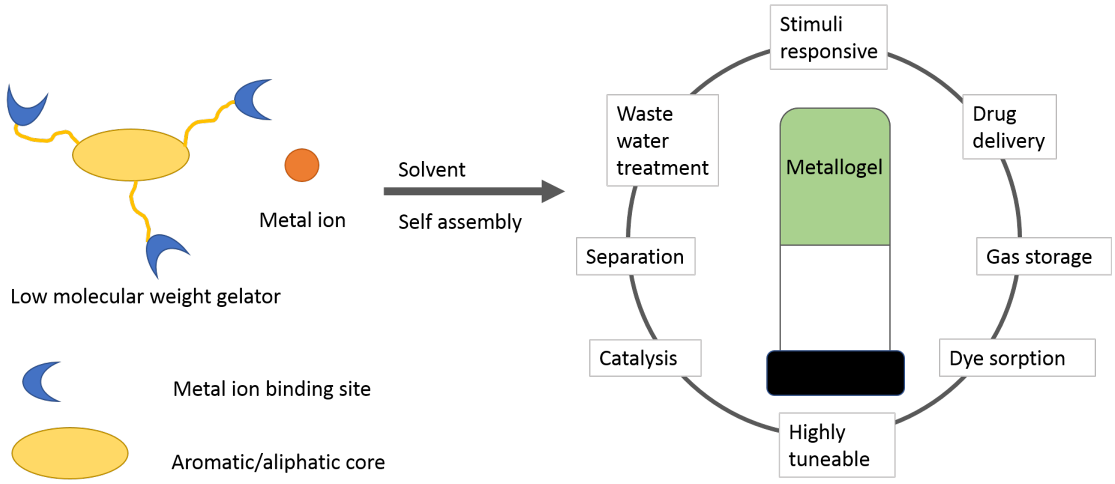

Figure 1.11: General synthetic procedure of metallogels and some of their application in various fields. Image adapted from Sutar and Maji.[10]

Coordination polymer based metallogels contain porous networks that are filled with a large volume of solvent. This results in metallogels possessing two intrinsic characteristics which are important for adsorbent materials, these materials have porous networks and functional groups on the porous surface which can interact with the guest molecules.

1.3.1 Dye adsorption

A metallogel of carboxymethyl-(3,5-di-*tert*-butyl-2-hydroxybenzyl)-amino acetic acid and CdCl$_2$ in methanol (MOG-1) has been shown to absorb the positively charged dye, Rhodamine B (Figure 1.12).[22] Only cationic dyes are adsorbed, this could be explained by the cation replacing the sodium cation in the gel. This gel can be used to separate cationic from anionic dyes.

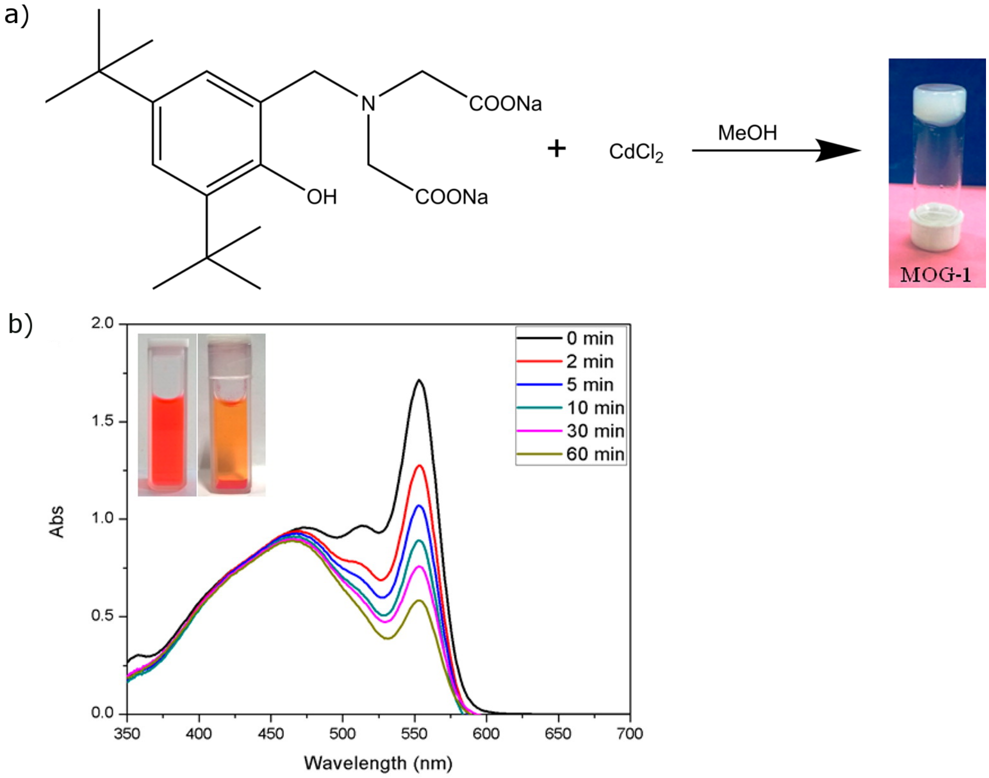

Figure 1.12: a) Synthesis of MOG-1. b) Dye sorption of Rhodamine B by MOG-1. The intensity of the dye solution decreases over time. The absorbance decreases from *ca.* 1.6 to *ca.* 0.5. Adapted form Karan *et al.*[22]

An interesting metallogel which is able to take up dye is the green gel from N^1,N^3-bis[5-(pyridin-2-yl)-1*H*-pyrazole-3-yl]-terephthalamide (BPPTP) and copper triflate (Figure 1.13).[44] The surface of the xerogel interacts with methyl orange *via* hydrogen bonding interactions and bleaching of the orange solution is seen over a 24 h period.

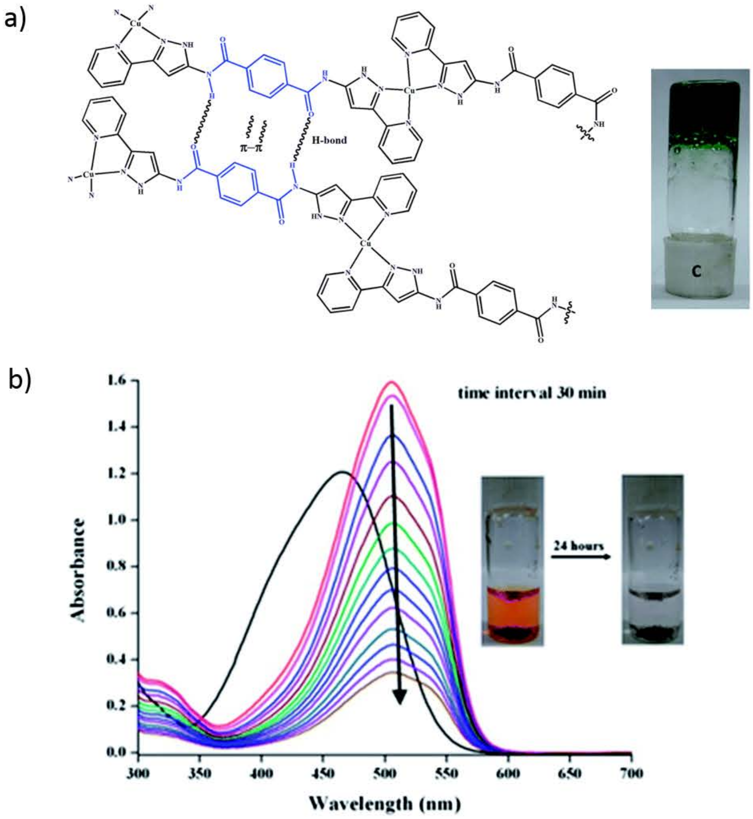

Figure 1.13: Adapted from Sengupta *el al* showing; a) The proposed structure and image of the green gel.[44] b) The uptake of methyl orange from solution, the orange solution becomes colourless over time. The absorbance at decreases from *ca.* 1.6 to *ca.* 0.3 after 30 min.

Gel can be used as a support system for photocatalysis.[49] Vilela and co-workers have demonstrated this using 4,7-Distyrene-2,1,3-benzothiadiazole copolymerized with styrene. The gel was shown to be successful as triplet photosensitizer in the production of $^1O_2$ and $O_2{}^{\bullet -}$.[49] Various dyes, including Rose Bengal, methylene blue or Eosin Blue, can be used for singlet oxygen production.[50,51] These can be absorbed into a gel and used as a photosensitizer. Singlet oxygen is generated when energy from a light source of the appropriate wavelength is absorbed by the photosensitizer. The photosensitizer is excited using electromagnetic waves to the triplet energy state. This energy is transferred to ground-state triplet oxygen, which results in the formation of singlet oxygen.[52] A few of the applications of singlet oxygen production include fine chemical synthesis, waste water treatment,[53] water and air purification,[54,55] and energy areas including hydrogen generation[56] or carbon dioxide reduction.[57]

1.3.2 Gas sorption

In order for gas sorption experiments to be carried out gels need to be dried as the presence of solvent will negatively affect the experiment. The N^1,N^3-bis[5-(pyridin-2-yl)-1H-pyrazole-3-yl]-terephthalamide (BPPTP) and copper triflate gel is able to take up a large volume of N_2 gas, *ca.* 62 $cm^3\ g^{-1}$ for a xerogel with a BET surface area of *ca.* 106.9 $m^2\ g^{-1}$.[44] CO_2 is also taken up by this compound which has a capacity of *ca.* 8 cm ^{3} g^{-1}. Hysteresis is shown as the adsorption-desorption pathways are not the same (Figure 1.14). This indicates the absorbed CO_2 is not immediately released from the xerogel when the external pressure is decreased and some of it even remains trapped at zero pressure.[44]

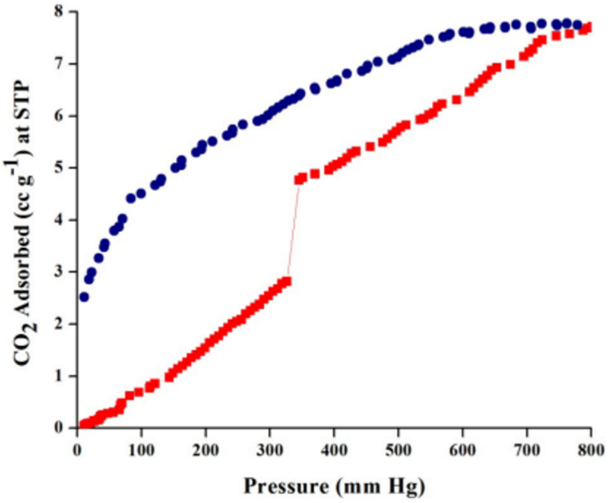

Figure 1.14: Adapted from supplementary information of Sengupta *el al* showing the hysteresis associated with the CO_2 adsorption (red)-desorption (blue) isotherm of copper triflate xerogel.[44]

Gas sorption can also trigger a colour change. An example of this was reported by Jung *et al.*[58] Here a gel synthesised from $CoBr_2$ and a bis(tetrazole) derivative changes colour from orange-yellow to blue-green in the presence of gases containing a chloride ion (Figure 1.15). This is a selective process and no colour change was observed when other halogen containing gases were used. It is proposed that the observed colour change is a result of the change in the coordination geometry of the Co(II) metal centre in the gel. In the orange-yellow gel, the Co(II) cation has an octahedral geometry. Upon exposure to $COCl_2$ gas, the chloride ions replace the bromine ions coordinated to the Co(II) and the colour of the gel changes to blue-green as the Co(II) now has a tetrahedral geometry.[58]

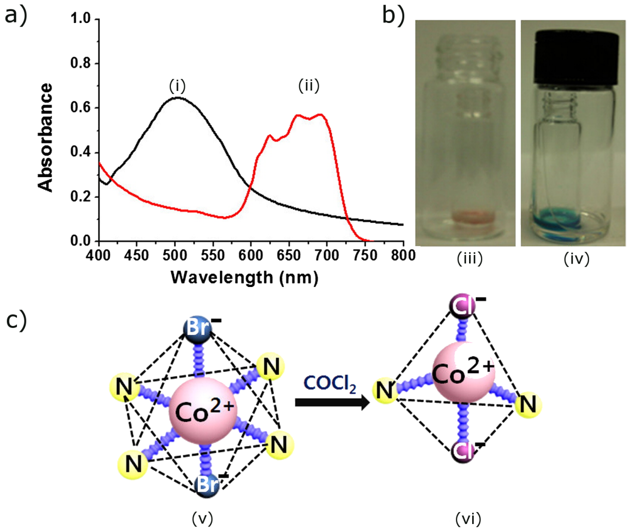

Figure 1.15: a) Uv-vis spectra of Co(II) gel before (i) and after (ii) exposure to $COCl_2$ gas. b) Colour change of gel from orange-yellow (iii) to blue-green (iv). c) The proposed change in geometry of the Co(II) metal centre coordinated to (v) $2Br^-$ and (vi) $2Cl^-$ respectively. Modified version from Jung and co-workers.[58]

1.4 Metal organic frameworks

As was illustrated by Nandi *et al*,[21] metal-organic framework building blocks can be used in gel formation. Metal organic frameworks (MOFs) are composed of metal ions or metal ion clusters which are linked by bridging organic ligands and form large two- and three-dimensional networks.[59–62] The dimensions and chemical composition of the pores can be tailored by modifying the combination of ligand and metal. This gives rise to an abundance of structural versatility in these porous materials.[63,64] These flexible materials can have large solvent accessible channels which allow them to respond to stimuli and display a number of interesting properties, such as “breathing” and “flexing”[65] and solvatochromism. These diverse physical properties lend themselves to a wide range of applications including: catalysis,[66] chemical separation,[67] drug delivery,[68,69] and gas storage.[70,71] Some of the applications, such as gas storage and drug delivery, are a result of the ability of MOFs to adsorp/desorp molecules. The interactions which govern these processes are supramolecular in nature much like supramolecular gels. The use of MOF type architecture, designed to lead to large pore formation, may enable gel synthesis under certain conditions.

1.5 The chemistry of aluminium, cobalt and iron

Not only do metal ions impart new properties to gels, they also provide added stability through metal-ligand coordination. This results in cross linking of the ligands and metal-metal interaction. Three metals were selected for this study: aluminium, cobalt, and iron. Each has different chemistry and these differences will be explored in gel formation.

Aluminium (Al) is the most abundant metal in the earth's crust. It is a group III element with an electronic structure of Al(III) [He]$2s^2 2p^6$ and an electronegativity (Allred-Rochow) value of 1.47. Aluminium has an atomic radius much larger than that of boron, 1.26 and 0.88 Å respectively, hence it is more metallic and ionic in its behaviour. However, it is still borderline between ionic and covalent in its compounds. The inert pair effect is the reluctance of a pair of *s* electrons to be lost, or participate, in order for the formation of a covalent bond. The inert pair effect first appears in this group of elements.
Aluminium is a hard, strong white metal with a high oxidation potential. It forms both octahedral and tetrahedral complexes. Octahedral complexes form with neutral ligands such as water, $[\mathrm{Al(H_2O)}]^{3+}$. Aluminium(III) and iron(III) form similar octahedral structures with acetate. Tetrahedral complexes are more rare, and predominantly form by addition of a neutral donor to Al(III). This neutral donor may be ammonia, amines, ethers, alcohols, ketones, phosphines, thioethers etc.

Cobalt and iron are both first row transition metals. Cobalt is a hard bluish white metal, which has a melting point of 1490 °C. It has been used to add a blue colour to ceramics, glass (Figure 1.16) and glazes by multiple cultures for centuries and was first isolated by Georg Brandt in 1735.[72]

Figure 1.16: Ribbed Bowl, a cobalt blue glass bowl with opaque white decoration from the 1st century BCE. Harvard Art Museums/Arthur M. Sackler Museum, Gift of Professor C.E. Norton and Richard Norton, 1895.[73] Cobalt has been used to add colour to objects for centuries.

Metallic cobalt is relatively unreactive when compared to iron and aluminium and is predominantly used in alloys that retain their properties at high temperatures. Octahedral complexes are the most common for Co(III), however tetragonal complexes have also been reported. The electronic configuration of Co(III) is $[\mathrm{Ar}]3d^6$ and it has an electronegativity of 1.88. Co(III) shows particular affinity for nitrogen donor atoms although complexes involving oxygen donors, such as cobalt(III) acetylacetonate and tris(oxalato)cobalt(III) are also known.

Iron is the second most abundant metal after aluminium. Pure iron is a white, lustrous metal which is fairly reactive and not very hard, it melts at 1528 °C. It is commonly found in ore, the most abundant being heamatite. Iron is an important metal in numerous industrial areas including as the catalyst for both the Haber and Fischer–Tropsch processes for the production of ammonia and the conversion of syngas into liquid fuels, respectively.[74] It is used in a variety of steels (an alloy with carbon and other metals) which are used in architecture, civil engineering, manufacturing, surgical instruments, cutlery, and bearings. Cast iron has a higher carbon content (3-5%) and is used for pipes, valves,[74] and cookware (Figure 1.17).

Figure 1.17: An example of cast iron.The 19^{th} century canon on Kanonkop, Cape Point, South Africa.[75]

Iron(III) also forms tetragonal, octahedral and pentagonal bipyramidal complexes, with octahedral being the most common. Iron(III) has a low affinity for amine ligands and no simple anime complexes are found in aqueous solution. Complexes with chelating ligands such as Ethylenediaminetetraacetic acid (EDTA) are found. The greatest affinity of iron(III) is for ligands which coordinate through the oxygen ligand. The electronic configuration of Fe(III) is $[\mathrm{Ar}]3d^5$ and its electronegativity is 1.83.

1.6 Organic ligands

1,3,5-Benzenetricarboxylic acid, or trimesic acid, has been shown to be a successful gelator with iron(III) salts and has been explored as a template for polymer formation[76] and CO_2 uptake.[77] A search of the Cambridge Structural Database[78] provides a multitude of MOFs with trimesic acid as a ligand. 3,5-pyridinedicarboxylic acid has formed gels with lanthanide salts of lanthanum(III) and cerium(III) in *N*,*N*-dimethylacetamide.[21]

Small benzene carboxylic acids similar to trimesic acid and 3,5-pyridinedicarboxylic acid were chosen for this study as the carboxylate moiety can be useful for both metal coordination and hydrogen bonding. A consequence of this is that the ligands chosen have at least two carboxylic acid groups: di-, tri-, and tetradentate ligands were used. In the case of the tridenate ligands, a pyridine group was used to see the effect of the electron withdrawing group and to introduce steric hindrance. Figure 1.18 shows the structures of the ligands used and highlights the features investigated for their role in gel formation.

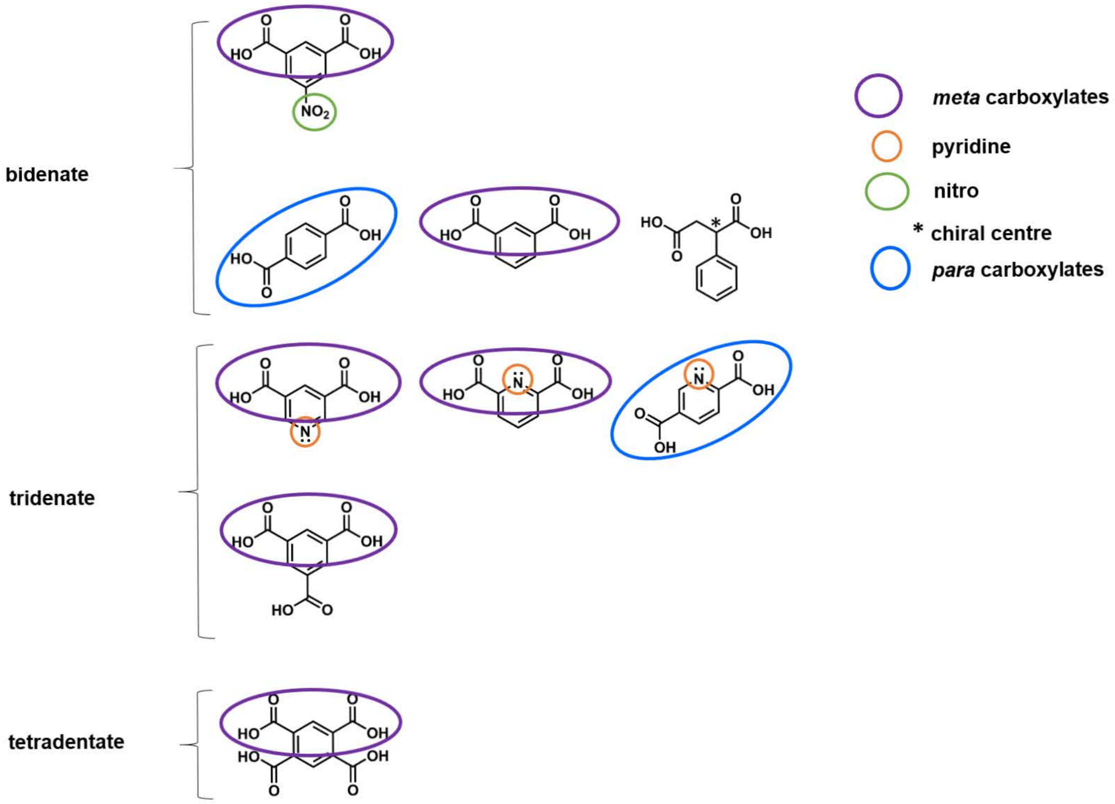

Figure 1.18: Structures of ligands used in this study, highlighting the features investigated for their role in gel formation.

1.7 Objectives

Although the factors influencing gel formation have been reported for various systems, there are few studies focused on investigating the role of each component, the cation, anion, solvent, and temperature, on a specific set of gelators. The objectives of this project were to better our understanding of the influence of each component in order to improve our ability to design gels.

To this end:

- systematic studies where various ligands were combined with several metal salts, focusing on Fe(III) salts, in a number of solvents at a range of temperatures were performed. These were carried out to establish under which conditions gelation occurs.
- the gels formed were characterised using a variety of techniques including thermal analysis, scanning electron microscopy, and Fourier transform-infrared spectroscopy to gain better understanding of the interactions and nature of the material.
- the iron(III)-carboxylate gels were exposed to external stimuli, to investigate the response of these materials for potential applications in dye sorption, gas sorption and chiral separation.
- factors which influence crystal growth instead of gel formation were explored. Such factors include counterion and solvent.
- where possible single crystals were elucidated to gain more information about the possible connectivities and interactions which may play a role in the series of metallogels explored here.

Chapter 2

Experimental

The reagents used in this project are identified in this chapter as well as the methods used. The general instrumentation, techniques, procedures used for the analysis and characterisation of the supramolecular metallogels are also presented. The abbreviations and compound codes can be found on pages vii and viii.

2.1 Reagents and solvents

All ligands (purity $\geq$ 98%) were supplied by Sigma-Aldrich. The ligands used for this work are as follows: 1,2,4,5-benzenetetracarboxylic acid, trimesic acid, isophthalic acid, terephthalic acid, phenylsuccinic acid, 5-nitroisophthalic acid, (*R*)-(-)phenylsuccinic acid, 2,5-pyridinedicarboxylic acid, 2,6-pyridinedicarboxylic acid, and 3,5-pyridinedicarboxylic acid (Figure 1.18).

The metal salts aluminium nitrate nonahydrate ($Al(NO_3)_3{\cdot}9H_2O$), iron acetylacetonate ($Fe(C_5H_7O_2)_3$), iron chloride hexahydrate ($FeCl_3{\cdot}6H_2O$), iron bromide ($FeBr_3$) and zinc nitrate hexahydrate ($Zn(NO_3)_2{\cdot}6H_2O$) were purchased from Sigma-Aldrich. Iron nitrate nonahydrate ($Fe(NO_3)_3{\cdot}9H_2O$) and ferric sulfate nonahydrate ($Fe_2(SO_4)_3{\cdot}9H_2O$) were purchased from BDH Chemicals Ltd and Hopkins and Williams Ltd respectively. M & B Chemicals supplied ferrous oxalate dihydrate ($FeC_2O_4{\cdot}2H_2O$). Bromocresol green was purchased from Saarchem. All chemicals were of a purity $\geq$ 98%.

The solvents acetonitrile, *N*,*N*-dimethylformamide, *N*,*N*-dimethylacetamide, dimethylsulfoxide, and ethanol were of reagent grade quality and purchased from Sigma-Aldrich.

All reagents were used without further purification.

2.2 General preparation method of gels

All reactions were carried out at standard pressure and were open to the atmosphere. When possible, each component was dissolved in the appropriate solvent prior to mixing. Thereafter, the metal salts (0.1 mmol in 1 mL solvent) and ligands (0.1 mmol in 4 mL solvent) were combined in a glass vial with a diameter of 2.4 cm. Various temperatures and solvents were used, details will be given in the relevant sections. Once the adequate time was reached to allow the gel to form, the inverted vial test[6] was performed to confirm gel formation. Xerogels were prepared by synthesising the required gel, followed by either freeze or oven drying. Unless otherwise stated, oven drying was carried out in a 90 °C for at least 72 h. To protect the delicate membranes in the freeze drier, the gels were synthesised in 500 μL quantities and flash frozen before drying until powder was obtained. A VirTis® BenchTop™ K Series Freeze Dryer was used.

2.3 General synthetic procedures of crystals

Single crystals were obtained by solvothermal techniques or directly from gel formation experiments involving solvent evaporation. Details for the different compounds are given in the relevant sections. For the solvothermal reactions the ligand and metal salt were dissolved in *N*,*N*-dimethylformamide, tightly sealed in an autoclave and heated in an oven at a predetermined temperature for a particular length of time.

2.4 Thermal analysis

Thermal analysis techniques used in this project include thermogravimetric analysis (TGA), differential scanning calorimetry (DSC) and hot stage microscopy (HSM). All three methods measure a change in the physical properties of the material as a function of temperature.

2.4.1 Thermogravimetric analysis

A TA-G500[79] from TA Instruments was used in conjunction with Universal Analysis 2000[79] software. A dry nitrogen flow rate of 50 cm^3 min^{-1} was employed. Thermogravimetric analysis (TGA) was used to determine the solvent composition of the gels. Typically 10 mg to 20 mg of gel or xerogel was used with a heating rate of 10 °C min^{-1}.

2.4.2 Differential scanning calorimetry

Differential scanning calorimetry (DSC) measures the difference in heat flow between the sample and reference as a function of temperature under controlled heating and atmosphere. This is used to determine the enthalpies of various thermal events. Endothermic and exothermic reactions correspond with upward and downward peaks in the DSC traces, respectively. The DSC was also used to determine the freezing and melting of the solvent within gel pockets and on the surface of the gel. Samples, weighing between 10 mg to 20 mg of the gel, were analysed in vented Tzero^{TM} aluminium pans. The purge gas was dry nitrogen at a flow rate of 60 cm^3 min^{-1}. Experiments were carried out on a TA Instruments DSC-Q200. Universal Analysis 2000[79] was used to analyse the results.

2.4.2.1 Glass transition

Phase transitions are defined as the spontaneous conversion from one phase to another for a particular substance and occur at a characteristic temperature for a given pressure.[80] The physical nature and composition of phase transitions can be used to classify these events. A few examples include: liquid-vapour, solid-liquid, solid-vapour, solid-solid, and semi solid-semi solid.

In some cases it is more convenient to use thermodynamic properties as a method of classification, such as the Ehrenfest classification which makes use of the chemical potential. Many phase transitions are accompanied by changes in enthalpy and volume, and these changes have implications for the slopes of the chemical potentials of the phases on either side of phase transition. Thus, at the transition from phase α to phase β (Equation 2.1 and 2.2),

$$\left(\frac{\partial\mu_\beta}{\partial_p}\right)_T - \left(\frac{\partial\mu_\alpha}{\partial_p}\right)_T = V_{\beta,m} - V_{\alpha,m} = \Delta_{\text{trs}}V \tag{2.1}$$

$$\left(\frac{\partial\mu_\beta}{\partial_T}\right)_p - \left(\frac{\partial\mu_\alpha}{\partial_T}\right)_p = -S_{\beta,m} - S_{\alpha,m} = \Delta_{\text{trs}}S = \frac{\Delta_{trs}H}{T_{trs}} \tag{2.2}$$

Where T$_{trs}$ is the transition temperature, T is temperature, p is pressure, μ is the chemical potential of each of the different phases α and β. S, V_m and H are entropy, molar volume and enthalpy respectively.

Both $\Delta_{\text{trs}}V$ and $\Delta_{trs}H$ are non-zero for melting and vaporisation, and because of this such transition slopes of chemical potential plotted against either pressure or temperature are different on either side of the transition. The first derivative of the chemical potentials with respect to pressure or temperature are discontinuous at the transition.

First-order phase transitions are ones in which the first derivative with respect to temperature are discontinuous. Enthalpy, H, changes by a finite amount of infinitesimal changes in temperature. Therefore the heat capacity is infinite. The physical reason for this phenomenon is that heating, rather than an increase in temperature, drives the transition.

A transition for which the first derivative of chemical potential with respect to temperature is continuous but its second order is discontinuous is classified as a second-order phase transition. A continuous slope of chemical potential (a graph with the same slope on either side of the transition) implies that the volume and entropy (and hence enthalpy) do not change at the transition. The heat capacity is discontinuous at the transition but does not become infinite there.[80]

The gel-glass transition is an example of a second-order phase transition. A glass transition (T_g) occurs when a material passes through a heat-capacity change without an accompanying latent heat.[81] This can be illustrated by transitions of synthetic polymers with mobile chains. At ambient temperature the chain has sufficient energy for limited bond rotation and the flexible chains are able to move and writhe. As the temperature is lowered the amplitudes of the writhing motion decreases until the movement is frozen and the sample forms a glass.[82] The specific temperature at which this freezing occurs is T_g.

2.4.3 Hot stage microscopy

Hot stage microscopy (HSM) allows for the visualisation of thermal events which can be correlated with the data obtained from TGA and DSC. Samples were heated at a controlled rate (10 °C min^{-1}) and the temperatures recorded for occurring events. The temperatures may differ from those recorded on the TGA and DSC. These differences are largely a result of the lack of purge gas and the differing geometries of sample holders. A Nikon SMZ-10 stereoscopic microscope fitted with a Sony Digital Hyper HAD colour video camera was used to view the samples. Heating took place on a Linkam THMS600 hot stage using a Linkam TP92 temperature control unit. Thermal events were monitored and captured in real-time using analySIS,[83] a Soft Imaging System program.

2.5 Fourier transform-infrared spectroscopy

The infrared (IR) region of the electromagnetic spectrum has a wavelength longer than that of visible light; ranging from 800 nm to 1 mm. This radiation can be emitted or absorbed by molecules when there is a change in their rotational and vibrational movement. The vibrational portion of the infra-red region, between 4000 cm^{-1} and 400 cm^{-1}, is the region used in infra-red spectroscopy.[84] The energy absorbed by the molecule is quantised and as a result the bending and stretching of the bonds give a unique spectrum which is characteristic of a specific compound. Each bond type has a different natural vibration frequency; this is altered by the electronic environment surrounding the bond in a compound. This means that the infra-red spectrum of a compound can be used as its fingerprint and is thus a uniquely identifying feature.

Spectra were collected on either a Perkin Elmer FT-IR Spectrum Two spectrometer fitted with a Universal ATR accessory or on a Bruker Alpha spectrometer with an ATR platinum Diamond 1 reflectance accessory for solid samples. All samples were scanned over the 4000 cm^{-1} to 400 cm^{-1} range at a rate of 4 s cm^{-1}.

2.6 UV-vis spectrophotometry

UV-vis spectrophotometry can be used to determine the electronic excitations of a compound in the ultraviolet (UV) and visible (vis) regions, that is the 190 – 800 nm wavelength range. The molar absorptivity of the compound gives an indication of the strength of the chromophore. All UV-vis work was performed on a Cintra 20-UV-visible spectrometer using 1 cm path-length quartz cuvettes (software GBC Spectral[85]).

Numerous methods were investigated to monitor the uptake of dye by the gel. Either the xerogel was prepared by oven drying the gel material until it was a powder, weighed (*ca.* 6 mg) and added to an indicator solution in DMF with an absorbance of one at the appropriate wavelength. Or 500 μL wet gel was prepared directly in the cuvette and allowed to stand in the oven at 90 °C for two to three hours. The gel was then soaked in fresh DMF for 24 h to remove any unreacted starting materials. Thereafter, the indicator solution (2000 μL) was gently poured on top of the gel (Figure 2.1). In all cases the system was kept at 25 °C for sorption experiments. UV-vis readings were taken at regular time intervals. Full kinetic studies were not performed as the sorption profiles were not reproducible and multiple interfaces were present as the solvent moved through the gel. Solvent within the gel pockets may have also left the gel which further complicated the kinetic profile. The dyes used (bromocresol green and methyl orange) do not interact with DMF and have λ_{max} at absorbances which do not overlap with those of the gel components.

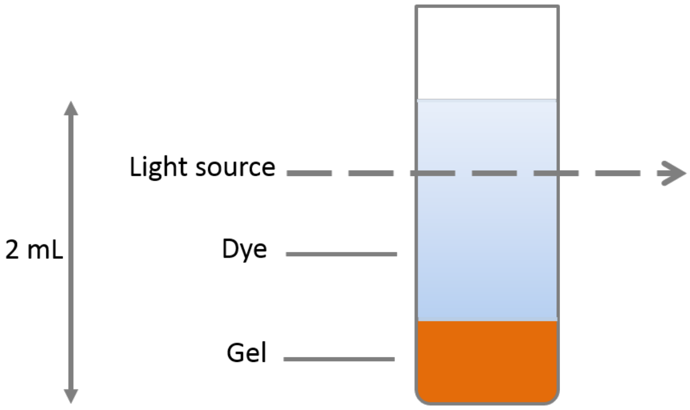

Figure 2.1: Set up of dye sorbance experiment. The total volume was 2 mL and either 0.5 mL of gel or approximately 6 mg of dry solid gel was used.

2.7 Elemental analysis

A Fisons EA1108 CHNS-O Elemental Analyser was used for elemental analysis experiments to determine the percentage of carbon, hydrogen and nitrogen present in a sample.

2.8 Microwave plasma – atomic emission spectroscopy

Microwave plasma – atomic emission spectroscopy (MP-AES) was performed using Agilent Technologies 4100 MP-AES running MP Expert Software on xerogels of Fe-tri-DMF and Fe-5nite-DMF. This was done in order to determine the percentage of iron(III) present in each compound. A multi element standard was used for the calibration. A solution of *ca.* 9×10^{-4} g of xerogel was dissolved in 5 mL HNO_3, and a calibration curve was established using a multi-element standard.

2.9 Electron spin resonance spectroscopy

The electron spin resonance (ESR) spectroscopy data in this work were collected on a Bruker EMX-Micro spectrometer at 298 K at the University of Stellenbosch, South Africa.

ESR or electron paramagnetic resonance (EPR) spectroscopy is a technique used in the characterisation of paramagnetic compounds, particularly those containing d- and f-block elements.[86] An electron has a spin quantum number of $s = \frac{1}{2}$ which gives rise to two allowed electron-spin angular momentum quantum numbers of $m_s = \frac{1}{2}$ and $m_s = -\frac{1}{2}$, the positive being higher in energy. The energy difference between these energy levels increases linearly with an increase in the magnetic field strength, and this is exploited by ESR spectroscopy.[87] The sample is exposed to constant frequency microwave radiation. When the magnetic field strength corresponds to an energy difference equal to the energy of the applied microwave frequency, electrons are promoted from lower to higher energy levels. These transitions can be observed as the absorption of a portion of the microwave intensity. Using the Bohr rule the ESR frequency can be determined to be (Equation 2.3):

$$v = \frac{g_s \beta H}{h} \tag{2.3}$$

where β is the Bohr magneton, H is the applied magnetic field and h is Planck's constant.[88] The value of g_s for a free electron-spin moment is 2.0023. There are internal magnetic fields which arise from orbital motions of the electrons and, because of this, weak internal fields can be induced by an applied magnetic field. This results in the slight displacement of the resonant frequency from the free electron value, and so the g value is not a constant, but a tensor. The g-tensor gives information about the orientation of certain bonds and the orbitals of the excited molecule.[88] The hyperfine coupling constant, A, arises from the magnetic coupling of an electron to any magnetic nuclei present and gives information about the donor atoms of the ligand. If the donor atoms are all the same the hyperfine coupling lines are of the same magnitude and are evenly spaced. The coupling to the nucleus with spin I results in the splitting of the ESR line into $2I + 1$ lines.

Magnetically, iron(III) usually forms high spin complexes except with strong ligands, where $[\mathrm{Fe(CN)_6}]^{3-}$, $[\mathrm{Fe(dipy)_3}]^{3+}$ and $[\mathrm{Fe}(o\text{-phens})_3]^{3+}$ are classic examples.[89]

Therefore a five-line ESR spectrum is expected for iron(III) compounds where the free-ion $3d^5$ character is retained. The electron spin is $\frac{5}{2}$ in these cases, leading to six electronic energy levels, which is a high-spin state.[90] This is typical of environments such as full cubic (8-coordination), octahedral (6-coordination), and tetrahedral (4-coordinate) environments: the six electronic levels split into four and two respectively in zero magnetic field.[90] There are examples of low-spin iron(III) complexes where the effective spin is $\frac{1}{2}$ (low-spin heme protein cytochrome P450, an enzyme found in the liver)[90] and intermediate $\frac{3}{2}$ cases such as the bacterial heme proteins ferricytochromes c.[91]

The g-tensor, for many paramagnetic species including iron(III), is dependent on the orientation of the sample in the magnetic field and is said to be anisotropic.[92] Figure 2.2 shows the absorption and first-derivative ESR spectra for the three different types of anisotropy. The g-tensor generally splits into three values for g following a Cartesian co-ordinate system which is symmetric along the diagonal: g_x, g_y and g_z. The magnitude of these values in relation to each other gives information about the geometry of the radical. When all the values of g are equal the spectrum is isotropic and is independent of the orientation of the magnetic field. An axial spectrum is one where $g_x = g_y > g_z$ and the g-tensor is compressed along the z-axis.

Another axial spectrum occurs when $g_x = g_y < g_z$, and reflects compression of the g-tensor in the xy plane. The spectrum is said to be rhombic when three large peaks corresponding to the different components of the g-tensor are shown and $g_x \neq g_y \neq g_z$.[92]

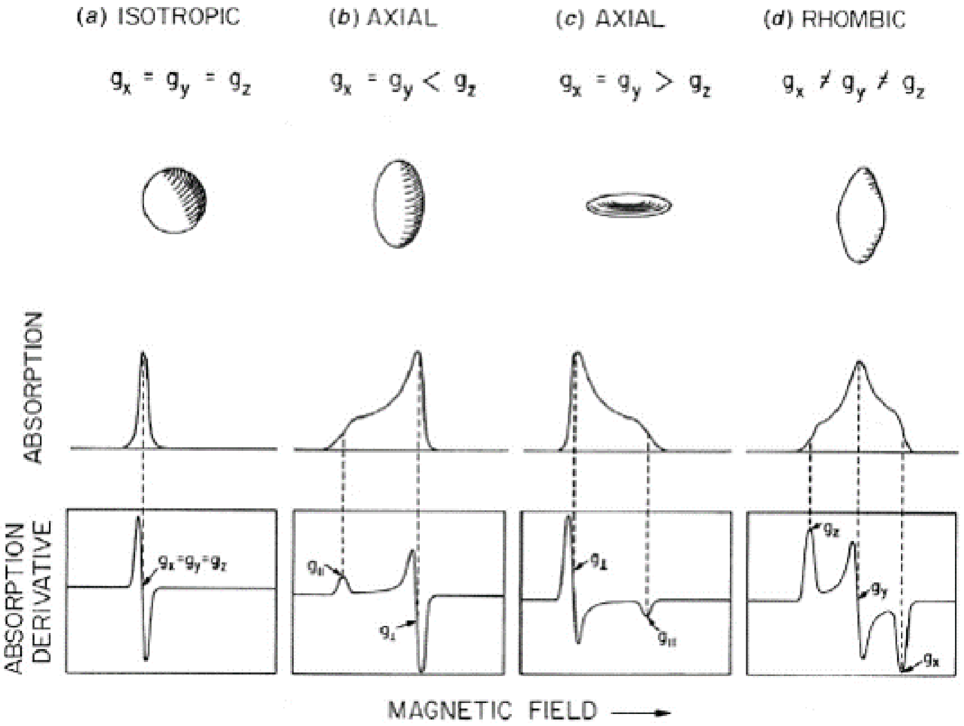

Figure 2.2: Reproduced schematic representation of the three different types of anisotropy and their resulting ESR spectra. The shapes associated with the different magnetic moments are represented by the solid bodies, (a) isotropic, (b, c) axial, and (d) rhombic. Beneath these are the absortion curve and corresponding first-derivative ESR curves.[93]

The spectra can be measured at different resonant frequencies. Table 2.1 gives the resonant frequencies and the corresponding band name.

Table 2.1: Band names and their corresponding resonant frequencies

Band	**Frequency** [GHz]
L	1-2
S	2-4
X	9
Q	35
W	95

The ESR spectra of compounds in the solid state are broadened by spin-lattice relaxation and this often obviates measurement of the hyperfine coupling constant. As a result of this broadening, the hyperfine coupling can often only be seen in solution. The solvent used plays a large role in the shape and intensity of the spectrum;[94] DMF is a lossy solvent as a result the wet gels could not be run so the hyperfine could not be calculated. A lossy solvent is one in which the electromagnetic radiation is converted to heat by interaction with the molecular dipole or ionic conduction of the substance, as a result the intensity is "lost".[95] DMF has a high dielectric constant and absorbs microwave radiation.

Solution studies could not be performed in this work as the xerogels were insoluble. Solid state ESR was done on the xerogels at room temperature. The gels obtained from DMF were used, despite DMF being a poor solvent for ESR, as they were the most stable.

2.10 Inductively coupled plasma optical emission spectrometry

Inductively coupled plasma optical emission spectrometry (ICP-OES) was performed using an ICP-OES Varian 730-ES for the analysis of oven dried gel samples. The gels were ashed in a furnace at 600 °C overnight before undergoing digestion with 4 mL of 4:1 of concentrated hydrogen fluoride and nitric acid (HNO_3) at 130 °C for 48 hours. These samples were then dried and washed twice with 2 mL of concentrated HNO_3 with drying between washes. The solid material remaining was diluted in a 5% HNO_3 solution before analysis.

2.11 Scanning electron microscopy

Scanning electron microscopy (SEM) was performed on xerogels which were sputter coated with gold/palladium. Either a Leo 1450 LaB6 scanning electron microscope or a Nova Nanosem 230 were used. A low vacuum detector was used for the samples for which charging was a problem. Energy dispersive spectroscopy (EDS) on the SEM was performed on selected parts of the gel to determine the iron content. This analytical technique uses the unique electromagnetic emission spectrum which results from the atomic structure to identify the atoms.

2.12 X-ray diffraction

2.12.1 Single crystal X-ray diffraction

Single crystals of suitable quality were selected from the mother liquor and immediately placed under paratone oil to prevent degradation or solvent loss from the crystal. If necessary crystals were cut to obtain the appropriate size. Crystals were mounted on a nylon loop connected to a rigid mounting, then placed on the goniometer head under a stream of cold nitrogen gas. A Bruker KAPPA APEX II Duo diffractometer using a MoKα ($\lambda = 0.71069$ Å) was used for the data collection. X-rays were generated by a Bruker K780 generator powered at 50 kV and 30 mA.

Unless otherwise stated, data collections were carried out at low temperature (173(2) K) using a Cryostream (Oxford Cryostreams, UK). Data reduction and unit cell refinement were done using the software SAINT.[96] SADABS[97] was used to correct for Lorentz-polarisation and absorption effects on all intensity data. The program XPREP[98] was used to confirm the space group and prepare input files used by SHELXS.[99] Direct methods employed by SHELXS[99] were used to locate the atomic co-ordinates. Once the atoms were placed in their postulated positions, SHELXL[99] was used in subsequent refinements. All non-hydrogen atoms were then refined anisotropically. The Fourier difference map was used to locate the hydrogen atoms. Then the hydrogen atoms were placed in idealised positions in a riding model. All hydrogen atoms were refined isotropically and assigned temperature factors 1.2 and 1.5 times that of the parent atoms.

The crystal structure of **V** is a non-merohedral twin with a minor component of 41.3%. This dataset was refined using CrysAlisPro 1.171.38.41.[100]

2.12.2 Powder X-ray diffraction

Powder X-ray diffraction (PXRD) patterns were collected on a Bruker D8 Advance diffractometer equipped with a Lynxeye detector using CuKα-radiation ($\lambda = 1.5406$ Å) at 298 K. Samples were lightly ground to a fine powder, placed on a zero background sample holder and scanned over a 2θ range of 4° to 40°. Unless otherwise stated, a step size of 0.02° to give a total of 1762 steps was used. The X-rays were generated by a current flow of 40 mA and accelerating voltage of 30 kV. A receiving slit of 0.6 mm and primary and secondary slits of 2.5 mm were used. The data were saved as text files and replotted using gnuplot to obtain the PXRD traces. Variable temperature powder X-ray diffraction (VT-PXRD) were conducted. The X-rays were generated by a voltage of 40 kV and a current of 40 mA. The same step size and total number of steps as used for PXRD were employed.

Mercury v3.7[101] was used to generate calculated powder X-ray diffraction patterns from single crystal data. The same X-ray source ($\lambda = 1.5406$ Å) was used in the calculation. These patterns were used to determine phase purity of the bulk material by comparison to the experimental data.

2.13 Headspace gas chromatography

Headspace gas chromatography was used to determine whether or not the gels could be used as a separation material of chiral-piperidines. The system used was an Agilent 6890 Gas Chromatograph/7697A Headspace sampler with a 30-m CB Wax 57 capillary column. Nitrogen was used as the carrier gas at a constant flow rate of 1 mL min^{-1}. The oven conditions included an initial temperature of 70 °C for an initial time of 2 min, followed by a heating rate of 8 °C min^{-1} until 200 °C was reached and held for 1 min. The inlet temperature was kept constant at 250 °C, and the flame ionisation detection (FID) unit was set at 250 °C with flow rates of hydrogen at 30 mL min^{-1}, air at 400 mL min^{-1} and nitrogen at 25 mL min^{-1}. Samples were equilibrated for 15 min at 120 °C with a loop temperature of 135 °C and the transfer line set at 140 °C.

Gelation was carried out in a column. The mixture to be separated comprised a 1:1 ratio of 2-methylpiperidine and 3-methylpiperidine (101 mg of each liquid was used). This mixture was loaded onto the gel (4.3 mL) and eluted with 10 mL of EtOH. The gel discoloured as the mixture moved through the gel and appeared to be degraded. The liquid and gel were collected for head-space gas chromatography (GC) analysis.

2.14 Gas sorption

A Micromeritics 3Flex Surface Area Analyzer was used to investigate the ability of the dried gels to absorb gas. As dry sample is required for the analysis, 150 – 200 mg of the freeze or oven dried gels were treated in a Micromeritics Flowprep with a constant flow of nitrogen gas over the sample at 60 °C for 24 hours followed by further heating at 60 °C under vacuum *in situ* before starting the analysis in order to evacuate the compound of any solvent. Complete details of gas sorption experiments, including Brunauer, Emmett, and Teller (BET) parameters and gases used, are given in the relevant sections.

Molecules or atoms can attach to surfaces by either physisorption or chemisorption.[102] Physisorption involves Van der Waals and other supramolecular interactions between the substrate and the molecules (or atom) being adsorped and the molecules retain their identity, although they may be distorted by the surface. Chemisorption on the other hand involves the formation of bonds (usually covalent in nature) and may result in the molecules being torn apart at the demand of the unsatisfied valencies of the surface atoms. Physisorption is associated with much lower enthalpy values (typically to the order of 20 kJ mol^{-1}) than chemisorption (typically to the order of 200 kJ mol^{-1}).

There are many models which can be used to relate the amount of a substance taken up onto a surface with pressure at a chosen temperature and these are plotted as adsorption isotherms. The Langmuir Isotherm is the simplest of these models[103] and is based upon three assumptions.[102] These are that all sites on the surface are uniform in behaviour, the surface becomes saturated with a monolayer at high pressure and there are no interactions between molecules in neighbouring sites. Equation 2.4 is derived from the rate of adsorption of the substance and the area of the surface covered by the adsorbed molecules.

$$\theta = \frac{k\,[A]}{1 + k\,[A]} \tag{2.4}$$

Where, θ is the fraction of the surface which is covered by adsorbed molecules (Equation 2.5),[102] A is the concentration of the molecules in the gas or liquid phase and k is the ratio of the adsorption rate to the desorption rate constant.

$$\theta = \frac{number\ of\ adsorption\ sites\ occupied}{number\ of\ adsorption\ sites\ available} \tag{2.5}$$

In 1938 Stephen Brunauer, Paul Emmett and Edward Teller proposed the BET Isotherm, it is an extension of the Langmuir isotherm to allow for the physisorption of a multilayer of adsorbed molecules.[103] Multilayer adsorption will occur under non-ideal conditions of low temperature and high pressure. It was derived by balancing the rates of adsorption and condensation for the various layers. A few assumptions were made including that there is one enthalpy of adsorption and condensation for the first layer, and that the enthalpy of liquification applies to the second and subsequent layers. The simplest form of this equation is shown here (Equation 2.6).

$$\frac{PP_0}{V\,(P_0 - P)} = \frac{1}{V_0K} + \frac{P}{V_0} \tag{2.6}$$

Where V is the volume of gas adsorbed at pressure, P, and V_0 the volume that can be adsorbed as a monolayer; P_0 is the saturation vapour pressure, and K is the equilibrium constant for the adsorption. This isotherm is particularly useful for determining surface area of solids.

Qualitative information about the adsorption process can be obtained from the shape of the adsorption curve.[104] “Although adsorption isotherms with shapes ranging from the monotonous to the fantastic have been reported”,[105] five basic types were identified by Brauner[105] and are shown in Figure 2.3. Type I is associated with systems which involve monolayer adsorption, Types II and III involve multilayer adsorption.[104] The shapes of Types IV and V are characteristic of multilayer adsorption on highly porous material. The flattening of the curves at high pressures can be attributed to capillary phenomena.

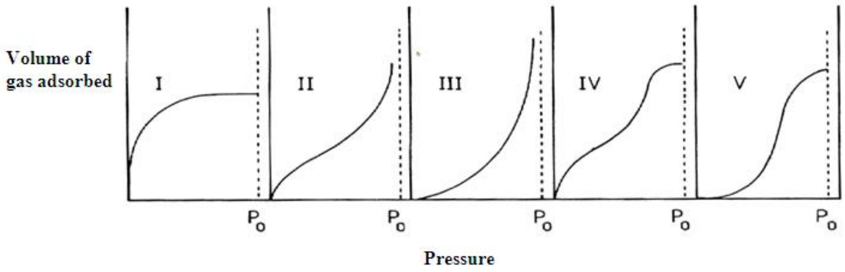

Figure 2.3: The five types of adsorption isotherms reproduced from National Programme on Technology Enhanced Learning.[106] The saturation vapour pressure is indicated as P_0.

2.15 Flow behaviour and viscosity

Flow curve measurements were performed on an Anton Paar MCR 72 Rheometer at 25 °C running RheoCompass$^{\mathrm{TM}}$ software. Shear stress, τ and shear strain $\dot{\gamma}$ were measured by placing the gel sample between two plates and the stress was applied by moving one plate relative to the other. There are two conditions which must be met to calculate rheological parameters; firstly the sample must adhere to both plate and must not slip between them, and secondly the resulting flow must be laminar in nature.[107]

Rheology is the study of flow and deformation under an applied force.[107] There are two extremes in flow behaviour, the flow of ideal viscous materials such as a low viscosity mineral oil and the deformation of ideal elastic materials such as a steel ball. All shear behaviour lies between these two extremes in a short time scale.

Two rheological parameters used to describe flow behaviour and viscosity are shear stress, τ and shear strain $\dot{\gamma}$. The definitions of each are given in Equations 2.7 and 2.8 respectively:

$$\tau = \frac{F}{A} \tag{2.7}$$

where shear stress, τ (Pa), is a ratio of shear force, F (N) and shear area, A (m^2)

$$\dot{\gamma} = \frac{v}{h} \tag{2.8}$$

where $\dot{\gamma}$ is the shear rate (s^{-1}) and v the velocity ($\mathrm{m\ s}^{-1}$) and h the gap between the plates (m).

There are frictional forces present between all molecules in fluids and because of this there is a resistance to flow, this is termed viscosity.[107]

Shear viscosity, η (Pa s), is the ratio of shear stress, τ (Pa), to the shear rate, $\dot{\gamma}$ (s^{-1}) (Equation 2.9). This is a constant for ideal viscous fluids at constant temperature. Viscoelastic materials have both viscous and elastic portions in their behaviour.

$$\eta = \frac{\tau}{\dot{\gamma}} \tag{2.9}$$

For non-Newtonian fluids, their viscosity is dependent on the shear rate (Figure 2.4). A fluid is shear-thickening if the viscosity of the fluid increases as the shear rate increases, an example is a mixture of cornstarch and water.[108] If the fluid is shear-thinning, the viscosity will decrease with an increase in shear rate.

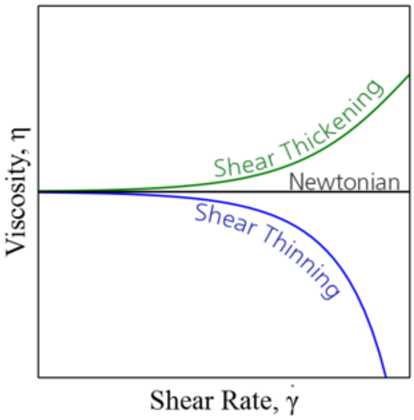

Figure 2.4: Viscosity curves showing shear thinning, shear thickening and a Newtonian fluid, reproduced from RheoSense.[108]

Chapter 3

Gel formation

The field of supramolecular gels is challenging as predicting their formation can be problematic. As a result their discovery is often serendipitous occurring while in the pursuit of other materials. A systematic investigation of a range of conditions, metal salts, ligands and solvents was performed to determine their role in gel formation. Characterisation of the gels will be discussed in the following chapter.

3.1 General preparation method

The metal salts and ligands were reacted in a 1:1 molar ratio, using 0.1 mmol of metal salt and ligand in 1 mL and 4 mL of solvent respectively. Each component was dissolved at room temperature, when possible, in the appropriate solvent and combined in one vial, 2.4 cm in diameter. When one component was not soluble at room temperature, the mixture was gently heated under stirring and the saturated solution was used. Various temperatures were used for the gel formation experiments. All reactions were carried out at standard pressure and were open to the atmosphere. The inverted vial test was performed to confirm gel formation. Figure 3.1 is an example of the trays used in the study where each ligand was combined with each metal salt in a different solvent and reacted at a different temperature, either room temperature (*ca.* 22 °C), 60 °C or 90 °C. At temperatures greater than 90 °C the solvent would evaporate before gelation could occur. The abbreviations of the components used can be found in the tables that follow.

Figure 3.1: An example of a tray used in gel formation experiments. Each row has a different metal salt and each column has a different carboxylic acid. The solvent and temperature are common to all the vials. This figure showcases the formation of gels.

3.2 Starting materials

Trimesic acid has been shown to form gels with Fe(III) as reported by Wei and James.[76] It serves as template for the formation of macroporous polymethylmethacrylate. The gel (originally from $Fe(NO_3)_3 \cdot 9H_2O$ and trimesic acid in ethanol) is stable and can be formed reproducibly in other solvents such as methanol and DMF. As trimesic acid is clearly a successful gelator, I chose similar ligands for this study. Unless specified, the gels presented are novel.

All of the ligands selected were single pyridyl or phenyl rings with at least two carboxylate moieties. The relative position of carboxylate moieties was varied, both in *meta* and *para* positions. Bi-, tri-, and tetra-dentate ligands were used. Different electronic structures were explored by using pyridines and the addition of a nitro group. A chiral ligand was also used to investigate whether such a material could be used for the separation of chiral compounds. This is discussed in Chapter 5, Response to stimuli.

Ligands of the type chosen for this work (Figure 3.2) have been shown to form metal organic frameworks (MOFs) or co-ordination polymers with various metal ions, such as copper acetate, cobalt nitrate, gadolinium nitrate, neodymium dichloride, and zinc nitrate salts.[109–115]

MOFs have been investigated for various applications, many of which utilise the void space within the framework. A few of these include the uptake and separation of gases and catalysis.[70,116,117] These voids usually hold solvent upon synthesis of the MOFs. There may be similar connectivity in the MOF and the gel, however MOFs are crystalline and regular whereas gels are not and will hold more solvent. The use of ligands which have been found to form MOFs may lead to porous structures in which a large amount a solvent may be trapped, leading to gel formation.

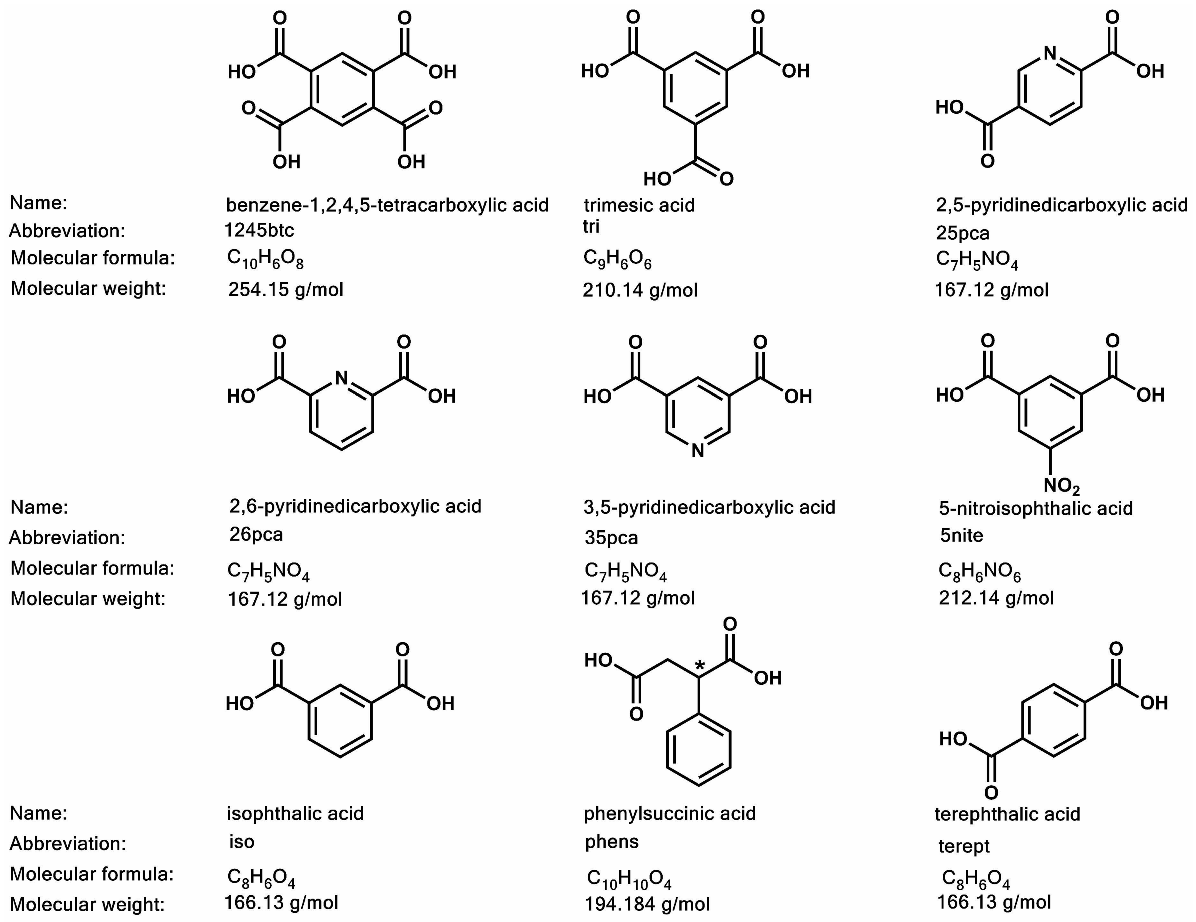

Name:	benzene-1,2,4,5-tetracarboxylic acid	trimesic acid	2,5-pyridinedicarboxylic acid
Abbreviation:	1245btc	tri	25pca
Molecular formula:	$C_{10}H_6O_8$	$C_9H_6O_6$	$C_7H_5NO_4$
Molecular weight:	254.15 g/mol	210.14 g/mol	167.12 g/mol

Name:	2,6-pyridinedicarboxylic acid	3,5-pyridinedicarboxylic acid	5-nitroisophthalic acid
Abbreviation:	26pca	35pca	5nite
Molecular formula:	$C_7H_5NO_4$	$C_7H_5NO_4$	$C_8H_6NO_6$
Molecular weight:	167.12 g/mol	167.12 g/mol	212.14 g/mol

Name:	isophthalic acid	phenylsuccinic acid	terephthalic acid
Abbreviation:	iso	phens	terept
Molecular formula:	$C_8H_6O_4$	$C_{10}H_{10}O_4$	$C_8H_6O_4$
Molecular weight:	166.13 g/mol	194.184 g/mol	166.13 g/mol

Figure 3.2: Carboxylic acids investigated for gel formation. All have at least two carboxylic moieties and are either single pyridyl or phenyl rings.

Tables 3.1 and 3.2 give details of the metal salts and solvents used, respectively. The role of the counterion and the metal ion were investigated using different metal salts. A variety of solvents from different chemical classes with different polarities were used to investigate the role of solvent in gel formation.

Table 3.1: Metal salts used in gel formation experiments

Name	**Formula**	**Abbreviation**
Aluminium(III) nitrate nonahydrate	$Al(NO_3)_3{\cdot}9H_2O$	Al
Cobalt(III) acetylacetonate	$Co(C_5H_7O_2)_3$	Co-acac
Iron(II) oxalate dihydrate	$FeC_2O_4{\cdot}2H_2O$	Fe-ox
Iron(III) acetylacetonate	$Fe(C_5H_7O_2)_3$	Fe-acac
Iron(III) bromide	$FeBr_3$	$FeBr_3$
Iron(III) chloride hexahydrate	$FeCl_3{\cdot}6H_2O$	$FeCl_3$
Iron(III) nitrate nonahydrate	$Fe(NO_3)_3{\cdot}9H_2O$	Fe
Iron(III) sulphate hydrate	$Fe_2(SO_4)_3{\cdot}9H_2O$	Fe-sul

Table 3.2: Properties of solvents used in gel formation experiments

Solvent	**Boiling point** [°C]	**Polarity index**	**Functional group/ Chemical class**	**Abbreviation**
Toluene	110.6	2.4	aromatic ring	MePh
Dichloromethane	39.6	3.1	haloalkane	DCM
Propanol	97	4.0	alcohol	PrOH
Benzonitrile	188	4.6	cyano group, aromatic ring	PhCN
Acetone	56	5.1	ketone	Ace
Acetonitrile	82	5.8	nitrile	MeCN
N,*N*-Dimethylacetamide	165	6.5	amide	DMA
N,*N*-Dimethylformamide	155	6.4	amide	DMF
Ethanol	78	5.2	alcohol	EtOH
Dimethylsulfoxide	189	7.2	sulfinyl	DMSO
Water	99.98	9		H_2O

The components do not form gels on their own but once they are combined in a particular solvent, gels of various shades of red, orange and yellow were formed. From the various combinations of ligand and metal salts in different solvents run at two or three different temperatures, it is possible to get a maximum of thirteen gels per ligand/metal salt combination. For example, Fe-5nite-solvent, in the following solvents; acetonitrile (room temperature and 60 °C), *N,N*-dimethylacetamide (room temperature, 60 °C, and 90 °C), *N,N*-dimethylformamide(room temperature, 60 °C, and 90 °C), ethanol (room temperature and 60 °C), and dimethylsulfoxide (room temperature, 60 °C, and 90 °C).

The naming convention for the gels is: metal salt-ligand-solvent. For example Fe-5nite-DMF refers to a gel which was formed using a combination of iron(III) nitrate nonahydrate, 5-nitroisophthalic acid and *N,N*-dimethylformamide.

3.3 Influence of ligand in gel formation

Of all the ligands investigated, the most successful gelators were 3,5-pyridinedicarboxylic acid (35pca), 5-nitroisophthalic acid (5nite), and trimesic acid (tri). This can be seen in Figure 3.3 which shows the number of gels formed for each ligand. All of these ligands have an electron withdrawing group in the *meta* position relative to both carboxylate groups.

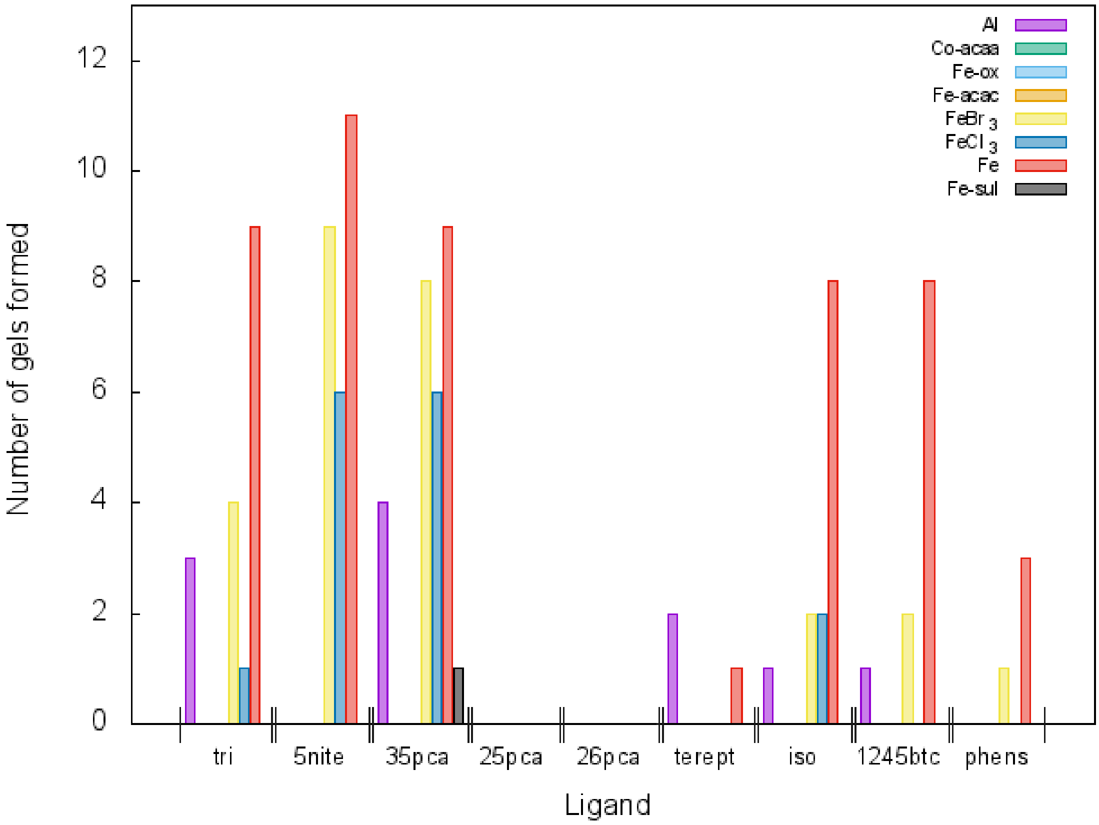

Figure 3.3: Number of gels formed per combination of metal salt and ligand.

We surmise that the different ligands and solvent combinations would give rise to different geometry of the synthons which may lead to different networks. A large porous space is required in order to immobilise solvent leading to gel formation. Tridenate ligands, trimesic acid, and 3,5-pyridinedicarboxylic acid may be successful as gelators as a result of the three potential binding sites which allow a porous network to form. While bidentate ligands terephthalic acid, isothphalic acid and phenylsuccinic acid do form gels, they do not do so in as great a number or with as many different metal salts as the tridentate counterparts. The relative positions of the carboxylic groups seems to play a role, *meta* is more successful than *para*. The least number of gels were formed with ligands with carboxylic groups in the *para* position such as 2,5-pyridinedicarboxylic acid and terephthalic acid. Figure 3.4 highlights features of the ligands which are important for the formation of gels.

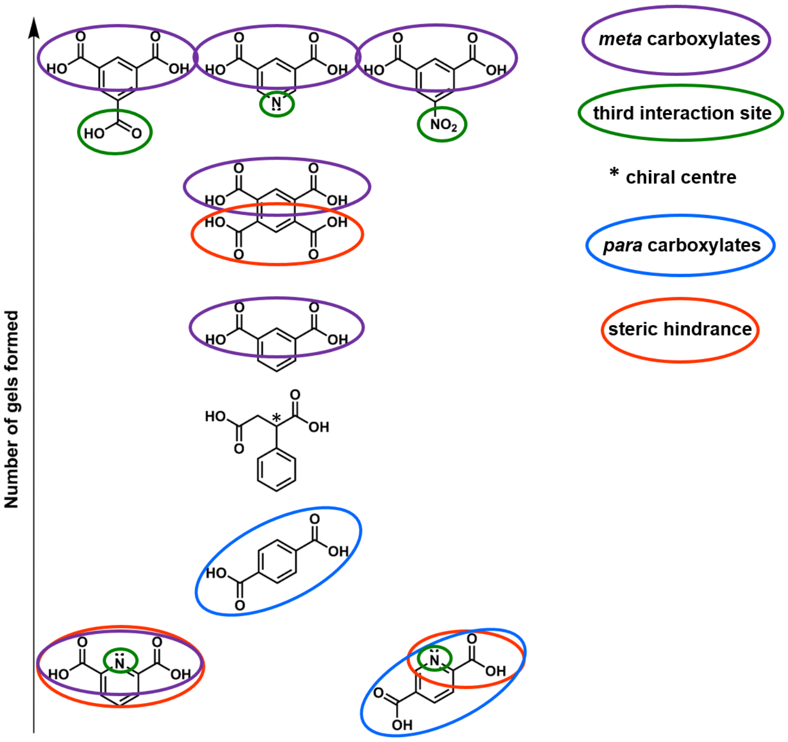

Figure 3.4: Ligand features which play a role in gel formation in this study.

Examining the trends in Figure 3.4, a tridentate ligand is more likely to form gels than a bidentate one. This is because the additional binding site will provide another node in the network making it easier to trap solvent. While the tetradentate ligand, 1,2,4,5-benzenetetracarboxylic acid, does result in gel formation, it does not form as many gels as the tridentate ligands. This can be attributed to too many binding sites resulting in smaller pockets and less solvent being trapped and stabilised. The chirality of the ligand did not play a role, in this case gel formed with both the racemate and the enantiomerically pure compound of phenylsuccinic acid.

5-nitroisophthalic acid formed the most gels, eleven out of a possible thirteen. Although not a tridentate ligand the relative positions of the carboxylate groups are favourable for gelation. It is thought that the nitro group plays a significant role in stabilising the network which leads to gel formation.

The bidentate pyridine ligands appear to be less favourable for gel formation as no gels were formed with 2,5- and 2,6-pyridinedicarboxylic acid. The trend suggest that the electron withdrawing nitrogen in the pyridine is favourable in the tridentate 3,5-pyridinecarboxylic acid, but is sterically hindered in 2,5- and 2,6-pyridinedicarboxylic acids, therefore not available for coordination. A few gels were formed with both isophthalic and terephthalic acids, which have the same relative positions of the carboxylic acids, suggesting the pyridine has an unfavourable impact on gel formation. Furthermore, iron(III) has a low affinity for amine coordination,[118] this coupled with steric hindrance resulted in no gel formation. Steric hindrance possibly leads to a lack of gels formed between aluminium(III) and 2,5- and 2,6-pyridinedicarboxylic acids as well. The role of the metal ion will be discussed in greater detail further on (Section 3.6).

The trend, for time taken for gel formation, suggests that the ligand also plays a role in this. Of the three most successful gelator ligands, 5-nitroisophthalic acid gels form the fastest, followed by trimesic acid (Figure 3.5). 3,5-pyridinedicarboxylic acid is the slowest, a further indication of the less favourable influence of the pyridine. There is no great difference in the gelation times for the other ligands.

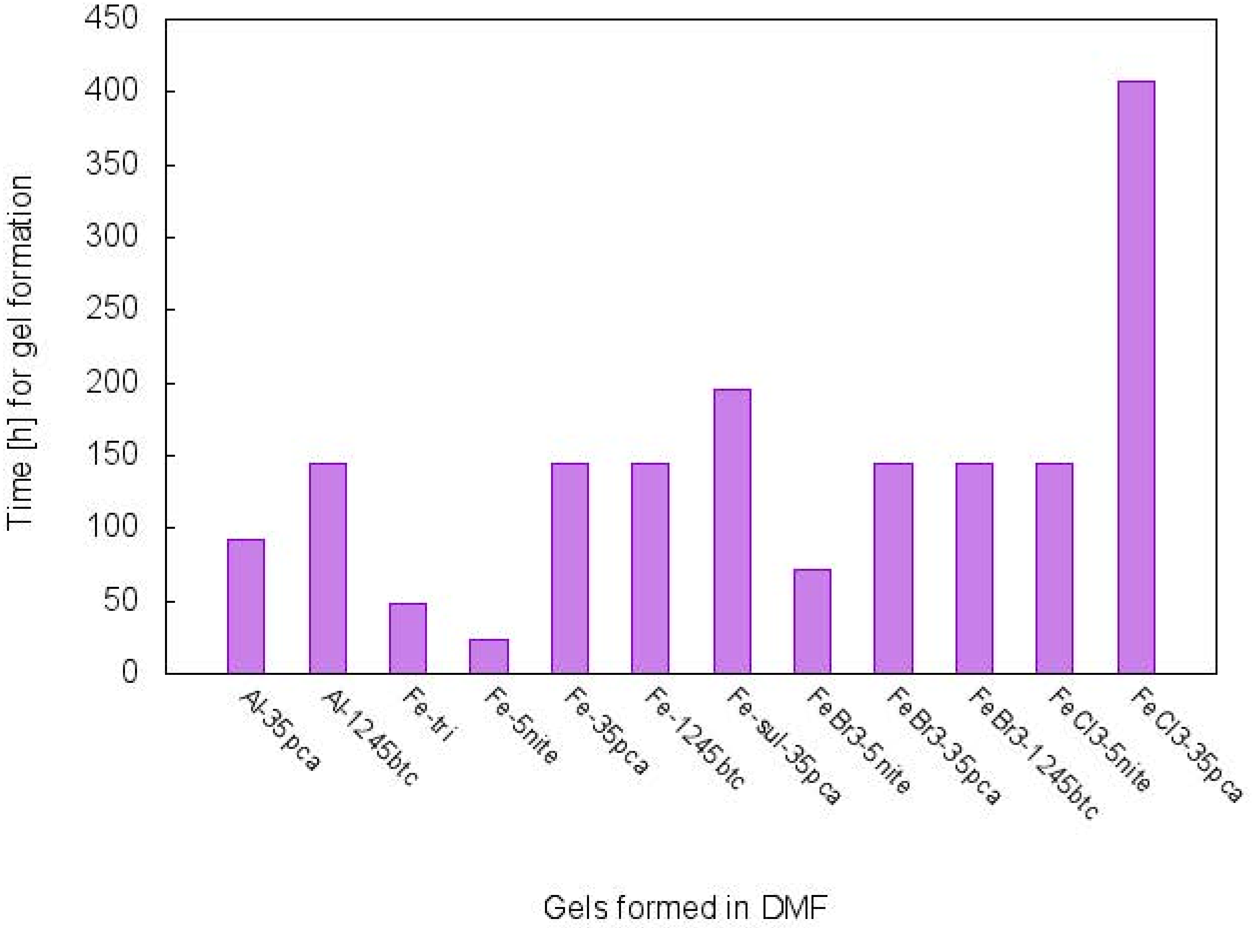

Figure 3.5: The time taken for gels to form in DMF at room temperature. Gels which took longer than 450 h are not included, such as Al-tri-DMF (1 month).

3.4 Trends in gel formation when the solvent is varied

A number of solvents were used for the formation of gels in preliminary studies with $Fe(NO_3)_3{\cdot}9H_2O$ as the metal salt. Some of these solvents where not employed further due to the poor solubility of components (Table 3.3). Solubility plays a role since the components need to be in solution in order to interact and trap a large volume of solvent, as does polarity. The polarity limit for gel formation was found to 7.2. Beyond this, gelation did not occur.

Table 3.3: Summary of the properties of solvents used in preliminary studies. Those in bold were studied further. Unless otherwise stated all experiments were carried out at room temperature

Solvent	**Boiling point**[119] [°C]	**Polarity index**[119]	**Result**
Toluene	111	2.4	Starting materials insoluble
Dichloromethane	41	3.1	Starting materials insoluble
1-Propanol	97	4.0	Clear gel after 24 h
Benzonitrile	188	4.6	Clear gel after 24 h
Acetone	56	5.1	Clear gel in minutes
Ethanol, 95%	78	5.2	Opaque gel – 30 min
Acetonitrile	82	5.8	One gel formed at 60 °C
***N,N*-Dimethylformamide**	155	6.4	Clear gel formed in less than 24 h
***N,N*-Dimethylacetamide**	165	6.5	Clear gel after 24 h
Dimethylsulfoxide	189	7.2	Pale yellow crystalline solid (5-nitroisophthalic acid), two different gels after 1 year
Water	100	9.0	Peach coloured precipitate forms as soon as solutions added together

The solvents in bold (ethanol, acetonitrile, DMF, DMA, and DMSO), were chosen for further study. The peach coloured precipitate formed in water is thought to be a mixture of various hydrated iron oxide species. The only gels to be formed using DMSO as the solvent were Fe-5nite-DMSO and $FeBr_3$-5nite-DMSO. Both are a golden honey colour and take one year to form.

Propanol and benzonitrile resulted in gelation during the preliminary investigation. As these gels formed more slowly, these volatile solvents were not used for further investigation. Gelation also occurred in acetone, however the slower systems could not be studied due to solvent evaporating before gelation could occur.

Figure 3.6 shows the time taken for gel formation at room temperature. In general those in DMF take the longest to form. It is also the most successful solvent for gel formation. The clearest gels are formed in DMF and DMA (Figure 3.7). The EtOH gels are in general opaque, this suggests the presence of iron oxide species. As the EtOH was not anhydrous, water was present during this experiment.

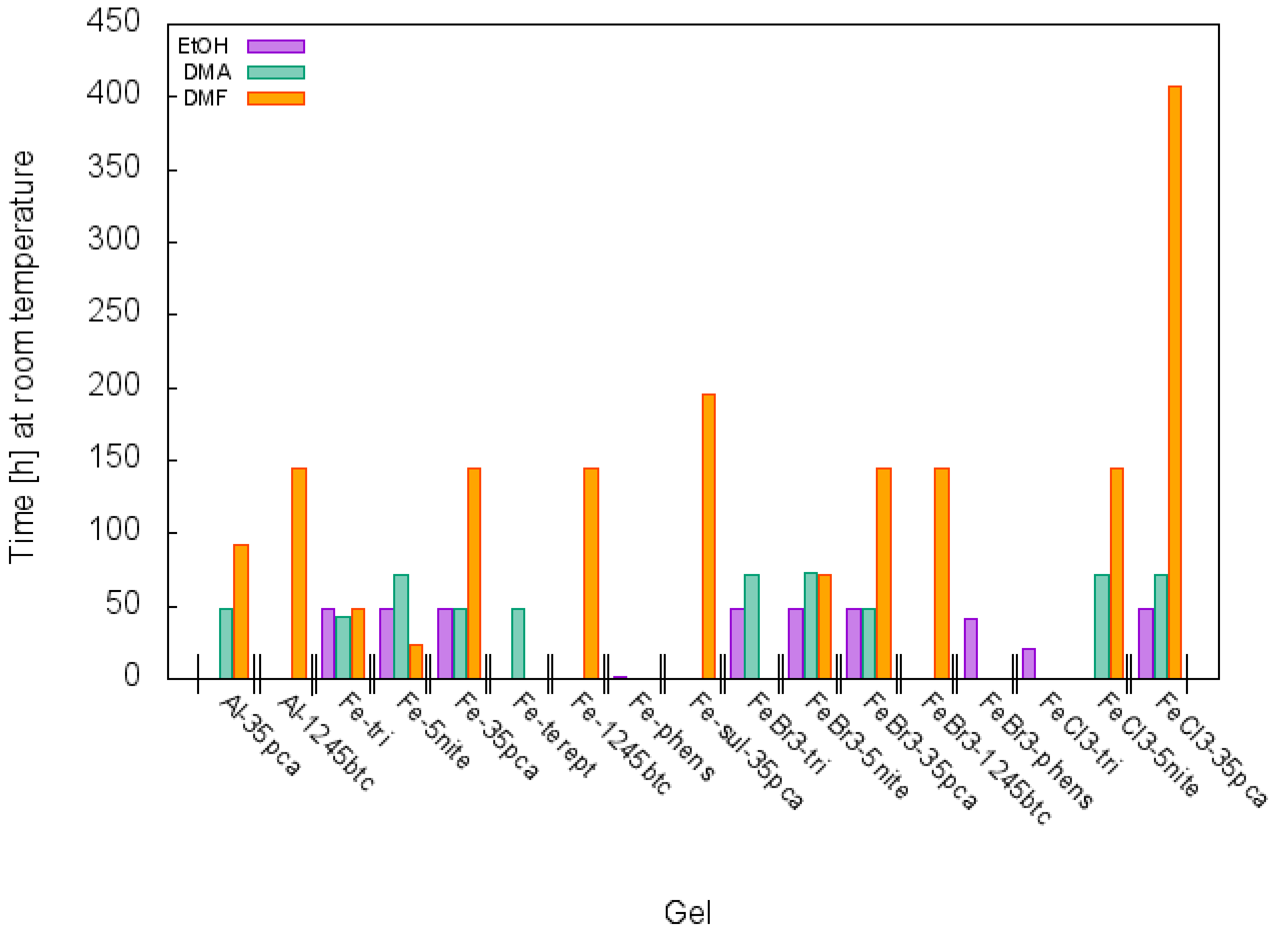

Figure 3.6: The time taken for gels to form in different solvents at room temperatures. Those in DMF take the longest to form. Gels which took longer than 20 days to form are not included. These gels are Al-tri-DMF (1 month), Fe-5nite-DMSO (1 year), FeBr$_3$-5nite-DMSO (1 year), Fe-iso-DMF (8 months), FeBr$_3$-iso-DMA (8 months), and FeCl$_3$-iso-DMA (8 months).

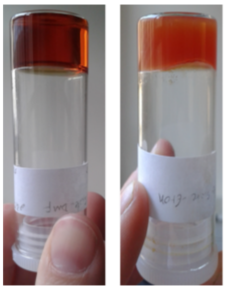

Figure 3.7: Fe-5nite-solvent gels formed in DMF, left, and ethanol, right. Commonly, those formed in DMF are clear while those from ethanol tend to be more opaque.

3.5 Range of temperatures used in gel formation

The role of temperature in gel formation was investigated using three temperatures, these were room temperature (*ca.* 22 °C), 60 °C and 90 °C (Table 3.4). Temperatures greater then 90 °C were not used as solvent evaporation would occur before gel formation. Acetonitrile (boiling point 82 °C) suffered from this problem and was therefore not run at 90 °C.

Table 3.4: Temperatures used for the investigation of gel formation

Solvent	**Temperature** [°C]
Acetonitrile*	Room temperature
	60
N,N-Dimethylacetamide	Room temperature
	60
	90
N,N-Dimethylformamide	Room temperature
	60
	90
Ethanol	Room temperature
	60
	90
Dimethylsulfoxide	Room temperature
	60
	90

*90 °C was not used as solvent evaporation would occur before gel formation.

In general the time for gelation decreased with an increase in temperature (Figure 3.8). A higher temperature corresponds to higher molecular energy; this may result in the faster formation of coordination networks and hence faster gelation. Specific metal salt/ligand combination plots for other gels can be found in Appendix A.

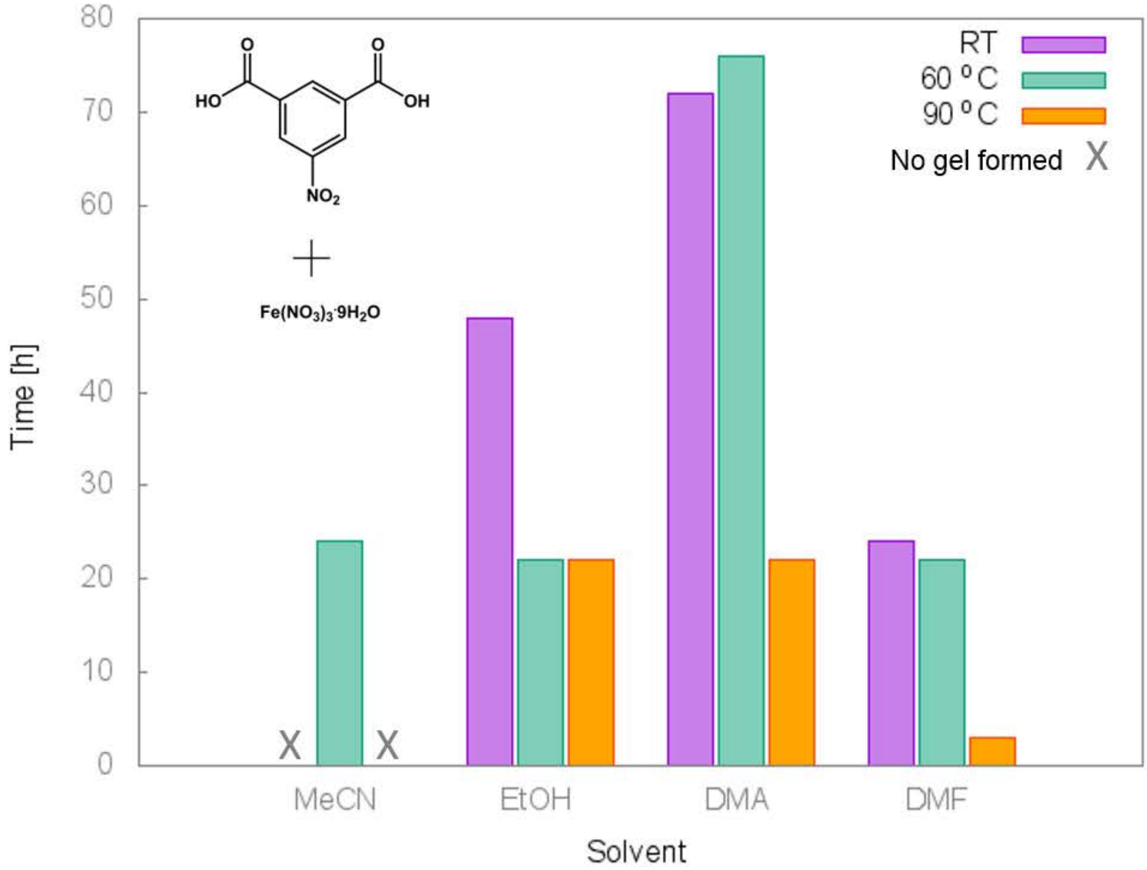

Figure 3.8: The time taken for Fe-5nite-solvent gels to form in different solvents at different temperatures. A Fe-5nite-MeCN only forms at 60 °C, at room temperature no gel was formed and the 90 °C reaction was not attempted due to the low boiling point of the solvent.

3.6 Influence of metal ion and counter ion

The formation of a gel is influenced by both the metal ion and the counterion. Figure 3.9 shows which gels formed using the different combination of ligand and metal salt. A range of counterions were explored, two organic (acetylacetonate and oxalate) and four inorganic (nitrate, sulfate, bromide, and chloride). The use of organic counterions did not result in the formation of gels, however nitrate, sulfate, and halogen salts produced gels. The sulfate counter ion only produced a single gel, Fe-sul-35pca-DMF, making it the least successful of the inorganic counterions.

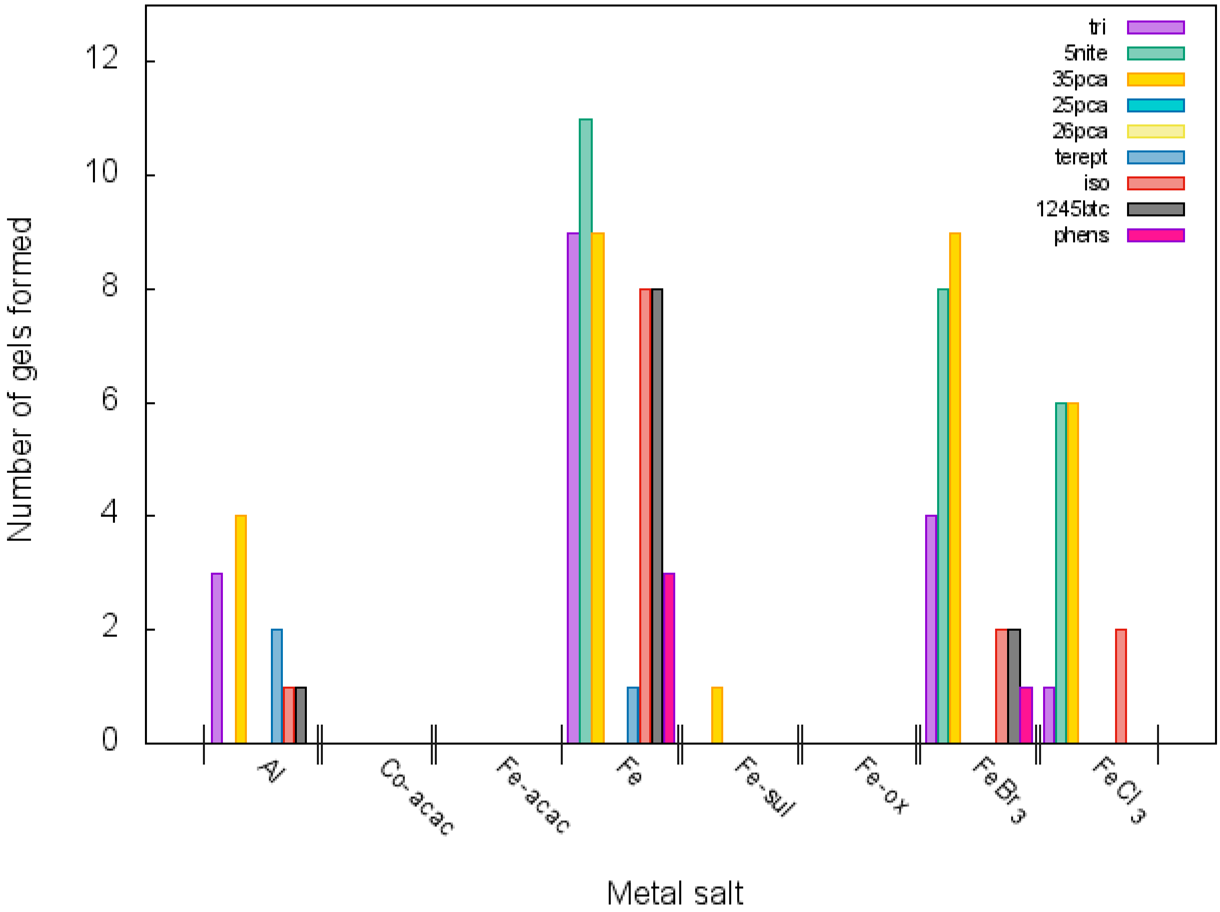

Figure 3.9: Number of gels formed per metal salt for each ligand under different synthesis conditions.

The anion is known to influence gel formation. There are examples where gel formation is stabilised by the anion, including a gaunosine $KB(OH)_4$ hydrogel.[120] The concentration of borate anion is vital as it forms a linker between two gaunosine molecules. In this study, the nitrate and halogen salts appear to stabilise the gel, and the most gels are formed with these anions. The gel formed with the halogen salts (Br^{-1} and Cl^{-1}) are firm and clear and there may be halogen bonding in these networks. A similar observation was reported by Piepenbrock *et al*[28] where a bis(pyridylurea) formed a metallogel in the presence of 0.5 equivalents copper(II) chloride, but gave rise to a 2:1 crystalline coordination polymer when exposed to 0.5 equivalents of copper(II) nitrate.

In this work, salts of aluminium(III), cobalt(III), iron(II), and iron(III) were used. The reactions involving aluminium(III) resulted in gels which were the least firm and stable of all the gels formed, and often degraded after a few hours. While cobalt(III) did not form gels, these reactions either resulted in crystals of insufficient quality for data collection or they matched the unit cell of COFORM01 which is cobalt formate dihydrate.[121] No gels formed when an iron(II) salt was used. This could have been expected since an organic counterion was present, which would also make this reaction unfavourable. Only iron(III) resulted in stable gel formation. When iron(III) acetylacetonate was used the viscosity of the reaction solution increased, but at room temperature the viscous solutions did not pass the inverted vial test.

The experiments using iron(III) acetylacetonate and 2,6-pyridinedicarboxylic acid resulted in the formation of red crystals. Single crystal structure elucidation shows the coordination of one 2,6-pyridinedicarboxylic acid and one acetylacetonate ligand. This is expanded upon in Chapter 6. The results suggest the salts with organic counter ions undergo a ligand substitution reaction. The remaining acetylacetonate blocks coordination sites and this is therefore less likely to result in a gel.

d-Metal complexes of d^3 and low-spin d^6 such as Fe(II) have large Ligand Field Stabilisation Energies and are generally nonlabile. Fe(III) is less labile and therefore, more likely to form gels than crystals. Relative to the other transition metals, such as cobalt, the kinetics of iron are comparatively slow. Iron evolves through a multitude of oxo species, which could contribute to the preferential formation of gels over solid materials.

In an aqueous environment iron(III) has a propensity to hydrolyse water forming oxo-bridges and precipitating as a hydrolytic polymer. Fe(III) forms many hydroxide species in aqueous solution,[122] these include $Fe(OH)^{2+}$, $Fe(OH)_2^+$, and $Fe_2(OH)_2^{4+}$ or Fe_2O^{4+}. Many minerals, such as lepidocrocite and ferrihydrite, form as a result of this hydrolysis and precipitation of Fe(III) solutions. The coordination of these oxide complexes is octahedral and a network is formed. The structure of the iron hydroxide mineral geothite is shown in Figure 3.10.

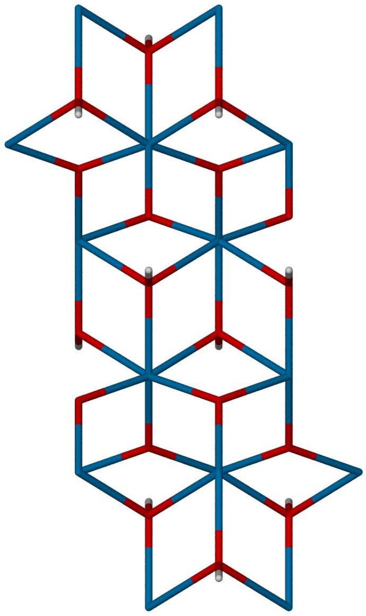

Figure 3.10: Structure of geothite, viewed along [100].[123] The Fe(III) centres are in octahedral sites connected by oxo-bridges. Fe(III) shown in blue and oxygen in red.

While water was not selected as a solvent for this study, hydrated salts and hygroscopic solvents were used, this led to the presence of water in each gelation experiment. The presence of water in the reaction medium suggests that the formation of such an iron(III) polymeric-type structure is likely. The inclusion of carboxylic acid bridging ligands would increase the pore-size/void space relative to the known oxo-polymers and the relatively slow kinetics of the formation of iron(III) oxide species could result in the immobilisation of a large volume of solvent, forming a gel. Xiang and co-workers have observed a small amount of water plays a stabilising role in the formation of Fe(III) and Cr(III) gels with carboxylate ligands.[124]

3.7 Conclusion

There are many factors which contribute to gel formation. For the systems investigated, the trends suggest that a tridentate ligand combined with a non-labile metal salt whose counter ion has the potential to play a stabilising role are most likely to result in gelation. Table 3.7 gives a summary of the gels formed in this study. None of the combinations result in all possible gels being formed.

Table 3.5: Summary of gel formation. No gels were formed using Co-acac, Fe-acac, and Fe-ox

Ligand	**Solvent**	**Fe**	**Fe-sul**	**$FeBr_3$**	**$FeCl_3$**	**Al**
tri	DMF	RT/60/90	none	RT/90		RT/90
	EtOH	RT/60/90		RT/60	60	
	DMA	RT/60/90				90
5nite	MeCN	60	none			none
	DMF	RT/60/90		RT/60/90	RT/60/90	
	EtOH	RT/60		RT/60		
	DMA	RT/60/90		RT/60/90	RT/60/90	
	DMSO	RT		RT		
35pca	DMF	RT/60/90	RT	RT/60/90	RT/90	RT/90
	EtOH	RT/60/90		RT/60	60	60
	DMA	RT/60/90		RT/60/90	RT/60/90	90
26pca		none	none	none	none	none
25pca		none	none	none	none	none
terept	DMA	RT	none	none	none	60/90
iso	DMF	RT/60/90	none	60	60	
	EtOH	RT/60				
	DMA	RT/60/90		RT/60	RT/60	90
1245btc	DMF	RT/60/90	none	RT/90	none	RT/90
	EtOH	RT/60				
	DMA	60/90				90
phens	EtOH	RT/60/90	none	RT	none	none

RT refers to room temperature, the temperatures were measured in °C. These are the temperatures at which gels formed.

Chapter 4

Gel Characterisation

Supramolecular gels consist of a large volume of solvent which can make characterisation of these materials difficult. Multiple techniques were used to gain an understanding of the composition and nature of the gels. The results from techniques such as thermal analysis, percentage composition, Fourier transform-infrared spectroscopy, powder X-ray diffraction, electron spin resonance, and flow behaviour and viscosity are discussed here. Several gels have been selected to illustrate the characterisation techniques: generally Fe-5nite-DMF and Fe-tri-DMF. Characterisation of other gels can be found in Appendix B.

4.1 Inverted vial test

Gels were identified using the inverted vial test. The gel resists gravitational force, and will not leave the bottom of the vial if turned upside down. The gels formed have different colours based on the combination of starting materials used (Figure 4.1). The colour ranged from a pale translucent white, to quince-jelly red. The change in colour as gelation occurs is evidence of metal binding during the gelation process. Gels would only form if both the iron(III) salt (or aluminium(III) salt) and carboxylate ligand were present in solution. If the individual gel components are dissolved in solvent and left to stand separately, gels do not form.

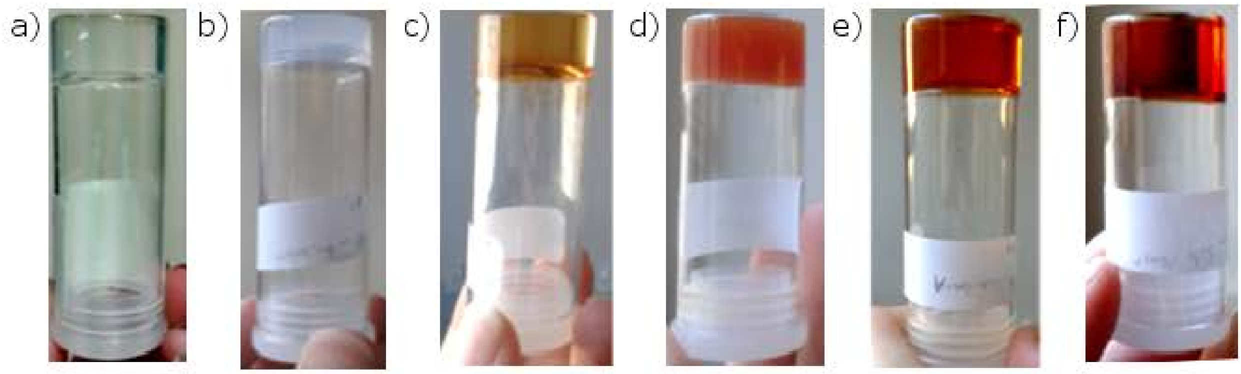

Figure 4.1: A few examples of the different colours of gels formed. From left to right: a) Al-tri-DMA, b) Al-tri-DMF, c) Fe-5nite-DMSO, d) Fe-5nite-EtOH, e) Fe-iso-DMA, and f) Fe-5nite-DMF.

4.2 Thermal analysis

Gels are multicomponent systems which immobilise a large volume of solvent.[6] The solvent content of the gels was determined using thermal gravimetric analysis (TGA). In this study, the gels comprised *ca.* 95-99% solvent. This large body of solvent masks the signals which result from the interaction between the ligand and metal salt. As a result of this large quantity of solvent, the gels had to be dried in order to perform further characterisation.

4.2.1 Hot stage microscopy

Hot stage microscopy (HSM) was performed on wet gel (Figure 4.2). Understanding at what temperature solvent is lost is useful when analysing TGA results. As an example, the Fe-5nite-DMF gel visibly reduces in size as temperature increases and the solvent leaves the gel. The gel begins to darken at approximately 220 °C and decomposes shortly thereafter. By 400 °C the material has decomposed leaving a black, dried out residue.

This behaviour is observed for all the gels. However the end temperatures vary with solvent. Those containing solvents with higher boiling points lose the solvent over a greater temperature range.

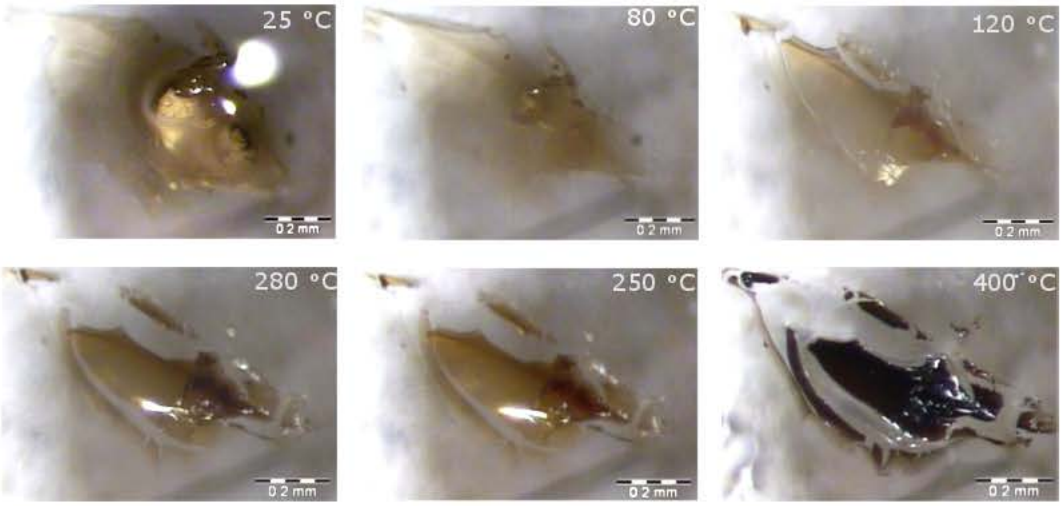

Figure 4.2: Hot stage microscopy images of Fe-5nite-DMF, the gel visibly decreases in size as the solvent is lost, and darkens before decomposing.

4.2.2 Thermal gravimetric analysis

Figure 4.3 shows the TGA trace of wet Fe-5nite-DMF. It is assumed, from the HSM results, that the mass loss of 97.79 ± 0.03% between 20.20 ± 0.3 °C and 124.04 ± 59.7 °C (n = 3) is solvent. The percentage of solvent present in various gels, in general between 97% and 99%, is presented in Table 4.1. Solvent loss begins immediately upon heating for all gels studied. In all cases, the end temperature is greater than the boiling point of the solvent concerned, suggesting that the solvent is stabilised within the gel lattice. The melting points of 5-nitroisophthalic acid, trimesic acid, and phenylsuccinic acid are all in excess of 166 °C (Table 4.2). The iron(III) coordination complexes are expected to decompose at a higher temperatures than are observed here.

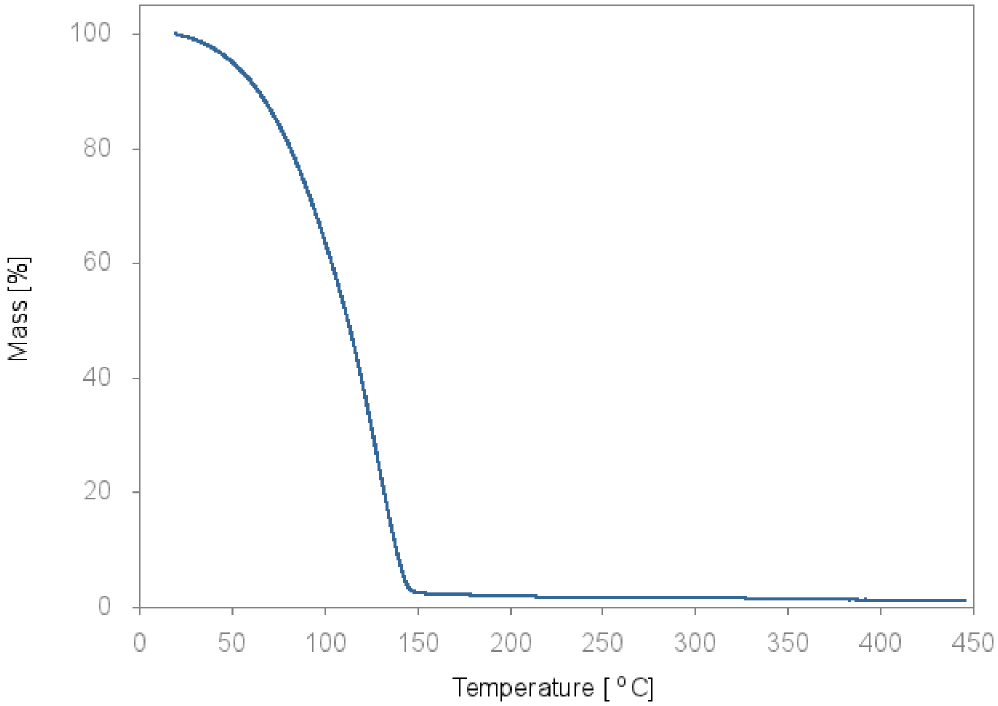

Figure 4.3: TGA trace of Fe-5nite-DMF showing a 97% mass loss.

Table 4.1: Mass loss from gel observed during TGA experiments

Gel	**Percentage loss** [%]	**Onset temperature** [°C]	**End temperature** [°C]
Fe-5nite-EtOH	98.68 ± 0.31	21.14 ± 0.66	95.91 ± 3.52
Fe-5nite-DMA	98.84 ± 0.1	20.93 ± 0.7	93.15 ± 1.6
Fe-5nite-DMF	97.89 ± 0.09	20.08 ± 2.95	153.8 ± 4.2
Fe-tri-EtOH	98.31 ± 0.22	21.57 ± 1.33	119.03 ± 1.77
Fe-tri-DMF	97.15 ± 0.86	21.46 ± 1.52	150.32 ± 0.79
Fe-phens-EtOH	98.77 ± 0.06	17.97 ± 1.51	117.66 ± 4.76

Table 4.2: Melting points of ligands used

Ligand	**Melting point** [°C]
5-nitroisophthalic acid	259-261
Trimesic acid	>300
Phenylsuccinic acid	166-168

Thermal analysis of Fe-tri-DMF indicates a mass loss of 97.15 ± 0.86% is seen between 21.46 ± 1.52 °C and 150.32 ± 0.79 °C (n = 3). This is attributed to loss of solvent. However, the TGA plot reported by Banerjee *et al* shows a mass loss of approximately 80% for Fe-tri-DMF which is attributed to solvent.[125] The reason for the difference seen in the mass losses (97% instead of 80%) is that Kurugot *et al* used 1.5 mL of DMF when forming the gel, however 5 mL of solvent was used in this study.

4.2.3 Differential scanning Calorimetry

A cooling DSC experiment was performed to determine the freezing point of the solvent in the gel. The surface solvent and the solvent in gel pockets may have different freezing points. This may be seen as two separate events or a shoulder on the main event.

A small amount of wet gel was prepared in a vented Aluminium pan of the type used for DSC. The gel was cooled to -90 °C followed by heating to 50 °C in order to see the freezing and then melting of the solvent in the gel pockets.

4.2.3.1 Glass transitions

No freezing nor melting events were seen for Fe-5nite-DMF as displayed in Figure 4.4, this may be a result of the suppression of the freezing point of the DMF in the gel pockets,[126] since the DMF freezing point in the literature is recorded at -60 °C and the DSC has a lower limit of -90 °C. Examination of the cooling DSC trace shows the gel undergoes a glass transition. This also occurs in gel prepared from ethanol (freezing point of -114 °C).

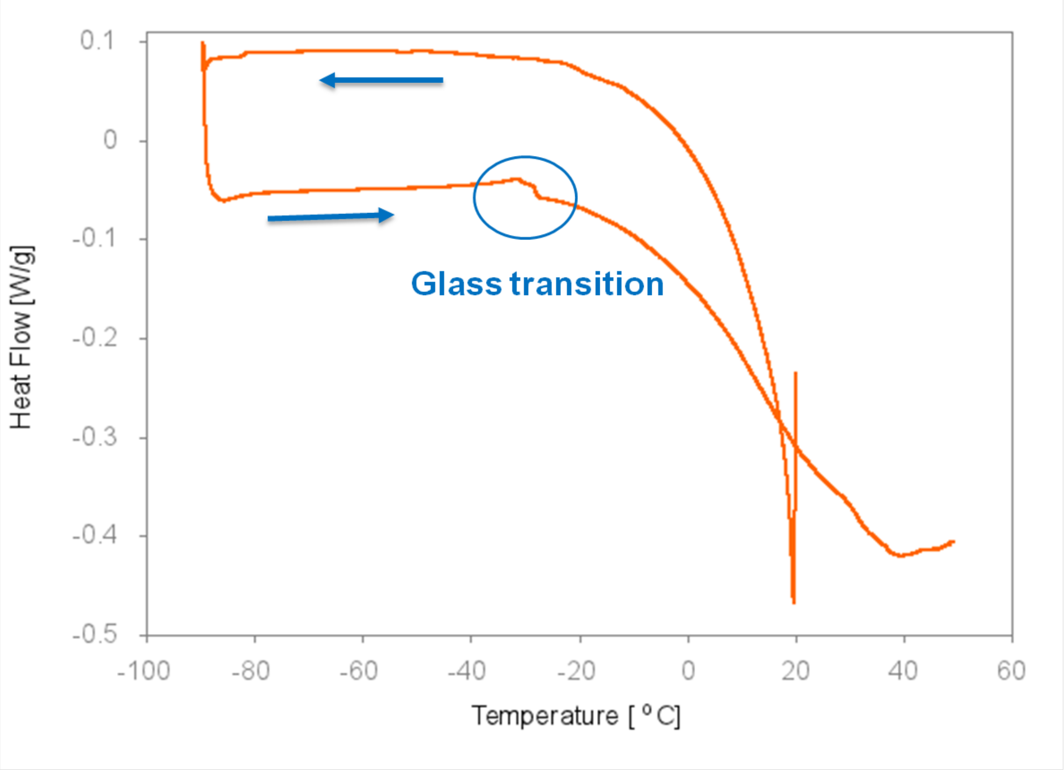

Figure 4.4: DSC trace cooling and heating cycle, both with a heating rate of 2 °C min^{-1}. During this experiment, the sample is cooled to -90 °C and then heated to 50 °C. Fe-5nite-DMF is presented here.

The glass transitions of selected gels are given in Table 4.3. There is a small temperature range over which the T_g is observed (approximately -29 °C to -45 °C).

Table 4.3: Glass transition of selected gels. There is small deviation in the temperature range of T_g

	Temperature		
Gel	**Onset** [°C]	**Midpoint** [°C]	**End** [°C]
Fe-5nite-DMF	-29.15 ± 1.16	-28.46 ± 1.36	-28.05 ± 1.27
Fe-tri-DMF	-33.87 ± 0.63	-33.19 ± 0.39	-32.34 ± 0.54
Fe-phens-EtOH	-34.9 ± 3.3	-34.2 ± 2.9	-30.8 ± 3.9

4.2.3.2 Freezing the solvent within the gel pockets

For the gels formed in solvents with higher freezing points, acetonitrile and DMA, which have freezing points of -45 °C and -20 °C respectively, very large exothermic events were seen upon cooling (Figures 4.5 and 4.6). These exothermic events were attributed to the freezing of the solvent in gel pockets. The DSC trace of Fe-5nite-MeCN shows an event at a temperature of -59.4 ± 1.8 °C and with an associated heat flow 71.7 ± 29.0 J g^{-1} (n = 3). Similarly, this occurred for Fe-5nite-DMA at a temperature of -55.7 ± 1.3 °C and a heat flow of 54.2 ± 14.1 J g^{-1} (n = 3). Both cases indicate a freezing point below that of the pure solvent. This suppression of the solvent freezing point has also been seen in polymers.[126] It can be attributed to the three-dimensional network of the gel preventing the formation of micro-crystals. I was unable to find an example of this phenomenon observed in gels. To the best of our knowledge this is the first such report.

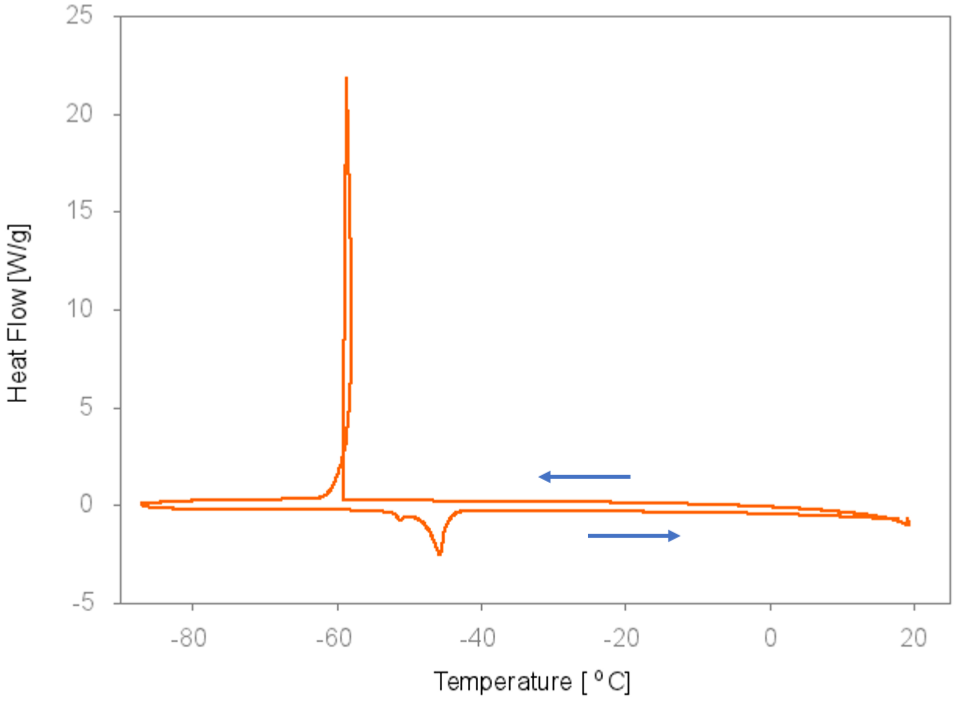

Figure 4.5: DSC trace of Fe-5nite-MeCN shows an exothermic event at -59.4 ± 1.8 °C followed by two endothermic events at -52.5 ± 0.7 °C and -47.7 ± 0.01 °C (n = 3).

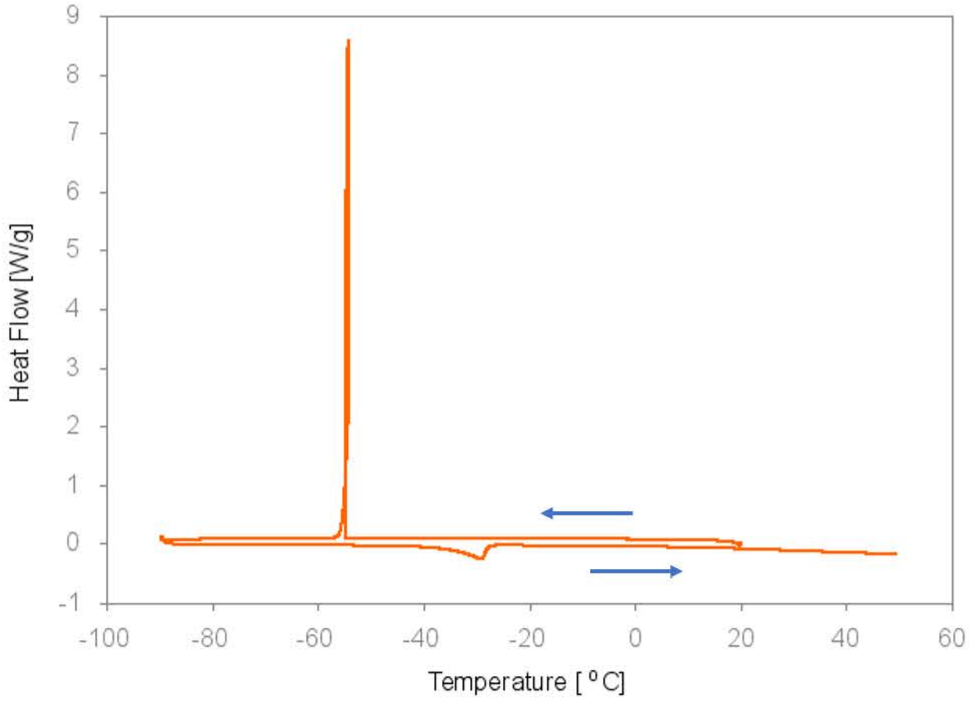

Figure 4.6: DSC plot of Fe-5nite-DMA, with an exothermic event at -51.4 ± 4.9 °C. Upon heating an endothermic event is observed at -44.6 ± 5.3 °C (n = 3).

The loop in the DSC curve indicates an exothermic event (Figures 4.5 and 4.6). This may be a result of the large enthalpy of fusions which are 8.2 kJ mol^{-1} for acetonitrile and 10.2 kJ mol^{-1} for DMA. Upon heating the materials from -90 °C endothermic events are observed. These are attributed to change of state from solid to liquid of solvent in the gel pockets and not glass transitions. The enthalpy of fusion is a first-order phase transition.

For both Fe-5nite-MeCN and Fe-5nite-DMA, the freezing temperature observed is lower that that of the melting temperature (Table 4.4). Supercooling occurs when a liquid freezes below its melting point.[127] This occurs when no nucleation sites for crystallisation are present and kinetic stabilisation occurs which prevents the thermodynamically stable phase from being attained. Water is a classic example, and will only freeze at very low temperatures if cooled in a very smooth containers. However, if disturbed in anyway, it will freeze within a short space of time. Fe-5nite-MeCN and Fe-5nite-DMA hindered the formation of micro-crystals and the observed freezing point is lower than that of the melting point.

Table 4.4: Temperatures of thermal events gels, these values are lower than those for the enthalpy of freezing

	Freezing	**Melting**	
Gel	**Onset** [°C]	**Onset** [°C]	**Peak** [°C]
Fe-5nite-MeCN, first	-59.4 ± 1.8	-52.0 ± 0.2	-52.5 ± 0.7
Fe-5nite-MeCN, second	-59.4 ± 1.8	-45.5 ± 0.2	-47.7 ± 0.01
Fe-5nite-DMA	-55.7 ± 1.3	-35.8 ± 9.1	-44.6 ± 5.3

Fe-5nite-DMA has an enthalpy of fusion of 55.1 ± 3.7 J g^{-1} (n = 3). Two endothermic events are observed for Fe-5nite-MeCN, while the onset and peaks for these events are reproducible the associated enthalpy of fusion obtained had a wide spread in the data. The range was from 1.5 J g^{-1} to 5.9 J g^{-1} for the first and 21.1 J g^{-1} to 67.1 J g^{-1} for the second. Despite great care being taken to ensure sample preparation was consistent, the large discrepancies in these data suggest differences in the gels. It is plausible that gelation did not occur to the same extent in each gel and varying amounts of solvent was encapsulated. The two events may be attributed to the solvent being in two different environments within the gel.

4.3 Percentage composition

Several techniques were used to determine the percentage composition of the elements in the gel. These include elemental analysis, microwave plasma - atomic emission spectroscopy (MP-AES), and inductively coupled plasma optical emission spectrometry (ICP-OES).

To determine the percentage composition of carbon, hydrogen and nitrogen, elemental analysis was used (Table 4.5). MP-AES and ICP-OES were used to determine the percentage of Fe(III) in the oven dried xerogel (heated at 85 °C for 72 h). The percentage of iron found in the oven dried gels using either MP-AES or ICP-OES is presented in Table 4.5. The percentages of the total mass of Fe(III) for Fe-5nite-DMF and Fe-tri-DMF xerogels using MP-AES were found to be 8.1% and 5.2%, respectively. The trimesic acid ligand is tridentate while 5-nitroisophthalic acid is bidentate, therefore the trimesic acid has the potential to coordinate more Fe(III) ions and hence the Fe-tri-DMF xerogel may contain a larger percentage of iron than the Fe-5nite-DMF counter part.

Table 4.5: Elemental analysis of Fe-5nite-DMF and Fe-tri-DMF xerogels, average over two sample analyses

Method	**Element**	**Fe-5nite-DMF** [%]	**Fe-tri-DMF** [%]
Elemental Analysis	**C**	27.89 ± 0.11	27.09 ± 0.04
	H	3.92 ± 0.06	5.84 ± 0.09
	N	10.72 ± 0.01	12.00 ± 0.14
MP-AES	**Fe**	8.05 ± 0.06	5.17 ± 0.04
ICP-EOS	**Fe**	8.32	5.64

4.4 Fourier transform infra-red spectroscopy

Thermal analysis shows that a large percentage of the gel is solvent. This high solvent content is problematic when attempting to characterise the material. Figure 4.7 is an example of the masking of signals by the solvent. To avoid this pitfall, the gels were dried, either oven or freeze dried in order to obtain a clear signal.

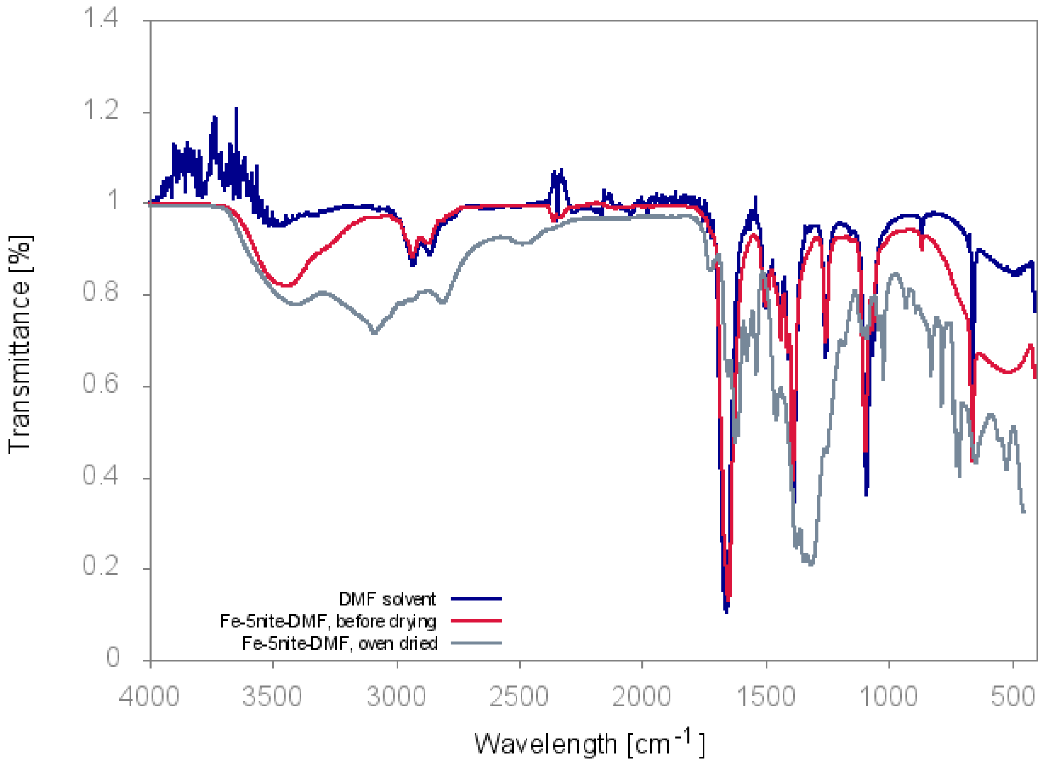

Figure 4.7: FT-IR pattern of wet and oven dried Fe-5nite-DMF. The pattern of the gel before drying matches that of the DMF solvent. More detail is seen in FT-IR pattern of the xerogel.

The spectrum of Fe-5nite-DMF xerogel is shown in Figure 4.8. The assignment of the FT-IR bands are shown in Table 4.6. It is evident that the metal centre, Fe(III), interacts with the ligand, 5-nitroisophthalic acid. The disappearance of the O-H stretch is a clear indication that the carboxylate proton from the ligand has been removed, allowing the oxygen to interact with the metal centre. The most marked difference is in the C=O stretch peak which shifts from 1705 cm^{-1} in the free ligand to 1620 cm^{-1} once the gel has formed.[128,129] The FT-IR spectra of other gels can be found in Appendix B.

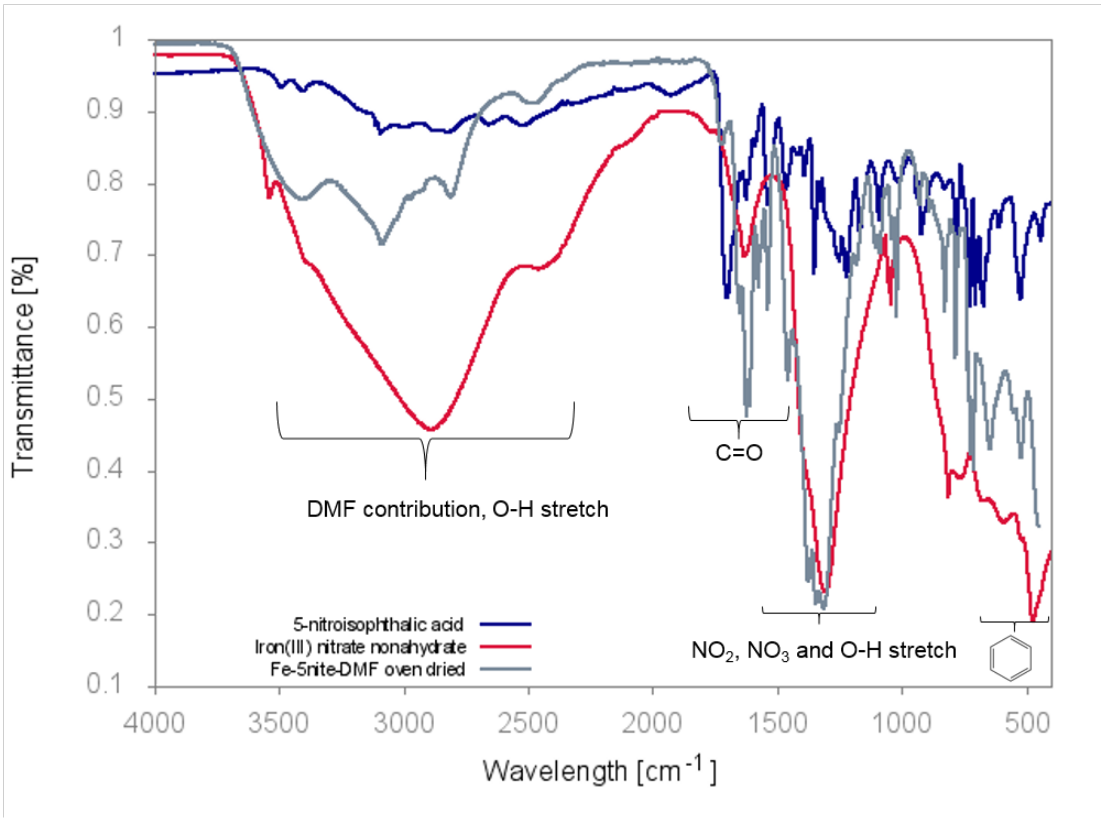

Figure 4.8: Comparison of FT-IR spectra of Fe-5nite-DMF xerogel and its starting materials.

Table 4.6: Infrared bands and their assignments for the free ligand (5-nitroisophthalic acid) and the Fe-5nite-DMF xerogel

Assignment	**5nite** υ [cm^{-1}]	**Fe-5nite-DMF** υ [cm^{-1}]
O-H stretch	3095 *bw*	
C=O stretch	1705 *m*	1620 *m*
Asymmetric NO_2 stretch	1350 *m*	1375 *m*
Symmetric NO_2 stretch	1221 *m*	1306 *m*
Benzene ring out of plane C-H bend and NO_2 scissors	774, 722, 705, 670 *m*	785, 721, 712, 635 *m*
*O-H stretch		3410 *bw*
*N-$(CH_3)_2$ stretch		2808 *bw*

m medium peak, *bw* broad, weak peak

*DMF contribution same as Fe-tri-DMF xerogel

4.5 Powder X-ray diffraction

Powder X-ray diffraction patterns were collected for the dried material (Figure 4.9). The pattern shows an amorphous material and no long range order is seen.

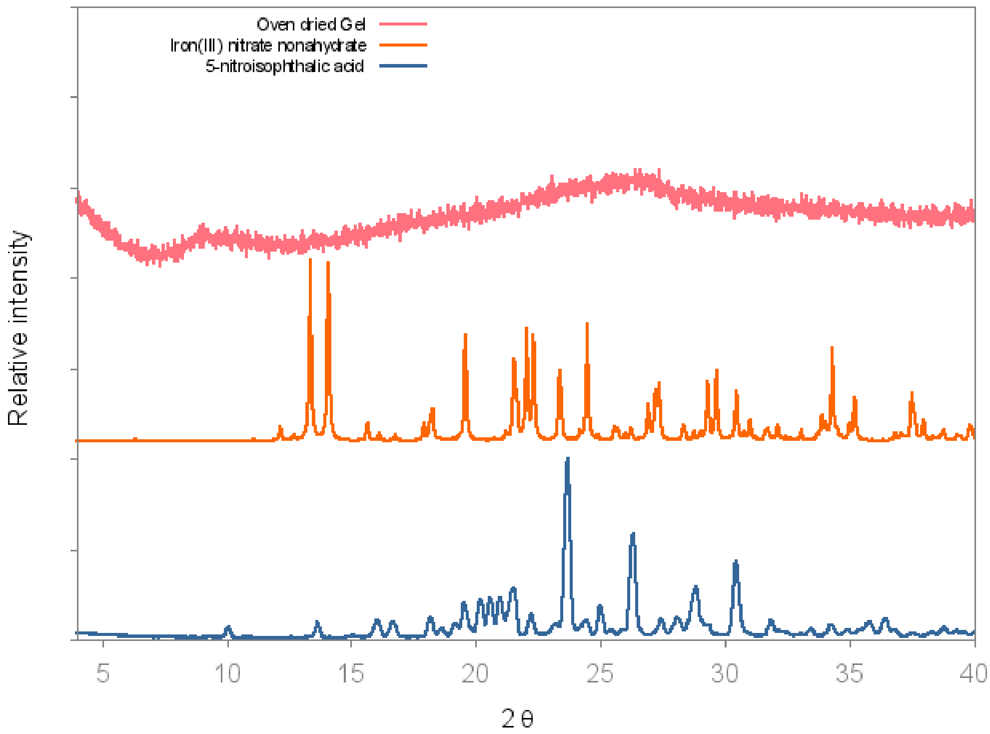

Figure 4.9: PXRD pattern of Fe-5nite-DMF xerogel and the starting materials. The sample is amorphous.

4.5.1 Variable temperature powder X-ray diffraction

To investigate the effect of solvent loss from the xerogel, variable temperature PXRD was performed for Fe-5nite-DMF. The sample was oven dried and freshly ground. There is very little change in the featureless diffractograms over the temperature range of 25 °C to 220 °C which may indicate there is no structural change in the xerogel upon heating.

4.6 Scanning Electron Microscopy

An examination of the gels' physical structure was undertaken using scanning electron microscopy (SEM). In the SEM images for some reported metallogels different features can be seen, such as the fibres observed in the aromatic–linker–steroidal (ALS) molecular gel with platinum[130] or short rods as seen in the copper(II) 4-(1H-pyrazol-3-yl)pyridine metallogel.[20] Another example of structure shows metallogels which have a block-like mophology, such as the calcium 5-(1,2,4-triazoleyl)isophthalic acid metallogel.[18] On the microscopic scale, the gels in this study are block-like in appearance.

The Fe-5nite-DMF gels were formed in vials and freeze dried. Freeze drying was chosen as it was less likely than oven drying to collapse the gel pockets. Figure 4.10 shows the material which is glassy and pockmarked in appearance. Glass transition (which was confirmed using DSC) during freeze-drying could explain the glassy appearance. Pockmarks on the surface of the gel may be a result of solvent loss during the freeze drying process. Energy dispersive spectroscopy (EDS) was performed on select parts of the gel to determine the elemental composition of the different areas of the gel. Iron was present in all of the areas tested, with a 9.20 ± 0.28% iron content, which is comparable to that found using MP-AES.

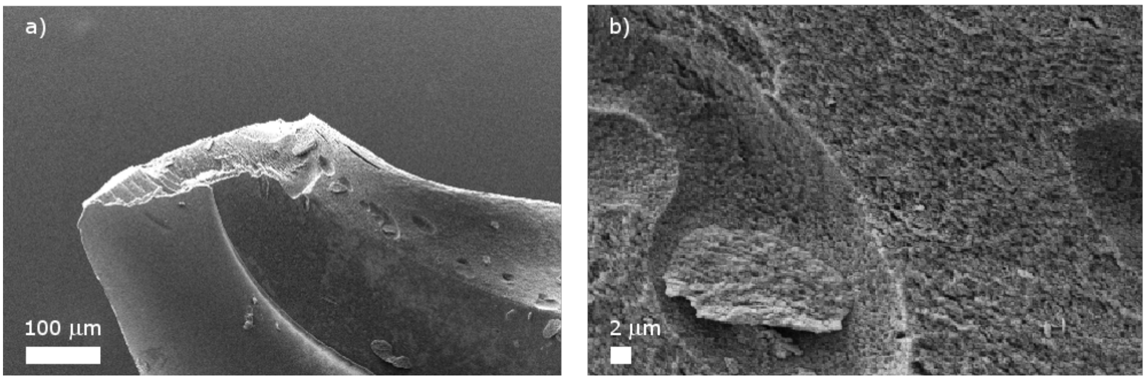

Figure 4.10: SEM images of Fe-5nite-DMF. a) Shows the glassy appearance of the gel, and b) shows the "pockmarks"on the surface created when solvent was removed from the gel during the freeze drying process.

To investigate the effect of the drying method on the morphology, further SEM images of Fe-5nite-DMF xerogel were collected (Figure 4.11). The oven dried sample is more powdery in appearance when compared to freeze dried sample. As this sample was dried in the oven, it has not undergone the glass transition which the freeze dried sample underwent.

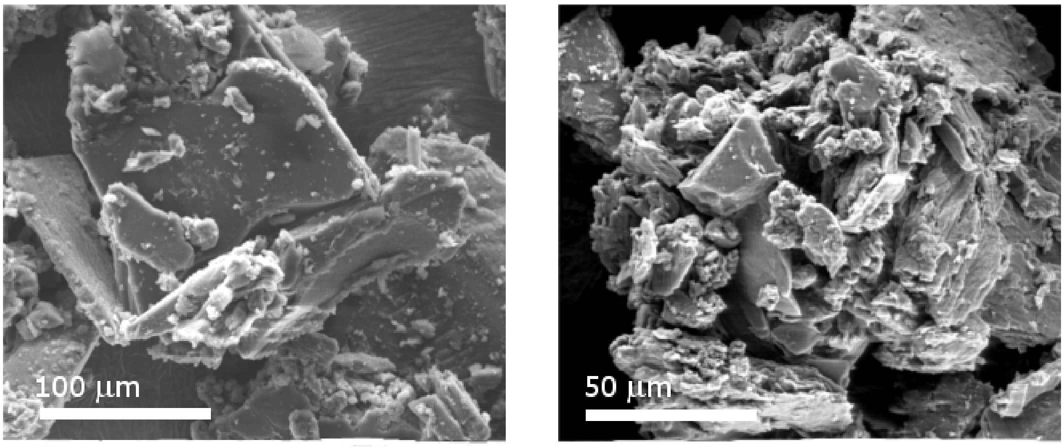

Figure 4.11: SEM images of Fe-5nite-DMF xerogel. The sample has a powdery appearance which may be attributed to oven drying.

In Figure 4.12, smooth surfaces can be seen for the freeze dried Fe-5nite-EtOH. Where the material has been ground slightly (Figure 4.12, c and d), the structure appears to be spongy/porous along the breaks. These porous areas could provide a surface for gas sorption.

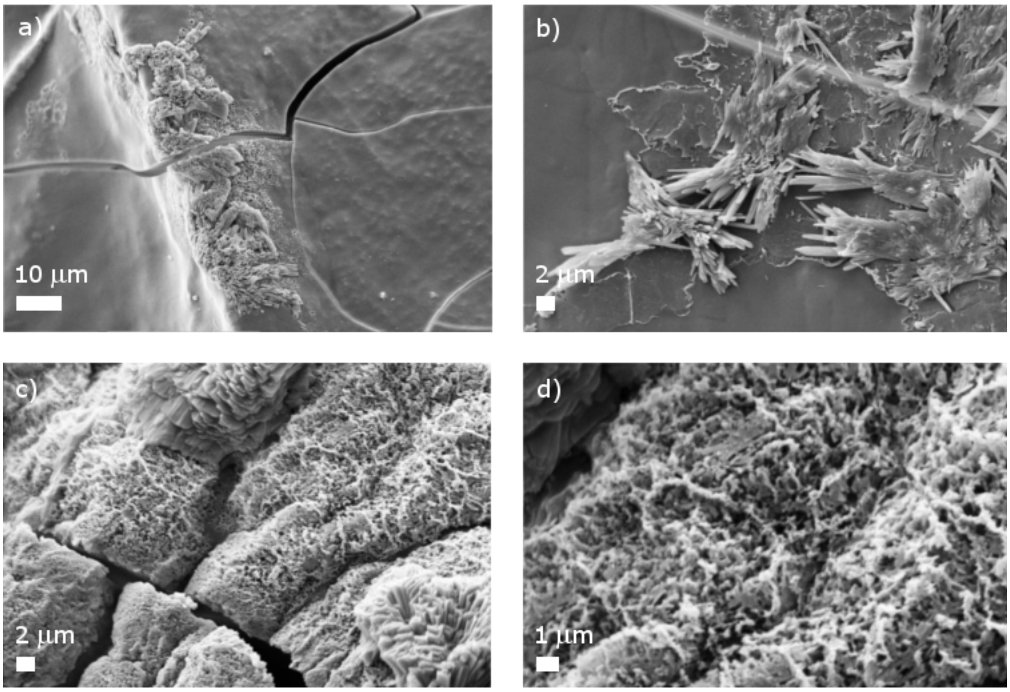

Figure 4.12: SEM images of freeze dried Fe-5nite-EtOH showing (a) a smooth surface with (b) small crystalline material. (c-d) A spongy area can also be seen.

The block-like appearance of the xerogels may be a result of the choice of ligand. Trimesic acid and 5-nitroisophthalic acid tend to form block-like crystals rather than needles. It is thought that this directs the formation of blocks rather than fibres.

4.7 Iron(III) or iron(II)

Iron(III) is paramagnetic and because of this, NMR spectroscopy cannot be used because the unpaired electron gives rise to an additional, extremely efficient, relaxation pathway *via* the paramagnetic moment of the metal centre. This results in loss of resolution and sensitivity. In the limiting case there are no signals in the ^{1}H NMR spectrum. In order to investigate the spin state of the iron cation in the gel samples, electron spin resonance and magnetic susceptibility studies were performed.

4.7.1 Electron spin resonance

Electron spin resonance (ESR) spectra for Fe-5nite-DMF and Fe-tri-DMF can be seen in Figures 4.13 and 4.14. These experiments were used to gain an understanding of the spin state and symmetry of the iron(III) centre.

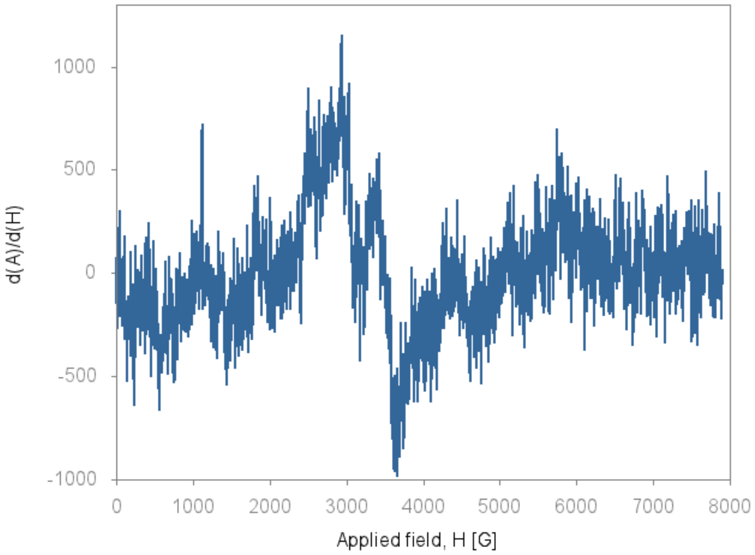

Figure 4.13: X-band ESR spectrum of Fe-5nite-DMF, in the solid state at 298 K. Experimental settings: gain, 1.00 × 10^2; modulation amplitude, 1.56 G; sweep time, 250.00 sec; number of scans, 1; and power, 1.912 mW.

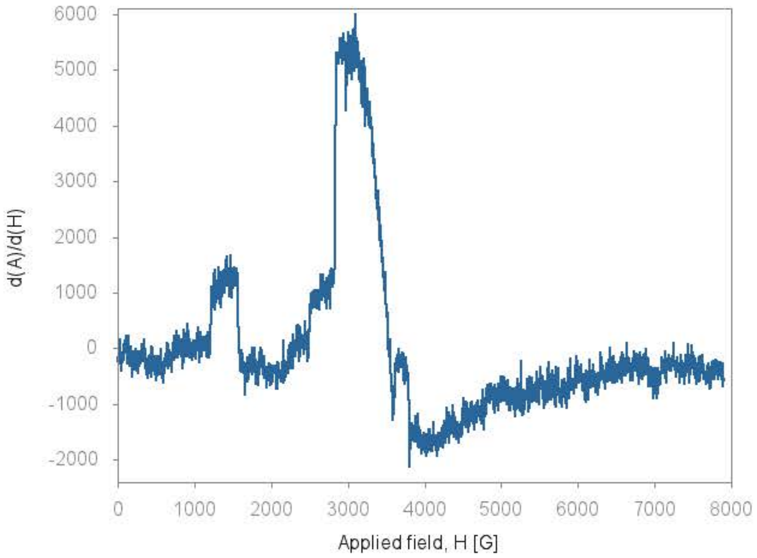

Figure 4.14: X-band ESR spectrum of Fe-tri-DMF, in the solid state at 298 K. Experimental settings: gain, 1.00 × 10^2; modulation amplitude, 1.56 G; sweep time, 250.00 sec; number of scans, 1; and power, 1.912 mW.

Both of these have broad and weak signals, two of the reasons for this are temperature, and DMF is a poor solvent for ESR studies. The intensity increases with a decrease in temperature and both samples were run at room temperature and contain approximately 12% DMF. A mixture of spin states of Fe(III) could also contribute to this, particularly in the case of Fe-5nite-DMF which most likely contains anti-ferromagnetic coupling which will reduce the signal intensity. As a consequence, it is difficult to determine the magnetic moment and g tensors for this sample.

As previously stated, it is plausible that the low-resolution, noisy spectrum of Fe-5nite-DMF is a result of a mixture of spin states of iron(III) in the gel and the DMF which is still present in the xerogel sample and the anti-ferromagnetic coupling which was suspected from the magnetic susceptibility results for Fe-5nite-DMF.

The ESR spectrum of Fe-tri-DMF xerogel shows a high spin iron(III) with axial magnetic moment, g values of 2.013 and 4.404. A low temperature experiment should be run on Fe-tri-DMF to eliminate the presence of rhombic magnetic moment as the broad lines, which are present in the room temperature run, may be obscuring other lines.

The ESR spectrum of Fe-tri-DMF is similar to that of a Fe(III)-content ZSM-5 type zeolite.[131] Fe(III)-content ZSM-5 is a catalyst of redox reactions, such as biomimetic oxidations, or selective catalytic reactions of pollutants,[131] and consists of pentasil units linked by oxygen bridges.[132] This provides further evidence that the Fe(III) centres are interacting with the carboxylate moieties during gel formation.

4.7.2 Magnetic susceptibility

An investigation into the magnetic susceptibility was performed to determine the response of the Fe-5nite-DMF and Fe-tri-DMF xerogels to a magnetic field.

The experiment gives information about whether the material is paramagnetic (positive magnetic susceptibility) or diamagnetic (negative magnetic susceptibility).[133] Paramagnetism arises from unpaired electrons and the compound will have a non-zero spin or orbital angular momentum.

A custom in-house built Evans balance (Figure 4.15) was used. Mercury(II) tetrathiocyanatocobaltate(II) was used for calibration and haemin was run as the standard. The value obtained experimentally for the magnetic susceptibility of haemin was 6.12 ± 0.20 $cm^3\ g^{-1}$ which lies within an acceptable range from the literature value of 5.9 $cm^3\ g^{-1}$.[134]

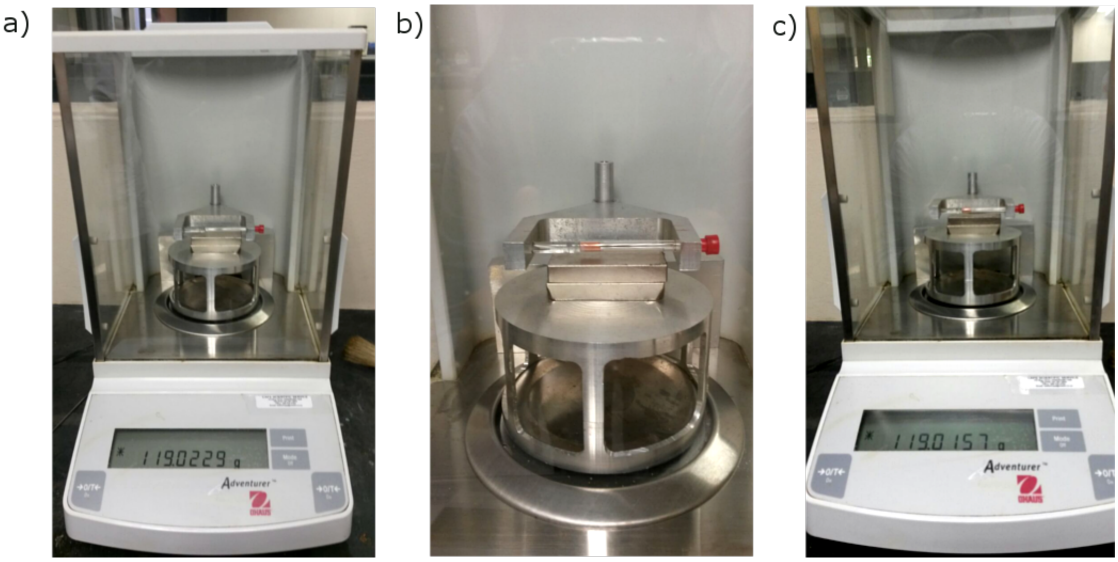

Figure 4.15: In-house Evans balance used for magnetic susceptibility studies. a) The empty tube is placed above the rare earth magnet and the mass is recorded. b) The xerogel is added to the tube, the length of the sample measured, and placed above the magnet. c) Mass of the magnet is recorded with the xerogel above it.

During the experiment, the difference in the mass of the rare earth magnet is measured. The attraction or repulsion of the magnet by the sample results in a change of mass and this is related to the magnetic susceptibility using the Equation 4.1 below:

$$\chi_g = \frac{C_{bal}\,(R_0 - R_1)\,L}{m \times 10^9} \tag{4.1}$$

where χ_g is the mass magnetic susceptibility ($cm^3\ g^{-1}$), C_{bal} is the calibration constant of the balance, R_0 is the mass of the magnet (g) when no sample is present, R_1 is the mass of the magnet when the sample is present, L is the length of the sample in the tube (cm) and m is the mass of the sample (g). The calibration was established using the magnetic susceptibility constant of a standard, mercury(II) tetrathiocyanatocobaltate(II), as reported by Figgis and Nyholm (χ_g = 16.44 × 10-6 cm^3 g^{-1}).[135] Diamagnetism is present in all atoms or molecules, therefore the diamagnetic contributions (χ_D) must be taken into account. The diamagnetic contribution can be calculated using Pascal's constants or approximated using Equation 4.2.[133]

$$\chi_D = \frac{-MW}{2} \times 1.0^{-6} \tag{4.2}$$

where MW is the molecular weight of the substance. It is acceptable to use this approximation for room temperature experiments.[133] χ_D is subtracted from the experimentally obtained (χ_g) values to give the magnetic susceptibility of the xerogels.

This experiment was run on xerogels, Fe-tri-DMF and Fe-5nite-DMF. In both cases the empirical formula per iron was used, instead of the molecular formula. This was calculated using the data gathered from MP-AES and mass spectrometry. It is very difficult to obtain a molecular formula for these gels as there is little long range order. Despite lengthy attempts to dry the gel completely, approximately 12% DMF remained. In light of this, the approximation was used to determine the diamagnetic contribution of each xerogel. These are non-trivial systems and the lack of long range order makes it difficult to determine the diamagnetic contribution based on the exact number of atoms present and the bonds in which these atoms are involved.

The Fe-tri-DMF has a magnetic susceptibility value of 5.68 ± 0.16 μB which indicates it is a high spin d_5 S = $\frac{5}{2}$ system. The theoretical value of a high spin system is 5.95 μB.

The theoretical value for an intermediate spin system is 3.87 μB. The calculated value for Fe-5nite-DMF is 3.47 ± 0.22 μB, indicating this material has a spin intermediate of S = $\frac{3}{2}$ species or is a mixture of spin states. In the case of a gel, which does not have long range order an intermediate spin state may also arise from a mixture of spin states as there is a possibility of μ-oxo bridges anti-ferromagnetically coupled Fe-O-Fe present in the sample. A possible method of determining this would be to use a SQUID magnetometer which measures the magnetic susceptibility as a function of temperature. Anti-ferromagnetic species have a temperature dependence while spin $\frac{1}{2}$ is constant. Such equipment was not readily available to permit carrying out such measurements. The electron spin resonance (ESR) spectra of Fe-5nite-DMF are very noisy which may also be a result of a mixture of spin states being present.

4.7.3 Reaction with ascorbic acid

A number of gels have been explored for interaction with ascorbic acid. It has been shown to enable switching between gel and sol phases.[136] Panda and co-workers developed a gel which was reported to entrap ascorbic acid, vitamin C, which may be useful for the delivery of vitamins.[137]

When iron(III) oxidises ascorbic acid,[138] the red-orange Fe(III) is reduced to Fe(II), and a dark blue colour is seen.[139] Using a solution of 0.15 M ascorbic acid, the transition was observed when Fe-tri-DMF and Fe-5nite-DMF were soaked in this solution (Figure 4.16 and 4.17). This indicated that iron(III) is present in the gel. The experiment was carried out using both water and DMF as the solvent and yielded similar results No gel-sol phase switching was seen.

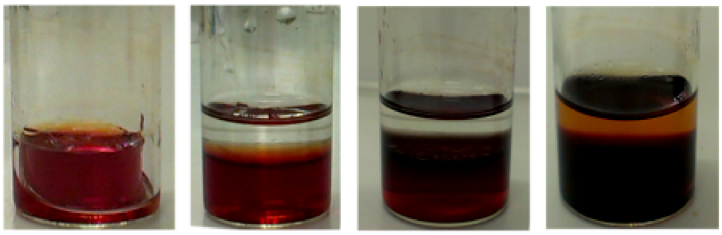

Figure 4.16: Reduction of ascorbic acid in DMF by Fe-5nite-DMF. The gel visibly darkens as the Fe(III) is reduced to Fe(II).

Figure 4.17: Reduction of ascorbic acid in water by Fe-tri-DMF. A dark blue colour can be seen on the edges as Fe(III) is reduced to Fe(II).

4.8 Flow behaviour and viscosity

To understand gels' properties, an understanding of their viscosity and flow behaviour is needed. Fe-5nite-DMF, Fe-5nite-EtOH, Fe-tri-DMF, Fe-tri-EtOH, and Fe-phens-EtOH all show shear thinning characteristics (Figure 4.18). The shear viscosity is dependent on the degree of the shear load and viscosity decreases with an increase in shear rate. Other materials which have this characteristic include shampoos and paints. Shear-thinning is seen in a number of gels and may be attributed to the fibres within the gel aligning along the axis of stress.[37]

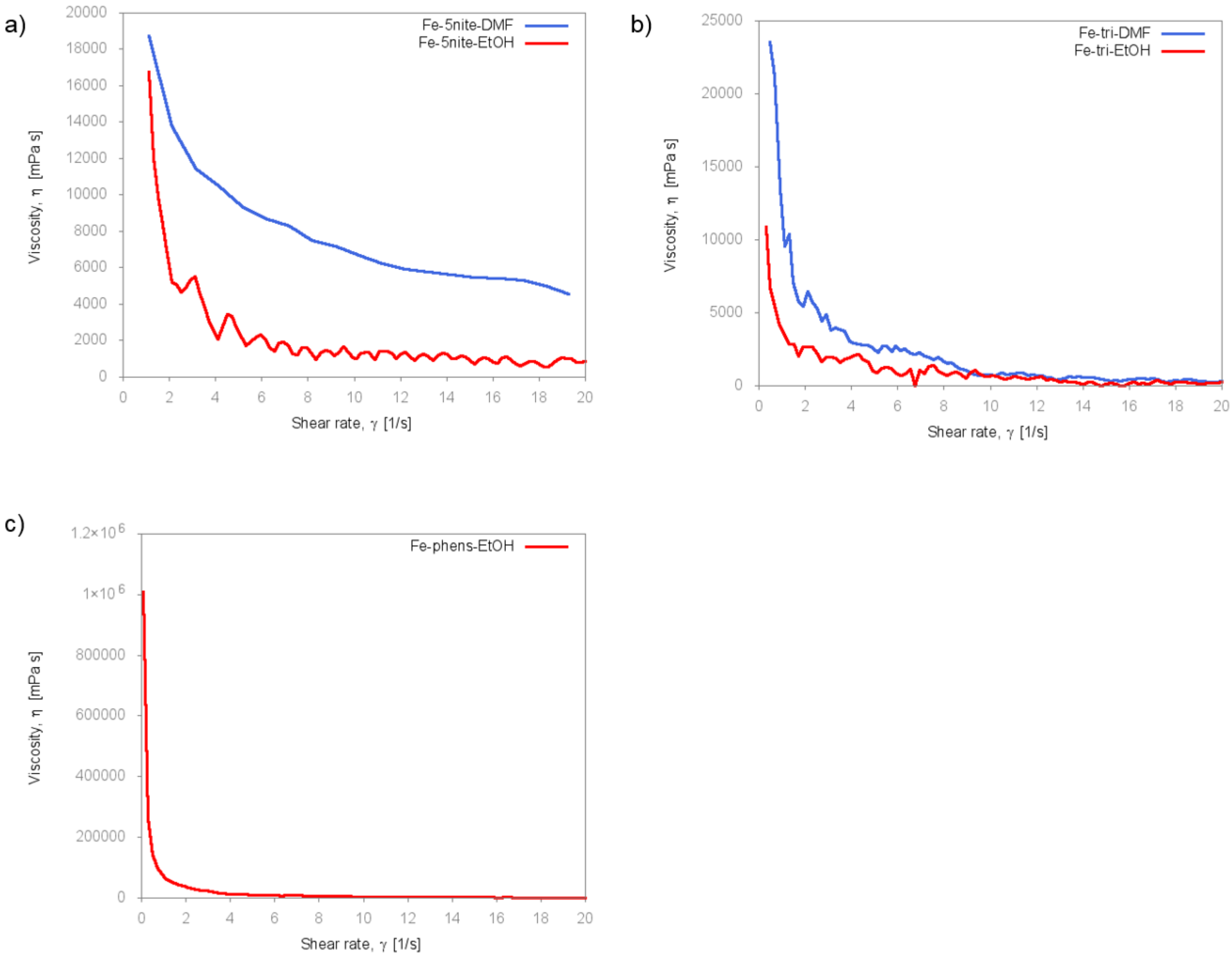

Figure 4.18: Viscosity curves of various gels. a) Fe-5nite-DMF (blue) and Fe-5nite-EtOH (red). b) Fe-tri-DMF (blue) and Fe-tri-EtOH (red). c) Fe-phens-EtOH (red). Shear thinning was observed for all the samples.

4.8.1 Thixotropy

Thixotropy is the property of becoming less viscous when subjected to an applied stress, this process is reversible. Thixotropic gels will become temporarily fluid when shaken or stirred and re-form after a period of rest.[25]

This mechanotropic property is reversible as the self-assembled aggregates are able to undergo structural reorganisations on the microscopic distance scale.[140] Weak, intermolecular interactions such as hydrogen bonding, π-π interactions, London forces and electrostatic forces can form and break during the microscopic changes. Many of the known thixotropic gels are organometallic in nature, and it is thought that the formation and loss of the relatively weak metal-ligand bonds enable the mechano-destruction and reformation of these organometallic gels. One example of a thixotropic metallogel was reported by S. Bhattacharjee and S. Bhattachary. In their study of a Cu(II) hydrogel of a *p*-pyridyl ended oligophenylenevinylene system was investigated. When shaken the metallogel transforms into a viscous sol, when allowed to stand undisturbed a robust gel is reformed.[32]

Fe-5nite-DMF was shaken by hand at room temperature, shear thinning was observed and the material began to flow. After one hour the gel had re-formed (Figure 4.19). The same experiment was performed on Fe-5nite-EtOH, however the Fe-5nite-EtOH gel did not re-form.

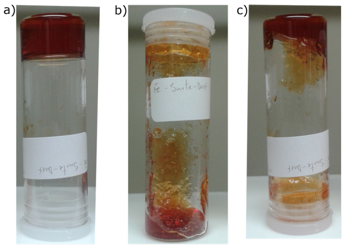

Figure 4.19: Thixotrophy experiment for Fe-5nite-DMF. a) Fe-5nite-DMF, a firm red gel. b) The material shears and decreases in viscosity after stress is applied, c) after one hour the gel has re-formed.

As seen in Section 4.8 the viscosity of Fe-5nite-EtOH, 855.43 mPa s, and Fe-phens-EtOH, 940.88 mPa s decreased to a far greater extent when shear stress was applied, than Fe-5nite-DMF, 4565.2 mPa s. The ability of the Fe-5nite-DMF to re-form after the application of external mechanical force is attributed to the multiple cooperative non-covalent interactions.[22] These forces are stronger in the DMF gel than the ethanol gel and the Fe-5nite-DMF gel re-formed (Figure 4.20).

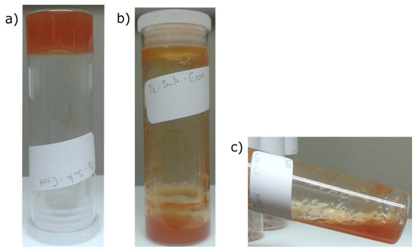

Figure 4.20: Thixotrophy experiment for Fe-5nite-EtOH. a) Fe-5nite-EtOH, orange gel. b) The material shears and decreases in viscosity after shaking, c) after one hour the gel has not re-formed.

Fe-phens-EtOH, Fe-tri-EtOH, and Fe-tri-DMF do not re-form upon standing. These gels also show a large decrease in viscosity as the shear rate is increased. There is a trend between the extent of shear thinning and whether or not the gel will re-form.

4.9 Response to temperature

Gels have been shown to be responsive to various stimuli, including temperature. In some cases the gel changes phase from gel to liquid when the temperature increases.[141]

Three gels, Fe-tri-DMF, Fe-5nite-DMF, and $FeBr_3$-5nite-DMF, were synthesised in the regular manner, on the bench top at room temperature, and exposed to different temperature conditions in order to determine their response (Figure 4.21 and Table 4.7). All three gels are stable on the bench top. When at -4 °C for at least 48 h, no visible changes were observed. At 120 °C, change becomes apparent. After five hours, Fe-tri-DMF breaks up into smaller gel pieces and both Fe-5nite-DMF and $FeBr_3$-5nite-DMF decrease in size, immobilising less solvent.

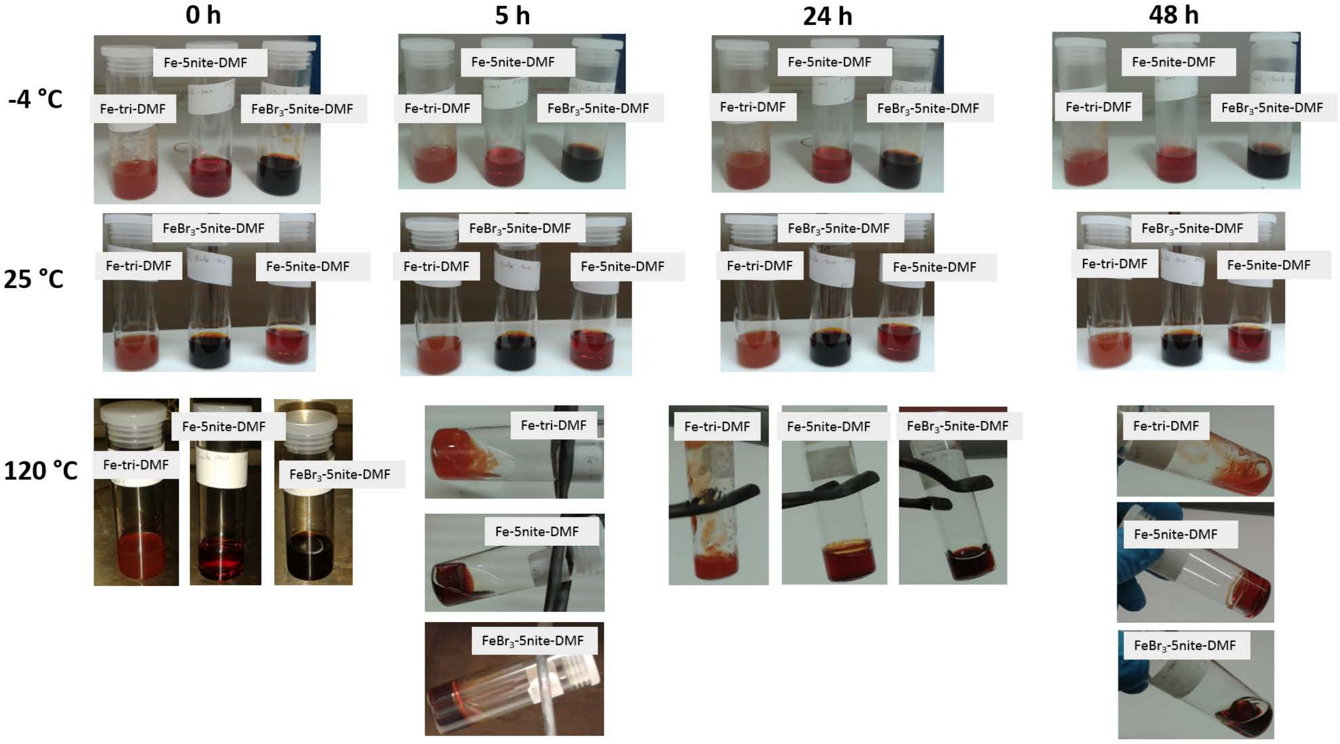

Figure 4.21: Response to temperature of three gels, Fe-tri-DMF, Fe-5nite-DMF, and $FeBr_3$-5nite-DMF. All of the gels are stable at −4 °C and room temperature. At elevated temperatures, Fe-tri-DMF breaks down after five hours, and Fe-5nite-DMF and $FeBr_3$-5nite-DMF visibly reduce in size and immobilise less solvent.

Table 4.7: Response to temperature of Fe-tri-DMF, Fe-5nite-DMF, and $FeBr_3$-5nite-DMF

Temperature [°C]	**Time** **0 h**	**5 h**	**24 h**	**48 h**
	Fe-tri-DMF			
-4	opaque orange gel	no visible change	no visible change	no visible change
25	opaque orange gel	no visible change	no visible change	no visible change
120	opaque orange gel	breakdown to smaller pieces	further breakdown	further breakdown
	Fe-5nite-DMF			
-4	clear red gel	no visible change	no visible change	no visible change
25	clear red gel	no visible change	no visible change	no visible change
120	clear red gel	decrease in gel size less DMF trapped	further decrease	further decrease
	$FeBr_3$-5nite-DMF			
-4	blood red gel	no visible change	no visible change	no visible change
25	blood red gel	no visible change	no visible change	no visible change
120	blood red gel	decrease in gel size less DMF trapped	further decrease	further decrease

4.10 Imposing order

To determine a model for the connectivity of the ligand and metal ion in the gel, two strategies were used. The first was an attempt to synthesise a metal organic framework (MOF) from the gel components using mechanochemistry. This has been shown to enable the formation of products which are difficult or impractical to obtain using solution based techniques.[142]
The second was to degrade the gel using palladium dichloride to obtain the MOF. Kurungot and co-workers have successfully used this method on Fe-tri-DMF.[125]

4.10.1 Mechanochemistry

A mechanochemistry approached was utilised in an attempt to synthesise a MOF from iron(III) nitrate nonahydrate and 5-nitroisophthalic acid, and from iron(III) nitrate nonahydrate and trimesic acid. Dry grinding was performed for 10 min and 30 min, these resulted in physical mixtures. A liquid assisted grinding experiment using ethanol or DMF did not yield a MOF either (Figure 4.22 and 4.23).

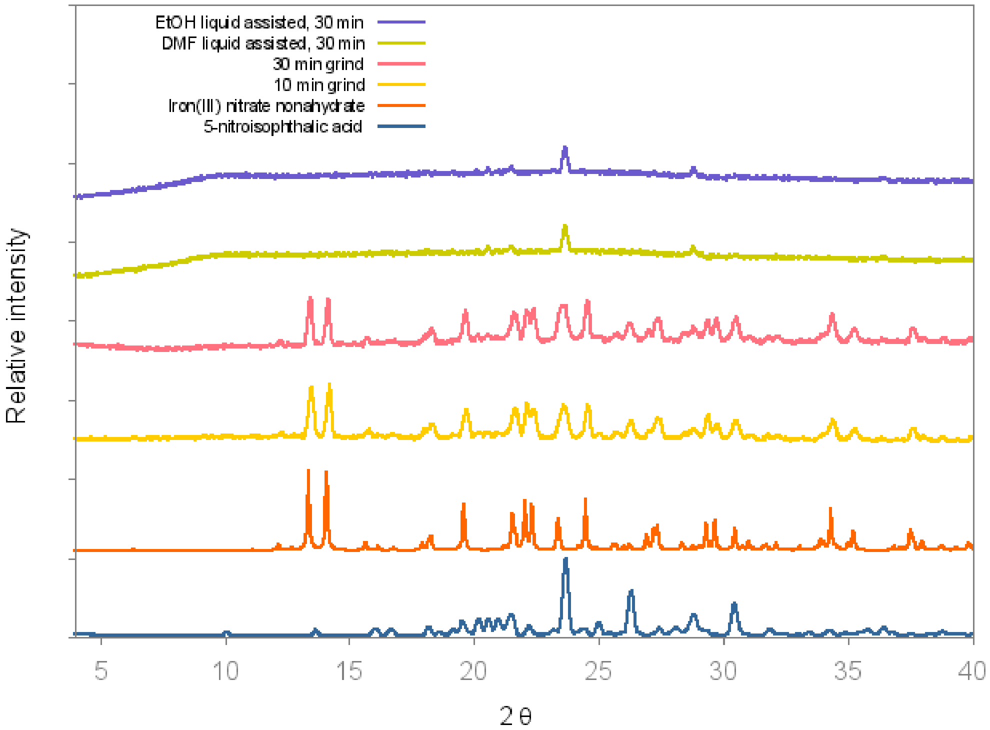

Figure 4.22: Plot of the PXRD patterns of the mechanochemistry experiments performed using iron(III) nitrate nonahydrate and 5-nitroisophthalic acid. Both dry and solvent-assisted experiments are depicted here.

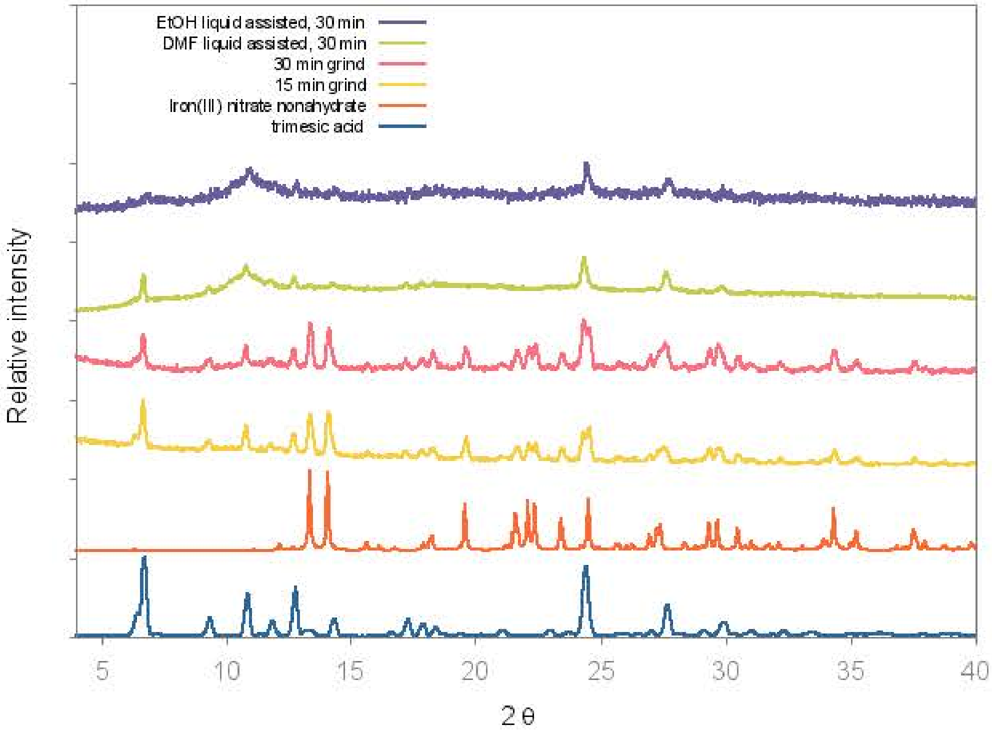

Figure 4.23: Plot of the PXRD patterns of the mechanochemistry of dry and solvent-assisted experiments performed using iron(III) nitrate nonahydrate and trimesic acid. Both dry and solvent-assisted experiments are depicted here.

4.10.2 Crystals from gel

Banerjee and co-workers developed a technique in which Fe-tri-solvent gels, where the solvent is either *N*-methylformamide (NMF), *N*,*N*-dimethylformamide (DMF), or *N*,*N*-diethylformamide (DEF), are converted to metal organic frameworks using degradation by $PdCl_2$.[125] An attempt was made to produce single crystals from Fe-5nite-DMF gel using this procedure[125] but no crystals were obtained. Various reaction conditions were used including different temperatures and reaction time to no avail. The gel was partially degraded in the oven and would re-form upon standing. Details of conditions used can be found in Appendix B.

However, the reaction using Fe-tri-DMF was successful and very small, brown crystals were obtained. The data obtained from the single crystal X-ray diffraction was poor, despite multiple data collections using different crystals. Table 4.8 gives the crystallographic information of (Fe-tri-DMF)$_{crystal}$. Data were refined using CrysAlisPro 1.171.38.41.[100] The refinement is unsatisfactory and is included simply for comparison with the structure reported by Banerjee.

Table 4.8: Crystal data of $(\text{Fe-tri-DMF})_{crystal}$

Molecular formula	$Fe(C_9O_6H_6)_4 \cdot x$solvent
Molecular mass [g mol^{-1}]	896.40
Crystal system	Cubic
Space group	$Fm\bar{3}$
Unit cell parameters	
a [Å]	27.2216(7)
Volume [$Å^3$]	20171.6(2)
Z	24
$Density_{calcd.}$ [g cm^{-3}]	1.771
μ [MoKα] [mm^{-1}]	0.559
F *(000)*	10992
Temperature [K]	173(2)
Crystal size [mm]	0.080 x 0.090 x 0.130
Range scanned θ [°]	2.116 to 25.038
Index range	h:-32,32; k:-22,32; l:-29,31
ϕ and ω scan angles [°]	
Dx [mm]	47.5
Total number of reflections	30057
Number of independent reflections	1607
Number of reflections with I > 2σ(I)	1306
R_{int}	2.584
R_1 [I > 2σ(I)]	0.3370
wR_2	0.6524
S	2.628
Number of parameters	38
Number of reflections omitted	
$(\delta/\sigma)_{mean}$	<0.001
$\Delta\rho$ excursions [e.$Å^3$]	-0.830;1.874

The unit cell matches that of NINVAI (the structure obtained by Banerjee *et al*) which was first reported by Xie *et al.*[143] Table 4.9 shows the unit cells of the two crystals. Despite both having the same space group and similar unit cell parameters, the connectivity of the trimesic acid to the Fe(III) metal centre is different (Figure 4.24).

Table 4.9: Unit cell parameters of NINVAI and (Fe-tri-DMF)$_{crystal}$

	NINVAI[143]	**(Fe-tri-DMF)**$_{crystal}$
Temperature [K]	293	173.1
Space group	$Fm\bar{3}m$	F m -3
a [$\AA$]	26.6328(4)	27.2
α [°]	90	90
V [$\AA^3$]	18890	20223
Z	24	24
R	7.6%	33.7%

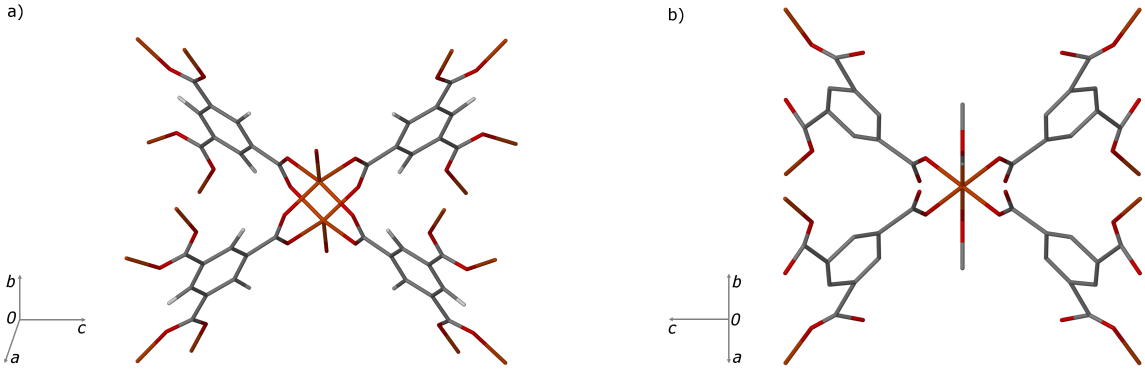

Figure 4.24: The different connectivities of a) NINVAI[143] and b)(Fe-tri-DMF)$_{crystal}$.

In NINVAI, a paddlewheel is formed from Fe_2(II, III) units and trimesic acid linkers and this results in a three dimensional (3D) framework.[143] In each paddlewheel unit, the two crystallographically equivalent Fe atoms have a square-pyramidal geometry with four equatorial carboxyl oxygen atoms and an axial water molecule.

(Fe-tri-DMF)$_{crystal}$ does not form a paddlewheel, the Fe(III) centre has a distorted octahedral geometry, coordinating to a single carboxyl oxygen atom for four trimesic acid ligands in the equatorial plane. Given the poor quality of the crystal data, detailed structural analysis would be inappropriate. However it is evident that (Fe-tri-DMF)$_{crystal}$ and NINVAI share some common features including a large scale 3D network which has space for encapsulating solvent molecules.

One of the features of gels is the lack of long range order in the material, the degradation of the gel material using $PdCl_2$ may force the system into a thermodynamic energy well. It is possible there are a number of crystalline states with similar energies, hence the possibility of forming a number of different structures.

4.11 Minimum gelation concentration

4.11.1 Open vials

A supergelator is a system which results in gel formation at a concentration below 1 %(w/v).[144] A series of experiments were performed to determine the minimum concentration of components in a 1:1 molar ratio required for gelation. These experiments were carried out at room temperature using the gels with the fastest formation times. The procedure used halved the number of moles (of ligand and metal salt) in each successive solution, 0.1 mmol, 0.05 mmol, 0.025 mmol, and 0.0125 mmol were used in 5 mL of solution. Figure 4.25 shows the results for Fe-5nite-DMF. Initially, all the solutions are yellow, these gradually darken over time (1 h) and after three hours all of the solutions are a burnt orange colour. The viscosity increased after 18 h and the colour changed to red (except for the 0.0125 mmol solution which remained burnt orange in colour).

After 48 h a gel formed in the 0.1 mmol solution as well as the 0.05 mmol solution. However, the 0.05 mmol solution could not trap the entire 5 mL of solution. It did not pass the inverted vial test, and there was 1.4 mL of DMF not immobilised in the gel. While in the 0.025 mmol and 0.0125 mmol solutions, partial gel was seen, these did not pass the inverted vial test. The gels were stable at room temperature and no change was seen after 91 h.

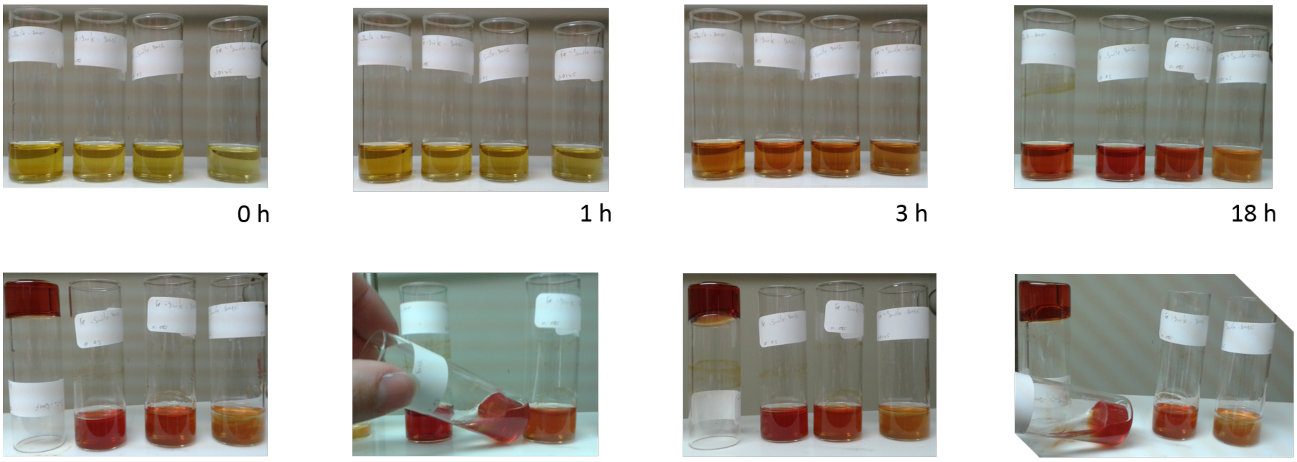

0 h 1 h 3 h 18 h

48 h 48 h 91 h 91 h

Figure 4.25: Minimum gelation experiments for Fe-5nite-DMF recorded over time. From left to right the molar amounts used are 0.1 mmol, 0.05 mmol, 0.025 mmol, and 0.0125 mmol. After 48 h, gel has formed in both the 0.1 mmol and 0.05 mmol solutions, but there is 1.4 mL DMF not immobilised by the gel components for the 0.05 mmol. The gels are time stable thereafter (91 h).

A similar trend can be seen in Figure 4.26 for the experiment carried out in ethanol. The three most concentrated solutions darken and increase in viscosity over time. The viscosity of the 0.1 mmol solution increases as soon as the metal and ligand are mixed. After 18 h is gel-like but does not pass the inverted vial test. After 43 h a dark orange gel has formed in the 0.1 mmol solution. Despite having a gel-like appearance, 0.05 mmol and 0.025 mmol do not pass the inverted vial test. The 0.0125 mmol remains pale yellow and viscosity does not increase, indicating this concentration is below the minimum gelation concentration.

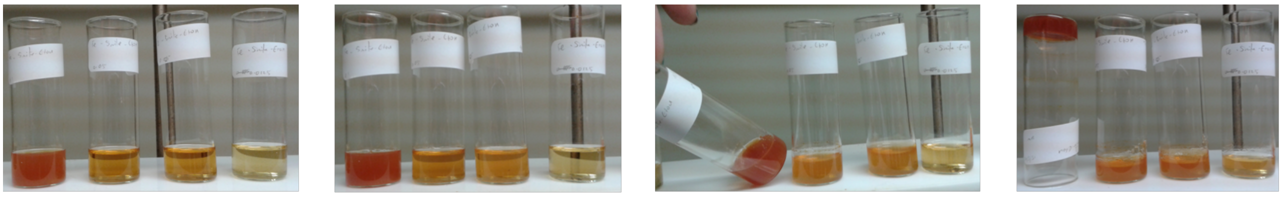

0 h 4 h 18 h 43 h

Figure 4.26: Minimum gelation experiments for Fe-5nite-EtOH recorded over time. From left to right the molar amounts used are 0.1 mmol, 0.05 mmol, 0.025 mmol, and 0.0125 mmol. Gel only forms in the 0.1 mmol solution after 18 h.

4.11.2 Capped vials

The minimum gelation experiments were repeated using capped vials, as before the 0.05 mmol solution formed a gel which did not immobilise the full 5 mL of solvent. However, it took 186 h for gel formation which could indicate that a small amount of evaporation needed to occur for the gel to form. When carrying out the experiments with capped vials, the darkening of the solution and increase in viscosity followed a similar time line as seen in the uncapped vials (Figure 4.27). In the cases where gel has not formed, the gelator concentration was insufficient to immobilise the solvent. The results for the minimum gelation experiments are tabulated in Table 4.10. Gels are formed in both ethanol and DMF at a concentration of 1.32 %(w/v). However only those in DMF form a gel at 0.68 %(w/v) (both capped and uncapped vials).

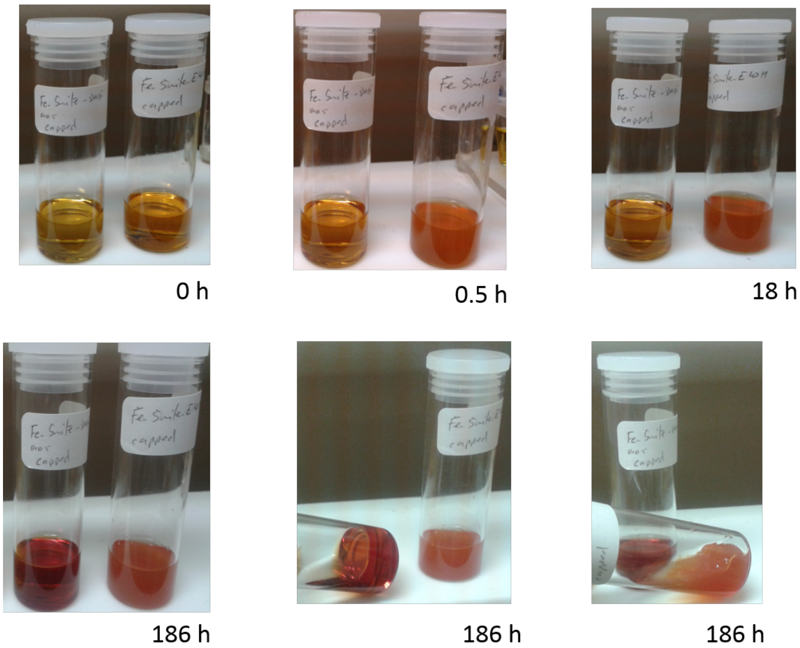

Figure 4.27: Minimum gelation experiments for 0.05 mmol solutions of Fe-5nite-DMF (left) and Fe-5nite-EtOH (right) recorded over time. Gelation occurs after 186 h suggesting a small amount of solvent evaporation must occur for gelation to be successful.

Table 4.10: Summary of minimum gelation experiments

Gel	**Moles** [mmol]	**Weight percent** [%(w/v)]	**Gel formed**	**Time** [h]
Fe-5nite-DMF				
	0.1	1.32	yes	48
	0.05	0.68	yes*	48
	0.025	0.34	no	
	0.0125	0.18	no	
Capped	0.05	0.68	yes*	186
Fe-5nite-EtOH				
	0.1	1.32	yes	43
	0.05	0.68	no	
	0.025	0.34	no	
	0.0125	0.18	no	
Capped	0.05	0.68	yes	186

*1.4 mL excess solvent

4.12 Conclusion

Thermal analysis shows the gels comprise *ca.* 95-99% solvent in most cases and a glass transition occurs when the gels are cooled and reheated. In general, this large amount of solvent masked signals arising from interactions within the gel so the gels were dried before further characterisation was performed. The FT-IR spectra show an interaction between the iron(III) and carboxylate moiety, further confirming that both constituents are required for gel formation. The SEM images do not show fibres but block like structures which appear glassy in some instances. The iron(III) does not undergo redox type reaction and remains as iron(III) during gelation. Fe-tri-DMF was degraded to form a MOF which has a similar unit cell to NINVAI. These systems are not classed as supergelators as 1.32 %(w/v) is the lowest concentration of metal and ligand required to form a gel in and entirely encapsulate 5 mL of solvent. In order to gain an in depth understanding of a gel, multiple tools and techniques need to be used.

These complex materials require both solid state and solution based characterisation techniques to be understood. These are highly variable materials and preparation must be carried out in a meticulous manner as a number of factors impact the characteristics of the gel and the xerogel.

Chapter 5

Response to stimuli

5.1 Introduction

The self assembly of metallogels is driven by non-covalent interactions such as hydrogen bonding, van der Waals forces, $\pi - \pi$ interactions, metal co-ordination and host-guest inclusion.[12] These weak interactions which hold the gel together result in the material being able to respond to stimuli[12] such as pH, temperature, or the presence of other compounds. The combination of elastic behaviour of a solid and microviscous properties of a liquid make gels ideal candidates for soft, stimuli-responsive materials.[44] As a result gels are being utilised for novel approaches to drug delivery, crystal growth media as well as energy capture,[41] a particularly urgent application. In addition, biomaterials, sensors, and electronic materials are also attracting great deal of attention.[145]

Metallogels are desirable candidates for the sorption of materials as they contain a porous network and have immobilised functional groups on their porous surface which are able to interact with foreign guest molecules.[44]

In this chapter, response of selected gels to stimuli will be explored for potential application in dye and gas sorption, and separation of small molecules.

5.2 Dye sorption

It has been shown that porous soft materials take up organic dyes from solution and have been studied for both sorption[146,147] and separation[148] of dye. This has the potential to be used in a method for the prevention of the contamination of water sources[22,149] or treatment of waste from the textile industry, that may contain toxic dyes.[150,151] Gels Fe-5nite-DMF and

Fe-tri-DMF were explored as dye absorbent materials.

Full kinetic studies were not performed as the sorption profiles were not reproducible. There are multiple interfaces present as the solvent moves through the gel. Solvent within the gel pockets may also move from the gel to the solution which further complicates the kinetic profile. Nonetheless an absorption capacity was calculated.

Two different dyes were selected: bromocresol green and methyl orange (Figure 5.1). This was done in an attempt to get further information about the environment inside the gel pockets. Bromocresol green is bulky and has the potential for halogen bonding through the bromide groups. Methyl orange is smaller and planar and is more likely to be involved in a chelation type interaction. Both of these dyes have a λ_{max} which does not overlap with those of the ligands and iron(III). 629.12 nm and 423.24 nm were monitored for bromocresol green and methyl orange respectively.

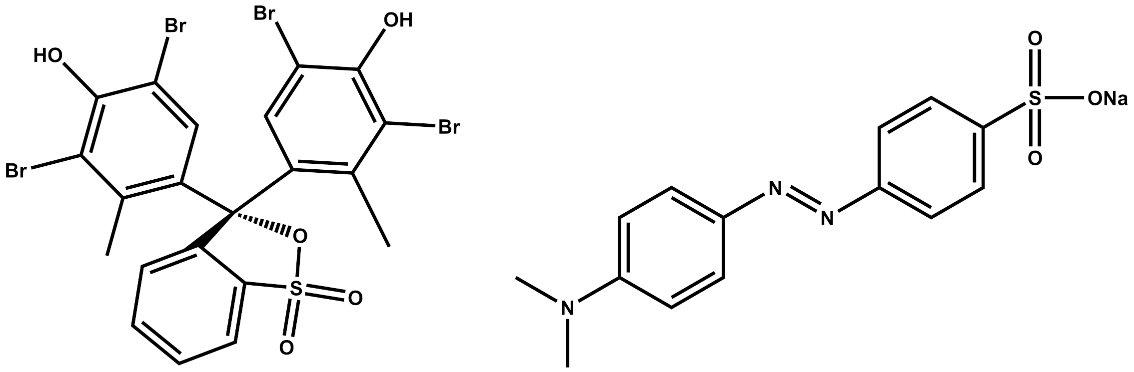

Figure 5.1: Structures of indicators used. Bromocresol green (left), which is bulky and has potential for halogen bonding and methyl orange (right), which is expected to be involved in a chelation type interaction.

A number of different experiment procedures were performed before reproducible results were obtained. The initial method placed portions of gel material into a solution of dye for set periods of time and did not give reproducible results. The next iteration involved synthesising the gel in separate vials to which dye solution was added. After a predetermined time period, the liquid phase was removed and analysed. This disturbed interfaces within the gel, and resulted in large variation in readings. Consistent results were achieved when the gel was synthesised in the cuvette. The dye solution was added very gently on top of the metallogel to not perturb the gel surface. The intensity of the dye solution was then monitored over time.

The absorption capacity of each run was calculated using the Equation 5.1:[151]

$$Q = \frac{(C_i - C_t)\,V}{m} \tag{5.1}$$

Where Q is the absorption capacity of the gel ([mg/L] for the gel and [mg/g] for xerogel), C_i is initial concentration of the dye, and the concentration at time t is C_t [mg/L], V is the volume of dye used [L] and m is the mass of gel [g]. In the case of the wet gel, Q is the absorption capacity of the gel [mg/L].

5.2.1 Bromocresol Green

The change in intensity of the bromocresol green solution over 25 h was visible to the naked eye (Figure 5.2). Figure 5.3 shows the decrease of intensity at 629 nm of bromocresol green at 25 °C which implies that the dye moved from the solution to the gel. The intensity decreases sharply within the first five minutes for Fe-tri-DMF. There is little change in the intensity after 9 h. The Fe-5nite-DMF experiment shows a more gradual loss of intensity, with very little change after 18 h. This suggests the initial rate of uptake of the dye is greater for Fe-tri-DMF than Fe-5nite-DMF, perhaps as a result of different pores sizes in each material.

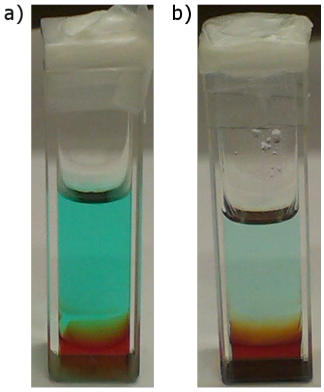

Figure 5.2: Visible decrease in intensity of bromocresol green after soak over Fe-5nite-DMF, a) initial intensity, b) after 48 h soak where the intensity has visibly decreased.

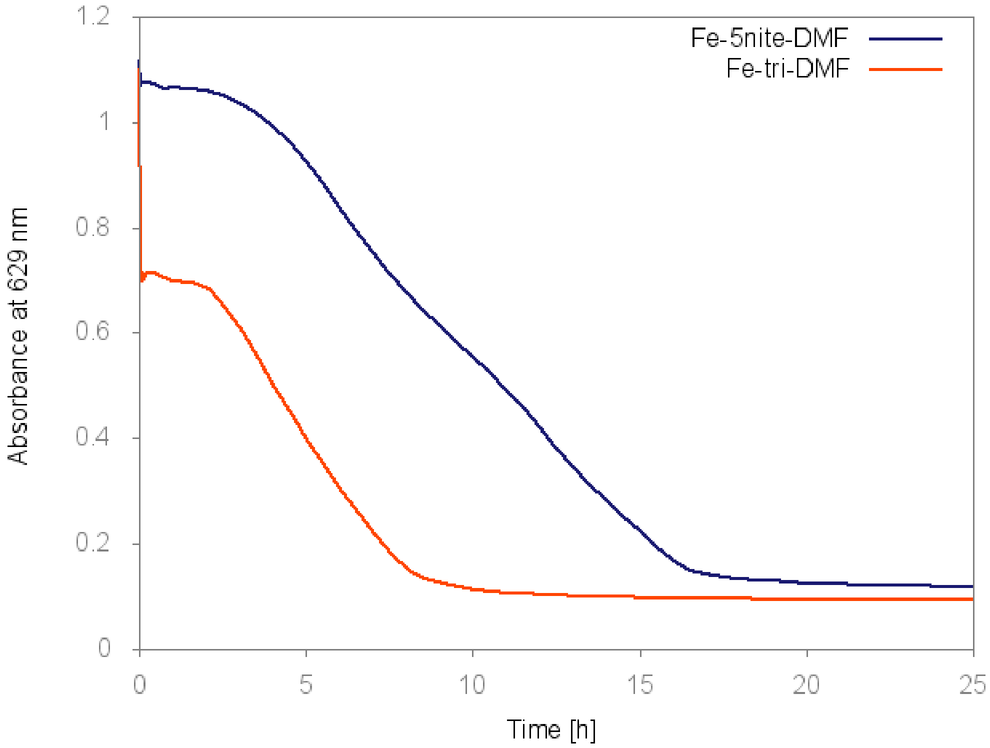

Figure 5.3: Absorbance vs time plot for bromocresol green taken up by Fe-5nite-DMF (blue) and Fe-tri-DMF (orange) at 25 °C. Both show a loss of intensity over time, indicating sorption of the dye into the gel material.

Both Fe-5nite-DMF and Fe-tri-DMF and their respective xerogels have similar absorption capacities (Table 5.1). This suggests the interactions involved in the absorption of bromocresol green are similar and this, rather than pore size, drives the uptake of bromocresol green.

Table 5.1: Absorption capacity of bromocresol green by wet gel Fe-5nite-DMF and Fe-tri-DMF after 25 h

	Gel	**Absorption capacity**	**Percentage absorbed** [%]
Wet	Fe-5nite-DMF	38.2 ± 4.1 mg L^{-1}	79.9 ± 9.5
	Fe-tri-DMF	41.7 ± 1.2 mg L^{-1}	89.2 ± 2.2
Xerogel	Fe-5nite-DMF	3.1 ± 0.28 mg g^{-1}	87.1 ± 8.9
	Fe-tri-DMF	2.7 ± 0.5 mg g^{-1}	85.5 ± 2.4

Cho *et al* reported similar percentages for bromocresol green sorption.[152] Terpyridine-based gelators possessing triethoxylsilane moiety with Cu(II) or Zn(II) show a bromocresol green uptake of 77.5%, and 74.2%, from aqueous solution, respectively.[152]

It is important that the gels are prepared in a consistent manner as it was found that the length of time allowed for gel formation in an oven at 90 °C affects the absorption capacity of the gel. Carrying out gelation for three hours instead of two had a significant impact on the absorption capacity (Table 5.2). It dropped from 38.2 ± 4.1 mg L^{-1} to 15.4 ± 2.0 mg L^{-1}. This is a result of collapse of the gel pockets as the gel began to dry. Not much change was seen in the absorption capacity after 25.5 h.

Table 5.2: Absorption capacity of Fe-5nite-DMF after 25.5 h to absorb bromocresol green

Gel formation time	**Absorption capacity** [mg L^{-1}]	**Percentage sorbed** [%]
2 h	38.2 ± 4.1	79.9 ± 9.5
3 h	15.4 ± 2.0	32.6 ± 3.9

5.2.1.1 Powder X-ray diffraction of xerogels before and after bromocresol green soak

Confirmation of the sorption of bromocresol green was obtained from UV-vis results. PXRD of xerogels Fe-5nite-DMF and Fe-tri-DMF before and after bromocresol green sorption experiments (Figures 5.4 and 5.5) were run in order to determine whether this occurrence could be monitored using PXRD. In neither cases bromocresol green was detected using PXRD.

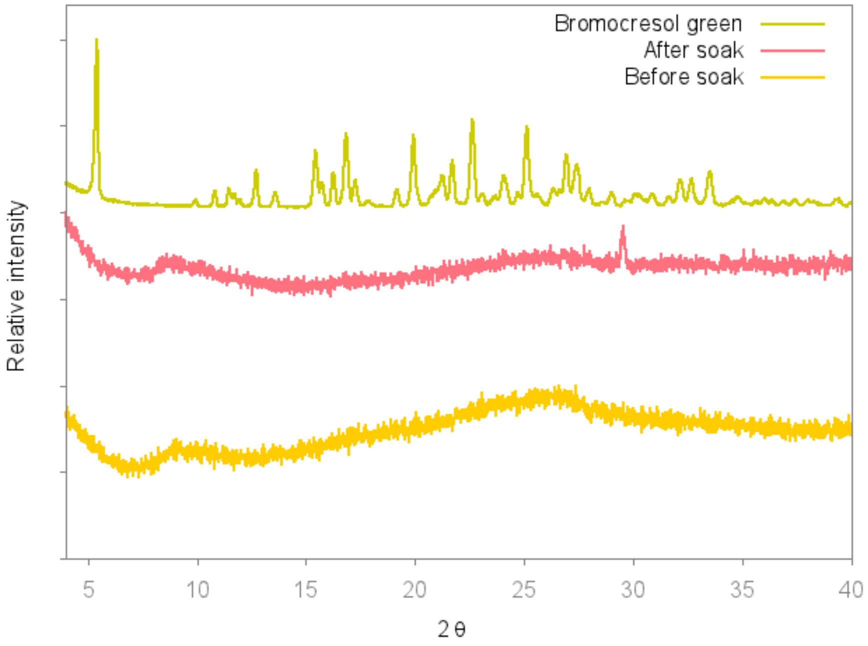

Figure 5.4: PXRD patterns of Fe-5nite-DMF oven dried sample before and after bromocresol green, and bromocresol green.

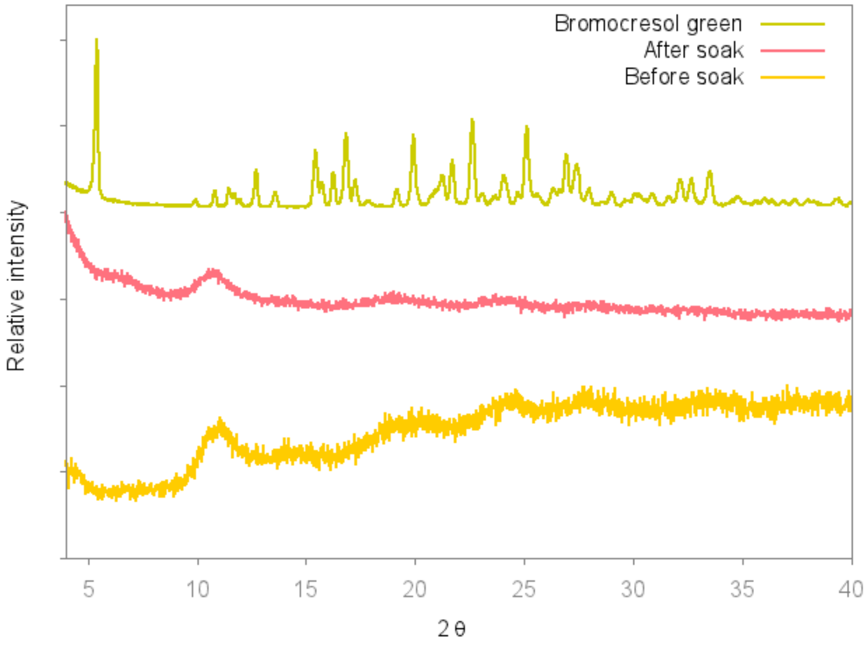

Figure 5.5: PXRD patterns of Fe-tri-DMF oven dried sample before and after bromocresol green, and bromocresol green.

5.2.1.2 Oven dried xerogel of Fe-5nite-DMF after bromocresol green soak

SEM images of the dried gel after the bromocresol green soak were collected to determine whether bromocresol green had altered the appearance of the oven dried gel and thus could be detected using SEM. The sample was powdery in appearance and there is no visible evidence of bromocresol green (Figure 5.6). The sorption of bromocresol green did not result in a structural change of the Fe-5nite-DMF xerogel.

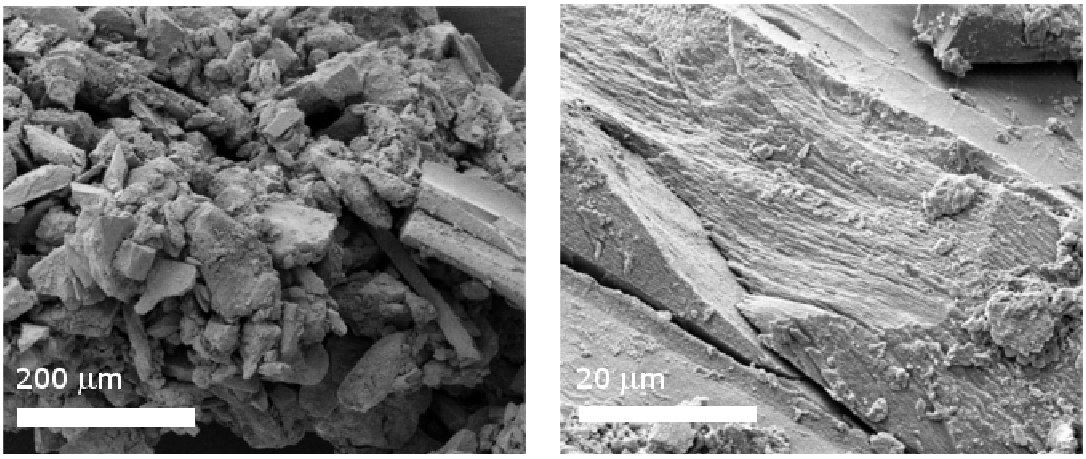

Figure 5.6: SEM images of oven dried Fe-5nite-DMF xerogels after sorption of bromocresol green.

5.2.2 Methyl orange

Methyl orange, a planar, azo group containing dye was also used to test the dye sorption ability of Fe-5nite-DMF and Fe-tri-DMF. Figure 5.7 shows a visible decrease in intensity of colour of the methyl orange solution over time when exposed to Fe-5nite-DMF.

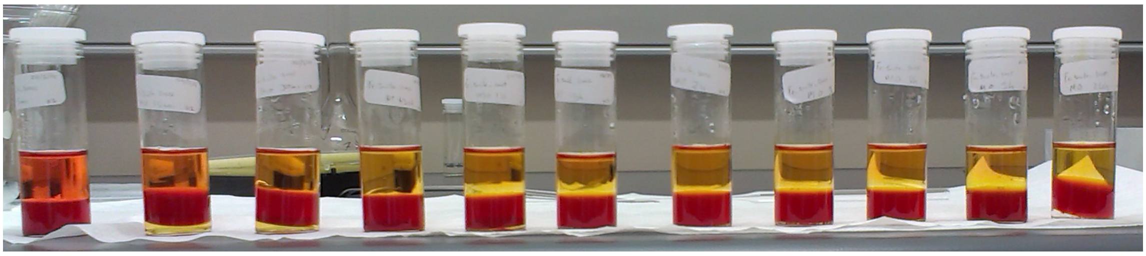

Figure 5.7: Decrease in intensity of methyl orange solution after soak over Fe-5nite-DMF, length of time of exposure increasing from left (5 min) to right (24 h).

Table 5.3 gives the absorption capacities of Fe-5nite-DMF and Fe-tri-DMF and their respective xerogels. The amount of bromocresol green sorbed is larger than that of methyl orange for both Fe-tri-DMF and Fe-5nite-DMF and their respective xerogels. The maximum methyl orange absorption occurred when Fe-tri-DMF was used, 42.2 ± 3.9% of the dye was absorbed from solution (Table 5.3). The percentage decreased significantly to 7.9 ± 0.4% when the xerogel was used. The change in the percentage absorbed when comparing the gel and the xerogel is smaller for Fe-5nite-DMF than Fe-tri-DMF. This is may be attributed to the differences in the structures of the dyes. It appears that halogen bonding plays a role rather than a chelating interaction. This only occurs with bromocresol green. The bromine atoms may be able to interact with the oxygen atoms of the carboxylates in the gel. The azo group is less favourable for dye sorption by Fe-5nite-DMF and Fe-tri-DMF. The oven dried material sorbs less dye than the fresh gel, which suggests the pores collapse or change shape upon drying.

Table 5.3: Absorption capacity of methyl orange by Fe-5nite-DMF and Fe-tri-DMF after 25 h

	Gel	**Absorption capacity**	**Percentage absorbed** [%]
Wet	Fe-5nite-DMF	38.7 ± 3.9 mg L^{-1}	27.1 ± 2.5
	Fe-tri-DMF	62.0 ± 7.6 mg L^{-1}	42.2 ± 3.9
Xerogel	Fe-5nite-DMF	1.9 ± 0.3 mg g^{-1}	16.0 ± 2.4
	Fe-tri-DMF	1.0 ± 0.1 mg g^{-1}	7.9 ± 0.4

Another azo dye, 1-(4-methoxyphenyl)-2-phenyldiazene (Figure 5.8) was also used in dye sorption experiments, however neither Fe-5nite-DMF nor Fe-tri-DMF absorbed this dye, as shown when the intensity at 348 nm did not decrease over a 24 h period. Both methyl orange and 1-(4-methoxyphenyl)-2-phenyldiazene contain an azo group, neither of which were taken up in large quantities.

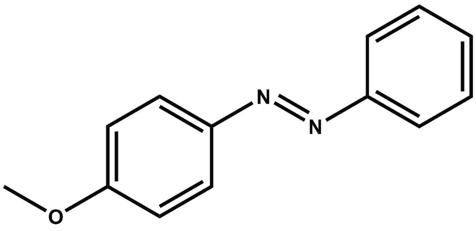

Figure 5.8: Structures of 1-(4-methoxyphenyl)-2-phenyldiazene, another azo dye which was not absorbed by neither Fe-5nite-DMF nor Fe-tri-DMF.

The absorption values are lower than those obtained for other metallogels. An aerogel from chromium and trimesic acid has a 98% methyl orange absorption from aqueous solution.[124] This is a result of a different drying method being used to create the aerogel. Supercritical $CO_2(l)$ was used which seems to lead to less collapse of the pores. Hu *et al* report a 95.69% methyl orange absorption when a 2,6-bis(2-benzimidazyl)pyridine, squaric acid and Zn(II) gel was used.[153] A similar system with Ni(II) instead of Zn(II) resulted in a decrease in the percentage absorbed, with only 71.77% of the dye solution being absorbed.[153] Small changes in the gel composition can have a large impact on the absorption ability of the gel.

5.3 Gas sorption

The SEM images of freeze dried xerogel of Fe-5nite-EtOH showed that the sample was spongy in appearance (Figure 4.12). Gas sorption was used to determine the ability of this spongy material to absorb gas. Oven dried xerogels of Fe-tri-DMF and Fe-5nite-DMF were investigated as the xerogels were prepared in the same manner for dye absorption studies.
Gas sorption was performed at a pressure range of 700 - 800 mm Hg using the following gases: Nitrogen (N_2) at 77 K, hydrogen (H_2) at 77 K and carbon dioxide (CO_2), both 195 K and 273 K, and water vapour (298 K) to varying degrees of success.

The following materials were run:

- Fe-5nite-EtOH both freeze and oven dried xerogel
- Fe-tri-EtOH both freeze and oven dried xerogel
- Fe-tri-DMF oven dried xerogel
- Fe-5nite-DMF oven dried xerogel

5.3.1 Freeze dried vs oven dried

Figure 5.9 gives the gas sorption plots for the uptake of different gases by either freeze dried or oven dried Fe-5nite-EtOH.

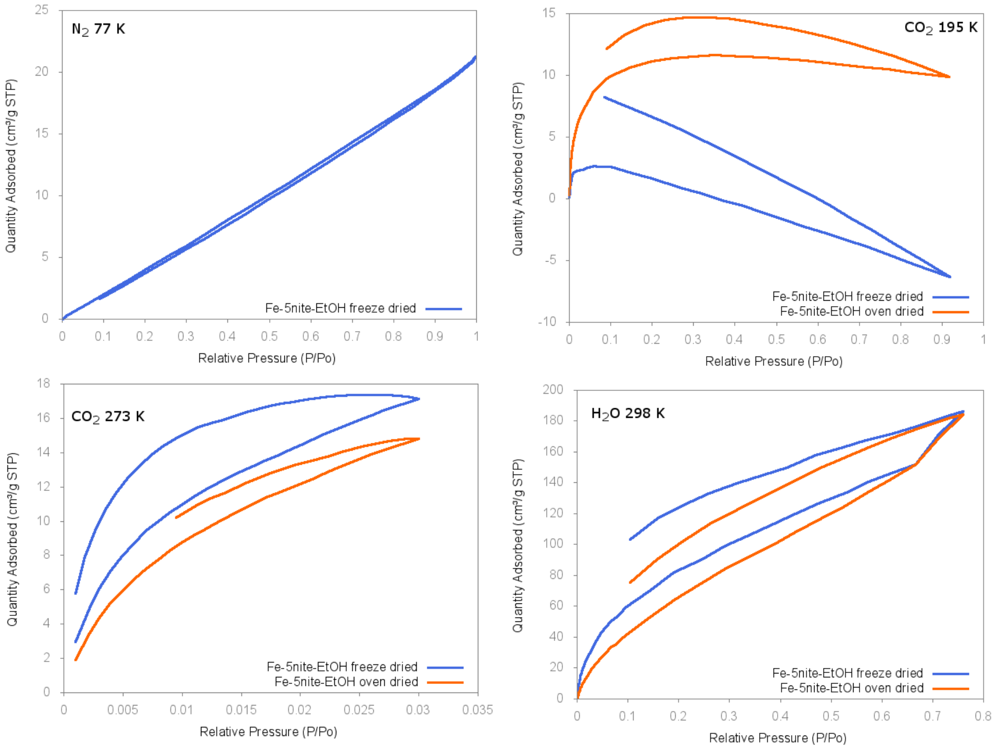

Figure 5.9: Gas sorption plots of freeze (orange) and oven dried (blue) Fe-5nite-EtOH xerogel. N_2 is the only case in which hysteresis is not seen.

Hysteresis is observed in all cases except N_2. It was found that the Brunauer–Emmett–Teller (BET) surface area of the oven dried xerogel was smaller than that of the freeze dried material (Table 5.4). This suggests the pores collapse to a greater extent when oven drying is used instead of freeze drying and is particularly noticeable for CO_2 and N_2. No difference in the isotherm types is seen for the freeze and oven dried materials: Type I for CO_2 and water and Type II for N_2. The Type I adsorptions are indicative of a monolayer adsorptive mechanism, and Type II of multilayer adsorption.[104] The BET surface area obtained using N_2 (10.17 m^2 g^{-1}) is similar to that obtained by Samai *et al* for a xerogel of pyridine-3,5-bis(benzimidazole-2-yl) ligand with either Cu(II) or Cd(II) metal salts, whose BET surface area ranges from 11.12 m^2 g^{-1} to 31.18 m^2 g^{-1}.[154] Both Fe-5nite-EtOH xerogels take up a similar amount of water vapour, 186.58 cm^3 (STP) g^{-1} and 184.54 cm^3 (STP) g^{-1} at a relative pressure of 0.760 for the freeze and oven dried material respectively. No adsorption of hydrogen was seen.

The negative slope of the curve for the CO_2 at 195 K for Fe-5nite-EtOH freeze dried xerogel can be explained as the result of condensation of the gas.

Table 5.4: BET results for freeze and oven dried Fe-5nite-EtOH xerogel when exposed to different gases

Gas	**Temperature** [K]	**Drying method**	**BET surface area** [m^2 g^{-1}]	**Total gas adsorbed at relative pressure** [P/P$_0$]
N_2	77.3	Freeze	10.17	17.37 cm^3 (STP) g^{-1} at 0.997
CO_2	195.15	Freeze	14.59	17.37 cm^3 (STP) g^{-1} at 0.026
		Oven	27.80	11.627 cm^3 (STP) g^{-1} at 0.350
	273.15	Freeze	96.52	2.607 cm^3 (STP) g^{-1} at 0.057
		Oven	75.59	14.807 cm^3 (STP) g^{-1} at 0.0300
H_2O	298	Freeze	243.01	186.58 cm^3 (STP) g^{-1} at 0.760
		Oven	226.09	184.54 cm^3 (STP) g^{-1} at 0.760

5.3.2 Comparison of Fe-5nite-DMF and Fe-tri-DMF xerogels

Figure 5.10 shows the BET plots for oven dried xerogels of Fe-5nite-DMF and Fe-tri-DMF. A high degree of correlation is seen.

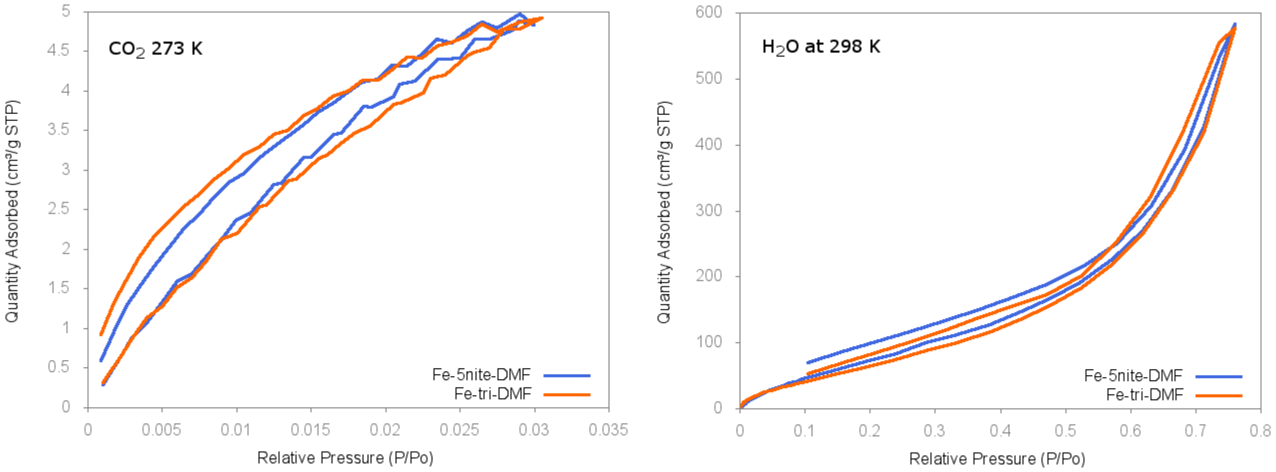

Figure 5.10: BET plots of oven dried Fe-5nite-DMF and Fe-tri-DMF xerogels. Similar profiles are observed for both xerogels, suggesting similar mechanisms for gas sorption and desorption.

Table 5.5 gives the values for the BET surface areas and total gas adsorbed for each gas. There is little difference in the uptake of all gases. Water vapour adsorption has a Type III isotherm. Both exhibit minor hysteresis. This suggests that the materials have similar mechanisms for the uptake and release of gas molecules.

Table 5.5: BET results for oven dried xerogels of Fe-5nite-DMF and Fe-tri-DMF when exposed to different gases

Gas	**Temperature** [K]	**Xerogel**	**BET surface area** [m^2 g^{-1}]	**Total gas adsorbed at relative pressure** [P/P$_0$]
$\mathbf{CO_2}$	273.15	Fe-5nite-DMF	34.71	4.82 cm^3 (STP) g^{-1} at 0.030
		Fe-tri-DMF	39.00	4.92 cm^3 (STP) g^{-1} at 0.031
$\mathbf{H_2O}$	298	Fe-5nite-DMF	218.88	538.67 cm^3 (STP) g^{-1} at 0.760
		Fe-tri-DMF	226.86	577.36 cm^3 (STP) g^{-1} at 0.760

The two xerogels adsorb comparable amounts of the different gases and have similar BET surface areas, although, that of Fe-5nite-DMF is slightly smaller. This can be attributed to differences in the ligand. When analysing the crystal structures of the trimesic acid ligand (CSD reference code BTCOAC[155]), a void space of 1278 Å^3 is obtained when using the contact surface model. A probe radius of 1.2 Å was used. The 5-nitroisophthalic acid crystal has a much smaller void space of 110 Å^3 when using the same probe conditions (CSD reference code COFDUW10[156]).

The uptake of water vapour by Fe-5nite-EtOH (Type II) has a different isotherm to that of Fe-5nite-DMF (Type III). Fe-5nite-DMF adsorbs approximately three times the amount of water vapour when compared with Fe-5nite-EtOH, 538.67 cm^3 (STP) g^{-1} vs 184.54 cm^3 (STP) g^{-1} at a relative pressure of 0.760. This can be attributed to the role of the solvent in xerogel formation. The gel pockets of the ethanol based gel appear to have collapsed to a greater extent. The isotherms either show monolayer or multilayer adsorption.

The isotherm data collected for the exposure of oven dried xerogels Fe-5nite-EtOH, Fe-5nite-DMF, and Fe-tri-DMF to N_2 at 77 K is not presented due to unreliable results. A large absorption of CO_2 was not observed for the xerogels. It is not expected that the results would differ significantly for N_2 absorption by xerogels therefore these experiments were not repeated.

The drying method is a critically important factor for the pore size of the dried gel. An aerogel was created from Fe-tri-DMF by Xiang and co-workers by drying the gel on supercritical CO_2(l).[124] This aerogel was reported to have a BET surface area of 1090 m^2 g^{-1}, which is significantly larger than the BET surface area obtained in this study.

5.4 Xerogel reconstitution

5.4.1 Exposure to DMF vapour

In order to test whether the xerogel could be reconstituted, xerogel ground material was exposed to DMF vapour for 24 h (Figure 5.11). The initial TGA of the xerogel shows a mass loss of 11.8% between 20.7 °C and 113.4 °C, after exposure to DMF for 24 h at ambient temperature the mass loss increased to 27.5% between 26.2 °C and 113.0 °C indicating that DMF vapour was sorbed (Figure 5.12). However the gel was not reconstituted to its original state (which has a 97% mass loss). This can be attributed to the collapse of gel pockets and/or channels during the drying process making them inaccessible to solvent vapour.

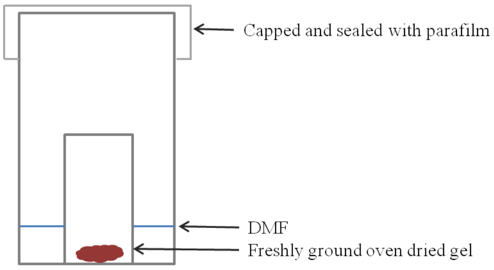

Figure 5.11: Schematic representation of a vapour chamber used for the exposure of xerogel to solvent vapour.

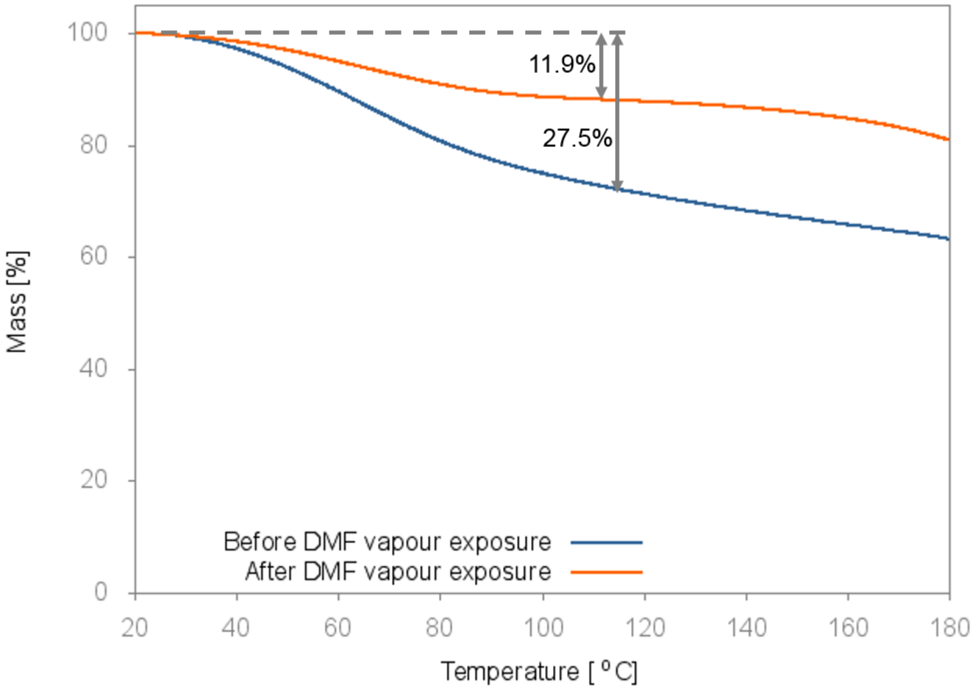

Figure 5.12: Thermal plot of oven dried Fe-5nite-DMF xerogel before (orange) and after exposure (blue) to DMF vapour for 24 h.

5.4.2 Exposure to DMF and ethanol liquid

A similar experiment was performed on xerogels of Fe-5nite-DMF and Fe-5nite-EtOH (Figure 5.13). The oven dried material (100 mg) was soaked in 10 mL of the solvent from which it was made at ambient temperature. There was no visible change in either xerogel after 24 h. Figure 5.14 shows the TGA plots collected before and 24 h after exposure to solvent. Fe-5nite-DMF showed an initial mass loss prior to exposure to DMF solvent of 8.9 ± 0.1% between 19.3 ± 4.5 °C and 106.3 ± 4.5 °C (n = 3). Following exposure for 24 h, the mass loss increased to 53.4 ± 2.8% between 20.3 ± 1.0 °C and 129.8 ± 4.5 °C (n = 3).

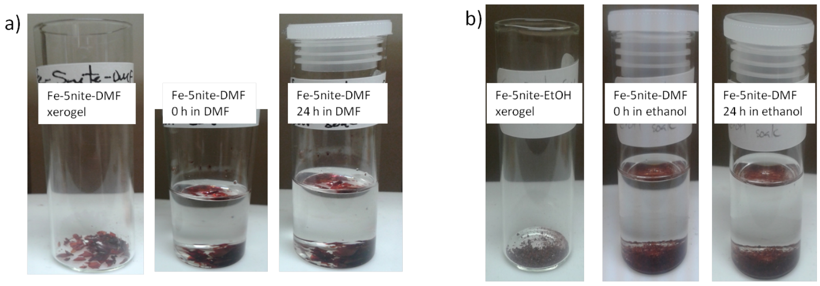

Figure 5.13: a) and b) show the reconstitution experiments of xerogels Fe-5nite-DMF and Fe-5nite-EtOH in DMF and ethanol, respectively. Reconstitution was not observed after 24 h.

Fe-5nite-EtOH did not show an appreciable change in mass loss. The mass loss before exposure to ethanol solvent was 11.3 ± 2.7% between 20.2 ± 2.1 °C and 190.7 ± 2.6 °C (n = 3). After soaking the xerogel in ethanol for 24 h the TGA results show a 10.9 ± 0.2% mass loss between 20.0 ± 3.5 °C and 197.9 ± 1.4 °C (n = 2). The values obtained for the mass loss before and after exposure lie within the standard deviations of each other. The difference in these values is insignificant.

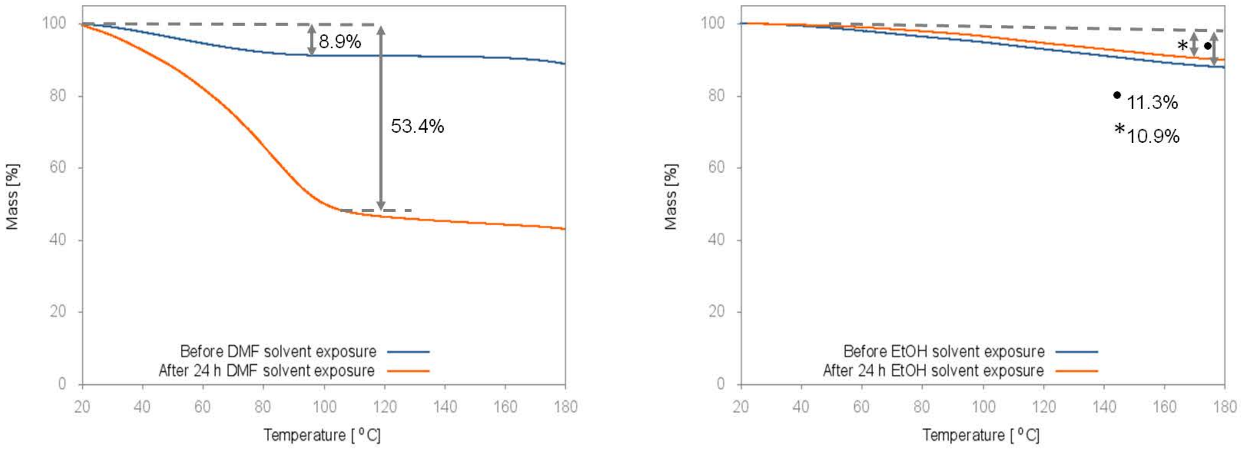

Figure 5.14: Left) Thermal plot of xerogel Fe-5nite-DMF before (blue) and after exposure (orange) to DMF solvent for 24 h. Right) Thermal plot of xerogel Fe-5nite-EtOH before (blue) and after exposure (orange) to ethanol solvent for 24 h. No significant change in mass loss was seen.

Neither xerogel is reconstituted. The Fe-5nite-DMF xerogel took up DMF solvent while the Fe-5nite-EtOH xerogel did not take up ethanol. It is concluded that the gel pockets within the ethanol xerogel collapsed to a greater extent than Fe-5nite-DMF.

5.5 Separation of 2- and 3-methylpiperidine

It is difficult to separate compounds which are structurally similar and have close boiling points by conventional techniques such as chromatography. Such techniques are useful for small scale separations.[157] However, there is a need for large scale, less energy intensive methods of separation. Additional methods under investigation include selective host-guest chemistry.[158, 159]

5.5.1 Fe-phens-EtOH

Both 2- and 3-methylpiperidine are chiral so a chiral ligand (phenylsuccinic acid) was chosen for the gel formation, using ethanol as the gelation solvent. Gelation of Fe-phens-EtOH was allowed to occur in a separation column. The mixture to be separated comprised of a 1:1 ratio of 2-methylpiperidine and 3-methylpiperidine (105 mg of each was used). This mixture was loaded onto the gel and eluted with 10 mL of EtOH and collected in 5 mL fractions. The properties of the components are given in Table 5.6 and the structures in Figure 5.15.

Table 5.6: Properties of components to be separated and phenylsuccinic acid, the ligand component of the gel

Component	**Melting point** [°C]	**pK**$_a$	**Molar mass** [g/mol]
2-methylpiperidine	118-119	10.99	99.17
3-methylpiperidine	125-126	11.28	99.17
phenylsuccinic acid	166-168	3.78	194.18

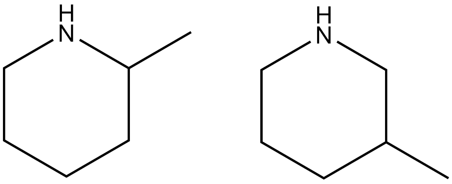

Figure 5.15: Structures of 2- and 3-methylpiperidine.

Figure 5.16 shows the degradation of the gel as the mixture moves through the material. It took 7.5 h for the solvent to diffuse through the gel. Drops fell at 15 drops per minute during the collection. Headspace gas chromatography was performed on the eluted liquid as well the remaining gel pieces. The latter was to determine if any compound had been encapsulated in the gel. It was found that no separation had occurred. The degradation is ascribed to the bases attacking the acid components and reacting, which disrupted the hydrogen bonding within the gel network.

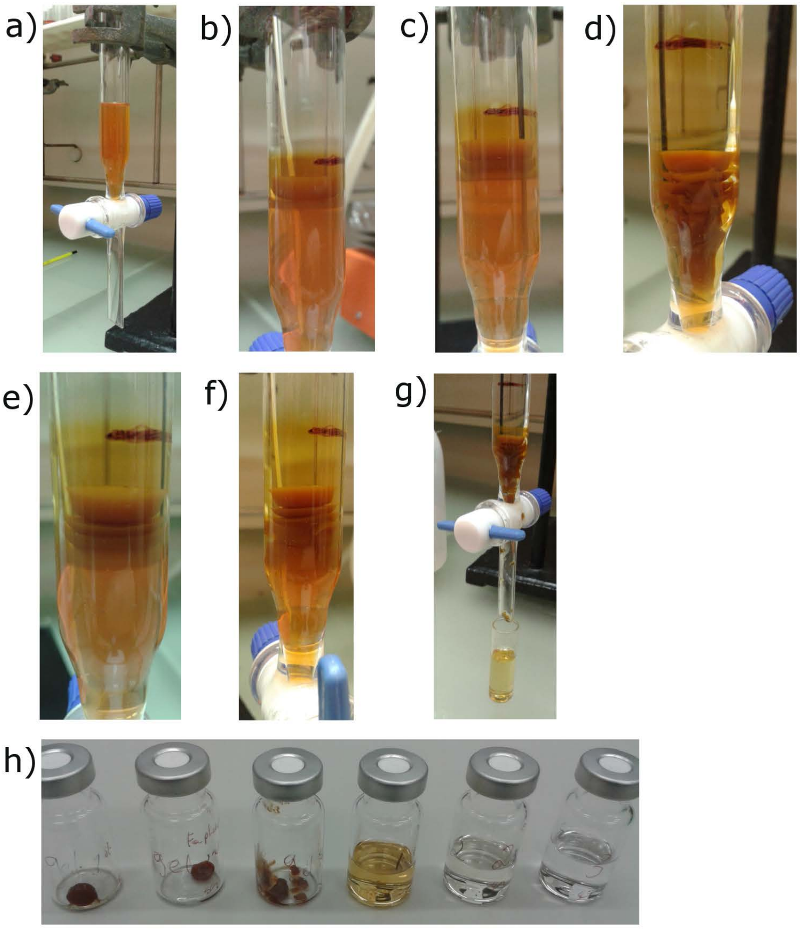

Figure 5.16: Degradation of Fe-phens-EtOH gel as the mixture diffuses through the material. a) Gel formed in column. b-g) Gel degrades as 2- and 3-methylpiperidine mixture diffuses through the gel. h) Samples collected for gas chromatography.

5.5.2 Other gels used for separation

Separation of chiral molecules was also attempted using Fe-5nite-EtOH and Fe-tri-EtOH with similar results to Fe-phens-EtOH. Table 5.7 gives the proprieties of the liquids to be separated and the starting ligand. These gels were also degraded by the 2- and 3-methylpiperidine. Figure 5.17 shows the degradation of Fe-tri-EtOH, which is the result of the disruption of the hydrogen bonds which stabilise the gel.

Table 5.7: Properties of components to be separated and the ligand components of the gels used, 5-nitroisophthalic acid and trimesic acid

Component	**Melting point** [°C]	**pK$_a$**	**Molar mass** [g/mol]
2-methylpiperidine	118-119	10.99	99.17
3-methylpiperidine	125-126	11.28	99.17
5-nitroisophthalic acid	259-261	2.81	211.13
trimesic acid	>300	3.12	210.14

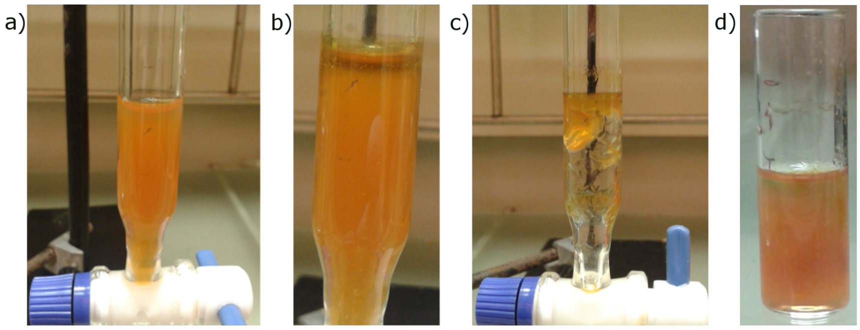

Figure 5.17: Degradation of Fe-tri-EtOH gel as the mixture diffuses through the material. a) Gel before addition of mixture. b) Degradation can be seen as the mixture moves through the gel. c) Degraded gel at the end of the experiment. d) Gel collected for GC analysis.

5.6 Conclusion

The interactions within the gel network play an important role in the potential application of these soft materials. For Fe-5nite-DMF and Fe-tri-DMF, halogen bonding appears to play a role. Both gels absorb more bromocresol green than methyl orange. This may be explained by the lack of halogen atoms in methyl orange as well as the presence of an unfavourable azo bond.

Drying may collapse the gel pockets as less dye was taken up by the xerogel when compared to the fresh gel. Despite this, the xerogels absorbed CO_2, N_2, and H_2O vapour as well as DMF vapour. The dried material could not be reconstituted by neither vapour nor liquid sorption as the pores collapsed during the drying process.

The non-covalent interactions involved in stabilisation of the gels were disrupted during the experiments which were designed to determine whether or not Fe-phens-EtOH, Fe-5nite-EtOH, Fe-tri-EtOH would be good candidates for separation of methylpiperidines.

Chapter 6

Crystal structures of gelator components with iron or cobalt

It has been previously noted in Chapter 3 that gel would not form when metal salts with organic counterions were used. In this chapter, crystals which were obtained from two different types of experiments will be discussed. First those obtained from gel formation experiments, and second those resulting from solvothermal methods using autoclaves.

An investigation into the role of different components in gel formation yielded red crystals from a combination of iron(III) acetylacetonate and 2,6-pyridinedicarboxylic acid in acetonitrile. $[Fe(C_5H_7O_2)(C_7H_3NO_4)(H_2O)]\cdot CH_3CN$ (**I**) was formed at room temperature in 18 hours and $Fe(C_5H_7O_2)(C_7H_3NO_4)$ (**II**) and $[Fe(C_5H_7O_2)(C_7H_3NO_4)]_4$ (**III**) were formed at 60 °C after two and 24 hours, respectively. A similar study using cobalt(III) acetylacetonate as the metal salt instead of iron(III) acetylacetonate, with 5-nitroisophthalic acid in *N*,*N*-dimethylacetamide (DMA) at 60 °C resulted in pink crystals, $Co(CHO_2)_2\cdot 2H_2O$ (**IV**).

Metal salts with the acetylacetonate counterion were also used in solvothermal reactions to determine the possible connectivities of the carboxylate ligands to the metal centre as well as the voids within the structure. Cobalt(III) acetylacetonate and trimesic acid in *N*,*N*-dimethylformamide (DMF) resulted in pink crystals, $3[Co(C_9H_3O_8)(C_3H_6NO)_2\cdot\frac{2}{3}(C_3H_6NO)]$ (**V**).

6.1 Single crystal structure of I

6.1.1 Formation of I

An equimolar ratio of $Fe(C_5H_7O_2)_3$ (0.1 mmol, 37 mg, 1 mL acetonitrile) and 2,6-pyridine dicarboxylic acid (0.1 mmol, 18 mg, 4 mL acetonitrile) were combined in a vial with diameter of 2.4 cm. Slow evaporation overnight yielded red block-like crystals (Figure 6.1).

Figure 6.1: The red block-like morphology of crystals of **I**.

6.1.2 Data collection and structure refinement of I

Data for the single crystal of **I** were collected using a Bruker KAPPA APEX DUO II using Mo radiation ($\lambda = 0.7107$ Å) at 173 ± 2 K. The crystal system was determined to be triclinic from the Laue system, which was found to be $\bar{1}$ (Table 6.1). The $|E^2\text{-}1|$ value of 0.869 unequivocally indicated a centrosymetric space group, $P\bar{1}$.[98]

Table 6.1: Crystal data of **I**

Molecular formula	$[Fe(C_5H_7O_2)(C_7H_3NO_4)(H_2O)]\cdot CH_3CN$
Molecular mass [g mol^{-1}]	379.13
Crystal system	Triclinic
Space group	$P\bar{1}$
Unit cell parameters	
a [Å]	8.645(2)
b [Å]	9.026(2)
c [Å]	10.773(2)
α [°]	93.169(5)
β [°]	100.097(4)
γ [°]	99.996(4)
Volume [Å^3]	811.8(3)
Z	2
Density$_{calcd.}$ [g cm^{-3}]	1.5510(6)
μ [MoKα] [mm^{-1}]	0.967
F (*000*)	390
Temperature [K]	173(2)
Crystal size [mm]	0.19 x 0.19 x 0.22
Range scanned θ [°]	1.9-28.5
Index range	h: -11, 11; k: -12, 12; l: -14, 14
ϕ and ω scan angles [°]	0.5
Dx [mm]	50
Total number of reflections	22935
Number of independent reflections	4072
Number of reflections with I > 2σ(I)	3573
Final R indices [I > 2σ(I)]	$R_1 = 0.0299$, $wR_2 = 0.0718$
R indices (all data)	$R_1 = 0.0358$, $wR_2 = 0.0752$
S	1.049
Number of parameters	222
Number of reflections omitted	11
Parameters a, b in $w = 1/[\sigma^2(F_0{}^2)+(aP)^2+(bP)]$	a = 0.0312, b = 0.3567
$(\delta/\sigma)_{mean}$	<0.001
$\Delta\rho$ excursions [e.Å^3]	-0.45, 0.44

6.1.3 Structure of **I**

The asymmetric unit comprises of an iron(III) metal ion coordinated to a single 2,6-pyridinedicarboxylate ligand, and a water molecule. An acetonitrile solvent molecule is also present. The iron(III) ion exhibits a distorted octahedral coordination geometry (Figure 6.2), which is typical of iron(III) complexes. The bond lengths and angles of the coordination group are given in Table 6.2. None of these values are outside the expected range for this coordination. The torsion angles O4-Fe1-O1-C1 and O6-Fe1-O5-C9 are -4.8(2)° and 3.2(2)° respectively, showing that each ligand has adopted near planar conformation. The dihedral angle between least squares planes defined by each ligand is 89.04°. Three rings are formed with the metal centre, two 5-membered (Ring 1: Fe1−O1−C1−C2−N1 and Ring 2: Fe1−O4−C7−C6−N1) and one 6-membered ring (Ring 3: Fe1−O5−C9−C10−C11−O6). None of these exhibit ring puckering and the greatest deviation from the least square plane occurs in Ring 2 where the O4 atom deviates by 0.013(1) Å.

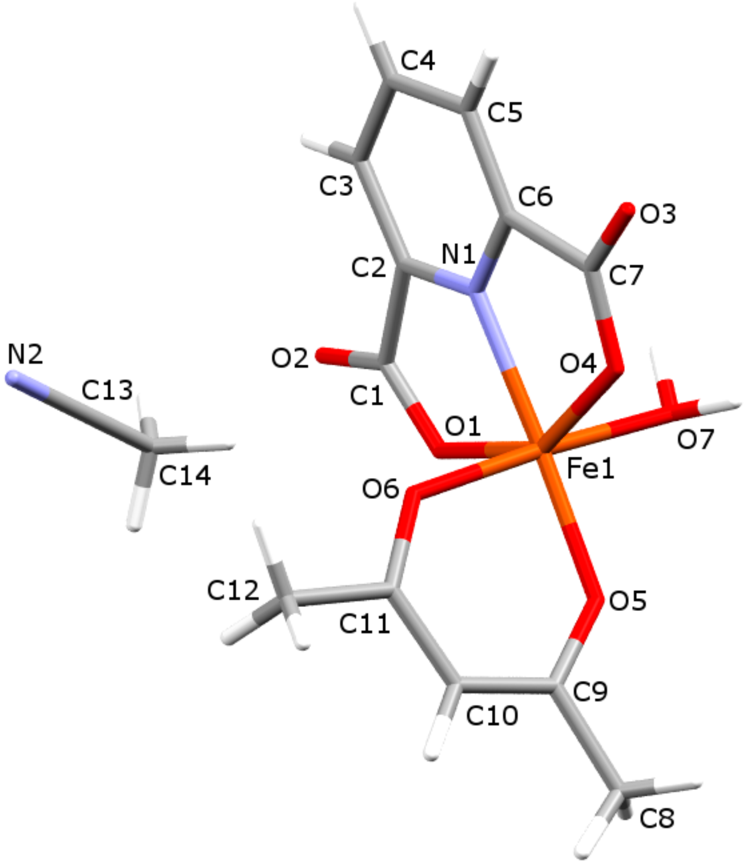

Figure 6.2: Asymmetric unit of **I** showing coordination to Fe(III) metal centre.

Table 6.2: Bond lengths and angles of atoms coordinated to the Fe(III) metal centre

Bond	**Length [Å]**	**Bonds**	**Angle [°]**
Fe1−O1	2.033(1)	N1−Fe1−O6	88.94(5)
Fe1−O4	2.034(1)	N1−Fe1−O7	94.09(5)
Fe1−O5	1.929(1)	O4−Fe1−O5	104.07(5)
Fe1−O6	1.998(1)	O5−Fe1−O1	104.56(5)
Fe1−O7	2.032(1)	N1−Fe1−O1	75.51(5)
Fe1−N1	2.068(1)	O4−Fe1−N1	75.95(5)

6.1.4 Hydrogen bonding and packing of I

Hydrogen bonds as a bridging interactions play a key role in biology and structural chemistry. As they are adequately strong and have sufficient directionality hydrogen bonds are able to control and direct molecular assemblies.[160] There are seven unique interactions of this type present in **I**. These comprised of two oxygen and five carbon donor atoms, while all of the acceptor atoms are oxygen (Table 6.3). Figure 6.3 shows the hydrogen bonds viewed down [100].

Table 6.3: Summary of hydrogen bond lengths and bond angles for **I**

Number	**Hydrogen bond**	**D−H*** [Å]	**H···A*** [Å]	**D···A** [Å]	**D−H···A*** [°]	**Symmetry Operation**
1	O7−H7A···O3	0.97	1.75	2.620(2)	148	*1-x*, *-y*, *2-z*
2	O7−H7B···O2	0.83	1.88	2.680(2)	161	*1-x*, *-y*, *1-z*
3	C4−H4···O7	0.95	2.58	3.438(2)	150	*1+x*, *y*, *z*
4	C5−H5···O3	0.95	2.43	3.253(2)	145	*2-x*, *-y*, *2-z*
5	C10−H10···O4	0.95	2.59	3.316(2)	133	*1-x*, *1-y*, *2-z*
6	C12−H12C···O2	0.98	2.57	3.473(2)	152	*1-x*, *1-y*, *1-z*
7	C14−H14B···O1	0.98	2.32	3.270(3)	164	*1-x*, *1-y*, *1-z*

*e.s.d values not calculated as hydrogen atoms were placed in geometrically idealised positions.

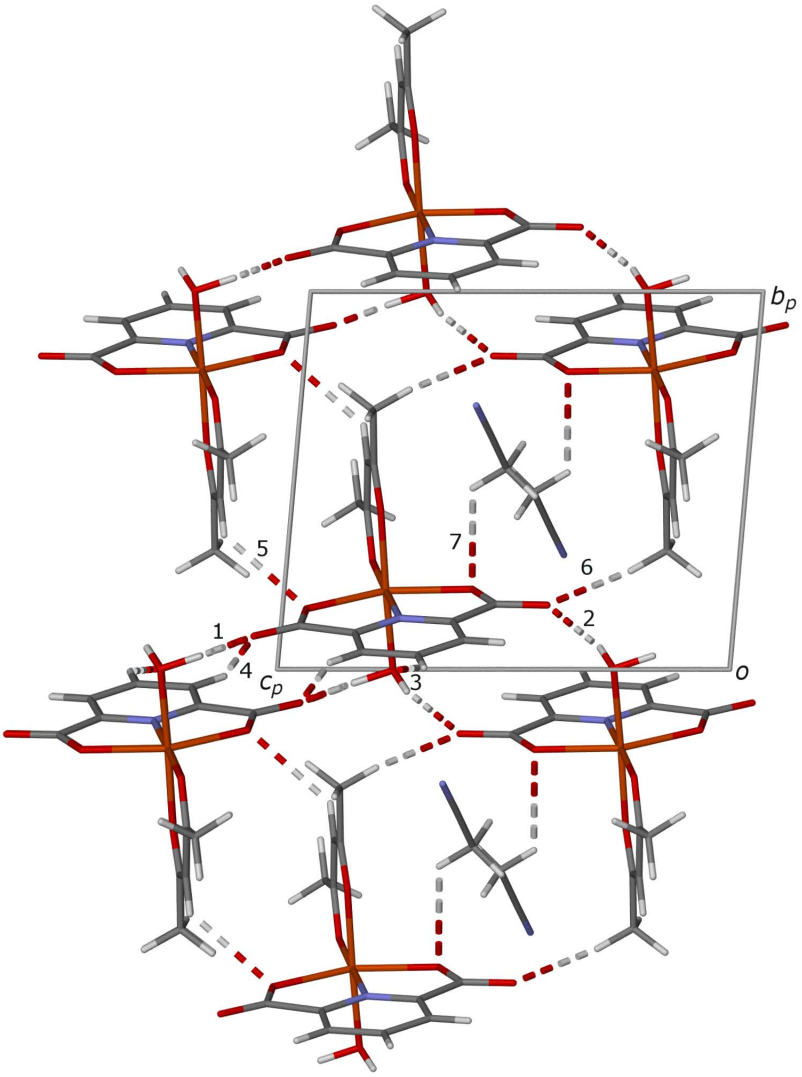

Figure 6.3: Hydrogen bonds in **I** viewed down [100]. Labels correlate with Table 6.3.

The coordinated water molecule participates in three hydrogen bonds. In hydrogen bonds 1 and 2, the water molecule acts as a donor while the oxygen atom (O7) acts as an acceptor in hydrogen bond 3. Hydrogen bonds 1 and 2 connect the unit to adjacent units along the [001] axis. These units are centrosymmetrically related to one another. The interpenetrated layers are linked by hydrogen bonds 5 and 6 from the acetylacetonate ligand to the 2,6-pyridinedicarboxylate ligand, connecting neighbouring units. These layers are further stabilised by hydrogen bonds 3 and 4. The atoms O2 and O3 act as bifurcated acceptors in the hydrogen bonds 2 and 6 and hydrogen bonds 1 and 4, respectively. They act as bridges between two layers in the direction of the [100] axis. Hydrogen bond 7 takes place between the acetonitrile molecule and the acetylacetonate ligand stabilising the position of this molecule within the interstitial space.

There are seven hydrogen bonding rings arising from the interactions of hydrogen bonds 1-6. These rings are described following the path along the least number of atoms (Figure 6.4). These rings can be described by graph set notation, which utilises graph theory in order to categorise hydrogen-bond patterns.[161]

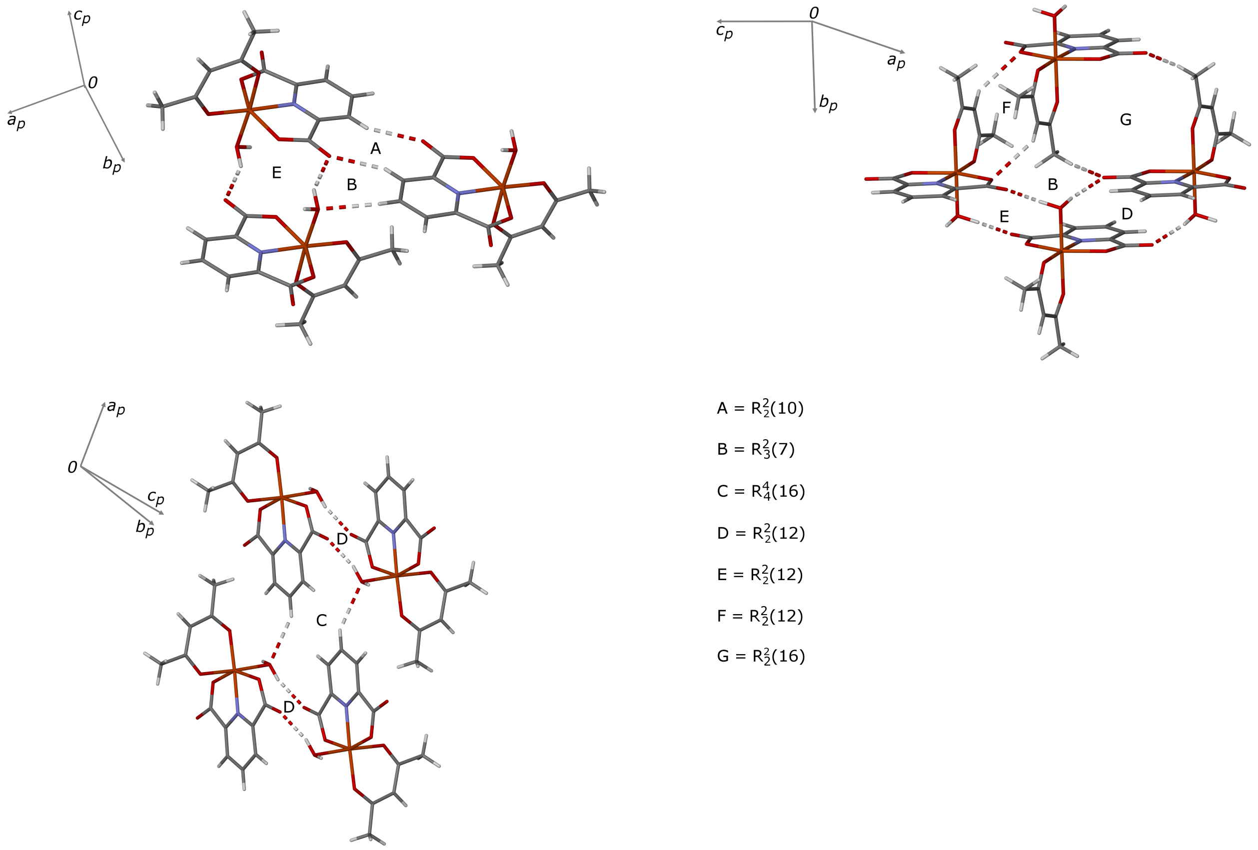

Figure 6.4: Graph set notation rings in **I**. Acetonitrile solvent, which is encapsulated in ring G, has been removed for clarity.

There is no void space present in this structure due to the sheets of interpenetrated bilayers (Figure 6.5). The packing of **I** is stabilised by the above mentioned hydrogen bonds. In **I** the packing is driven by the geometry of the coordination and the hydrogen bonds.

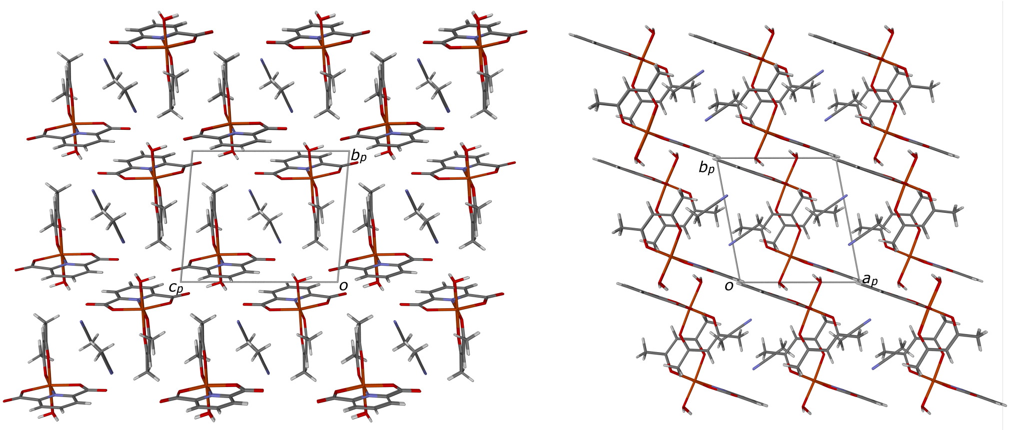

Figure 6.5: Packing of **I**, viewed down [100] (left) and down [001] (right). The acetonitrile solvent molecule is found in channels propagating parallel to [100].

Figure 6.6 shows the FT-IR spectrum for **I**. The peak at 2927 cm^{-1} shows an O-H stretch which is a result of the coordinated water molecule. Acetonitrile is present and the broad peak at 2251 cm^{-1} originates from the nitrile bond. 1527 cm^{-1} corresponds to the aromatic C=C stretches. The peaks at 598 cm^{-1} and 436 cm^{-1} indicate coordination, and are assigned to Fe−O and Fe−N respectively. The carbonyl C−O and C=O peaks are assigned to the peaks at 1278 cm^{-1} and 1628 cm^{-1} respectively.

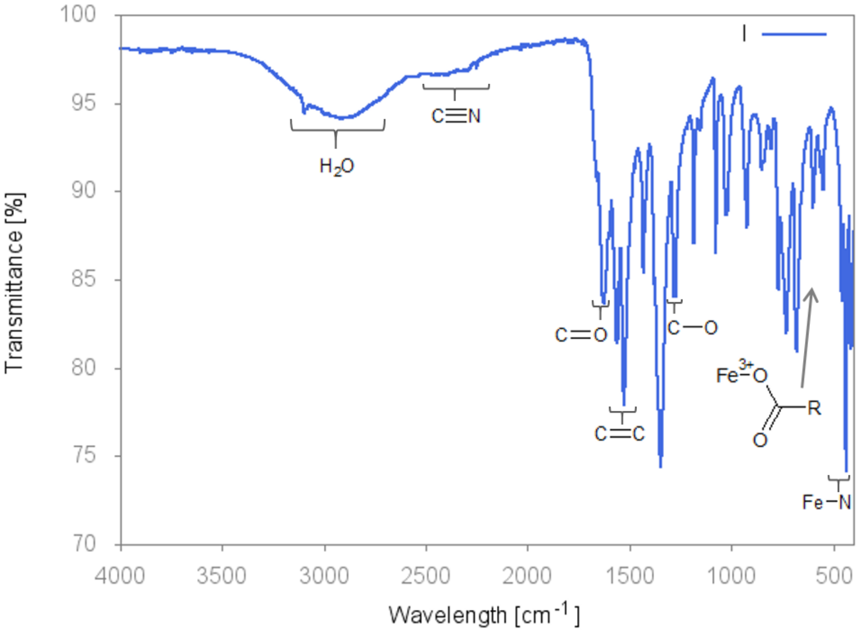

Figure 6.6: FT-IR spectrum of **I** grown at room temperature.

6.2 Similar structures in the literature

An analogue of **I** which contains half an ethanol solvent molecule disordered around the binary axis was published by Lainé *et al*[162] (CSD code ZIMBIG). It crystallises in the monoclinic crystal system C2/c and has distorted octahedral coordination of the ligands to the Fe(III) metal centre (Figure 6.7). These purple-blue crystals were obtained using reflux methods.[162] Table 6.4 gives the coordination bond lengths and angles. These values are comparable with those of **I**, the bond angles and lengths are similar in both structures.

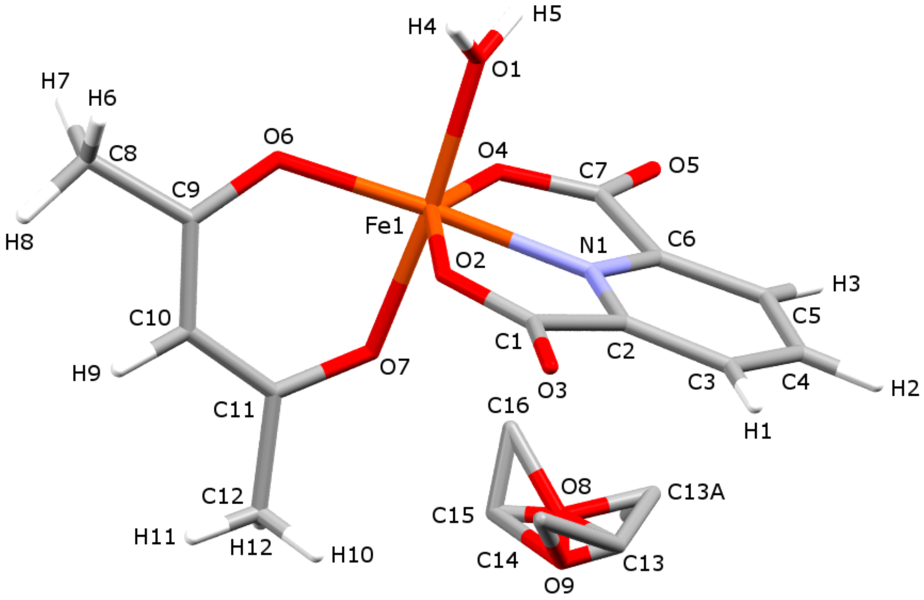

Figure 6.7: Asymmetric unit of ZIMBIG showing coordination to Fe(III) metal centre and the disordered ethanol molecule.[162]

Table 6.4: Summary of bond lengths and angles of atoms coordinated to the Fe(III) metal centre of ZIMBIG

Bond	**Length [Å]**	**Bonds**	**Angle [°]**
Fe1−O1	2.002(2)	N1−Fe1−O7	92.16(9)
Fe1−O2	2.046(2)	N1−Fe1−O1	92.80(8)
Fe1−O4	2.035(2)	O4−Fe1−O6	111.64(9)
Fe1−O6	1.936(3)	O4−Fe1−O2	97.26(9)
Fe1−O7	1.977(2)	N1−Fe1−O2	75.42(7)
Fe1−N1	2.069(2)	O4−Fe1−N1	74.69(7)

An overlay of the two asymmetric units, without the uncoordinated solvent molecule, can be seen in Figure 6.8. A value of 0.093 Å is obtained for the root mean square deviation (RMSD) of the asymmetric units indicating strong similarities between them.

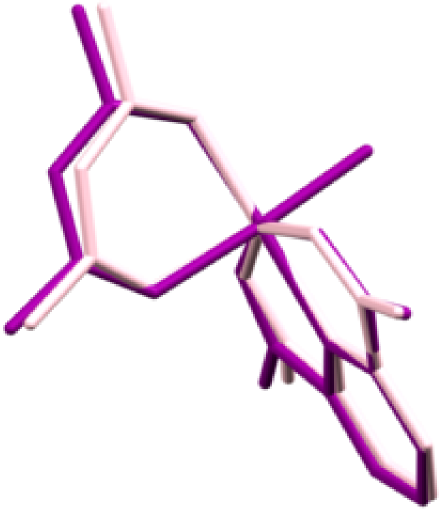

Figure 6.8: The root mean square deviation fit of the asymmetric units of ZIMBIG[162] (pink) and **I** (purple). Hydrogen atoms and solvent molecules were omitted for clarity. RMSD fit between the two molecules is 0.093 Å.

Despite the similarities in the coordinated moiety, there are only three hydrogen bonds present in the ZIMBIG network (Table 6.5), unlike **I** where there are seven. None of the carbon atoms in the acetylacetonate ligand are involved in these interactions. As with **I**, the coordinated water molecule plays a role in hydrogen bonding and the donor oxygens are on adjacent units. Hydrogen bond 3, which is similar to hydrogen bond 4 in **I**, connects 2,6-pyridinedicarboxylate ligands of adjacent units in the same plane.

Table 6.5: Summary of hydrogen bond lengths and bond angles for ZIMBIG

Number	**Hydrogen bond**	**D–H*** [Å]	**H···A*** [Å]	**D···A** [Å]	**D–H···A*** [°]	**Symmetry Operation**
1	O1–H4···O3	0.86	1.79	2.641(3)	170	$-x$, $-y$, $-z$
2	O1–H5···O5	0.83	1.77	2.590(3)	174	$-x$, y, $\frac{1}{2}$-z
3	C3–H1···O3	0.98	2.38	3.297(4)	156	$\frac{1}{2}$-x, -$\frac{1}{2}$-y, -z

*e.s.d values not calculated as hydrogen atoms were placed in geometrically idealised positions.

Using graph set notation, rings have been identified (Figure 6.9). Hydrogen bond 3 forms a ring with itself and results in ring B_z. The parallel layers along [001] are connected by rings A_z and ring $\mathrm{C}_z$which is formed by hydrogen bonds 1 and 2, respectively. The angle between least square planes through the 2,6-pyridinedicarboxylate ligands in the layers along [010] and along [001] is 43.63°.

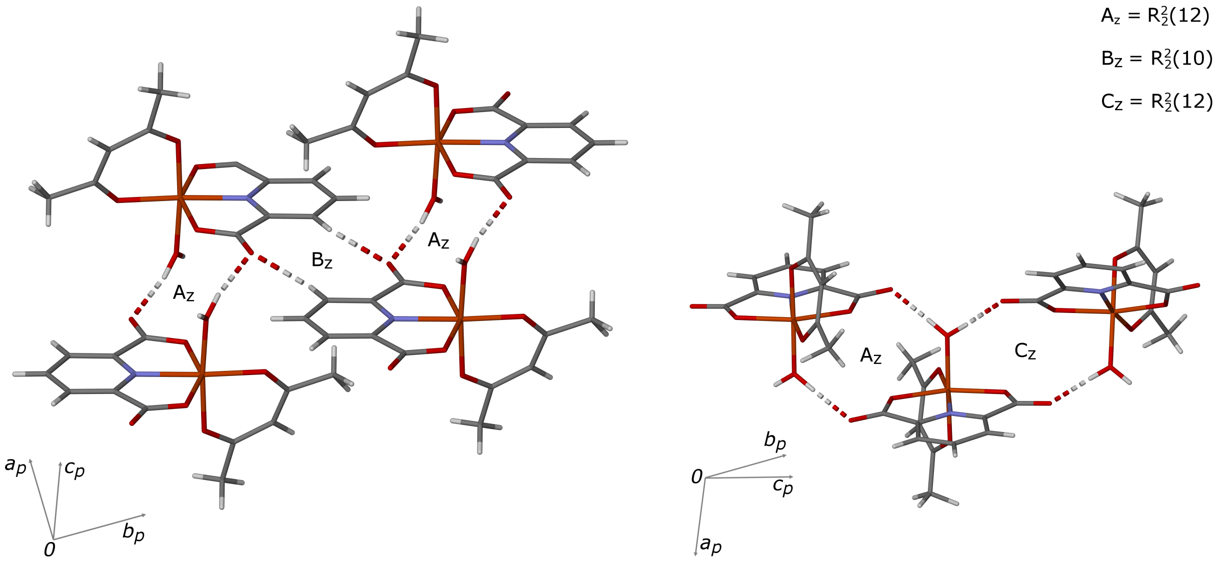

Figure 6.9: Graph set notation rings for ZIMBIG.[162]

The hydrogen bonds in ZIMBIG, which has a higher crystal symmetry than **I**, result in a very different packing to that of **I**. In the case of ZIMBIG the solvent molecule, ethanol, may play a role in hydrogen bonding however, the disorder[162] in the molecule prevents definitive analysis. In **I** the solvent molecule, acetonitrile, is involved in hydrogen bonding. These compounds have different packing arrangements which may arise from the use of different solvents with different hydrogen bonding properties. The packing of ZIMBIG along each axis can be seen in Figure 6.10. The hydrogen bonded units alternate in orientation in the layer parallel to [001]. Layers are also formed parallel to [100] and interdigitation of the pyridyl rings is observed.

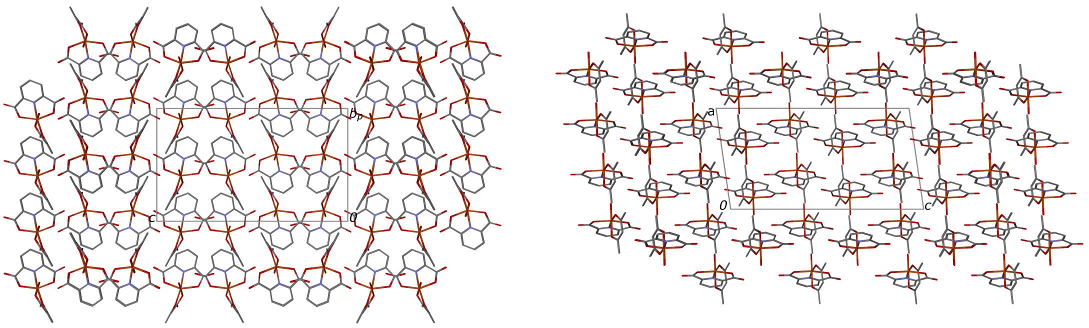

Figure 6.10: Packing of ZIMBIG viewed down [100] on the left and [010] on the right.[162] Hydrogen atoms and ethanol solvent molecule are omitted for clarity. The disordered ethanol molecule can be found in a channel propagating along [010]. This packing arrangement is different to that seen for **I** (Figure 6.5).

6.3 Single crystal structure of II

6.3.1 Formation of II and III

While **I** was obtained by slow evaporation at room temperature, **II** and **III** were obtained at an elevated temperature. An equimolar ratio of $Fe(C_5H_7O_2)_3$ (0.1 mmol, 37 mg, 1 mL acetonitrile) and 2,6-pyridinedicarboxylic acid (0.1 mmol, 18 mg, 4 mL acetonitrile) were combined in a vial with a diameter of 2.4 cm. The red prism shaped crystals grew in the oven at 60 °C. Initial results for thermal analysis showed inconsistencies which suggested that the material obtained was a mixture of compounds. The synthesis conditions were adjusted with careful attention to temperature and time. Two different structures were elucidated. **II** and **III** were obtained when synthesis was carried out for 2 h and 24 h, respectively. The compounds display the same morphology and the crystals could not be distinguished with the naked eye (Figure 6.11).

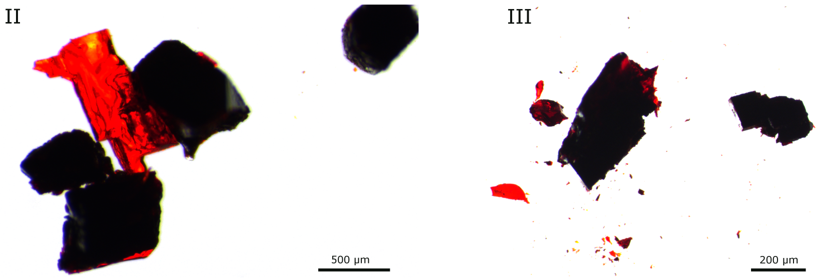

Figure 6.11: Morphology of **II** and **III**. Red block-like crystals, similar to those observed for **I**.

6.3.2 Data collection and refinement II

A Bruker KAPPA APEX DUO II, Mo radiation ($\lambda = 0.7107$ Å), was used to collect the single crystal intensity data for **II**. The Laue system was found to be 4/mmmm and was used to determine the crystal system, tetragonal in this case. A non-centrosymmetric space group was indicated by the $|E^2\text{-}1|$ value of 0.752.[98] This was determined to be $P\bar{4}2_1c$, after an examination of the systematic absences. The conditions limiting reflection were hkl: $h{+}k{+}l = 2n$, hhl: $l = 2n$, $00l$: textitl $= 2n$, $h00$: $h = 2n$ confirming the assignment. The crystallographic data for **II** can be found in Table 6.6.

Table 6.6: Crystal data of **II**

Molecular formula	$Fe(C_5H_7O_2)(C_7H_3NO_4)$
Molecular mass [g mol^{-1}]	322.076
Crystal system	Tetragonal
Space group	$P\bar{4}2_1c$
Unit cell parameters	
a [Å]	13.242(1)
c [Å]	14.998(2)
Volume [Å^3]	2629.7(6)
Z	2
Density$_{calcd.}$ [g cm^{-3}]	1.617
μ [MoKα] [mm^{-1}]	1.171
F (*000*)	1304.0
Temperature [K]	173(2)
Crystal size [mm]	0.50 x 0.25 x 0.12
Range scanned θ [°]	2.716 - 25.87
Index range	h: -15, 15; k: -17, 17; l: -20, 20
ϕ and ω scan angles [°]	0.5
Dx [mm]	48
Total number of reflections	36874
Number of independent reflections	3279
Number of reflections with I > 2σ(I)	2913
Final R indices [I > 2σ(I)]	$R_1 = 0.0294$, $wR_2 = 0.0637$
R indices (all data)	$R_1 = 0.0369$, $wR_2 = 0.0670$
S	1.039
Number of parameters	183
Number of reflections omitted	4
Parameters a, b in $w = 1/[\sigma^2(F_0{}^2)+(aP)^2+(bP)]$	a = 0.0302, b = 0.6617
$(\delta/\sigma)_{mean}$	<0.001
$\Delta\rho$ excursions [e.Å^3]	-0.255, 0.270

6.3.3 Structure of II

One iron(III) coordinated to one acetylacetonate and one 2,6-pyridinedicarboxylate makes up the asymmetric unit (Figure 6.12). There are four such units generated through a 4-fold axis to form a tetramer. The iron(III) centres are linked through coordination to an oxygen (O3) on the 2,6-pyridinedicarboxylate ligand. The iron(III) has distorted octahedral coordination (Table 6.7). All of the values obtained are within the expected range for these types of complexes. Both ligands adopt a planar configuration with torsion angles of -3.4(4)° and 7.4(3)° for O4−Fe1−O1−C1 and O6−Fe1−O5−C9 respectively. The angle between two least square planes through each of the coordinated ligands is 82.18°. Two 5-membered (Ring 1: Fe1−O1−C1−C2−N1 and Ring 2: Fe1−O4−C7−C6−N1) and one 6-membered ring (Ring 3: Fe1−O5−C9−C10−C11−O6) are formed with the metal centre. There is no puckering of the rings and the greatest deviation from the least square plane occurs in Ring 3 where the O5 atom deviates by 0.0440 Å.

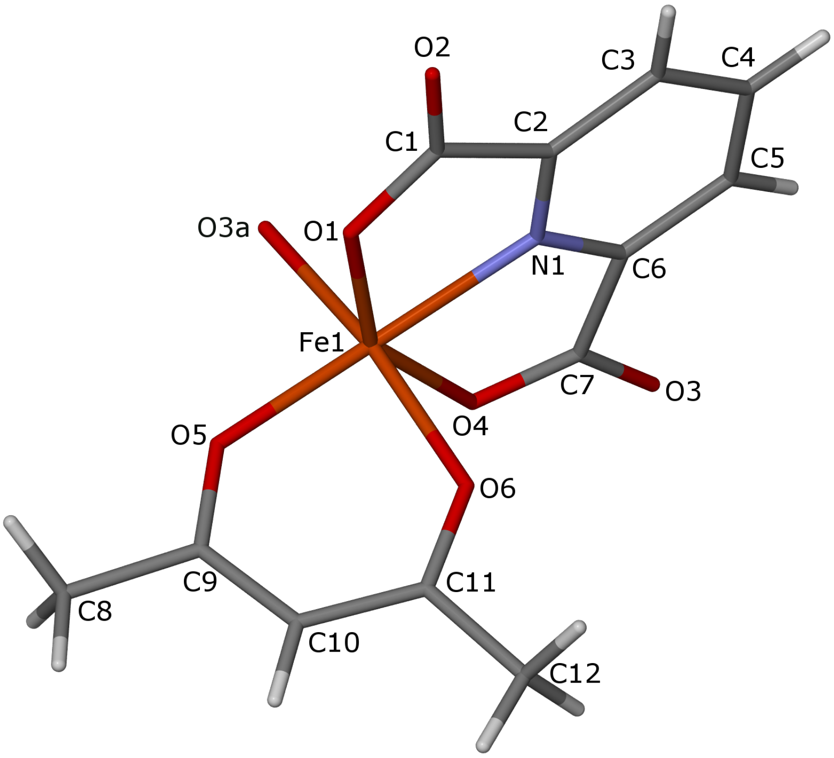

Figure 6.12: The distorted octahedral coordination around the Fe(III) metal centre of **II**. The atoms in the asymmetric unit are labelled along with O3a. O3a links the Fe(III) metal centres and is generated through the symmetry operation *1 +* y, *1* - *x*, *1* - *z*.

Table 6.7: Coordination geometry of the ligands to the metal centre of **II**

Bond	**Length [Å]**	**Bond**	**Angle [°]**
Fe1−O1	1.9891(2)	O1−Fe1−N1	76.52
Fe1−O4	2.0864(2)	O4−Fe1−N1	74.60
Fe1−O5	1.9406(2)	O6−Fe1−N1	88.87
Fe1−O6	1.9817(2)	O5−Fe1−O6	88.06
Fe1−N1	2.0764(2)	O5−Fe1−O3a	86.60
Fe1−O3a	2.0409(2)	N1−Fe1−O3a	97.70

6.3.4 Hydrogen bonding and packing, II

Table 6.8 gives the details for the single hydrogen bond present in **II**. This connects one tetramer to four others (Figure 6.13) and involves atoms from the 2,6-pyridinedicarboxylate ligands (C4−H4· · · O1). This results in a staggered chain along [001].

Table 6.8: Summary of hydrogen bond lengths and bond angles for **II**

Hydrogen bond	**D−H*** [Å]	**H· · · A*** [Å]	**D· · · A** [Å]	**D−H· · · A*** [°]	**Symmetry Operation**
C4−H4· · · O1	0.95	2.37	3.2934(4)	164	$\frac{1}{2}+y$, $-\frac{1}{2}+x$, $\frac{1}{2}+z$

*e.s.d values not calculated as hydrogen atoms were placed in geometrically idealised positions.

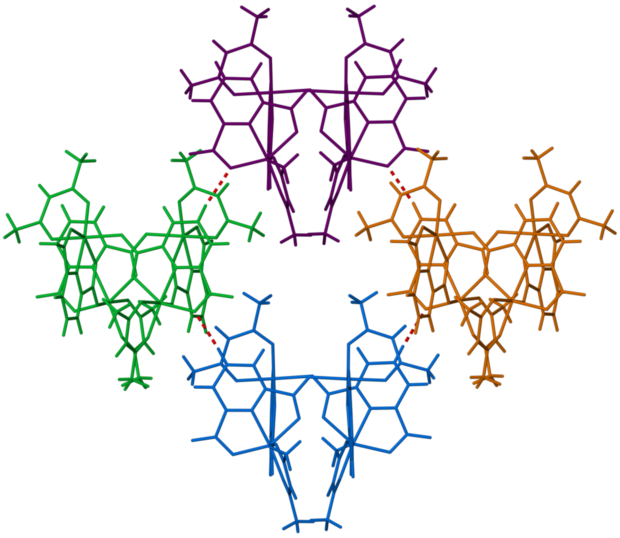

Figure 6.13: Hydrogen bonding of **II**. There is one unique hydrogen bond which connects tetramers viewed along [101].

The centres of the tetramers run in a straight line and the bound ligands form a gently undulating pattern though the hydrogen bond. There are two such chains which intersect and form a cross. No void space is present in the structure. Other interactions which may lead to stabilisation of the structure include $\pi\cdots\pi$ interactions. These are considered to be any close contact between any π- or delocalised-electron system and a donor atom or another π-system.[163] A separation of 3.3 - 3.8 Å for face-to-face and offset face-to-face interactions is an accepted distance, while up to 5 Å is acceptable for edge-to-face separations. **II** is further stabilised by one such interaction between the centroid of Rings 3 and 4, 3.9995(5) Å is the distance between the rings. The undulating pattern as well as the overlap of the rings can be seen in Figure 6.14

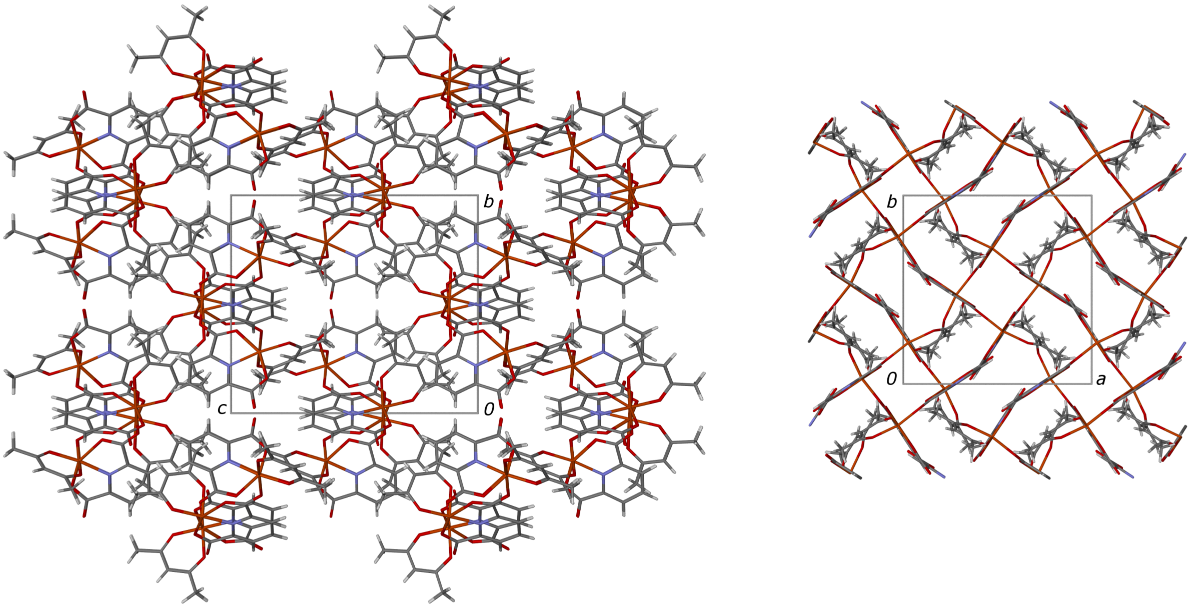

Figure 6.14: Packing of **II** from left to right viewed down [100] and [001]. The hydrogen bond which links each tetramer to four others stabilises this formation. An undulating pattern can be seen along the *a*-*b* plane.

Figure 6.15 shows the FT-IR spectrum for **II**. No signals in the 3000 to 2500 cm^{-1} indicates no water is present. Peaks for both bidentate bridging coordination of oxygen to iron(III) and monodenate binding nitrogen to iron(III) are present at 601 cm^{-1} and 434 cm^{-1}, respectively (Table 6.9).

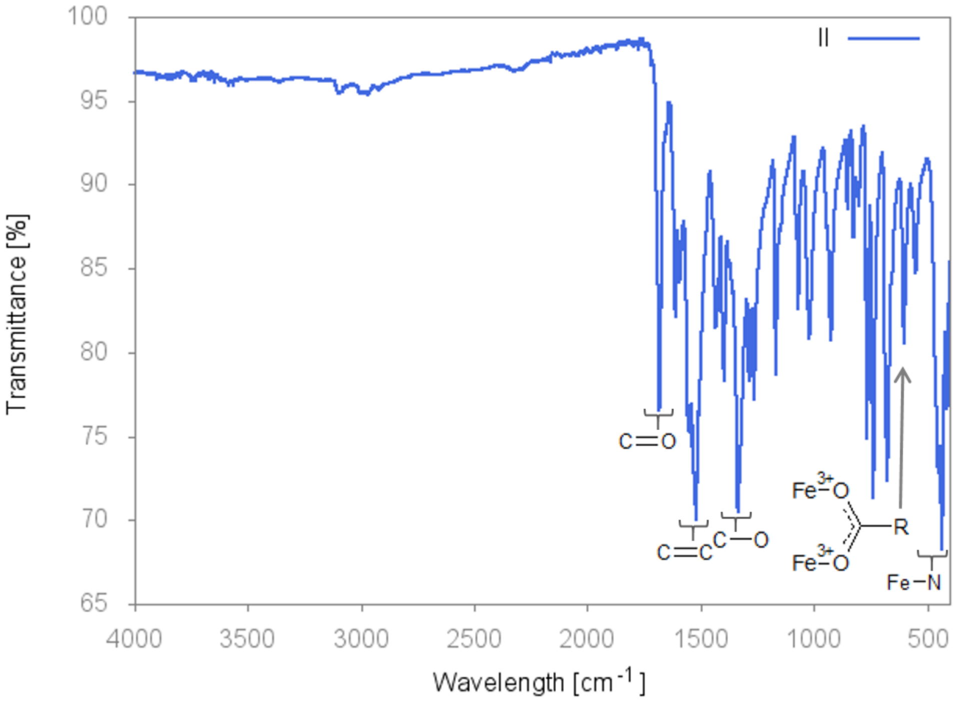

Figure 6.15: FT-IR spectrum of **II**.

Table 6.9: FT-IR assignments of **II**

Bond	ν **[cm^{-1}]**
434	Fe−N
601	Fe−O
1261	C−O
1525	C=C aromatic
1682	C=O

6.4 Single crystal structure of III

6.4.1 Formation of III

An equimolar ratio of $Fe(C_5H_7O_2)_3$ (0.1 mmol, 37 mg, 1 mL acetonitrile) and 2,6-pyridinedicarboxylic acid (0.1 mmol, 18 mg, 4 mL acetonitrile) were combined in a vial with a diameter of 2.4 cm. The red prism shaped crystals were obtained from the oven at 60 °C for 24 h, and have the same morphology as **II**.

6.4.2 Data collection and refinement of III

A Bruker KAPPA APEX DUO II, Mo radiation ($\lambda = 0.7107$ Å), was used to collect the single crystal intensity data for **III**. The Laue system was found to be $\bar{1}$ and was used to determine the crystal system, triclinic in this case. A centrosymmetric space group, $P\bar{1}$, was indicated by the $|E^2\text{-}1|$ value of 0.944.[98] The crystallographic information is given in Table 6.10.

Table 6.10: Crystal data of **III**

Molecular formula	$[Fe(C_5H_7O_2)(C_7H_3N_1O_4)]_4$
Molecular mass [g mol^{-1}]	1288.304
Crystal system	Triclinic
Space group	$P\bar{1}$
Unit cell parameters	
a [Å]	14.5961(7)
b [Å]	14.7434(8)
c [Å]	15.2140(8)
α [°]	112.713(1)
β [°]	106.080(1)
γ [°]	105.946(1)
Volume [Å^3]	2619.1(2)
Z	4
Density$_{calcd.}$ [g cm^{-3}]	1.6231
μ [MoKα] [mm^{-1}]	1.18
F (*000*)	1304.0
Temperature [K]	173(2)
Crystal size [mm]	0.113 x 0.022 x 0.022
Range scanned θ [°]	2.463-22.98
Index range	h: -19, 19; k: -19, 19; l: -19, 20
ϕ and ω scan angles [°]	0.5
Dx [mm]	50
Total number of reflections	45405
Number of independent reflections	12959
Number of reflections with I > 2σ(I)	7760
Final R indices [I > 2σ(I)]	$R_1 = 0.0485$, $wR_2 = 0.1013$
R indices (all data)	$R_1 = 0.1030$, $wR_2 = 0.1226$
S	1.008
Number of parameters	729
Number of reflections omitted	17
Parameters a, b in $w = 1/[\sigma^2(F_0{}^2)+(aP)^2+(bP)]$	a = 0.0502, b = 0.0133
$(\delta/\sigma)_{mean}$	<0.001
$\Delta\rho$ excursions [e.Å^3]	-0.454, 1.632

6.4.3 Structure of III

The asymmetric unit of **III** is comprised of four iron(III) each coordinated to one acetylacetonate and one 2,6-pyridinedicarboxylate ligands, in a similar manner to **II**. Each unit (labelled A - D) is linked through its iron(III) centre to the oxygen atom of the 2,6-pyridinedicarboxylate ligand (O1A-D) belonging to the adjacent unit (Figure 6.16).

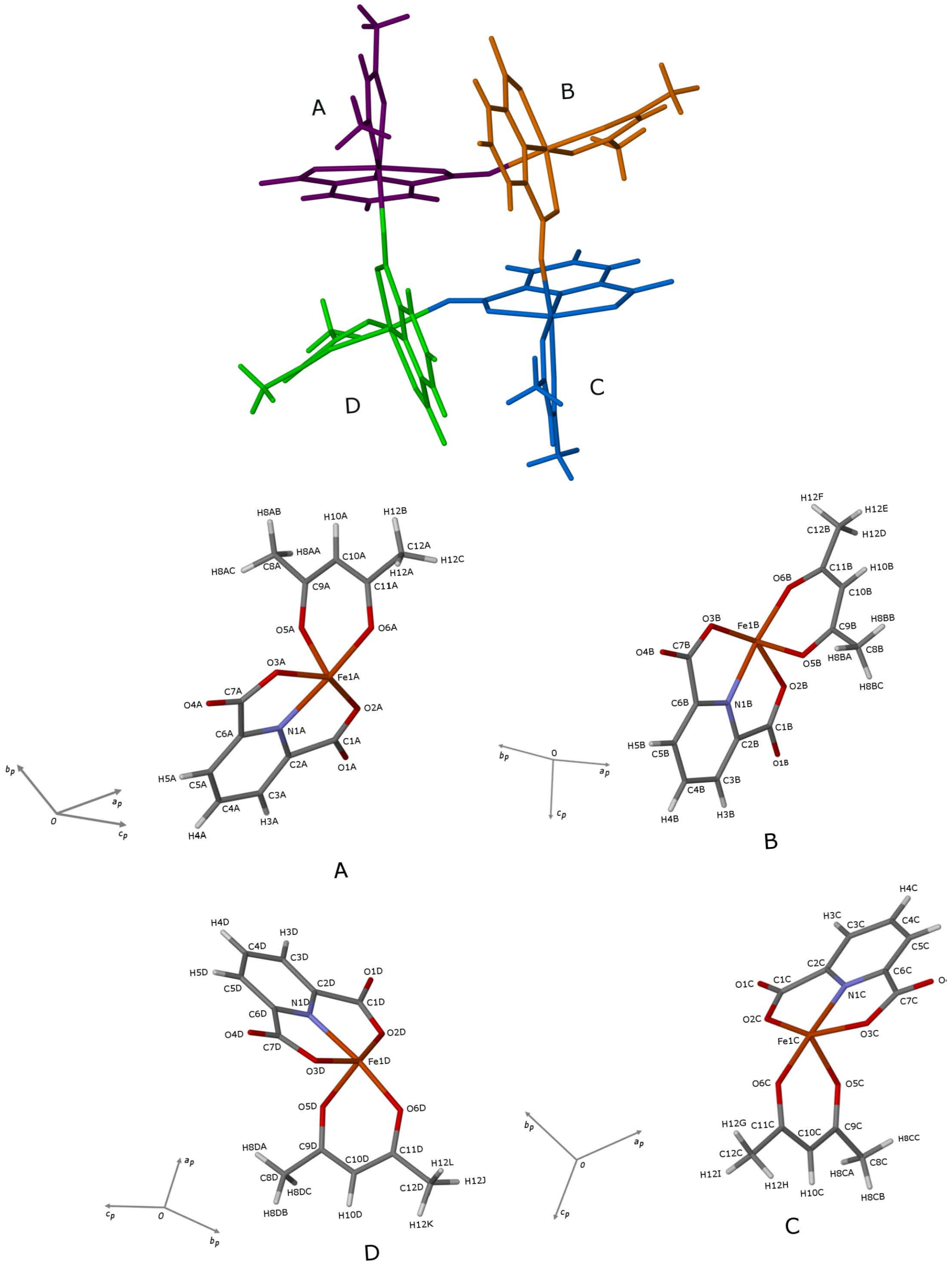

Figure 6.16: Asymmetric unit showing the tetramer formed by coordination to Fe(III) metal centres in **III**. Above) the connected tetramer, with each unit in a different colour: unit A in purple, B in orange, C in blue, and D in green. Below) labelled units A - D which have been positioned to minimise atom overlap.

The resulting tetramer has a neutral charge and no solvent is present in the structure. Like **I** and **II**, the iron(III) has distorted octahedral coordination geometry (Tables 6.11 and 6.12) and the ligands bind in a planar fashion. None of the rings are puckered nor do they lie perpendicular or parallel to one another.

Table 6.11: Bond lengths of the coordination geometry of the ligands to the metal centre of **III**

Bond	**Length** [Å]	**Bond**	**Length** [Å]	**Bond**	**Length** [Å]	**Bond**	**Length** [Å]
Fe1A−O1D	2.0286(1)	Fe1B−O1A	2.0603(1)	Fe1C−O1B	2.0477(1)	Fe1D−O1C	2.0596(1)
Fe1A−O2A	2.0959(1)	Fe1B−O2B	2.0728(1)	Fe1C−O2C	2.0936(1)	Fe1D−O2D	2.0988(1)
Fe1A−O3A	1.9776(1)	Fe1B−O3B	2.0089(1)	Fe1C−O3C	1.9870(1)	Fe1D−O3D	2.0026(1)
Fe1A−O5A	1.9925(1)	Fe1B−O5B	1.9927(1)	Fe1C−O5C	1.9906(1)	Fe1D−O5D	1.9873(1)
Fe1A−O6A	1.9569(1)	Fe1B−O6B	1.9295(1)	Fe1C−O6C	1.9577(1)	Fe1D−O6D	1.9445(1)
Fe1A−N1A	2.0903(1)	Fe1B−N1B	2.0814(1)	Fe1C−N1C	2.0983(1)	Fe1D−N1D	2.0762(1)

Table 6.12: Bond angles of the coordination geometry of the ligands to the metal centre of **III**

Bond	**Angle** [°]	**Bond**	**Angle** [°]
O2A−Fe1A−N1A	73.72(1)	O2B−Fe1B−N1B	74.97(1)
O1D−Fe1A−N1A	96.69(1)	O1A−Fe1B−N1B	96.81(1)
O5A−Fe1A−O6A	87.56(1)	O5B−Fe1B−O6B	88.27(1)
O2A−Fe1A−O5A	86.60(1)	O2B−Fe1B−O5B	91.72(1)
O3A−Fe1A−N1A	76.29(1)	O3B−Fe1B−N1B	76.43(1)
O1D−Fe1A−O3A	95.62(1)	O1A−Fe1B−O3B	91.83(1)
O2C−Fe1C−N1C	73.71(1)	O2D−Fe1D−N1D	74.78(1)
O1B−Fe1C−N1C	100.78(1)	O1C−Fe1D−N1D	98.18(1)
O5C−Fe1C−O6C	87.49(1)	O5D−Fe1D−O6D	87.24(1)
O2C−Fe1C−O5C	88.68(1)	O2D−Fe1D−O5D	89.72(1)
O3C−Fe1C−N1C	76.34(1)	O3D−Fe1D−N1D	76.49(1)
O1B−Fe1C−O3C	92.76(1)	O1C−Fe1D−O3D	92.27(1)

6.4.4 Hydrogen bonding and packing, III

There are 12 hydrogen bonds in **III**, all of the donor atoms are carbon and all of the acceptor atoms are oxygen (Table 6.13). None of these bonds are intramolecular nor do they occur between atoms within the asymmetric unit. All of the hydrogen bonds link to other tetramer units. All of the acceptors are oxygen atoms on a 2,6-pyridinedicarboxylate ligand, except for hydrogen bond 2. The acceptor in this bond is O5D, which is an oxygen atom in the acetylacetonate ligand of monomer D. The majority of these hydrogen bonds are from the methyl moieties of the acetylacetonate ligands. This results in a tangled web of interconnected rings (Figure 6.17).

Table 6.13: Summary of hydrogen bond lengths and angles for **III**

Number	**Hydrogen bond**	**D−H*** [Å]	**H···A*** [Å]	**D···A** [Å]	**D−H···A*** [°]	**Symmetry Operation**
1	C8B−H8BA···O4A	0.98	2.54	3.2779(2)	132	*1+x*, *y*, *z*
2	C3D−H3D···O5D	0.95	2.46	3.2591(2)	142	*-x*, *2-y*, *1-z*
3	C4B−H4B···O3C	0.95	2.46	3.1603(2)	131	1-*x*, *2-y*, *1-z*
4	C8D−H8DB···O4C	0.98	2.37	3.3124(2)	162	*-1+x*, *y*, *z*
5	C5A−H5A···O3B	0.95	2.51	3.2647(2)	137	*-x*, *2-y*, *1-z*
6	C5C−H5C···O3D	0.95	2.60	3.3000(2)	131	*-x*, *1-y*, *-z*
7	C8C−H8CB···O3A	0.98	2.56	3.2807(2)	130	*x*, *-1+y*, *z*
8	C12B−H12D···O4D	0.98	2.58	3.2315(2)	124	*-x*, *1-y*, *-z*
9	C12B−H12F···O4A	0.98	2.42	3.3276(2)	153	*-x*, *2-y*, *-z*
10	C12C−H12I···O4A	0.98	2.59	3.5526(2)	168	*-x*, *2-y*, *1-z*
11	C12D−H12J···O4B	0.98	2.57	3.4551(2)	150	*-x*, *2-y*, *-z*
12	C12D−H12L···O4C	0.98	2.22	3.1513(2)	159	*-x*, *1-y*, *-z*

*e.s.d values not calculated as hydrogen atoms were placed in geometrically idealised positions.

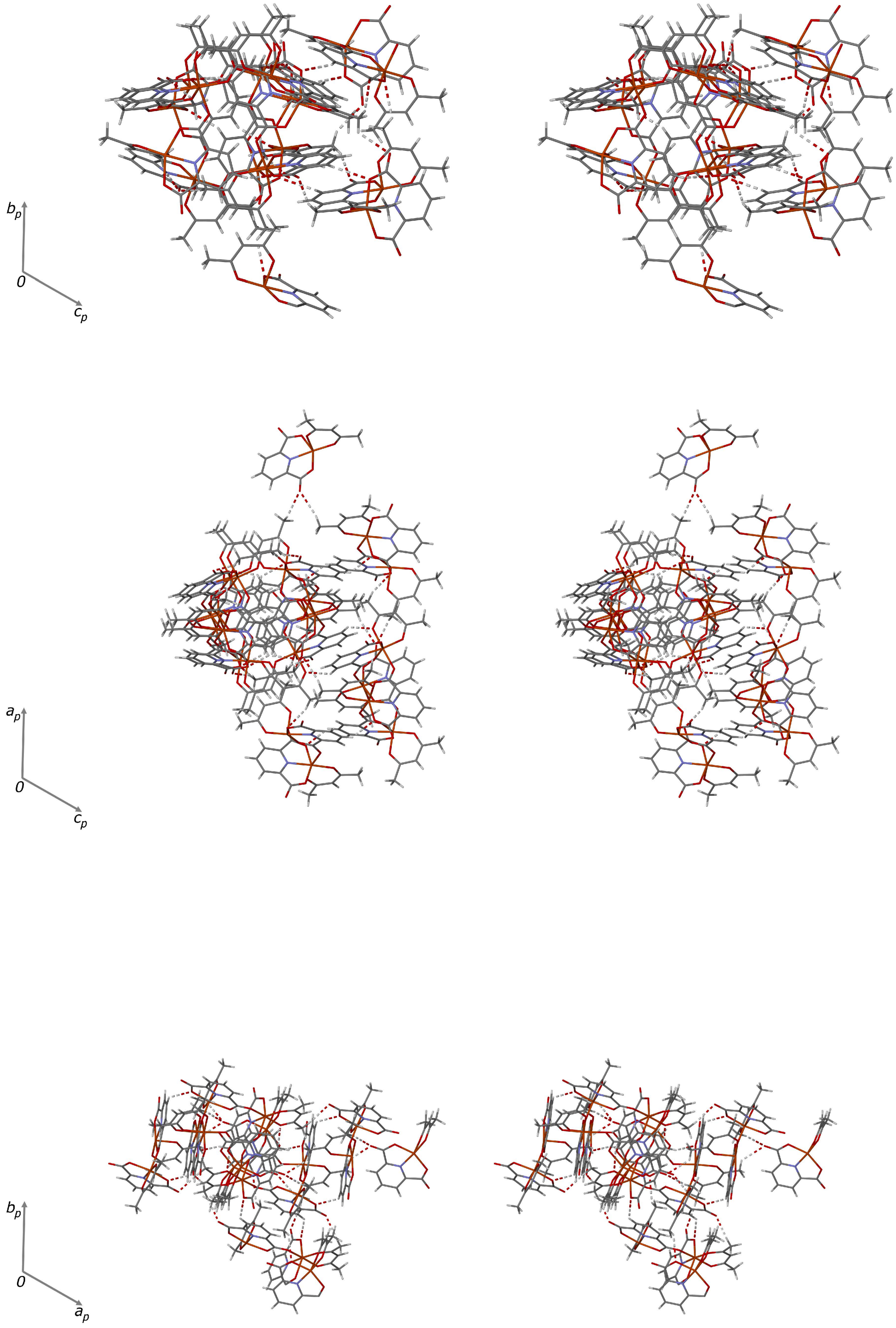

Figure 6.17: From top to bottom stereo diagrams of **III** viewed down [100], [010], and [001]) showing the interconnected hydrogen bonding network. Only the monomer which is directly involved in hydrogen bonding to the asymmetric unit is shown.

Figure 6.18 shows the bifurcated and trifurcated hydrogen bonds where O4C and O4A are the bifurcated and trifurcated acceptors respectively. Hydrogen bonds 4 and 12 connect monomers C and D. Monomers A, B, and C, are linked through hydrogen bonds 1, 9, and 10 respectively.

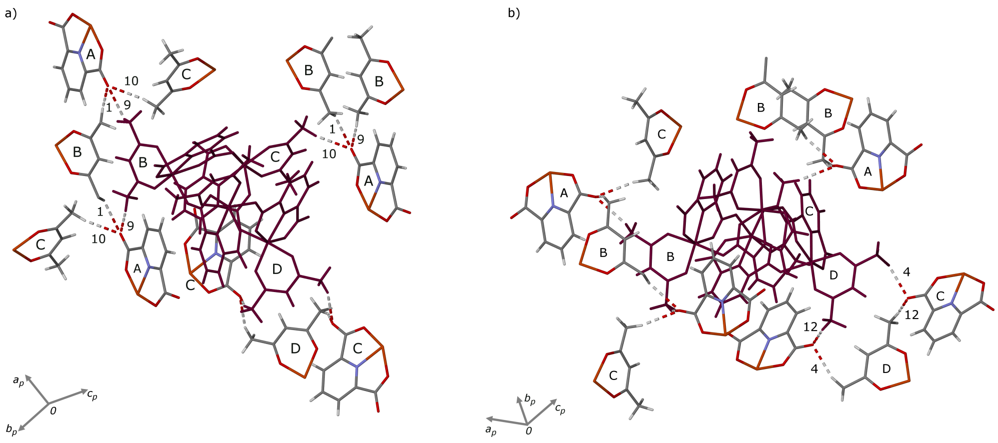

Figure 6.18: a) Trifurcated acceptor bonds in **III** involving hydrogen bonds 1, 9, and 10. b) Bifurcated acceptor bonds involving hydrogen bonds 4 and 12. The asymmetric unit is shown in purple and each monomer is labelled.

When viewed down [100], it can be seen that the tetramers pack in such a way that interpenetrated layers are stabilised by hydrogen bonds 1 - 12 (Figure 6.19). There are many points of interaction which stabilise the structure. No void space is present. As with all crystalline materials the structure is further stabilised by van der Waals forces.

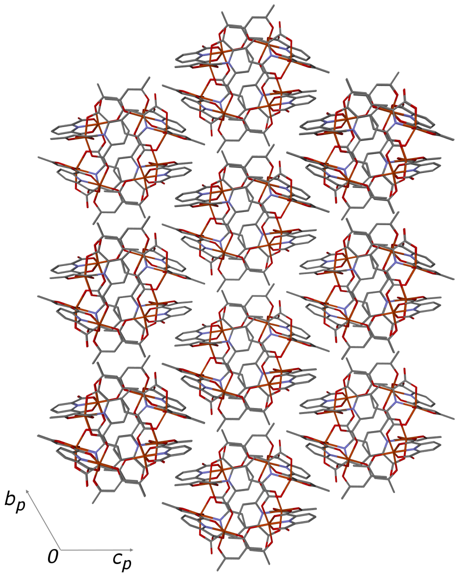

Figure 6.19: Packing of the tetramers of **III** with hydrogen bond stabilised layers viewed down [100]. Hydrogen atoms have been removed for clarity.

Figure 6.20 shows the FT-IR spectrum for **III**, the spectrum matches that of **II**. This is not surprising as the coordination is the same in both complexes. The absence of signals in the 3000 to 2500 cm^{-1} confirms no water is present, like in **II**.

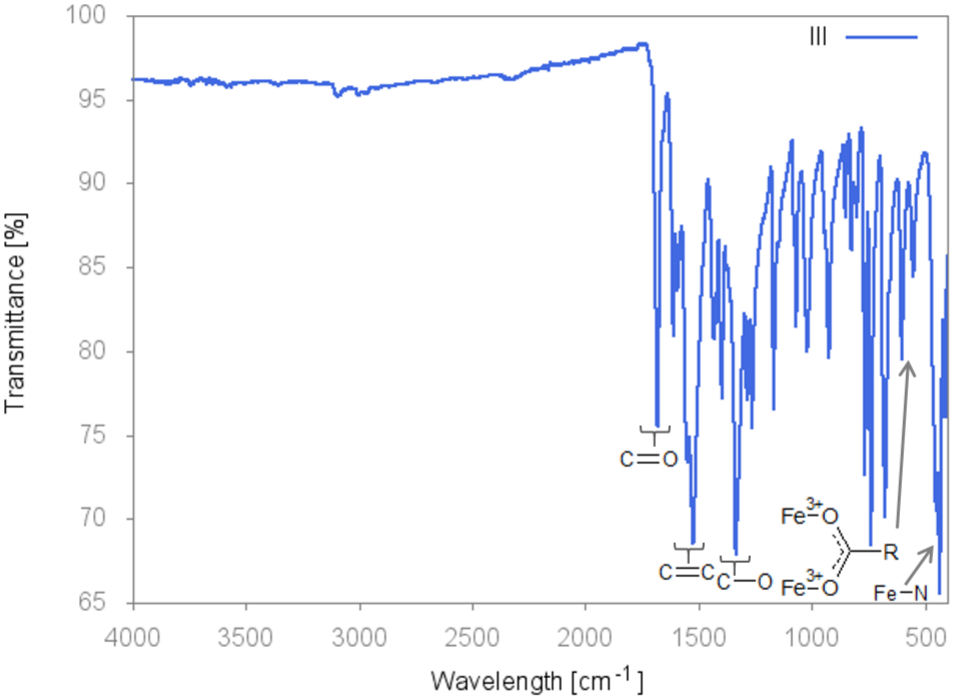

Figure 6.20: FT-IR spectrum of **III**.

6.5 Powder X-ray diffraction of I, II, and III

Powder X-ray diffraction (PXRD) traces of each compound and the starting materials can be seen in Figures 6.21, 6.22, and 6.23. In all cases the trace of the experimental pattern differs from the sum of the traces of the starting materials. This indicates the formation of a new crystalline phase. There is reasonable agreement between the calculated and experimentally obtained patterns for **II** confirming the homogeneity of the bulk material for phases. **I** and **III** show small discrepancies which may indicate that the bulk material is not purely one phase and there is a small amount of contamination. In general, the calculated pattern shows a shift to lower 2θ which is caused by the data collection, on which the calculated pattern is based, being done at low temperature while the experimental pattern is measured at room temperature. The unit cell shrinks at low temperature which results in smaller d-spacing, therefore 2θ is lower.

Figure 6.24 shows an overlay of the calculated patterns of **I**, **II**, and **III**. Each is different, this is not surprising as each has distinct hydrogen bonding configurations and hence dissimilar packing arrangements. 6

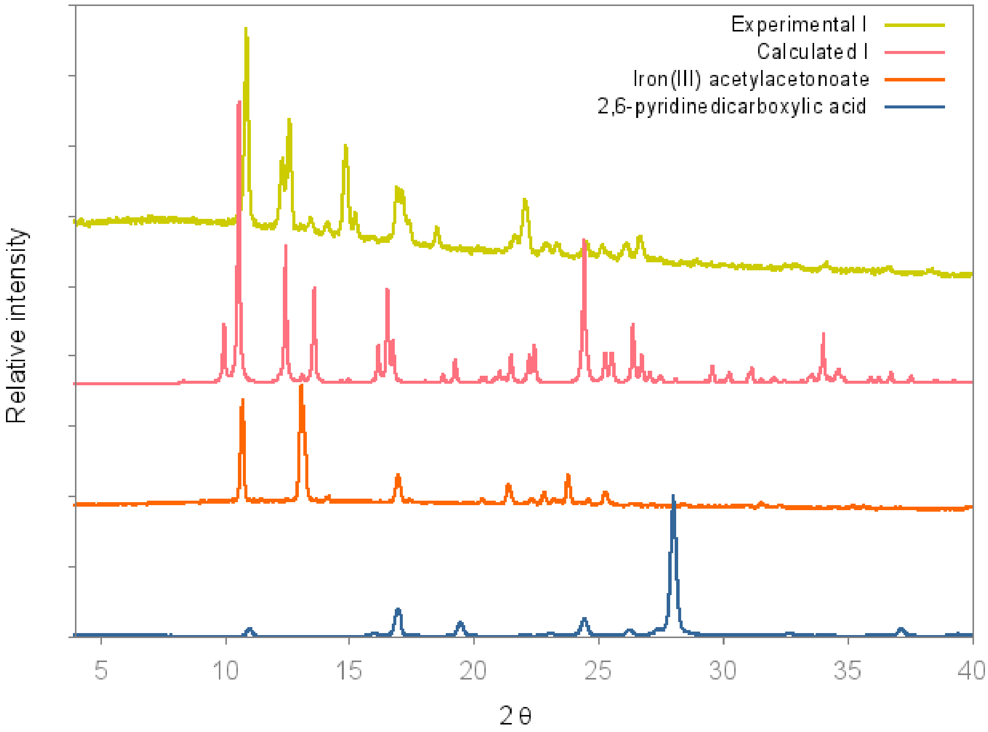

Figure 6.21: PXRD trace of **I** and starting materials. There is partial agreement between the experimental and calculated traces, indicating that the bulk material may be a mixture of compounds.

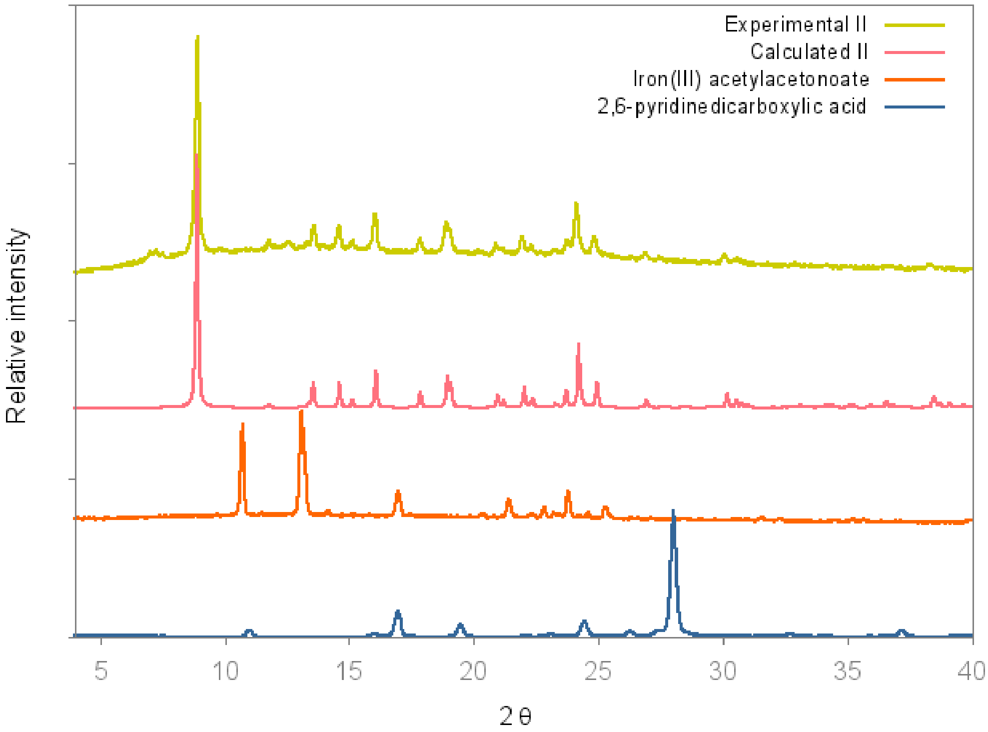

Figure 6.22: PXRD trace of **II** and starting materials. A new phase has formed and there is good agreement between the experimental and calculated patterns.

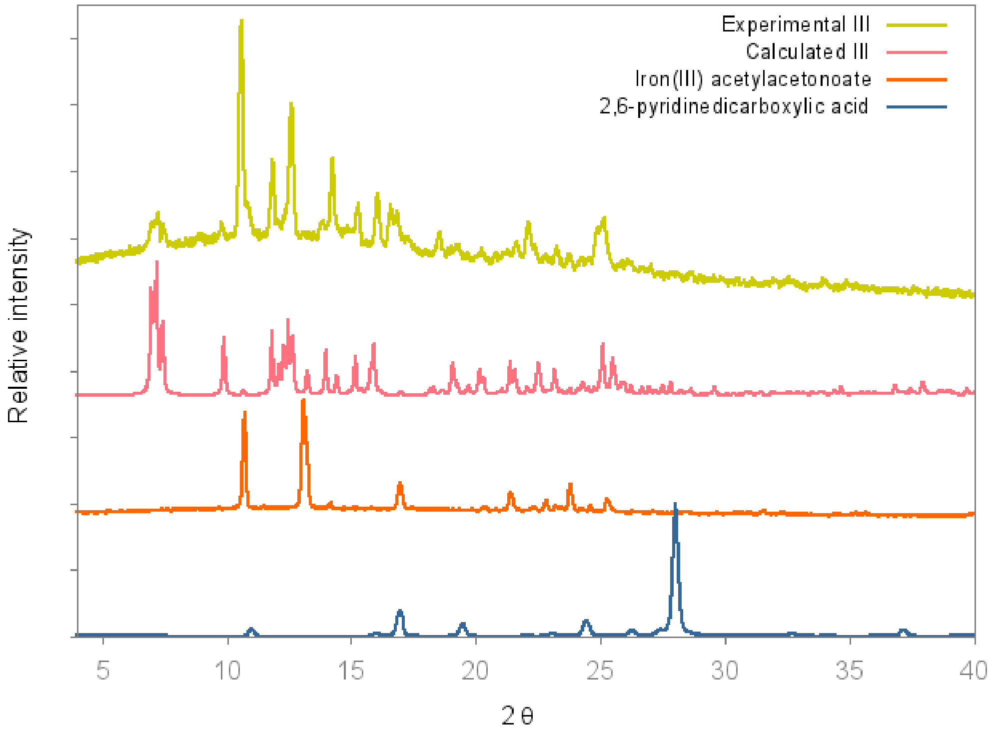

Figure 6.23: PXRD trace of **III** and starting materials. A new phase is present but some discrepancy between the experimental and calculated patterns may indicate that the phase is not pure.

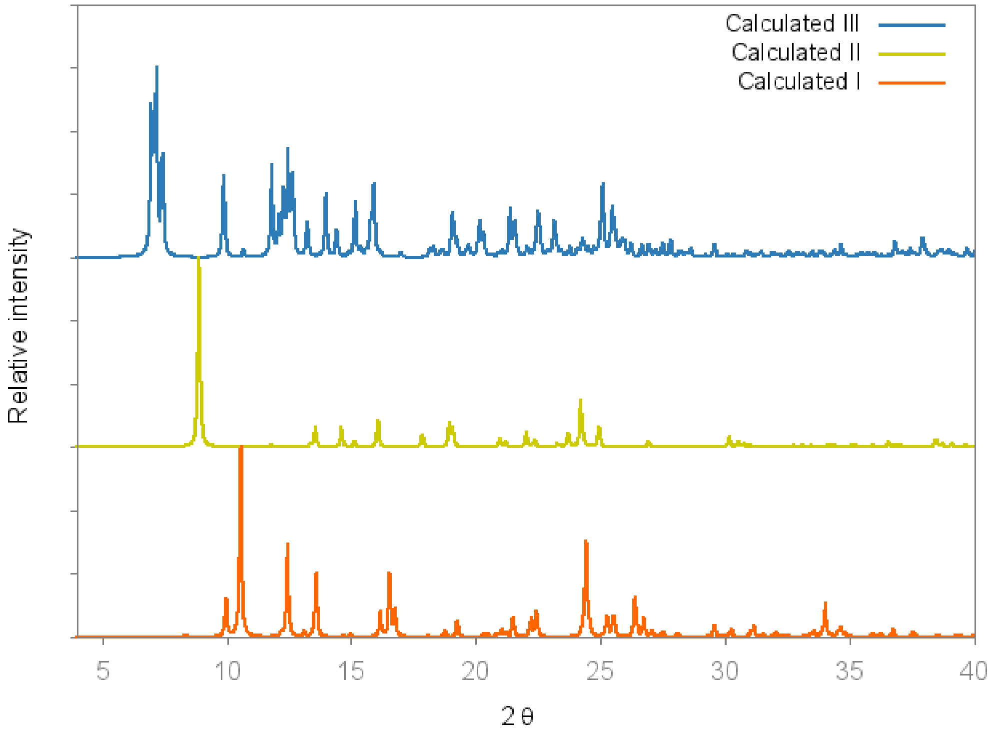

Figure 6.24: Comparison of the calculated PXRD traces of **I**, **II**, and **III**. Three different phases are observed which is dependent on the reaction conditions used.

6.6 Thermal analysis of I, II, and III.

The melting point of 2,6-pyridinedicarboxylic acid is 248 °C and that of iron(III) acetylacetonate is 180 °C. The boiling point of acetonitrile is 82 °C, as this is lower than those of the coordinated ligands, it it most likely that the first mass loss is acetonitrile. **I** is thermally stable until 87.0 ± 1.4°C, following which there are three distinct mass loss steps upon heating the red crystals (Figure 6.25). The first mass loss is a complex two step loss of 10.7 ± 0.3% between 87.0 ± 1.4°C and 198.8 ± 2.2 °C (n = 3), which may correspond to the loss of 1 mol of acetonitrile (calculated mass loss of 10.8%). This is followed by a loss of 3.8 ± 0.6% between 198.8 ± 2.2 °C and 246.4 ± 2.0 °C, which is attributed to the removal of the coordinated water molecule. The subsequent mass losses are most likely the result of decomposition of **I** as the ligands are partially degraded and removed. The acetylacetonate comes off first followed by 2,6-pyridinedicarboxylic acid. This is in agreement with the data obtained from the differential scanning calorimetry (DSC) which shows four broad endothermic peaks at temperatures corresponding to the events in the TGA trace. Table 6.14 shows the theoretical and experimental mass losses for **I**, **II**, and **III**.

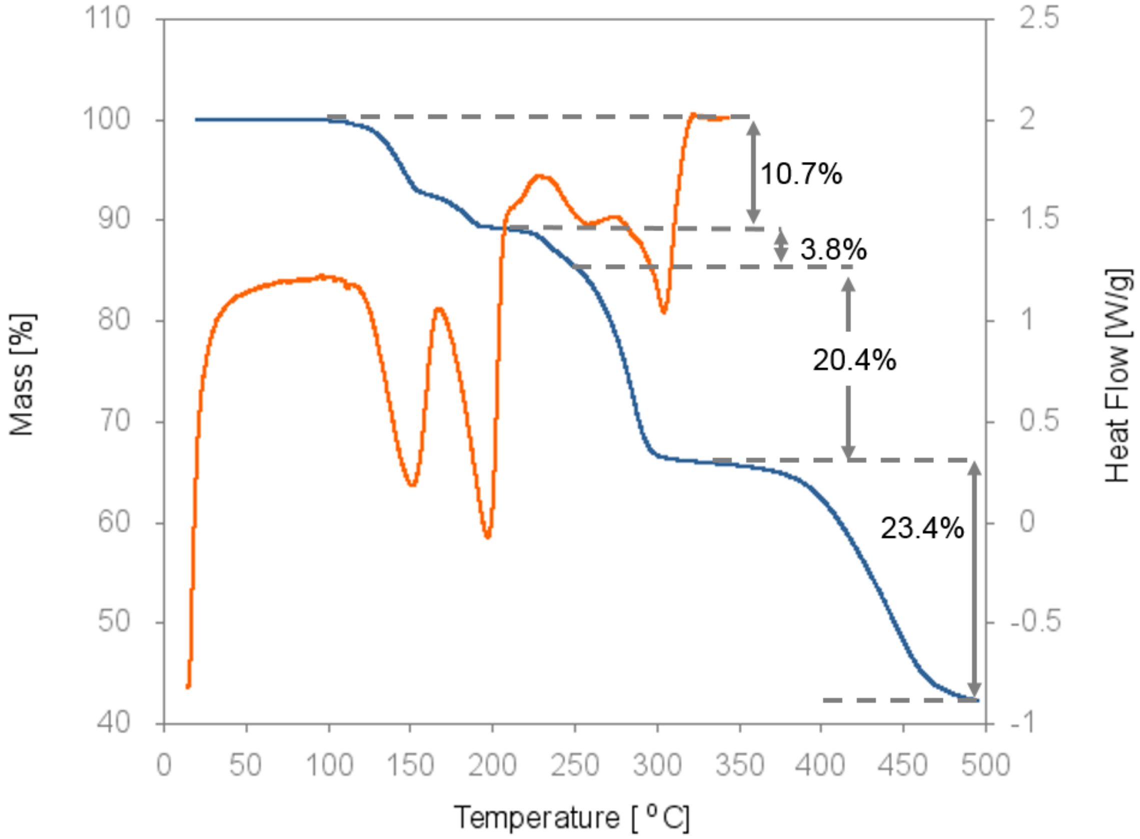

Figure 6.25: Overlay of TGA and DSC traces of **I**. The sequential loss of acetonitrile, water, acetylacetonate, 2,6-pyridinedicarboxylic acid is shown.

Table 6.14: Theoretical and experimentally obtained mass losses of **I**, **II**, and **III**. The components are given in the order in which they are lost

	Component	**Mass loss** [%] **(calculated)**	**Mass loss** [%] **(observed)**
I	**[Fe($C_5H_7O_2$)($C_7H_3N_1O_4$)(H_2O)]·CH_3CN**		
	Acetonitrile	10.8	10.7 ± 0.3
	Water	4.7	3.8 ± 0.6
	Acetylacetonate	26.4	20.4 ± 0.4 partial
	2,6-pyridinedicarboxylic acid	43.6	23.4 ± 0.4
	Fe(III)	14.4	
	FeO_4	31.6	
II	**Fe($C_5H_7O_2$)($C_7H_3NO_4$)**		
	Acetylacetonate	31.3	32.7 ± 0.4
	2,6-pyridinedicarboxylic acid	51.6	30.9 ± 1.1 partial
	Fe(III)	17.3	
	FeO_4	37.5	
III	**[Fe($C_5H_7O_2$)($C_7H_3NO_4$)]$_4$**		
	Acetylacetonate	31.3	31.2 ± 2.4
	2,6-pyridinedicarboxylic acid	51.6	26.2 ± 1.2 partial
	Fe(III)	17.3	
	FeO_4	37.5	

The thermal analysis profiles of **II** and **III** are similar, both exhibit complex and partial decomposition of ligands, acetylacetonate and 2,6-pyridinedicarboxylic acid.

Figure 6.26 shows that **II** is thermally stable until 132.0 ± 2.5 °C (n = 3) where a 32.7 ± 0.2% mass loss is observed (Table 6.14). This may correspond to a loss of the acetylacetonate ligand in a two step process. From the DSC trace decomposition begins at 272.6 ± 3.9 °C. 30.9 ± 1.1% is lost between 310.2 ± 2.5 °C and 495.7 ± 1.1 °C. The remaining ∼37% after 500 °C corresponds to an iron oxide species (FeO_4).

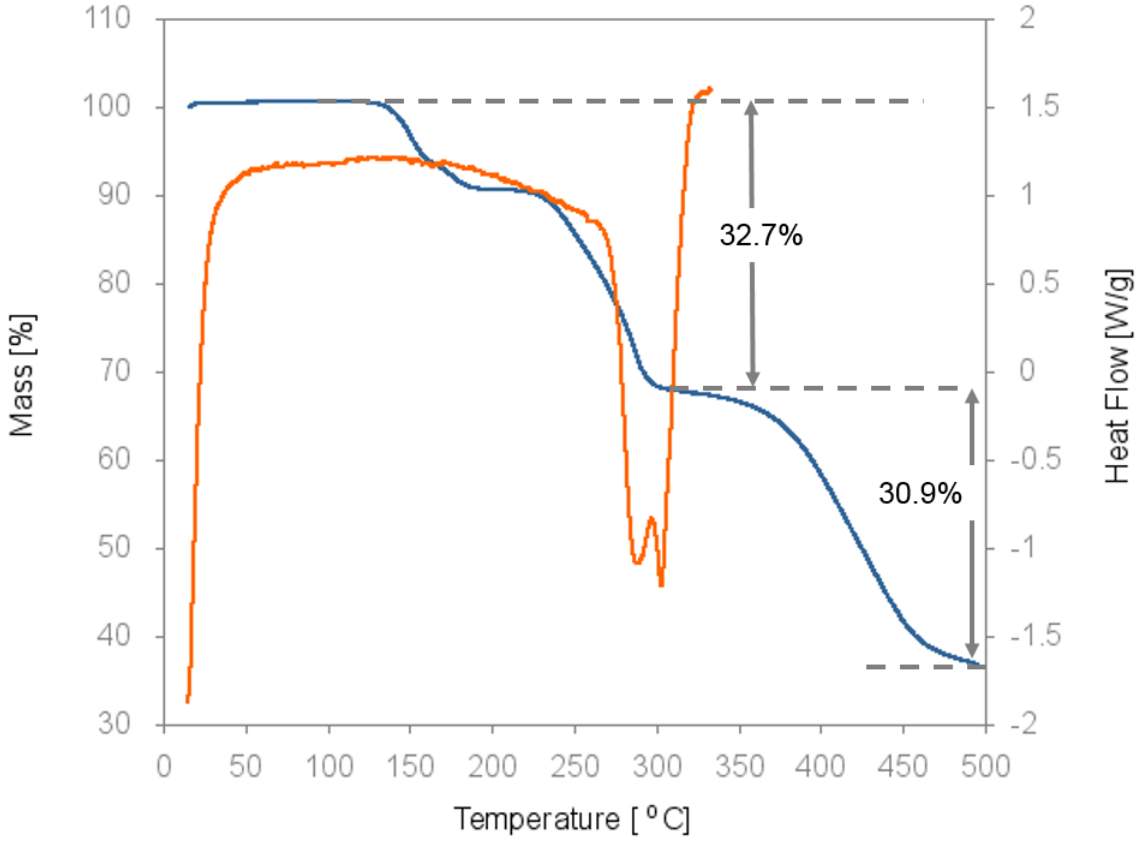

Figure 6.26: The complex multistep loss of acetylacetnoate followed by the partial loss of 2,6-pyridinedicarboxylic acid can be seen in the overlay of TGA and DSC traces of **II**.

Similarly, Figure 6.27 shows complex mass loss (31.2 ± 2.4 %) from 112.7 ± 5.2 °C to 311.6 ± 1.2 °C (n = 3) for **III**. This corresponds to a loss of the acetylacetonate ligand. This is followed by partial loss of the 2,6-pyridinedicarboxylic acid.

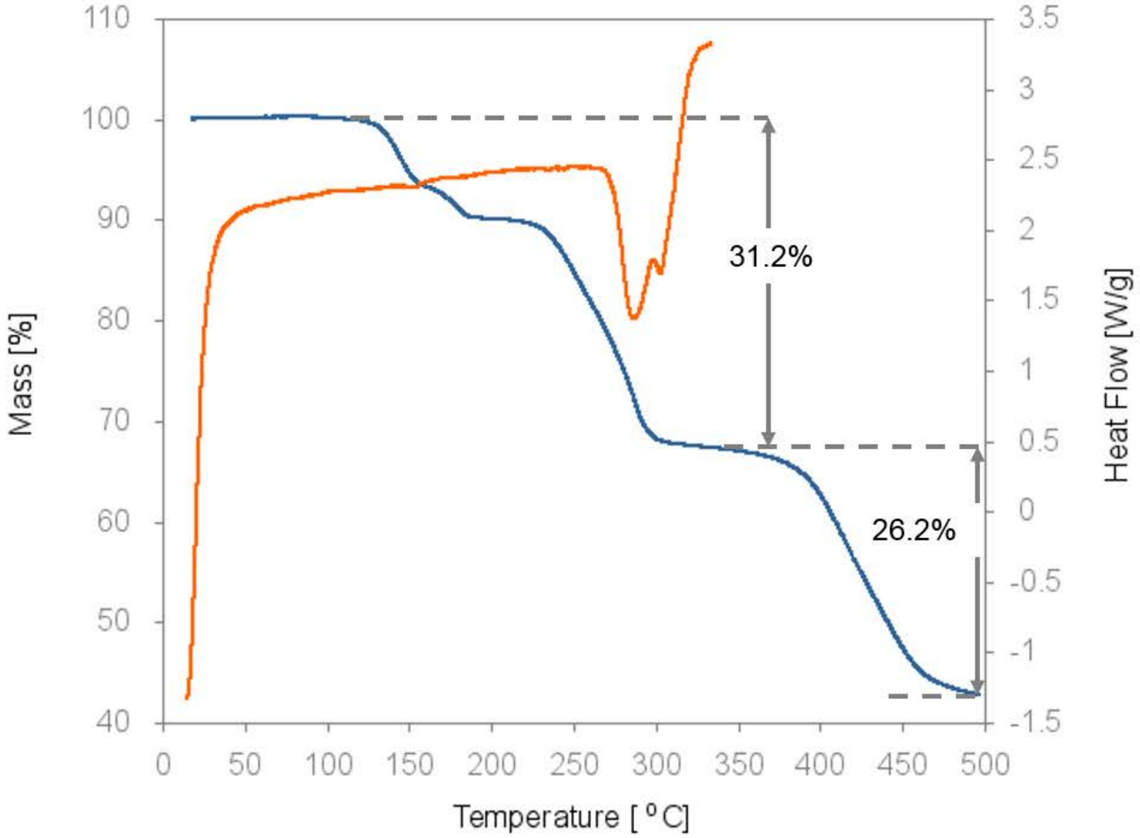

Figure 6.27: Overlay of TGA and DSC traces of **III** showing the complex degradation of acetylacetonate followed by the partial loss of 2,6-pyridinedicarboxylic acid.

6.7 Comparison of crystal structures of II and III

In general the larger the number of hydrogen bonds, the more stable the compound. Kitaigorodskii expressed the principle for closest packing for molecular crystals, 'orientation of molecules in a crystal is conditioned by the shortest distances between the atoms in adjacent molecules'.[164] This implies that the most stable structure will be the one with the most efficient packing. **III** results from crystallisation at elevated temperature for a longer period, and we surmise that the resulting energy allows for the closer packing to emerge. The centres of inversion in **III** result in the tetramers being able to make closer contact than in **II** and more hydrogen bonds are present. The thermal profiles of both complexes are similar (see Section 6.6), which implies that although more hydrogen bonds are favourable, in this case there was no large impact on the thermal stability. This may be the driving force which results in the change in the crystal phases to lower symmetry from **II** to **III** (Figure 6.28).

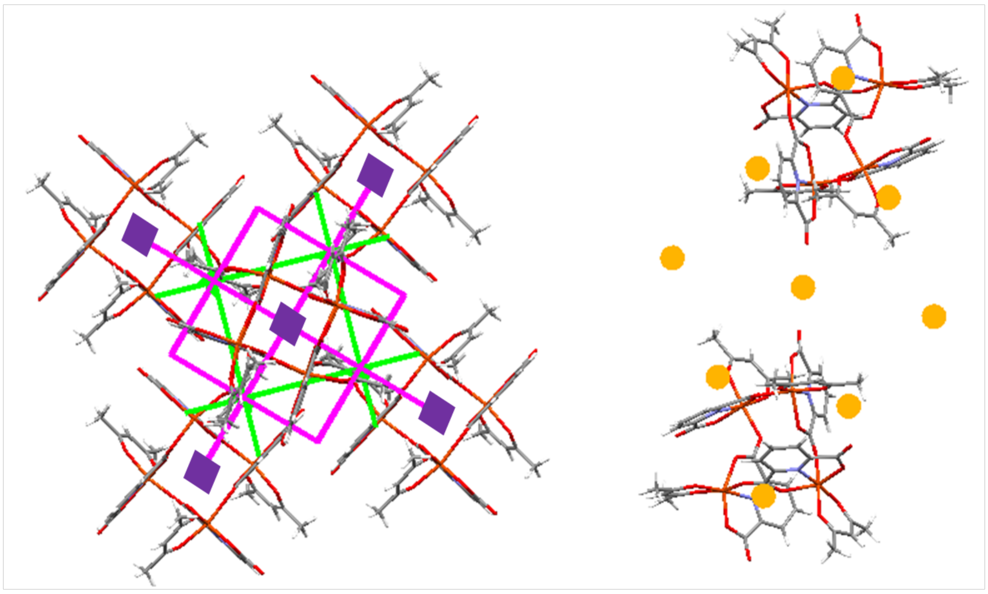

Figure 6.28: Symmetry differences of the crystals grown from iron(III) acetylacetonate and 2,6-pyridinedicarboxylic acid in acetonitrile at 60 °C for (left) **II** and (right) **III**. The centres of inversion as shown as orange circles, 4-fold rotation in purple, 2-fold in green and glides in pink. Both are viewed down the [001] axis.

6.8 Single crystal structure of IV

As is the case with **I**, **II**, and **III**, crystals of **IV** were obtained from studies where the roles of various components in gel formation were investigated.

6.8.1 Synthesis of IV

Pink crystals were obtained during a reaction between cobalt(III) acetylacetonate (0.1 mmol, 36 mg, 1 mL DMA) and 5-nitroisophthalic acid (0.1 mmol, 23 mg, 4 mL DMA) in a vial with a diameter of 2.4 cm at 60 °C.

6.8.2 Unit cell parameters and structure of IV

The unit cell (Table 6.15) matches that of cobalt formate dihydrate, $Co(CHO_2)_2{\cdot}2H_2O$, reported by Kaufman and co-workers.[121] A radical can be generated by the one-electron oxidation of a carboxylate ion, which may lead to decarboxylation.[165] Co(III) is known to perform this type of chemistry and has been used on a number of substrates.[166] During the reaction the 5-nitroisophthalic acid undergoes decarboxylation and the resulting formate ion complexes with the cobalt(II) cation. This unexpected formation of a cobalt formate compound has been reported by H. S. Huh and S. W. Lee[167] where 2,2'-bipyridine-5,5'-dicarboxylic acid was reacted with $Co(NO_3)_2$ under solvothermal conditions in a mixed solvent system of DMF, water and ethanol. Furthermore, decarboxylation of other aromatic carboxylates has been reported by numerous research groups.[168–170]

Table 6.15: Unit cell parameters of Cobalt formate dihydrate and **IV**

	Cobalt formate dihydrate	**IV**
Temperature [K]	293	293
Crystal system	monoclinic	monoclinic
Space group	$P2_1/c$	
a [$\AA$]	8.680(2)	8.70
b [$\AA$]	7.160(2)	7.18
c [$\AA$]	9.272(2)	9.30
$\alpha = \gamma =$ [°]	90	90
$\beta =$ [°]	97.43(2)	97.56
Volume [$\AA^3$]	571.4(3)	576
Z	4	
R	3.8%	

6.9 Single crystal structure of V

Gels were not formed when the acetylacetonate counter ion was used. In order to glean an idea of the porosity and interactions that may occur using the gelators, solvothermal reactions were performed in an attempt to produce crystal using the metal salts with acetylacetonate. A reaction between a cobalt(III) salt and trimesic acid was successful.

6.9.1 Synthesis of V

A solvothermal reaction using cobalt(III) acetylacetonate (26 mg, 7.3 x 10^{-5} mol in 2 mL DMF) and trimesic acid (22 mg, 1.0 x 10^{-4} mol in 3 ml DMF). The solutions were added to an autoclave which was heated in 105 °C oven for 20 h followed by a slow cool (10 °C h^{-1}). The result was pink plate-like crystals with heart shaped trillings of structure **V** (Figure 6.29). Crystals of this shape tend to be twins,[171] and this was indeed the case.

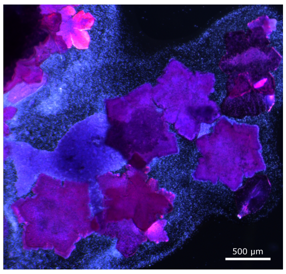

Figure 6.29: Morphology of crystals of **V**.

6.9.2 Data collection and structure refinement of V

A Bruker KAPPA APEX DUO II diffractometer, Mo radiation (λ = 0.7107 Å), was used to collect the intensity data at 173(2) K. The X-ray diffraction pattern was determined to have Laue symmetry of $2/m$, indicating the monoclinic crystal system (Table 6.16). XPREP[98] was used to determine the space group and the $|E^2\text{-}1|$ value of 0.938 indicated centrosymmetry. The crystal was a non-merohedral twin with a BASF factor of 0.2, this was determined using Cell_now.[172] Data scaling and absorption correction were performed using TWINABS,[173] and SAINT[96] was used for integration. The BASF value refined to 0.416 over the course of the structure refinement. The models of the uncoordinated DMF molecules were adjusted so that one has a site occupancy factor of 1 and the other two with a site occupancy factor of 0.5. This resulted in acceptable refinements with high residual peaks in the vicinity of the guests.

Table 6.16: Crystal data of **V**

Molecular formula	$3[\mathrm{Co(C_9H_3O_8)(C_3H_6NO)_2\cdot\frac{2}{3}(C_3H_6NO)}]$
Molecular mass [g mol^{-1}]	1382.90
Crystal system	Monoclinic
Space group	$P2_1/n$
Unit cell parameters	
a [Å]	16.6748(18)
b [Å]	14.1341(16)
c [Å]	28.845(3)
β [°]	89.974(2)
Volume [Å^3]	6798.3(13)
Z	4
Density$_{calcd.}$ [g cm^{-3}]	1.351
μ [MoKα] [mm^{-1}]	0.804
F (*000*)	2864
Temperature [K]	173(2)
Crystal size [mm]	0.020 x 0.130 x 0.220
Range scanned θ [°]	1.410 to 26.500
Index range	h: -20 20 ; k: 0 17 ; l: 0 36
ϕ and ω scan angles [°]	0.5
Dx [mm]	55
Total number of reflections	13515
Number of independent reflections	13515
Number of reflections with I > 2σ(I)	8940
Final R indices [I > 2σ(I)]	$R_1 = 0.0898, wR_2 = 0.2455$
R indices (all data)	$R_1 = 0.1368$, $wR_2 = 0.2768$
S	1.047
Number of parameters	783
Number of reflections omitted	6
Parameters a, b in $w = 1/[\sigma^2(F_0{}^2)+(aP)^2+(bP)]$	a = 0.1222; b = 39.7435
$(\delta/\sigma)_{mean}$	<0.001
$\Delta\rho$ excursions [e.Å^3]	2.200 and -0.746

6.9.3 Structure of V

Figure 6.30 shows the asymmetric unit of **V** which consists of three cobalt(III) metal centres, three deprotonated trimesic acid ligands, and eight *N*,*N*-dimethylformamide (DMF) molecules. Each Co(III) ion is coordinated to five different ligands: two DMF molecules occupy the axial position and three deprotonated trimesic acid ligands, two through a η^1 mode of binding and the third through a chelating η^2 mode, in the equatorial position. The Co(III) ions are bridged by a deprotonated trimesic acid along [100]. Two DMF molecules are present as solvent in the asymmetric unit of **V**, while three are shown, two are only present half of the time.
The bond lengths and angles for the coordination to the Co(III) are given in Table 6.17. These bond lengths are within the typical range of these types of bonds, 2.103 Å and 2.0337 Å for Co-O terminal and chelated carboxylates respectively.[174] The metal centres all display a distorted octahedral geometry with bond lengths and angles within the expected ranges and none of the trimesic acid ligands exhibit ring puckering.

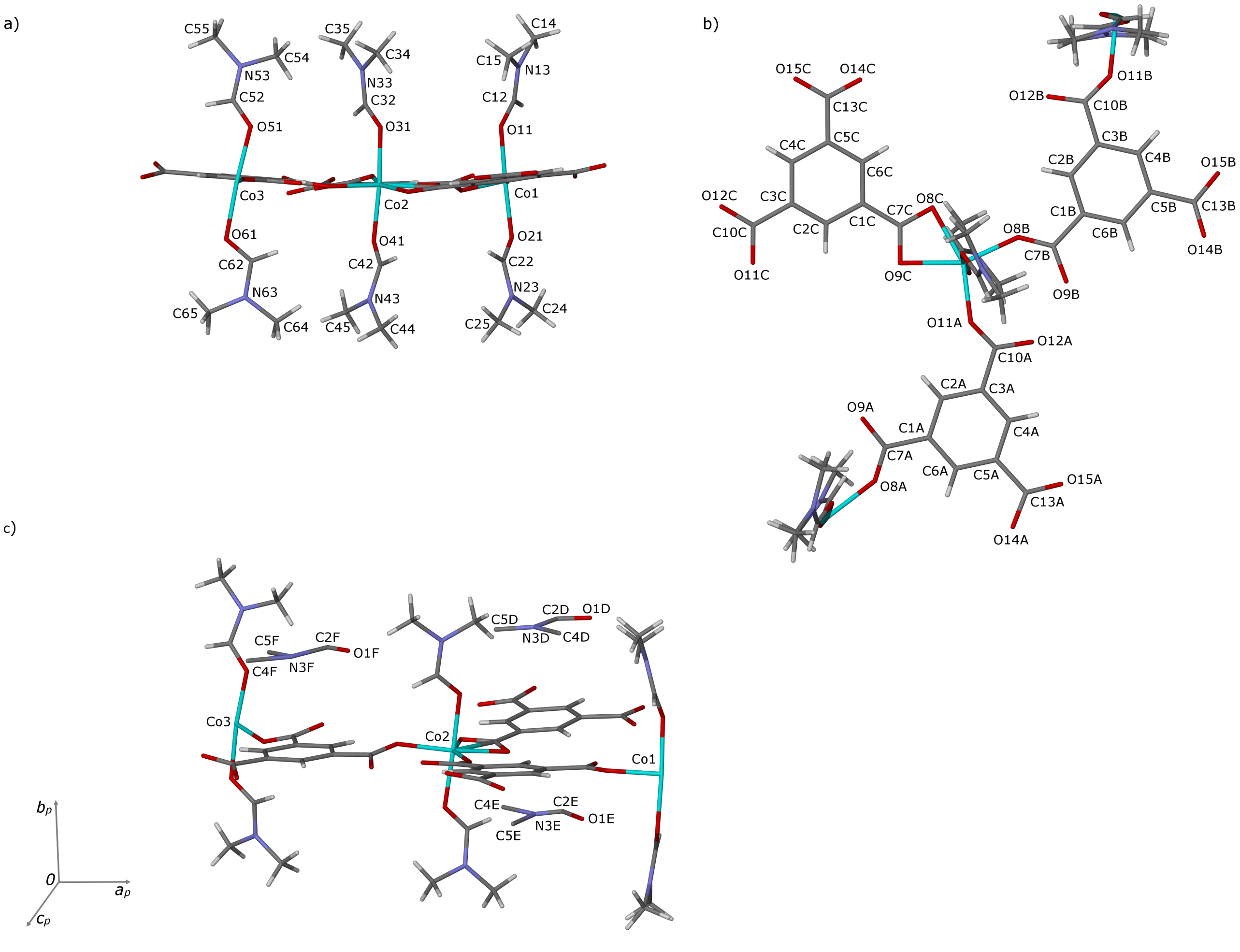

Figure 6.30: Asymmetric unit of **V** viewed along a) [100] and b) [010], the DMF solvent molecules have been omitted for clarity. c) The positioning of the DMF solvent molecules within the asymmetric unit. Three different views are given to allow for labelling of the symmetric unit with minimal atom overlap.

Table 6.17: Coordination geometry of the ligands to the metal centres of **V**

Bond	**Angle** [°]	**Bond**	**Angle** [°]
Co1−O8A	2.058(5)	O8A−Co1−O11	88.3(2)
Co1−O11	2.052(6)	O8A−Co1−O21	90.1(2)
Co1−O21	2.117(6)	O11−Co1−O21	174.0(3)
Co2−O8B	2.053(6)	O8B−Co2−O8C	94.3(2)
Co2−O8C	2.153(5)	O8B−Co2−O11A	107.7(2)
Co2−O9C	2.142(6)	O9C−Co2−O8C	61.3(2)
Co2−O11A	2.059(7)	O9C−Co2−O11A	96.7(2)
Co2−O31	2.120(6)	O31−Co2−O41	175.3(3)
Co2−O41	2.103(7)		
Co3−O61	2.119(7)	O11B−Co3−O51	87.2(3)
Co3−O51	2.079(7)	O11B−Co3−O61	98.1(3)
Co3−O11B	2.057(7)	O51−Co3−O61	175.1(3)

6.9.4 Hydrogen bonding and packing of V

Table 6.18 gives the hydrogen bond distances and angles for **V**. Fourteen hydrogen bonds are present, all of which are carbon-hydrogen to oxygen type hydrogen bonds. Three distinct types of hydrogen bond can be seen in the structure (Figure 6.31). Five of these are intramolecular, two of which are intramolecular within one layer. The third is from the axially bound DMF in one layer to the carboxylate oxygen atoms in subsequent layers. The intramolecular hydrogen bonds 1 - 5 result in 5-membered rings between the coordinated DMF and the oxygen atom from the carboxylate of the trimesic acid ligand. 5-membered rings are favourable as there is little steric strain. The uncoordinated DMF solvent molecule is held in place by hydrogen bond 6.

Table 6.18: Summary of hydrogen bond lengths and angles for **V**

Number	**Hydrogen bond**	**D−H*** [Å]	**H···A*** [Å]	**D···A** [Å]	**D−H···A*** [°]	**Symmetry Operation**
1	C22−H22···O8A	0.95	2.50	3.068(10)	118	
2	C32−H32···O11A	0.95	2.47	3.051(11)	119	
3	C42−H42···O8C	0.95	2.57	3.191(11)	124	
4	C52−H52···O11C	0.95	2.60	3.219(14)	123	$\frac{1}{2}+x$, $\frac{3}{2}$-y, $\frac{1}{2}+z$
5	C62−H6···O15A	0.95	2.47	3.029(11)	118	*1+x*, *y*, *z*
6	C14−H141···O1D	0.98	2.51	3.47(2)	164	*-1+x*, *y*, z
7	C24−H242···O15C	0.98	2.57	3.444(15)	149	*1-x*, *1-y*, *-z*
8	C25−H251···O12C	0.98	2.47	3.345(15)	148	*1-x*, *1-y*, *-z*
9	C25−H252···O12A	0.98	2.60	3.565(15)	170	$\frac{1}{2}$-x, $-\frac{1}{2}+y$, $\frac{1}{2}$-z
10	C35−H352···O14C	0.98	2.58	3.421(15)	143	$\frac{3}{2}$-x, $\frac{1}{2}+y$, $\frac{1}{2}$-z
11	C44−H442···O12B	0.98	2.50	3.434(15)	161	$\frac{3}{2}$-x, $-\frac{1}{2}+y$, $\frac{1}{2}$-z
12	C44−H443···O8C	0.98	2.56	3.377(14)	141	$\frac{3}{2}$-x, $-\frac{1}{2}+y$, $\frac{1}{2}$-z
13	C64−H643···O9C	0.98	2.48	3.267(16)	137	$\frac{3}{2}$-x, $-\frac{1}{2}+y$, $\frac{1}{2}$-z
14	C65−H653···O11C	0.98	2.52	3.411(14)	151	$\frac{3}{2}$-x, $-\frac{1}{2}$+y, $\frac{1}{2}$-z

*e.s.d values not calculated as hydrogen atoms were placed in geometrically idealised positions.

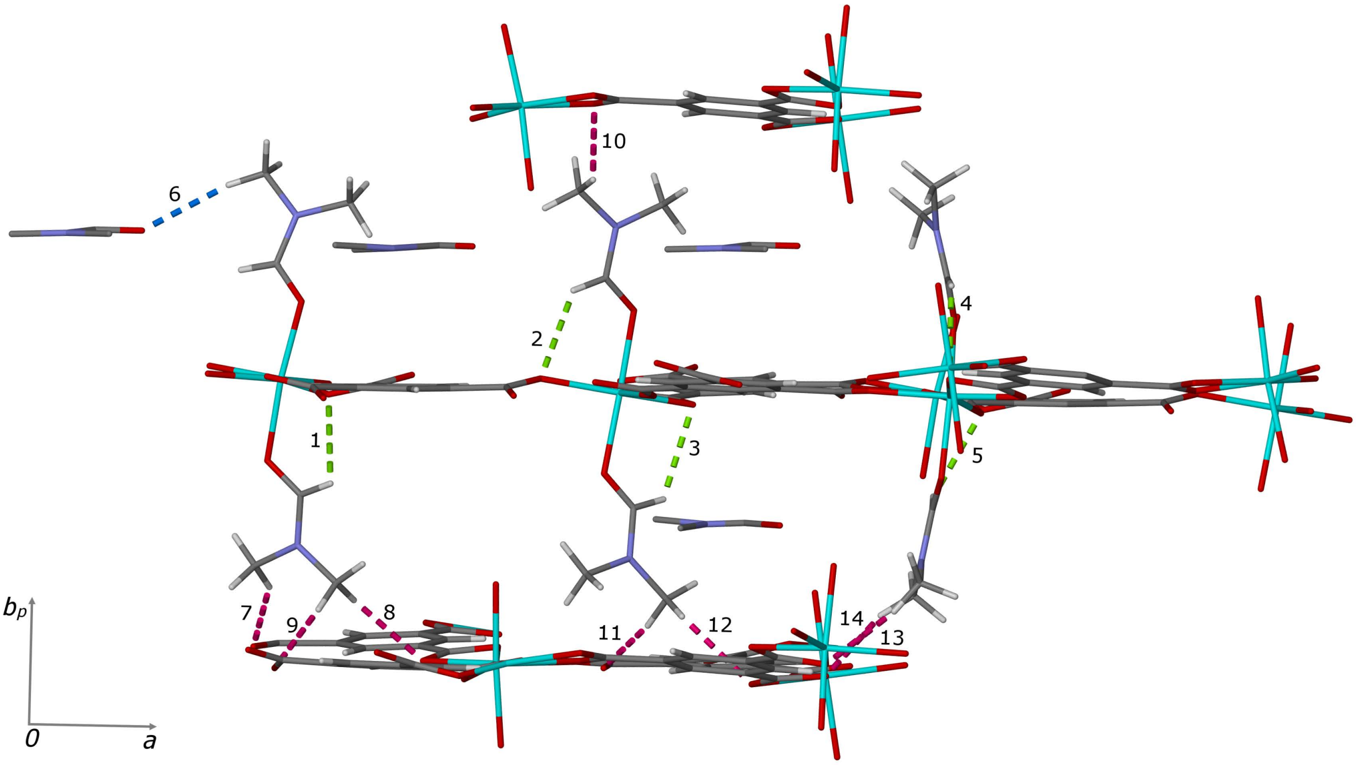

Figure 6.31: Hydrogen bonding in **V**. The three types found within the structure are coloured, blue shows the hydrogen bond (6) between the coordinated DMF and the solvent DMF, green the intramolecular hydrogen bond (1 - 5) from the coordinated DMF to the carboxylate oxygen, and pink the hydrogen bonds (7 - 14) between the axially bound DMF molecules to the carboxylate oxygen atoms of subsequent layers. The numbers correspond to those given in Table 6.17.

The resulting packing of the coordination polymer consists of interdigitated sheets along the [100] and [001] axes, stabilised by hydrogen bonds 7 - 14 (figure 6.32). The uncoordinated DMF molecules are found in the channels formed between the layers along the [001] axis. The phenyl ring overlap is seen down [010].

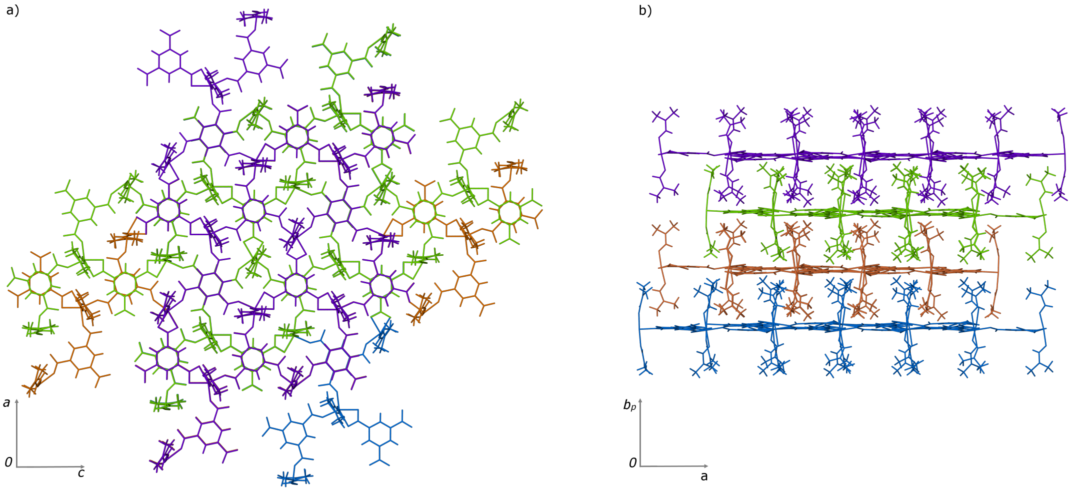

Figure 6.32: Packing of **V**, viewed down a) [010] and b) [001]. The interdigitated layers propagate along [100] and [001]. The unbound DMF solvent has been omitted for clarity.

There is a large amount of potential void space present in this coordination polymer, should the uncoordinated solvent be removed and the structural identity of **V** be retained. Using Mercury v3.7[101] potential void space was calculated using a probe radius 1.2 Å with approximate grid spacing of 0.7 Å, this resulted in a contact surface area of 1525 Å^3 (22.4% of unit cell volume). The cavities extend parallel to [001] and run in a zig-zag pattern. The uncoordinated DMF solvent molecules are found in these cavities.

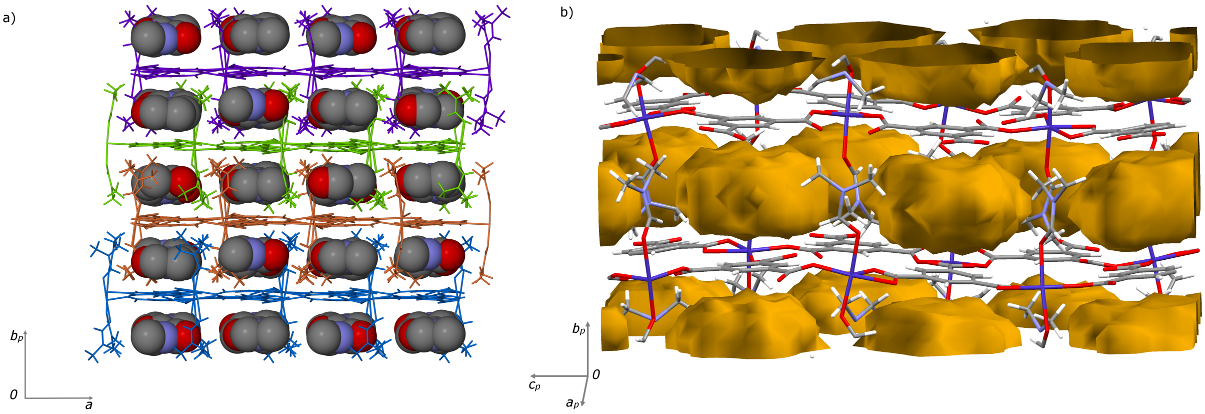

Figure 6.33: a) The DMF solvent molecules, in space-fill display, are in the channels formed between layers along the [001] axis. b) Calculated cavities which stack one above the other parallel to [010] and form a zig-zag pattern parallel to [001].

6.9.5 Powder X-ray diffraction of V

Figure 6.34 shows the PXRD patterns of the calculated and experimental of **V** as well as the starting materials. The experimental pattern is not a sum of the patterns of the starting materials, indicating a new phase has been formed. The reasonable agreement between the calculated and experimentally obtained patterns shows the homogeneity of the bulk material.

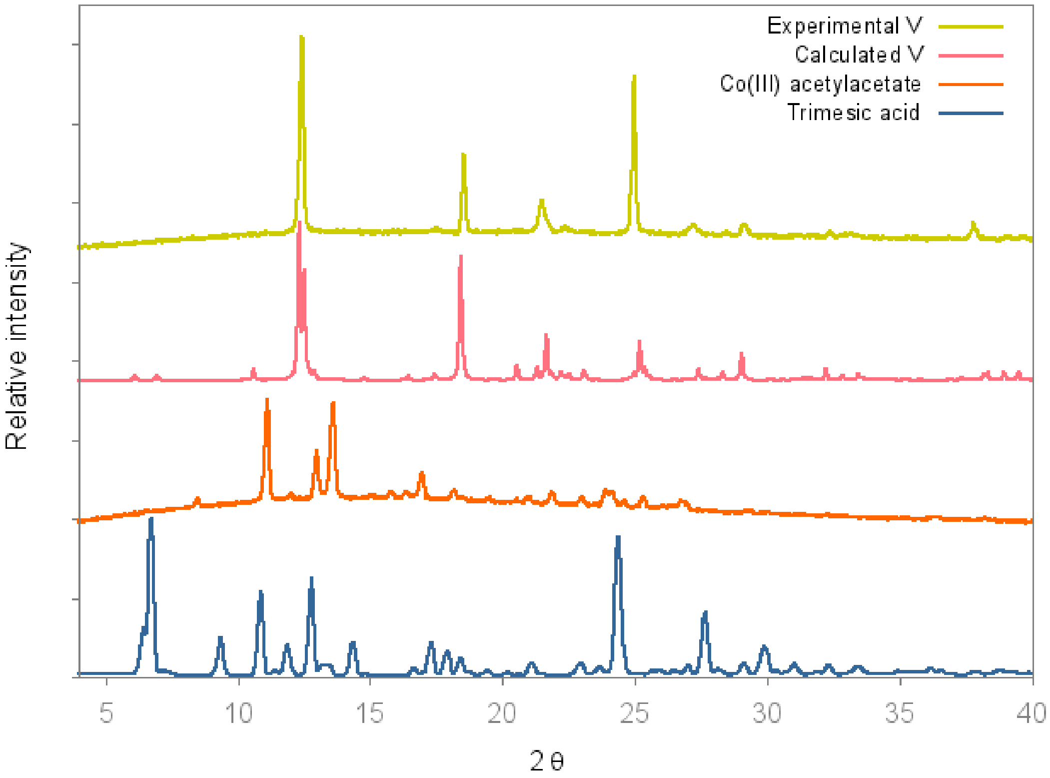

Figure 6.34: PXRD patterns of cobalt(III) acetyl acetate, trimesic acid and the calculated and experimental patterns of **V**. A new phase is present.

6.9.5.1 Variable temperature powder X-ray diffraction of V

Variable temperature PXRD was performed on **V**. Crystallinity was lost after 75 °C (Figure 6.35) with the removal of the DMF molecules, and there is very little change to the pattern upon heating to 275 °C to cooling to 25 °C. The collapse of crystallinity corresponds to the onset of loss of DMF from the material as seen in the thermal analysis, Section 6.9.6. The DMF molecules are instrumental to the retention of the crystalline structure.

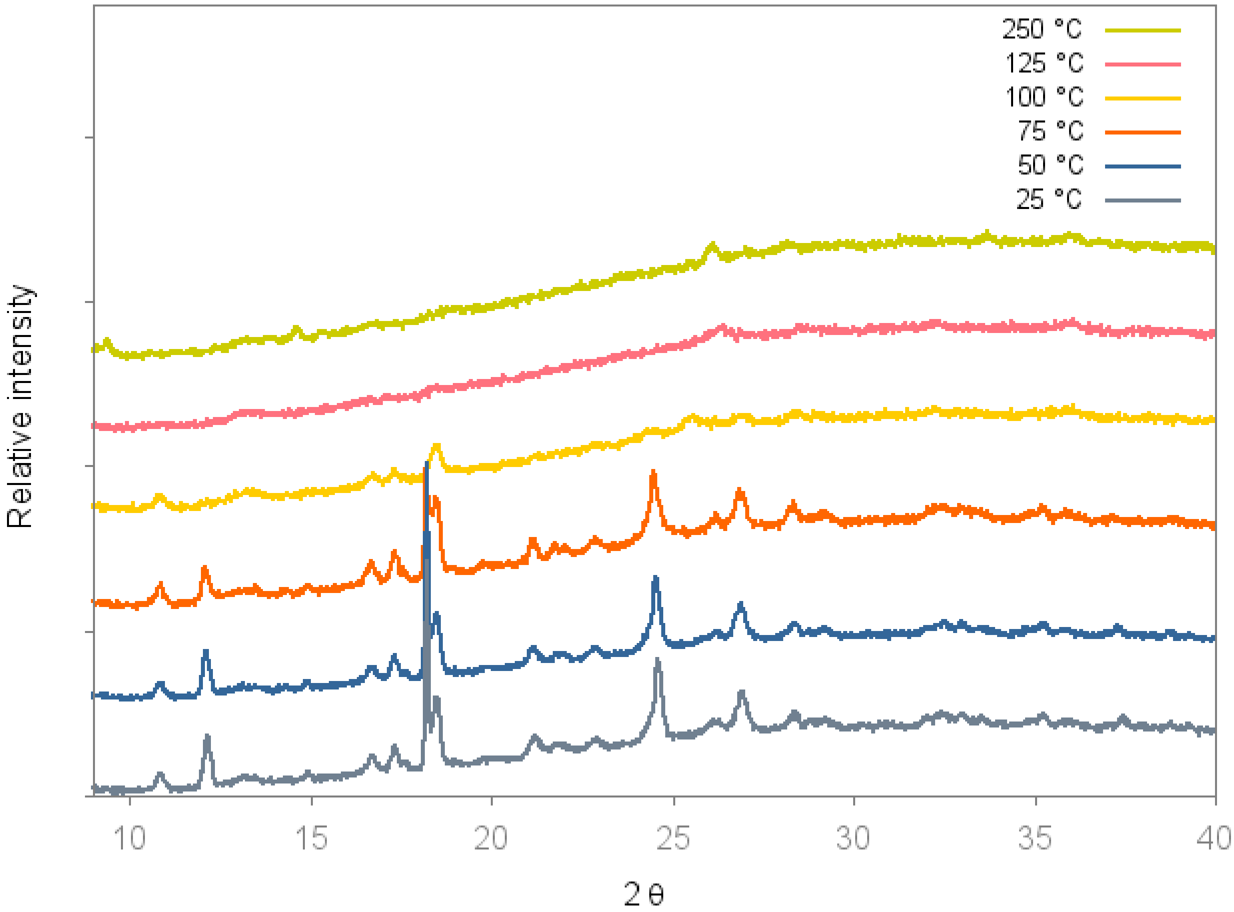

Figure 6.35: Variable temperature PXRD patterns of **V** from 25 °C to 125 °C, after which the pattern is unchanged. Crystallinity is lost after 75 °C as the DMF solvent has been removed.

6.9.6 Thermal analysis of V

Figure 6.36 shows the hot-stage microscopy results of **V**. The pink crystals darken upon heating and are purple by 200 °C as solvent is lost. This colour change may be attributed to a change in the geometry of the Co(III) metal centre from octahedral to tetrahedral as the axial coordinated DMF are removed.[175] Bubbling starts at 200 °C and the crystal turn opaque once bubbling has stopped. The material continues to darken and is black at 400 °C. The overall shape of the crystals are maintained, however hairline cracks can be seen as the material is heated.

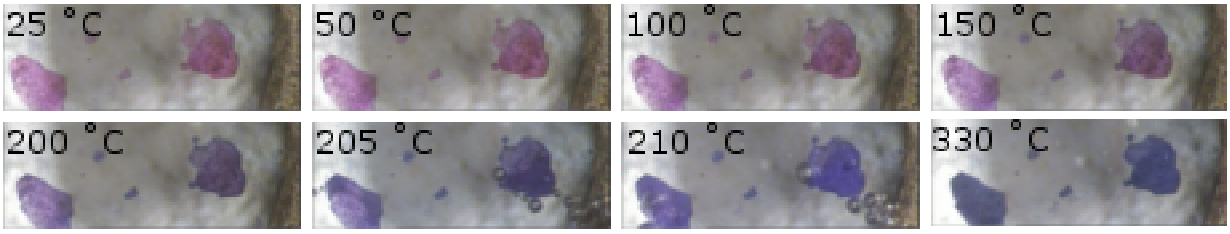

Figure 6.36: Hot stage images of **V**. The crystals darken from pink to purple upon heating. All solvent has been lost after 220 °C.

Figure 6.37 shows the TGA trace of **V** showing a three step mass loss of 40.8 ± 0.8% between 88.6 ± 2.7 °C and 248.0 ± 0.6 °C (n = 3) (Table 6.19). This corresponds to the loss of the eight DMF molecules present in the crystal structure. The first step is most likely the loss of DMF in the channels, followed by the loss of the coordinated DMF molecules as more energy is required to remove them. The subsequent loss of 31.4 ± 0.3% between 343.81 ± 2.2 °C and 495.1 ± 0.7 °C is the loss of the trimesic acid ligand as the material begins to decompose.

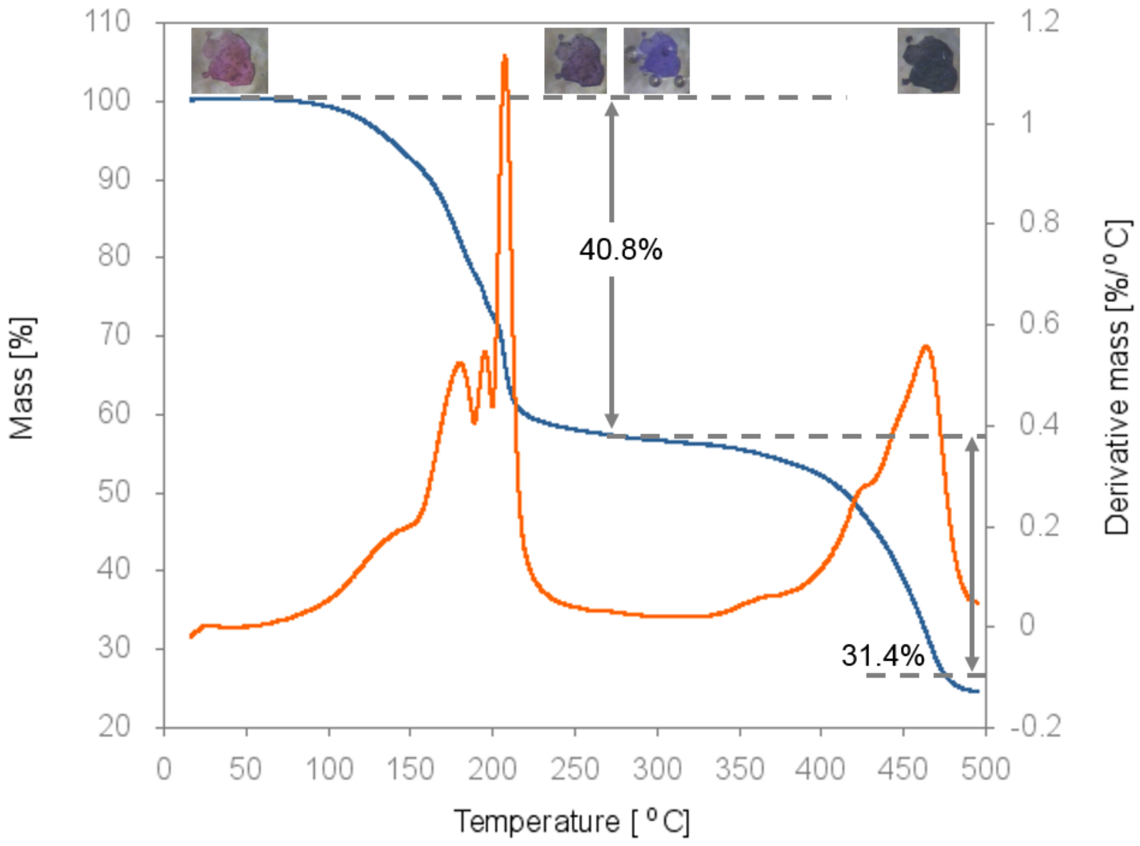

Figure 6.37: Overlay of TGA and first derivative plots of **V**. Showing a three step mass loss of the uncoordinated and coordinated DMF.

Table 6.19: Theoretical and experimentally obtained mass losses of **V**. The components are given in the order in which they are lost

Component	**Mass loss [%] (calculated)**	**Mass loss [%] (observed)**
DMF	5.3	
8 DMF	42.4	40.8 ± 0.8
Trimesic acid	44.9	31.4 ± 0.3
Cobalt	12.8	

Figure 6.38 show the differential scanning calorimetry (DSC) trace of **V**, there is an enthalpy of 388.1 ± 9.7 J/g between 203.0 ± 3.6 °C and 208.3 ± 0.1 °C (n = 4) associated with the loss of DMF molecules. The shoulder indicating the uncoordinated DMF molecules come off first, followed by the coordinated DMF.

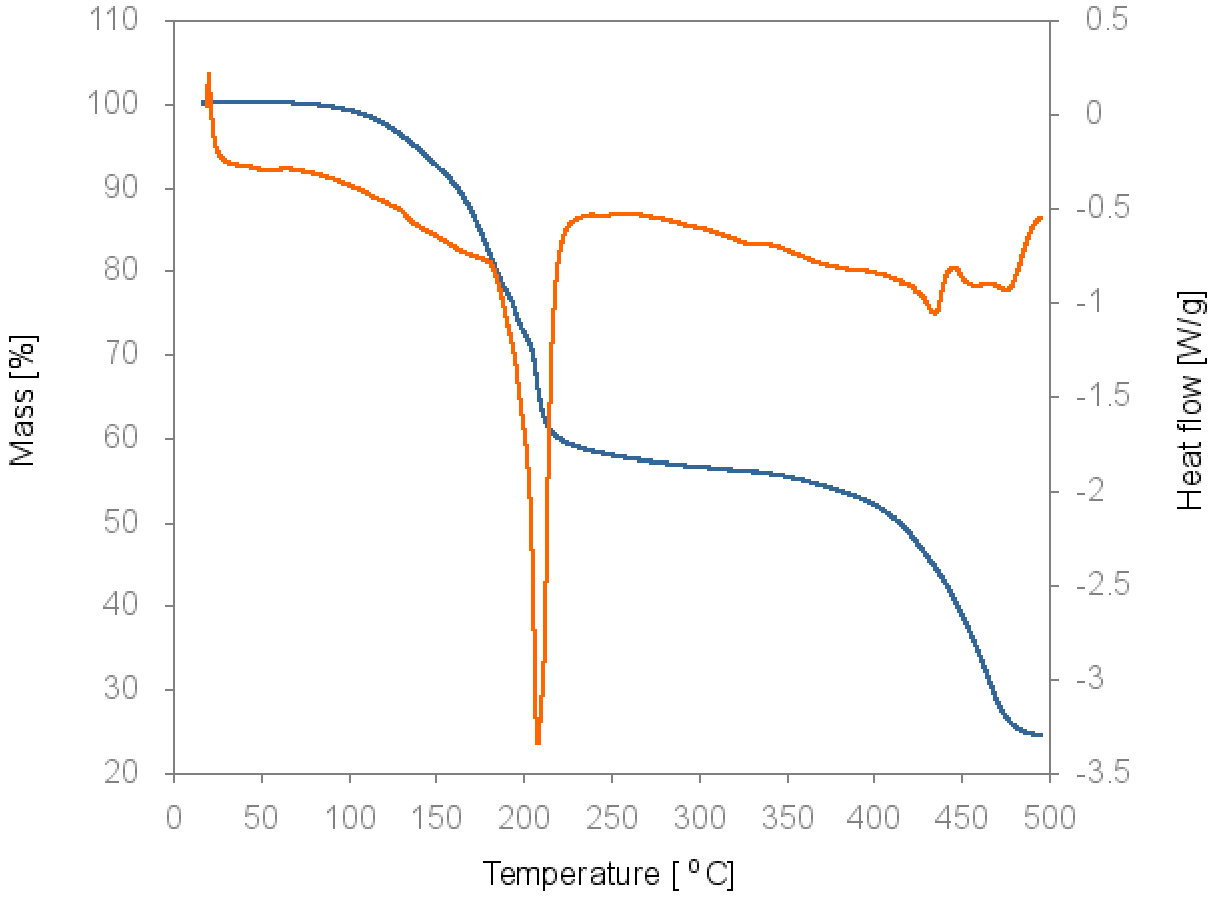

Figure 6.38: Overlay of TGA and DSC plots of **V**. The endothermic peak at 208 °C corresponds to the loss of DMF.

6.10 Conclusion

Crystals **I**, **II**, **III**, and **IV** were obtained during systematic studies to explore the factors which influence gel formation. Four novel crystal structures have been elucidated, **I**, **II**, **III**, and **V**.

Structures **I**, **II**, and **III** were synthesised under the same conditions used for gel formation experiments. Each of these has the same starting materials, but different reaction conditions. Two crystallise in a triclinic space group, $P\bar{1}$ and the third (**II**) in tetragonal, $P\bar{4}2_1c$. All three had the same morphology of red block-like crystals. There are many factors which play a role in the outcome of crystallisations. Temperature has been shown to impact the density of the crystal, with those formed at higher temperatures having a higher density. **I** which was formed at room temperature has a density of 1.551 g cm^{-3}, and **II** and **III**, formed at 60 °C have densities of 1.617 g cm^{-3} and 1.623 g cm^{-3} respectively. In the latter case, it was temperature and time which contributed to the compounds obtained.

V was formed solvothermally during experiments to produce crystals to glean information about the possible interactions within a gel. The pink crystals of the coordination polymer crystallise in the monoclinic space group, $P2_1/n$. There are large cavities in the structure which encapsulate the solvent molecules. The DMF molecules play a stabilising role in the structure, this is seen in the loss of crystallinity once these molecules are removed. These stabilising interaction between solvent and metal complex are also involved in gel formation.

The organic counterion promotes crystal growth rather than gelation. As the non-labile organic counter ion results in greater long range order through the sample. Naked cation formed by the removal of inorganic counterions give less ordered interactions and hence less long range order is present. Resulting in gelation instead of crystal growth. Hydrogen bonding plays a key role in stabilising these structures as well as supramolecular gels.

Chapter 7

Conclusion

7.1 Summary

The influence of various components such as the counter anion in the metal salt, solvent, temperature, as well as the nature of the organic ligand have been explored in this work. It is clear that multiple features must be taken into account when designing gels. The gels obtained have been shown to be responsive to external stimuli, including the ability to take up dyes and gases.

7.1.1 Formation and characterisation

Systematic investigation into the role of various components in gel formation were performed. It was found that multiple factors influence gel formation. The greatest number of gels were formed using ligands trimesic acid, 3,5-pyridinedicarboxylic acid, and 5-nitroisophthalic acid. The first two ligands are tridenate and provide multiple metal-ligand coordination sites which may result in extended three-dimensional networks capable of immobilising large quantities of solvent. The nitro moiety on the 5-nitroisophthalic acid provides a great deal of stabilisation, potentially through hydrogen bonding and electrostatic interactions, to iron(III) metallogels. This group is probably involved in hydrogen bonding and electrostatic interactions.

Gelation only occurs when inorganic counterions are used and gels did not form when metal salts of acetylacetonate and oxalate were used. Organic counterions are less labile than their inorganic counterparts (such as nitrate, bromide, and chloride), and it is plausible that fewer Fe(III) ions are available for gel formation.

The role of solvent in gel formation is highly complex and case specific. Of the solvents investigated for this system, only those with polarities between 4 and 7.2 resulted in gel formation.

Furthermore, an increase in temperature led to a decrease in gel formation time, provided the solvent did not evaporate before gelation could occur.

A summary of the gels formed in the study can be seen in Table 7.1.1. There are thirteen possible gels for each ligand/metal salt combination, none of the combinations resulted in the formation of all thirteen.

Table 7.1: Summary of gel formation. No gels were formed using Co-acac, Fe-acac, and Fe-ox.

Ligand	**Solvent**	**Fe**	**Fe-sul**	**FeBr$_3$**	**FeCl$_3$**	**Al**
tri	DMF	RT/60/90	none	RT/90		RT/90
	EtOH	RT/60/90		T/60	60	
	DMA	RT/60/90				90
5nite	MeCN	60	none			none
	DMF	RT/60/90		RT/60/90	RT/60/90	
	EtOH	RT/60		RT/60		
	DMA	RT/60/90		RT/60/90	RT/60/90	
	DMSO	RT		RT		
35pca	DMF	RT/60/90	RT	RT/60/90	RT/90	RT/90
	EtOH	RT/60/90		RT/60	60	60
	DMA	RT/60/90		RT/60/90	RT/60/90	90
26pca		none	none	none	none	none
25pca		none	none	none	none	none
terept	DMA	RT	none	none	none	60/90
iso	DMF	RT/60/90	none	60	60	
	EtOH	RT/60				
	DMA	RT/60/90		RT/60	RT/60	90
1245btc	DMF	RT/60/90	none	RT/90	none	RT/90
	EtOH	RT/60				
	DMA	60/90				90
phens	EtOH	RT/60/90	none	RT	none	none

RT refers to room temperature, temperatures are reported in °C. These are the temperatures at which the gels were synthesised.

Thermal analysis of the gels indicates they all comprised of a very large volume of solvent, *ca.* 95-99% in most cases. Cooling the gel sample using differential scanning calorimetry gave freezing temperatures of the solvent within the gel pockets. In all cases a suppression of the freezing point was seen. The freezing points of acetonitrile and DMA are -45 °C and -20 °C, respectively. Fe-5nite-MeCN had an event at a temperature of -59.42 ± 1.8 °C (n = 3). Similarly for Fe-5nite-DMA, this occurred at a temperature of -55.71 ± 1.3 °C (n = 3). A freezing event was not seen for Fe-5nite-DMF, DMF has a freezing point of $-60\,°\mathrm{C}$ and the DSC has a lower limit of $-90\,°\mathrm{C}$. We assumed that this event may have occurred beyond the limits of the equipment. The DSC traces also show the gels have a glass transition when cooled to -90 °C.

The scanning electron microscope images show blocks, rather than fibres, which are glassy in appearance. The crystal structures from components used tend to form three-dimensional blocks rather than needles. Perhaps this has an impact on the gel morphology. This seems to be corroborated by the novel structures obtained during this study, all of which formed block-like crystals. However, Fe-5nite-EtOH had a spongy appearance along a break in the surface. This material was therefore selected for gas sorption studies.

Powder X-ray diffraction of the xerogels shows no long range order is present and this does not change when the xerogel is submitted to an increase in temperature.

Viscosity studies identified shear thinning materials. This behaviour can be attributed to the alignment of the gel fibres when stress is applied.[37] Thixotropy experiments showed Fe-5nite-DMF reformed after one hour following stress while Fe-5nite-EtOH did not reform after 24 h. These results suggest that the non-covalent interactions in the DMF gel are stronger than those of its ethanol counter part.

The response to temperature of three gels, Fe-tri-DMF, Fe-5nite-DMF, and $FeBr_3$-5nite-DMF, was tested. These gels are stable at -4 °C and room temperature. At 120 °C the gels visibly shrink, and no longer immobilise the same amount of solvent. It is possible that the increased temperature resulted in a partial collapse of the gel pores and less solvent is trapped.

$PdCl_2$ was used in an attempt to convert the gels Fe-5nite-DMF and Fe-tri-DMF to metal organic frameworks. Fe-5nite-DMF could not be degraded using $PdCl_2$. The non-covalent interactions involving the nitro moiety results in greater stability of Fe-5nite-DMF when compared to Fe-tri-DMF. Fe-tri-DMF was converted and very small crystals where obtained. The structure of a three dimensional metal organic framework was elucidated. Despite multiple collections the data remained poor, however it was possible to determine the connectivity within the structure. This was different to the structure elucidated by Banerjee *et al.*[125] Gels lack long range order, and the use of $PdCl_2$ to degrade the material may force the system into a thermodynamic energy well. Different crystalline structures with similar energies may be possible as it is probable that a number of such wells exist.

7.1.2 Response to stimuli

Fe-tri-DMF and Fe-5nite-DMF are both able to sorb methyl orange and bromocresol green dyes from a DMF solution. At least 27% of the methyl orange and 79% of the bromocresol green in solutions were sorbed. More bromocresol green is sorbed in both cases indicating halogen bonding plays a role in this mechanism. Halogen bonding is only possible in the case of bromocresol green as the bromine of the dye ions may be able to form halogen bonds with the oxygen atoms from the carboxylic acids present in the gel network.

Gas sorption was performed on xerogels of Fe-5nite-EtOH both freeze and oven dried, Fe-tri-EtOH both freeze and oven dried, Fe-tri-DMF oven dried, and Fe-5nite-DMF oven dried. The drying method influences the structure and in general, the freeze dried materials have larger BET surface than their oven dried counter parts. Oven drying appears to collapse the gel pockets to a greater extent than freeze drying. None of the materials sorbed hydrogen. N_2, CO_2 and water vapour were also used. Water vapour was adsorbed in the greatest quantity in all cases. This is a result of the hydrogen bonding interactions between the water vapour and the xerogel.

A gel formed using the chiral ligand phenylsuccinic acid was tested for separation of 2- and 3-methylpiperidine. No separation took place as the gel was degraded once the compounds to be separated were loaded. The methylpiperidines may disrupt the stabilising interactions within the gel, resulting in degradation. Similar results were obtained for Fe-5nite-EtOH and Fe-tri-EtOH. These materials should not be ruled out for separation applications, molecules which are less likely to attack the carboxylic acids groups should also be tested.

7.1.3 Crystals of similar components

The gel formation experiments using iron(III) acetylacetonate and 2,6-pyridinedicarboxylate in acetonitrile did not result in gel formation. However, crystals from these components were obtained during these experiments. Three different crystal structures (**I**, **II**, and **III**) were elucidated. The structure obtained is dependent on the temperature and length of time of reaction. **I** was grown on the bench top at room temperature for 18 h. **II** and **III** were isolated after two hours and 24 h at 60 °C respectively. Two structures **I** and **II**, crystallise in the triclinic space group, $P\bar{1}$ and the third (**II**) in the tetragonal space, $P\bar{4}2_1c$.

The Fe(III) metal centre is coordinated in a distorted octahedral fashion in all three structures **I**, **II**, and **III** and none of the coordinated ligands exhibit ring puckering. Both 2,6-pyridinedicarboxylate and acetylacetonate ligands are coordinated in all three structures. The asymmetric unit of **I** also contains a coordinated water molecule and an uncoordinated acetonitrile solvent molecule.

Structures **II** and **III** have similar connectivities of the ligands. Each unit, made up of a coordinated iron(III) is linked by an oxygen atom from the 2,6-pyridinedicarboxylate ligand. However **II** was found to have higher symmetry. A greater number of hydrogen bonds are present in **III**. This increase in hydrogen bonds, and hence stability, may the driving force for the change in the crystal structure over time.

To better understand the possible porosity and interactions between their components within the gels, metal salts with organic counterions were used in solvothermal reactions. One such reaction using cobalt(III) acetylacetonate and trimesic acid resulted in pink crystals of **V**, a coordination polymer. The asymmetric unit consists of three cobalt(III) metal centres, three deprotonated trimesic acid ligands, and eight *N*,*N*-dimethylformamide molecules. **V** crystallises in the monoclinic space group $P2_1/n$. This is a two dimensional structure where the DMF molecules are found between the sheets and interacts with the Co(III) trimesic acid network *via* hydrogen bonding. Similar interactions occur between the gelator and the solvent within a gel network.

All of these crystals were grown using metal salts with an organic counterion, acetylacetonate. The non-labile organic counter ion results in greater long range order through the sample and crystallisation rather than gelation is favoured.

7.2 Closing remarks

These interesting materials are influenced by a number of factors: the metal salt, solvent, temperature, as well as the nature of the organic ligand. Because of this, these materials are highly tunable. Gel formation is a multi-component process. A better understanding of the role of various factors in gel formation and hence tuneability of gels will lead to the reliable design and production of materials for a specific purpose. Additional features such as, reusability and selectivity, may be incorporated. Multiple techniques need to be employed in order to gain in depth knowledge into the structure and characteristics of supramolecular gels. The preparation of these highly variable materials needs to be performed conscientiously to ensure reproducibility.

Chapter 8

Future work

The primary objectives were achieved; however, this project could be extended in a myriad of interesting ways.
To further explore the role of the metal ion in gel formation other metals could be used such as ruthenium and osmium salts, which are d^5 transition metals but have slower kinetics than iron. The role of kinetics of the metal cation which influences the formation of gels should be investigated.

Preliminary studies show that chromium acetylacetonate does not result in gel formation with the ligands 5-nitroisophthalic acid, trimesic acid, and 3,5-pyridinedicarboxylic acid. This was not unexpected since similar results were obtained when iron(III) acetylacetonate was used. Salts with other anions, such as chloride and nitrate, should be explored.

During the course of this study, it became evident that the amount of water present in the solvent might play a role in gel formation. The postulation is that gelation could be prevented by larger concentrations of hydrated iron oxide species, which remove Fe(III) ions from availability for gelation. An experiment to investigate this would involve increasing the water content in the solvent, starting with completely anhydrous starting material, until gel formation no longer occurs. We surmise that gelation may be prevented by a large concentration of hydrated iron oxide species which may reduce the iron cations availability for gelation. $FeBr_3$, which is an anhydrous salt, may be a good candidate for this experiment. However, gels from $FeBr_3$ are among the slowest forming, so this experiment would have to be carried out under anhydrous conditions to ensure minimal uptake of water from the environment. Gels with shorter gelation times are Fe-5nite-DMF and Fe-5nite-DMA, so these are possible choices. An anhydrous DMF or DMA must be used, although water will still be present from the hydrated salts.

It would be useful to determine the ligand to metal ion stoichiometry of the metallogels formed. This could be done by preparing fresh material, then soaking the gel in the appropriate solvent to remove excess ligand trapped in the gel. The iron could then be dissolved using an acid such as 1 M sulfuric acid, separating the ligand from the iron and measuring each component using gravimetric analysis.

A permeability study of the gel could be performed, whereby deuterated solvent is eluted to evaluate the diffusion of solvent through the gel. This may give better insight into the use of the gels for separation.

Additional indicators could be used for dye sorption, each with a different characteristic, for example positively or negatively charged dyes or radicals. This would give greater insight into the interactions within the gel pockets after adsorption. Dye separation could be carried out using the gels, as this study showed a difference in the adsorbance capacity of bromocresol green and methyl orange. *N*,*N*-dimethyl-4-(2-phenyldiazenyl)-benzenamine, brilliant green, and 4-phenyl-1,2,3,5-dithiadiazolyl radical are not good choices as these have been shown to interact with DMF. The radical degrades in DMF and brilliant green loses colour upon standing in solution. To counteract this, another solvent could be chosen however it will introduce the added complication of solvent exchange using two different solvents.

A greater understanding of the kinetics could be achieved through carrying out dye uptake experiments starting with different initial concentrations of dye. Pseudo-first and -second order kinetic models could be used to determine the best fit.[176]

Since those interesting materials are responsive to stimuli there are a number of ways in which this research could be extended in terms of potential applications. Treatment of waste water could investigated.

Rich possibilities abound to further explore these soft materials, as they have been shown to be responsive to stimuli.

References

[1] N. McCreesh, A. Gize and A. David, *J. Archaeol. Sci.*, 2011, **38**, 3432–3434.

[2] D. Jordan Lloyd, *Colloid Chemistry*, The Chemical Catalogue Co., New York, Alexander, edn., 1926, pp. 767–782.

[3] P. Terech and R. G. Weiss, *Chem. Rev.*, 1997, **97**, 3133–3160.

[4] T. Graham, *Philos. Trans. R. Soc. London*, 1861, **151**, 183–224.

[5] P. J. Flory, *Faraday Discuss. Chem. Soc.*, 1974, **57**, 7–18.

[6] J. W. Steed and J. L. Atwood, *Supramolecular Chemistry*, John Wiley & Sons, Ltd, Wiltshire, 2nd edn., 2009, pp. 888–893.

[7] J. W. Steed, *Chem. Commun.*, 2011, **47**, 1379–1383.

[8] P. Terech, G. Gebel and R. Ramasseul, *Langmuir*, 1996, **12**, 4321–4323.

[9] J. H. Jung, J. H. Lee, J. R. Silverman and G. John, *Chem. Soc. Rev.*, 2013, **42**, 924–936.

[10] P. Sutar and T. K. Maji, *Chem. Commun.*, 2016, **52**, 8055–8074.

[11] M.-O. M. Piepenbrock, N. Clarke and J. W. Steed, *Soft Matter*, 2011, **7**, 2412–2418.

[12] L. E. Buerkle and S. J. Rowan, *Chem. Soc. Rev.*, 2012, **41**, 6089–6102.

[13] M. Häring and D. D. Díaz, *Chem. Commun.*, 2016, **52**, 13068–13081.

[14] M.-O. M. Piepenbrock, G. O. Lloyd, N. Clarke and J. W. Steed, *Chem. Rev.*, 2010, **110**, 1960–2004.

[15] T. Graham, *J. Chem. Soc.*, 1864, **17**, 318–327.

[16] A. Y.-Y. Tam and V. W.-W. Yam, *Chem. Soc. Rev.*, 2013, **42**, 1540–1567.

[17] C. A. Offiler, C. D. Jones and J. W. Steed, *Chem. Commun.*, 2017, **53**, 2024–2027.

[18] A. Mallick, E.-M. Schön, T. Panda, K. Sreenivas, D. D. Díaz and R. Banerjee, *J. Mater. Chem.*, 2012, **22**, 14951–14963.

[19] T. H. T. Hsu, J. J. Naidu, B.-J. Yang, M.-Y. Jang and I. J. B. Lin, *Inorg. Chem.*, 2012, **51**, 98–108.

[20] W. J. Gee and S. R. Batten, *Chem. Commun.*, 2012, **48**, 4830–4832.

[21] G. Nandi, H. M. Titi, R. Thakuria and I. Goldberg, *Cryst. Growth Des.*, 2014, **14**, 2714–2719.

[22] C. K. Karan and M. Bhattacharjee, *ACS Appl. Mater. Interfaces*, 2016, **8**, 5526–5535.

[23] A.-Y. Tam, K.-C. Wong and V.-W. Yam, *Chem. - A Eur. J.*, 2009, **15**, 4775–4778.

[24] S. M. Ramalhete, K. P. Nartowski, N. Sarathchandra, J. S. Foster, A. N. Round, J. Angulo, G. O. Lloyd and Y. Z. Khimyak, *Chem. - A Eur. J.*, 2017, **23**, 8014–8024.

[25] P. Dastidar, *Chem. Soc. Rev.*, 2008, **37**, 2699–2715.

[26] J. H. van Esch, *Langmuir*, 2009, **25**, 8392–8394.

[27] G. O. Lloyd and J. W. Steed, *Soft Matter*, 2011, **7**, 75–84.

[28] M. O. M. Piepenbrock, N. Clarke and J. W. Steed, *Langmuir*, 2009, **25**, 8451–8456.

[29] M. H.-Y. Chan, M. Ng, S. Y.-L. Leung, W. H. Lam and V. W.-W. Yam, *J. Am. Chem. Soc.*, 2017, **139**, 8639–8645.

[30] S. Basak, J. Nanda and A. Banerjee, *Chem. Commun.*, 2356, **50**, 2356–2359.

[31] P. Byrne, G. O. Lloyd, L. Applegarth, K. M. Anderson, N. Clarke and J. W. Steed, *New J. Chem.*, 2010, **34**, 2261–2274.

[32] S. Bhattacharjee and S. Bhattacharya, *Chem. Commun.*, 1169, **50**, 11690–11693.

[33] C. Mondal, M. Ganguly, J. Pal, R. Sahoo, A. K. Sinha and T. Pal, *Chem. Commun.*, 2013, **49**, 9428.

[34] A. Gasnier, G. Royal and P. Terech, *Langmuir*, 2009, **25**, 8751–62.

[35] Y. Lan, M. G. Corradini, R. G. Weiss, S. R. Raghavan and M. A. Rogers, *Chem. Soc. Rev.*, 2015, **44**, 6035–6058.

[36] M. A. Rogers and R. G. Weiss, *New J. Chem.*, 2015, **39**, 785–799.

[37] C. D. Jones and J. W. Steed, *Chem. Soc. Rev.*, 2016, **45**, 6546–6596.

[38] H. Danjo, K. Hirata, S. Yoshigai, I. Azumaya and K. Yamaguchi, *J. Am. Chem. Soc.*, 2009, **131**, 1638–1639.

[39] F. Rodriguez-Llansola, B. Escuder, J. F. Miravet, D. Hermida-Merino, I. W. Hamley, C. J. Cardin and W. Hayes, *Chem. Commun.*, 2010, **46**, 7960–7962.

[40] M. D. Segarra-Maset, V. J. Nebot, J. F. Miravet and B. Escuder, *Chem. Soc. Rev.*, 2013, **42**, 7086–7098.

[41] G. Yu, X. Yan, C. Han and F. Huang, *Chem. Soc. Rev.*, 2013, **42**, 6697–6722.

[42] B. O. Okesola and D. K. Smith, *Chem. Soc. Rev.*, 2016, **45**, 4226–4251.

[43] L. Yan, G. Li, Z. Ye, F. Tian and S. Zhang, *Chem. Commun.*, 2014, **50**, 14839–14842.

[44] S. Sengupta and R. Mondal, *RSC Adv.*, 2016, **6**, 14009–14015.

[45] A. Dey, S. K. Mandal and K. Biradha, *CrystEngComm*, 2013, **15**, 9769–9778.

[46] S. Sengupta and R. Mondal, *J. Mater. Chem. A*, 2014, **2**, 16373–16377.

[47] J. Zhang, X. Wang, L. He, L. Chen, C.-Y. Su and S. L. James, *New J. Chem.*, 2009, **33**, 1070–1075.

[48] H. Lee, S. H. Jung, W. S. Han, J. H. Moon, S. Kang, J. Y. Lee, J. H. Jung and S. Shinkai, *Chem. - A Eur. J.*, 2011, **17**, 2823–2827.

[49] J. M. Tobin, T. J. D. Mccabe, A. W. Prentice, S. Holzer, G. O. Lloyd, M. J. Paterson, V. Arrighi, P. A. G. Cormack and F. Vilela, *ACS Catal.*, 2017, **7**, 4602–4612.

[50] S. Lacombe and T. Pigot, *Catal. Sci. Technol.*, 2016, **6**, 1571–1592.

[51] J. Lamberts and D. Neckers, *Tetrahedron*, 1985, **41**, 2183–2190.

[52] M. C. DeRosa and R. J. Crutchley, *Coord. Chem. Rev.*, 2002, **233-234**, 351–371.

[53] E. Díez-Mato, F. Cortezón-Tamarit, S. Bogialli and D. García-Fresnadillo, *Appl. Catal. B, Environ.*, 2014, **160-161**, 445–455.

[54] M. N. Chong, B. Jin, C. W. Chow and C. Saint, *Water Res.*, 2010, **44**, 2997–3027.

[55] Y. Paz, *Appl. Catal. B, Environ.*, 2010, **99**, 448–460.

[56] T. Hisatomi, J. Kubota and K. Domen, *Chem. Soc. Rev.*, 2014, **7520**, 7520–7535.

[57] A. Dhakshinamoorthy, S. Navalon, A. Corma and H. Garcia, *Energy Environ. Sci.*, 2012, **5**, 9217–9233.

[58] J. H. Lee, Y. E. Baek, K. Y. Kim, H. Choi and J. H. Jung, *Supramol. Chem.*, 2016, **28**, 870–873.

[59] S. Qiu and G. Zhu, *Coord. Chem. Rev.*, 2009, **253**, 2891–2911.

[60] C. Janiak and J. K. Vieth, *New J. Chem.*, 2010, **34**, 2366–2388.

[61] H.-C. Zhou, J. R. Long and O. M. Yaghi, *Chem. Rev.*, 2012, **112**, 673–674.

[62] H.-C. J. Zhou and S. Kitagawa, *Chem. Soc. Rev.*, 2014, **43**, 5415–5418.

[63] J. L. C. Rowsell and O. M. Yaghi, *Microporous Mesoporous Mater.*, 2004, **73**, 3–14.

[64] Y. Chen and S. Ma, *Dalt. Trans.*, 2016, **45**, 9744–9753.

[65] R. Matsuda, *Nature*, 2014, **509**, 434–435.

[66] Y.-B. Huang, J. Liang, X.-S. Wang and R. Cao, *Chem. Soc. Rev.*, 2017, **46**, 126–157.

[67] K. J. Hartlieb, J. M. Holcroft, P. Z. Moghadam, N. A. Vermeulen, M. M. Algaradah, M. S. Nassar, Y. Y. Botros, R. Q. Snurr and J. F. Stoddart, *J. Am. Chem. Soc.*, 2016, **138**, 2292–2301.

[68] M.-X. Wu and Y.-W. Yang, *Adv. Mater.*, 2017, **29**, 1606134.

[69] P. Horcajada, C. Serre, G. Maurin, N. A. Ramsahye, F. Balas, M. Vallet-Regí, M. Sebban, F. Taulelle and G. Férey, *J. Am. Chem. Soc.*, 2008, **130**, 6774–6780.

[70] W. Yang, A. J. Davies, X. Lin, M. Suyetin, R. Matsuda, A. J. Blake, C. Wilson, W. Lewis, J. E. Parker, C. C. Tang, M. W. George, P. Hubberstey, S. Kitagawa, H. Sakamoto, E. Bichoutskaia, N. R. Champness, S. Yang and M. Schröder, *Chem. Sci.*, 2012, **3**, 2993–2999.

[71] K. Sumida, D. L. Rogow, J. A. Mason, T. M. Mcdonald, E. D. Bloch, Z. R. Herm, T.-h. Bae and J. R. Long, *Chem. Rev.*, 2012, **112**, 724–781.

[72] *Cobalt (Co)*, 2017, https://www.britannica.com/science/cobalt-chemical-element.

[73] *Gallery Talk: Household Objects from Ancient Rome — Harvard Art Museums*, 2016, http://www.harvardartmuseums.org/visit/calendar/gallery-talk-household-objects-from-ancient-rome.

[74] *Iron - Element information, properties and uses — Periodic Table*, http://www.rsc.org/periodic-table/element/26/iron.

[75] S. C. Zacharias, *Cannon Cape Point 2016*, 2016.

[76] Q. Wei and S. L. James, *Chem. Commun.*, 2005, **24**, 1555–1556.

[77] S. K. Nune, P. K. Thallapally and B. P. McGrail, *J. Mater. Chem.*, 2010, **20**, 7623–7625.

[78] C. R. Groom, I. J. Bruno, M. P. Lightfoot and S. C. Ward, *Acta Crystallogr. Sect. B Struct. Sci. Cryst. Eng. Mater.*, 2016, **B72**, 171–179.

[79] *Universal Analysis 2000 for Windows 2000/XP/Vista.*

[80] P. Atkins and J. de Paula, *Atkins' Physical Chemistry*, Oxford University Press, Oxford, 8th edn., 2006, pp. 117–131.

[81] J. L. Ford and P. Timmins, *Pharmaceutical thermal analysis: Techniques and applications*, Ellis Horwood Limited, Chichester, 1989, p. 191.

[82] P. Atkins and J. de Paula, *Atkins' Physical Chemistry*, 2006, p. 674.

[83] *Soft Imaging Sysmtem GmbH: Digital Solutions for Imaging and Microscopy.*

[84] P. Pavia, G. M. Lampman and G. S. Kriz, *Introduction to Spectroscopy: A Guide for Students of Organic Chemistry*, Brooks/Cole Thomson Learning Inc., USA, 2001, pp. 353–366.

[85] *GCB Spectral*, 1998.

[86] P. Atkins, T. Overton, J. Rouke, M. Weller and F. Armstrong, *Shriver and Atkins, Inorganic Chemistry*, Oxford University Press, 4th edn., 2006, pp. 181–183.

[87] R. Biswas, H. Kuhne, G. Brudvig and V. Gopala, *Sci. Prog.*, 2001, **84**, 45–68.

[88] W. Gordy, *Theory and Applications of Electron Spin Resonance*, Wiley-Interscience, New York, 1980.

[89] F. A. Cotton and G. Wilkinson, *Advanced Inorganic Chemistry, A Comprehensive Text*, John Wiley & Sons, Ltd, London, 1962, pp. 714–718.

[90] J. Pilbrow, *Transition Ion Electron Paramagnetic Resonance*, Clarendon Press, Oxford, 1990, pp. 16–17.

[91] M. M. Maltempo, *J. Chem. Phys.*, 1974, **61**, 2540.

[92] C. Bovet and A. Barron, *ESR Spectroscopy: An Overview*, TheConnections Project, 2009, pp. 1–5.

[93] E. Duin, *Electron Paramagnetic Resonance Theory*, https://coraifeartaigh.files.wordpress.com/2008/04/epr.pdf.

[94] A. Lutskii, N. Kotelevaskii, O. Osipov and K. Zamaraev, *Teor. i Eksp. Khimiya*, 1968, **4**, 463–467.

[95] *Biological Magnetic Resonance. Volume 24. Biomedical EPR - Part B: Methodology, Instrumentation, and Dynamics*, ed. S. S. Eaton, G. R. Eaton and L. J. Berlinger, Kluwer Academic/Plenum Publishers, New York, 2005, pp. 24–25.

[96] *SAINT 7.60a*, Bruker AXS Inc, Madison, Wisconsin, USA, 2006.

[97] G. M. Sheldrick, *SADABS 2.05*, 2007.

[98] *XPREP, Data Preparation and Reciprical Space Exploration, 5.1.*, Bruker Analytical X-ray Systems, Madison, Wisconsin, USA, 1997.

[99] G. M. Sheldrick, *Acta Crystallogr. A.*, 2008, **64**, 112–122.

[100] *Oxford Diffraction. CrysAlis Pro; Rigaku Corporation*, 2017.

[101] C. F. Macrae, I. J. Bruno, J. A. Chisholm, P. R. Edgington, P. McCabe, E. Pidcock, L. Rodriguez-Monge, R. Taylor, J. van de Streek and P. A. Wood, *J. Appl. Crystallogr.*, 2008, **41**, 466–470.

[102] P. Atkins and J. de Paula, *Atkins' Physical Chemistry,*, Oxford University Press, Oxford, 8th edn., 2006, pp. 916–922.

[103] K. J. Laidler and J. H. Meiser, *Physical Chemistry*, Houghton Mifflin Company, 3rd edn., 1999, pp. 848 – 855.

[104] D. Young and A. Crowell, *Physical Adsorption of Gases*, Butterworths, London, 1962, pp. 3–5.

[105] S. Brunauer, L. S. Deming, W. E. Deming and E. Teller, *J. Am. Chem. Soc.*, 1940, **62**, 1723–1732.

[106] NPTEL, *NPTEL*, http://nptel.ac.in/courses/103103026/module1/lec3/2.html.

[107] G. Mezger, Thomas, *The Rheology Handbook*, Vincentz Verlag, Hannover, 2002, p. 13.

[108] *RheoSense*, 2016, http://www.rheosense.com/applications/viscosity/newtonian-non-newtonian.

[109] L. Gao, B. Zhao, G. Li, Z. Shi and S. Feng, *Inorg. Chem. Commun.*, 2003, **6**, 1249–1251.

[110] D. Min, S. Soo Yoon, J. Hwa Lee, M. Suh and S. W. Lee, *Inorg. Chem. Commun.*, 2001, **4**, 297–300.

[111] L. Wang, L. Duan, D. Xiao, E. Wang and C. Hu, *J. Coord. Chem.*, 2004, **57**, 1079–1087.

[112] D. Saha, D. K. Hazra, T. Maity and S. Koner, *Inorg. Chem.*, 2016, **55**, 5729–5731.

[113] K. Davies, S. A. Bourne, L. Ohrström and C. L. Oliver, *Acta Crystallogr. B.*, 2012, **68**, 528–535.

[114] X. Li, Y. Wang, Z. Ma, R. Zhang and J. Zhao, *J. Coord. Chem.*, 2010, **63**, 1029–1037.

[115] K. K. Gangu, S. Maddila, S. B. Mukkamala and S. B. Jonnalagadda, *Inorganica Chim. Acta*, 2016, **446**, 61–74.

[116] M. P. Suh, H. J. Park, T. K. Prasad and D.-W. Lim, *Chem. Rev.*, 2012, **112**, 782–835.

[117] U. Mueller, M. Schubert, F. Teich, H. Puetter, K. Schierle-Arndt and J. Pastré, *J. Mater. Chem.*, 2006, **16**, 626–636.

[118] F. A. Cotton and G. Wilkinson, *Advanced Inorganic Chemistry, A Comprehensive Text*, Interscience Publishers, Inc., London, 3rd edn., 1972, pp. 864–868.

[119] Phenomenex, *Solvent Miscibility Table*, https://erowid.org/archive/rhodium/pdf/solvent.miscibility.pdf.

[120] G. M. Peters, L. P. Skala, T. N. Plank, B. J. Hyman, G. N. Manjunatha Reddy, A. Marsh, S. P. Brown and J. T. Davis, *J. Am. Chem. Soc.*, 2014, **136**, 12596–12599.

[121] A. Kaufman, C. Afshar, M. Rossi, D. E. Zacharias and J. P. Glusker, *Struct. Chem.*, 1993, **4**, 191–198.

[122] C. M. Flynn Jr., *Chem. Rev.*, 1984, **84**, 31–41.

[123] H. Yang, R. Lu, R. T. Downs and G. Costin, *Acta Crystallogr. Sect. E Struct. Reports Online*, 2006, **62**, i250–i252.

[124] S. Xiang, L. Li, J. Zhang, X. Tan, H. Cui, J. Shi, Y. Hu, L. Chen, C.-Y. Su and S. L. James, *J. Mater. Chem.*, 2012, **22**, 1862–1867.

[125] H. B. Aiyappa, S. Saha, B. Garai, J. Thote, S. Kurungot and R. Banerjee, *Cryst. Growth Des.*, 2014, **14**, 3434–3437.

[126] W. Kuhn, E. Peterli and H. Majer, *J. Polym. Sci.*, 1955, **16**, 539–548.

[127] P. Atkins and J. de Paula, *Atkins' Physical Chemistry*, Oxford University Press, Oxford, 2006, p. 645.

[128] N. B. Colthup, L. H. Daly and S. E. Wiberley, *Introduction to infrared and Raman spectroscopy*, Academic Press, 3rd edn., 1990, p. 350.

[129] B. C. Smith, *Infrared spectral interpretation: a systematic approach*, CRC Press LLC, Boca Raton, Florida, 2000, pp. 50, 102, 141–145.

[130] T. Tu, W. Fang, X. Bao, X. Li and K. H. Dötz, *Angew. Chemie Int. Ed.*, 2011, **50**, 6601–6605.

[131] P. Fejes, I. Kiricsi, K. Lázár, I. Marsi, A. Rockenbauer, L. Korecz, J. B. Nagy, R. Aiello and F. Testa, *Appl. Catal. A Gen.*, 2003, **242**, 247–266.

[132] E. G. Derouane, S. Detrewrie, Z. Gabelica and N. Blom, *Appl. Catal.*, 1981, **1**, 201–224.

[133] G. A. Bain and J. F. Berry, *J. Chem. Educ.*, 2008, **85**, 532–536.

[134] D. Kuter, S. J. Benjamin and T. J. Egan, *J. Inorg. Biochem.*, 2014, **133**, 40–49.

[135] B. N. Figgis and R. S. Nyholm, *J. Chem. Soc.*, 1958, 4190–5216.

[136] C. Wang, Q. Chen, F. Sun, D. Zhang, G. Zhang, Y. Huang, R. Zhao and D. Zhu, *J. Am. Chem. Soc.*, 2010, **132**, 3092–3096.

[137] J. J. Panda, A. Mishra, A. Basu and V. S. Chauhan, *Biomacromolecules*, 2008, **9**, 2244–2250.

[138] M. M. Taqui Khan and A. E. Martel, *J. Am. Chem. Soc.*, 1967, **89**, 4176–4185.

[139] G. S. Laurence and K. J. Ellis, *J. Chem. Soc. Dalt. Trans.*, 1972, 1667–1670.

[140] V. A. Mallia and R. G. Weiss, *Soft Matter*, 2016, **12**, 3665–3676.

[141] B. Jiang, L.-J. Chen, G.-Q. Yin, Y.-X. Wang, W. Zheng, L. Xu and H.-B. Yang, *Chem. Commun.*, 2017, **53**, 172–175.

[142] S. L. James and T. Friščić, *Chem. Commun.*, 2013, **49**, 5349.

[143] L. Xie, S. Liu, C. Gao, R. Cao, J. Cao, C. Sun and Z. Su, *Inorg. Chem.*, 2007, **46**, 7782–7788.

[144] R. G. Weiss and P. Terech, *Molecular Gels Materials with Self-Assembled Fibrillar Networks*, Springer, Dordrecht, 2006.

[145] R. C. T. Howe, A. P. Smalley, A. P. M. Guttenplan, M. W. R. Doggett, M. D. Eddleston, J.-C. C. Tan and G. O. Lloyd, *Chem. Commun.*, 2013, **49**, 4268–4270.

[146] N. Cheng, Q. Hu, Y. Guo, Y. Wang and L. Yu, *ACS Appl. Mater. Interfaces*, 2015, **7**, 10258–10265.

[147] B. Xing, M.-F. Choi, Z. Zhou and X. Bing, *Langmuir*, 2002, **18**, 9654–9658.

[148] S. Deng, H. Xu, X. Jiang and J. Yin, *Macromolecules*, 2013, **46**, 2399–2406.

[149] B. Adhikari, G. Palui, A. Banerjee, A. Moreac, C. Valéry, V. Marchi-Artzner, T. Weiss, A. Renault, M. Paternostre and F. Artzner, *Soft Matter*, 2009, **5**, 3452.

[150] F. Ibney Hai, K. Yamamoto and K. Fukushi, *Crit. Rev. Environ. Sci. Technol.*, 2007, **37**, 315–377.

[151] P. K. Sukul and S. Malik, *RSC Adv.*, 2013, **3**, 1902–1915.

[152] E. J. Cho, I. Y. Jeong, S. J. Lee, W. S. Han, J. K. Kang and J. H. Jung, *Tetrahedron Lett.*, 2008, **49**, 1076–1079.

[153] A. B. Hu, H. Zhou, Z. Q. Pan and Q. R. Cheng, *J. Porous Mater.*, 2016, **23**, 663–669.

[154] S. Samai and K. Biradha, *Chem. Mater.*, 2012, **24**, 1165–1173.

[155] D. J. Duchamp and R. E. Marsh, *Acta Crystallogr. Sect. B Struct. Crystallogr. Cryst. Chem.*, 1969, **B25**, 5–19.

[156] A. Domenicano, G. Schultz, I. Hargittai, M. Colapietro, G. Portalone, P. George and C. W. Bock, *Struct. Chem.*, 1990, **1**, 107–122.

[157] N. M. Sykes, H. Su, E. Weber, S. A. Bourne and L. R. Nassimbeni, *Cryst. Growth Des.*, 2017, **17**, 819–826.

[158] *Separations and Reactions in Organic Supramolecular Chemistry;*, ed. F. Toda and R. Bishop, Wiley, Chichester, 2004.

[159] G. Gokel, *Crown Ethers & Cryptands. Monographs in Supramolecular Chemistry*, Royal Society of Chemistry, Cambrodge, 1991.

[160] G. R. Desiraju and T. Steiner, *The Weak Hydrogen Bond in Structural Chemistry and Biology*, Oxford University Press, Oxford, 2001.

[161] M. C. Etter, J. C. MacDonald and J. Bernstein, *Acta Crystallogr. B.*, 1990, **B46**, 265–262.

[162] P. Laine, A. Gourdon and J.-P. Launay, *Inorg. Chem.*, 1995, **34**, 5156–5165.

[163] L. Loots and L. J. Barbour, in *Importance Pi-Interactions Cryst. Eng.*, ed. E. Tiekink and J. Zukerman-Schpector, John Wiley & Sons, Ltd, Chichester, 2012, ch. 4, pp. 109–124.

[164] J. Bernstein, *Polymorphism in Molecular Crystals*, Clarendon Press, Oxford, 2002, pp. 40–41.

[165] H. S. Huh and S. W. Lee, *Bull. Korean Chem. Soc.*, 2006, **27**, 1839–1843.

[166] S. S. Lande and J. K. Kochi, *J. Am. Chem. Soc.*, 1968, **90**, 5196–5207.

[167] H. S. Huh and S. W. Lee, *Bull. Korean Chem. Soc.*, 2008, **29**, 2383–2389.

[168] X.-M. Zhang, *Coord. Chem. Rev.*, 2005, **249**, 1201–1219.

[169] Z.-B. Han, X.-N. Cheng, X.-F. Li and X.-M. Chen, *Zeitschrift für Anorg. und Allg. Chemie*, 2005, **631**, 937–942.

[170] Y. Yan, C.-D. Wu and C.-Z. Lu, *Zeitschrift fur Anorg. und Allg. Chemie*, 2003, **629**, 1991–1995.

[171] P. Lof, *Minerals of the World*, 1983.

[172] *Cell_now*, Bruker AXS Inc, Madison, Wisconsin, USA, 2008.

[173] G. M. Sheldrick, *TWINABS*, University of Gottingen, Germany, 2001.

[174] A. G. Orpen, L. Brammer, F. H. Allen, O. Kennard, D. G. Watson and R. Taylor, *J. Chem. Soc. Dalt. Trans.*, 1989, **0**, S1–S83.

[175] F. A. Cotton and G. Wilkinson, *Advanced Inorganic Chemistry, A Comprehesive Test*, John Wiley & Sons, Ltd, 3rd edn., 1972, pp. 644–645.

[176] E. Rojas Garcí, R. L. Medina, M. M. Lozano, I. As, H. Pé Rez, M. J. Valero and A. M. M. Franco, *Materials (Basel).*, 2014, **7**, 8037–8057.